Spectroscopic and electrochemical studies of models of the cell membrane envelope of Gram-negative bacteria

(Spektroskopische und elektrochemische Studien zu Modellen der Zellhülle Gram-negativer Bakterien)

der Fakultät für Mathematik und Naturwissenschaften
der Carl von Ossietzky Universität Oldenburg
zur Erlangung des Grades und Titels eines

Doktors der Naturwissenschaften (Dr. rer. nat.)

angenommene Dissertation

von Herrn **Bishoy Khairalla**, M.Sc.
geboren am 22.03.1989 in Alexandria

Oldenburg, Februar 2022

This research for this Ph.D. thesis was carried out from January 2017 to March 2020 at the Carl von Ossietzky University of Oldenburg, School of Mathematics and Sciences, Department of Chemistry, under the supervision of PD Dr. Izabella Brand in laboratories of Prof. Dr. Gunther Wittstock. The research was enriched by a collaboration with Prof. Dr. Slawomir Sek from University of Warsaw, Faculty of Chemistry, Biological and Chemical Research Center in Warsaw in Poland. This research project was funded by DFG (project number BR 3961-4). DAAD (project number 57215882) facilitated the scientific cooperation with Prof. Dr. Slawomir Sek.

Erstgutachter: PD Dr. Izabella Brand
Zweitgutachter: Prof. Dr. Gunther Wittstock
Zusätzliches Gutachten: Prof. Dr. Rüdiger Beckhaus
Tag der Disputation: 07.07.2022

Acknowledgment

First of all, I would like to express my deep gratitude to my supervisor PD Dr. Izabella Brand for the opportunity to do research in a fascinating field of science with a clear connection to applied sciences. PD Dr. Izabella Brand corrected my thesis, helped me in the analysis of PM IRRAS data and answered all my questions with such patience.

My thanks go to members of my examination committee, PD Dr. Izabella Brand, Prof. Dr. Gunther Wittstock and Prof. Dr. Rüdiger Beckhaus for their time in reading and criticizing my thesis.

Also I would like to thank Prof. Dr. Gunther Wittstock for the opportunity to work in his laboratories with his international research group. I also want to thank my former group members for the productive atmosphere and many inspiring conversations.

Special thank is addressed to Prof. Dr. Slawomir Sek and Dr. Joanna Juhaniewicz-Debinska from the University of Warsaw in Poland for their help, fruitful discussions and an overall very enjoyable time during my electrochemical AFM measurements in Warsaw.

Many thanks go to Prof. Dr. Vlad Zamlynny for sharing OpticalConstants and Fresnel comutation programs.

I would like to express sincere appreciation to my wife Marina and my family for the unconditional support without which my studies and this work would not have been possible.

Last but not least, I want to thank the Deutsche Forschungsgemeinschaft (DFG) for financial support (BR 3961-4).

Abstract

Langmuir-Blodgett and Langmuir-Schaefer (LB-LS) transfers are used to deposit asymmetric lipid bilayers mimicking the composition of the inner (IM) and the outer membrane (OM) of Gram-negative bacteria onto the Au(111) electrode surface.

Results of electrochemically controlled polarization modulation infrared reflection absorption spectroscopy (PM IRRAS) and quartz crystal microbalance with energy dissipation studies reveal two different types of electric potential-dependent structural rearrangements in models of the IM. They are correlated to the geometry of the lipid molecule.

An asymmetric 1-palmitoyl-2-oleoyl-*sn*-glycero-3-phosphoethanolamine (POPE) - di[3-deoxy-D-mannooctulosonyl]-lipid A (KLA) bilayer models the OM. Observed changes in the orientation of the hydrocarbon chains in hydrogenated POPE-KLA bilayer reflect rearrengements in the outer KLA leaflet.

In situ PM IRRAS results show that melittin interacts not only with the polar head group in KLA, but also with the hydrophobic region of the POPE-KLA bilayer.

Zusammenfassung

Langmuir-Blodgett und Langmuir-Schaefer (LB-LS) Methoden werden verwendet, um die asymmetrische Lipiddoppelschichten, die innere (IM) und äußere Membran (ÄM) von Gram-negativen Bakterien modellieren, auf Au(111) Elektrodenoberfläche herzustellen.

Ergebnisse der elektrochemisch kontrollierten Polarisationsmodulation-Infrarotreflexionsabsorptionsspektroskopie (PM IRRAS) und Quarzkristallmikrowaage mit Energiedissipation zeigen zwei verschiedene Arten von potentialabhängigen Strukturänderungen in den Modelmembranen. Diese Charakteristik hängt von der Geometrie der Lipidmoleküle ab.

Eine asymmetrische 1-palmitoyl-2-oleoyl-*sn*-glycero-3-phosphoethanolamin (POPE) - Di[3-desoxy-D-mannooctulosonyl]- Lipid A (KLA) Doppelschicht modelliert die ÄM. Die Änderungen der Kettenneigung in der POPE-KLA Membran zeigen eine Umorientierung der Kohlenwasserstoffketten in der äußeren KLA Schicht.

In situ PM IRRAS Ergebnisse zeigen, dass Melittin nicht nur mit der polaren Kopfgruppe in KLA interagiert, sondern auch mit der hydrophoben Region der POPE-KLA Doppelschicht.

Table of Contents

1 Introduction

A biological cell membrane is the most common interface in nature.[1–7] All cells have a plasma membrane, which gives the shape to the cell and regulates the transport between the cell and the outside environoment. Microb's cell envelope may contain one (Gram-positive bacteria) or two (Gram-negative bacteria) membranes. Due to the complex composition and structure, cell membranes are difficult to study. Therefore, fabrication model of cell membranes becomes an important research object.[1–7] In its natural environoment, a natural cell membrane is exposed to high electric fields in order of 10^5 to 10^9 V m^{-1}.[8] To provide physiological electric fields to model membranes, the application of electrochemical techniques is essential.[1–7] Electrochemical methods provide physical data such as the capacitance, charge and potential drop across the membrane adsorbed on the electrode surface.[9–13] A combination of infrared spectroscopy (IRS) and electrochemical methods gives the possibility to monitor simultaneously potential-dependent changes in the structure, hydration and orientation of lipid molecules in realistic models of lipid bilayers and their interaction with peptides.[9–13]

Reflection-based IRS techniques provide the opportunity to analyze the structure of lipids and proteins. Since various functional groups absorb the infrared (IR) light at specific frequencies, a sub-molecular level analysis of a supramolecular assembly of lipids and proteins is possible. Additionally, reflection-based IRS techniques have successfully been applied for the analysis of the electrode|electrolyte interface.[14–17] However, reflection-based IRS techniques do not provide information about changes in water content in the lipid bilayers. For this reason, other techniques, e.g, X-ray reflectometry (XR), neutron relectometry (NR), quartz crystal microbalance with energy dissipation (QCM-D) are used.[18–21] These methods and reflection-based IRS techniques provide information on changes of the orientation, hydration of lipid molecules and changes in water content in the bilayer, providing a molecular scale picture of potential-dependent changes in the entire supramolecular assembly.

A cell membrane of Gram-negative bacteria interacting with antimicrobial peptides (AMPs) represents a complex supramolecular asssemply. A perfect antimicrobial peptide drug should act selectively on bacterial cell membranes and not attack the host cell membranes.[22,23] In 1920, the first AMPs which led to cell-lytic were isolated.[24,25] Now,

hundreds of natural or synthetic AMPs are known.[26] Peptide-membrane interactions are involved in numerous biological processes, such as antimicrobial defense mechanisms, viral translocation, membrane fusion, transport of therapeutic compounds and disruption of integrity of membranes.[26–30] During peptide-membrane interactions, both the peptide and the membrane undergo series of structural changes. Thus, experimental studies of the peptide-membrane interactions are very difficult.

The peptide-membrane interaction was studied in literature.[13,31–33] Even less is known about the impact of the membrane potentials on the interacton between lipids and peptides (proteins). The lipid-peptide interactions may lead to phase transitions of the hydrocarbon chains in lipid molecules, change the thickness of the membrane and water content in the membrane.[34,35] Electrochemical studies showed a significant increase in the permeability of cell membranes to electroactive ions upon AMPs binding.[36,37] Insertion of AMPs into the lipid membrane occurs according to different mechanisms.[27,34,38–42] The interaction with the cell membrane involves electrostatic interactions and adsorption of peptides on the surface of cell membranes. PM IRRAS was used to investigate the interaction of model cell membranes with melittin.[36,43] Melittin is an example of membrane-active peptide.[27,36,43] It is a major toxic component in the venom of the European honeybee *Apis mellifera*.[44] It displays high antimicrobial[28] and antiviral[45,46] activities.

This thesis describes changes in the capacitance, structure and orientation of the lipid molecules in the model IM and OM of Gram-negative bacteria exposed to changing potentials and interacting with melittin. The OM of Gram-negative bacteria is the first contact surface for melittin. It was proposed that the selectivity of AMPs depends on the lipid composition of the bacterial cell membranes.[26] Bacterial membranes contain a large amount of negatively charged lipids, which are supposed to interact electrostatically with cationic antibacterial peptides.

The goal of this thesis is to understand details of the interaction between the model of biological membranes and AMPs.[23–26] Chapter 2 provides an overview on model of the cell membranes and their relevance for biomimetic studies. Chapter 3 describes the three main experimental techniques used in this thesis: LB-LS transfer, electrochemical methods and PM IRRAS. All three techniques have a wide range of applications in many fields of research resulting in a variety of their modalities and specialized approaches to suit particular types of experiments. Therefore, the most basic general principles of the

studied methods are explained with emphasis on aspects relevant to the characterization of lipid bilayers. The experimental methods and procedures are described in chapter 4. In chapter 5, results of studying the model IM and OM of Gram-negative bacteria and their interaction with melittin are presented. Conclusions and an outlook are summarized in chapter 6.

2 Overview on biological membranes and their interaction with peptides

2.1 Biological cell membrane

Ultrathin films of water-insoluble surfactants are scientifically interesting and find applications in molecular electronics devices[47,48] as well as in chemical, biochemical and physical sensors.[48,49] One of the scientific interests in these ultrathin films comes from their close resemblance to cell membranes. Natural cell membranes contain many components that accomplish different functions, making these membranes difficult to study.[1] Therefore, models of these membranes are used in research.[4,5,50–54]

A biological cell membrane is a highly complex system, 5-6 nm thick and largely composed of lipids, proteins and carbohydrates (Figure 1).[55–57] Proteins are embedded into a lipid bilayer.[49,55,56,58] Carbohydrates are covalently bound to either proteins or lipids and represent less than 10% of the membrane weight.[57] There is a need and a strong interest to understand properties of the lipid bilayers and how electric fields affect the lipid bilayer structure.[2] The cell membrane is a semipermeable membrane, which regulates the transport of substances to and from a cell.[55,59–62] It separates the interior of the cell from the extracellular environoment.[61–63] In addition, the cell membrane plays an important role in cell signaling and anchoring the cytoskeleton to provide the shape to the cell.[55,59–63] In 1895, Overton investigated the osmotic properties of cells, where the diffusion of water and solvents took place through a semipermeable membrane.[64] He proposed that the cell membrane is composed of phospholipids and cholesterol.[64] In 1917, Langmuir indicated that interactions between the lipid molecules are important to determine the supramoleculer level structures.[65] In 1925, Gorter and Grendel domenstrated that the basic structure of biological cell membranes is probably a lipid bilayer, where cell membranes are composed of two oppositing thin monolayers.[60] The earliest model of the biological membrane was proposed by Danielli and Davson in 1935.[66] They took into account that proteins adsorb to the lipid layers, separating lipid leaflets from each other.[66] In 1958, Robertson confirmed these models based on electron microscopy data.[67] He has determined that the dark electron dense bands belong to head groups and proteins of two opposed lipid monolayers.[67] The fluid mosaic model was

proposed in 1972 by Singer and Nicolson.[68,69] In this model, phospholipids are arranged in the bilayer with their polar head groups facing outwards to the aqueous environment and their hydrophobic tails forming the bilayer interior (Figure 1). Membrane proteins are divided into two classes: peripheral and integral proteins (transport and transmembrane proteins).[68,69] Membrane proteins may adsorb to one side of the membrane (peripheral) or span through the membrane (integral proteins) (Figure 1). Singer and Nicolsen noted that the biological membrane is most likely asymmetric.[68,69] In 1984, Mouritsen and Bloom proposed a mattress model.[63] It is a thermodynamic model, which is based on the description of phase digrams of the lipid bilayer mixtures and proteins.[63] The basic variables of this model are the thickness of the hydrophobic region of the lipid bilayer and the length of the hydrophobic region of the protein.[63] The mismatch concept is an important part of this model for the hydrophobic regions of lipids and proteins.[63] In 1997, Simons and van Meer proposed the presence of lipid rafts in the lipid fluid matrix.[70–72] Cholesterol and glycolipids are able to form micro domains in a fluid lipid matrix that are densely packed and ordered.[70–72] These lipid rafts have an important role in cell signaling.[70–72]

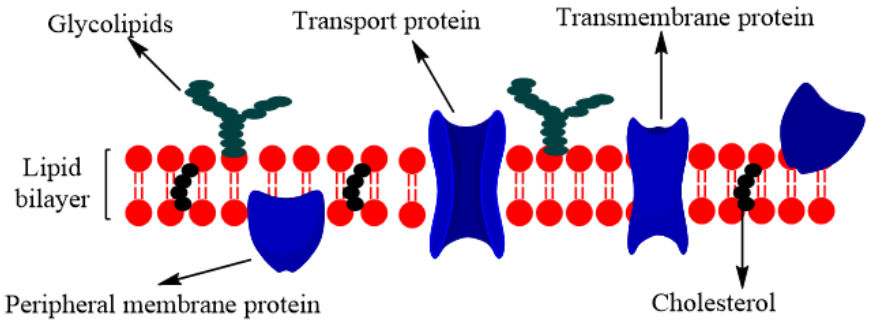

Figure 1: Scheme of the natural cell membrane.

The membrane fluidity influences membrane-protein interactions.[55,59] The fluidity is affected by temperature,[73,74] cholesterol content[54,75–77] and lipid composition.[78] At low temperature, hydrocarbon chains of the lipid bilayer can pack closely together to adopt with *all-trans* conformation, typical for a gel phase.[73,74] As temperature increases, the hydrocarbon chains gain *gauche* conformation and undergo a transition to a liquid phase.[73,74] The presence of unsaturated chains does not allow for a close packing of chains in lipids, so the bilayer fluidity is increased.[78] Phospholipid molecules have a hydrophilic

head group, containing phosphate moiety, an alcohol and usually two hydrocarbon chains, which are attached to this alcohol by ester linkages. Phospholipids are classified into two classes based on an alcohol present in their backbone. They are glycerophospholipids and sphingophospholipids. Glycerophospholipids contain glycerol as an alcohol in their backbone and sphingophospholipids have sphingosine as an alcohol. The hydrocarbon chains may vary in length and typically contain between 12 and 20 carbon atoms. They can be unsaturated or saturated.[47,61,62]

Lipid bilayers supported on a solid surface are attractive models of biological membranes.[4,5,50–54,79] These models have been investigated in recent years.[6,52–54,58,80–83] Three methods are used to prepare supported lipid bilayers:[84–87] spontaneous vesicles spreading,[3,4,52,84] LB-LS transfer[5,50,80,85] and tethered lipid bilayers[86,87]. In 1984, Brain and McConnel demonstrated that the small unilamelar vesicles spread to form a lipid bilayer on a solid surface.[84] Preparation procedures were elaborated for asymmetric vesicles containing different lipids in the inner and outer leaflets.[88,89] The packing of the lipid molecules produced by vesicles spreading is difficult to control. Easy preparation procedure and presence of water on both sides of the membrane increased the usage of the vesicle spreading method. The presence of water on both side of the lipid bilayer is necessary for the incorporation of integral proteins into the lipid bilayer to avoid protein denaturation.[1] Morever, the transport of ions across the lipid bilayer is possible only via ion channels, if an aqueous layer is interposed between the lipid bilayer and the solid surface.[1] In 1985, Tamm and McConnel showed that the LB-LS transfer led to a formation of a well organized lipid bilayer on solid surfaces.[85] LB-LS transfer provides symmetric and asymmetric lipid bilayers.[85] This technique allows controlling the packing and the physical state of the lipid molecules.[85] In addition, LB-LS transfer is a highly reproducible procedure.[85] One of disadvantages of the use of LB-LS transfer method arises from a direct contact of the lipid molecules with a solid surface. Preparation of tethered lipid bilayers represents an alternative method, which results in the separation of the lipid bilayers from a solid surface.[86,87,90,91] Formation of the tethered lipid bilayers provides high stability to the bilayer and ensures a separation of the bilayer from the solid surface, providing an aqueous environoment on the both sides of the model

membrane.[86,87,90,91] One of disadvantages of the use of this method arises from complex preparation procedures.

Surface sensitive techniques, IRS[3–5,52] and atomic force microscopy (AFM)[74,92–94] are used to study the supported lipid bilayers. Cellular lipids and proteins are constantly exposed to static electric fields in the order of 10^5 to 10^9 V m^{-1}.[8] The high electric fields may cause charge separation, structural rearrengements of molecules in the membrane and eventually lead to membrane breakdown.[8,95] Studies of the electrical properties of lipid membranes have been carried out using capacitance,[96–100] conductivity and charge density[6,7,19,101] measurements. It is important to deposit the lipid bilayers onto metal electrode surfaces. The interaction of a lipid bilayer with the supporting substrate affects its biophysical properties. Lipkowski[2] has studied the structure of lipid bilayers on Au(111) electrodes. The physical state of a lipid bilayer is mainly determined by the length and the degree of saturation of the lipid hydrocarbon chains.[102] In mammalian cell membranes, attractive interactions can lead to the formation of cholesterol-phospholipid domains between cholesterol and phospholipids with saturated hydrocarbon chains, which exist in a liquid-ordered phase.[103–105] Lipid mixtures containing two or more components have often been selected for fabrication of the cell membrane models. PE, phosphatidylcholines (PC) and anionic phospholipids such as phosphatidylserine (PS) are found in inner leaflet of the mammalian cell membranes, whereas sphingomyelin and cholesterol are the dominant components in outer leaflet.[106] Capacitance measurements have shown that the 1,2-dimyristoyl-*sn*-glycerol-3-phosphoethanolamine (DMPE) film undergoes a phase transition, similar to that observed for 1,2-dimyristoyl-*sn*-glycerol-3-phosphatidylcholine (DMPC).[6] In addition, the DMPE bilayers have a lower capacitance than the DMPC bilayers.[6] Madrid et al.[6] have investigated the effect of the head group size of the lipid molecules on the molecule packing in the DMPE and DMPC bilayers. DMPE has the same hydrocarbon chains as DMPC.[6] The head group in DMPE is smaller than in DMPC.[6] The smaller head group allows for a closer packing of the DMPE molecules and thus is responsible for an almost vertical orientation of the hydrocarbon chains.[6] The tighter packing of DMPE molecules reduces the permeability to water and ions and increases slightly the bilayer thickness.[6] *In situ* PM IRRAS measurements showed that the tilt angle for DMPE chains is 17° vs. the surface normal, which is smaller than that reported for DMPC chains (20° - 24°).[6] The average tilt is 82.5° for the ester

carbonyl group in the DMPE bilayers. It indicates that the ester carbonyl groups lye almost parallel to the surface normal.[6] It is consistent with a small tilt angle of the DMPE hydrocarbon chains.[6] Cholesterol modifies the fluidity and the electrical properties of the DMPC bilayers.[2] Yuan et al.[92] have successfully demonstrated the coexistence of the ordered and disordered phases in 1,2-dioleoyl-*sn*-glycero-3-phosphocholine (DOPC) and 1,2-dipalmitoyl-*sn*-glycero-3-phosphocholine (DPPC) bilayers on mica surface by means of AFM. They investigated the diffusion of the lipid molecules in the inner and outer leaflets of the DOPC-DPPC bilayer.[92] The DOPC lipid molecules flip-flopped to the outer leaflet from the inner leaflet, as evidenced by fluorencence contrast and height changes in the outer leaflet DPPC domains.[92] Molecule-molecule interactions and molecule-substrate interactions were also investigated by means of force mapping and correlation with other imaging results.[92] The lateral diffusion of the lipid molecules was found to occur more slowly in the inner leaflet than in the outer leaflet, indicating that the interaction between the lipid molecules and the solid surface restrict the mobility of the lipid molecules on the mica surface.[92] Zawisza et al.[5,52] have compared the properties of the DMPC bilayer formed by the LB-LS method with the properties of the bilayer produced by vesicle spreading. LB-LS method provides DMPC bilayer with a control of the packing and the physical state of the DMPC molecules.[5,52] Independent of the preparation method, pure DMPC bilayers adsorbed on the Au(111) electrode have a high capacitance (6 - 9 $\mu F\ cm^{-2}$).[52–54] In addition, AFM measurements showed that the thickness of 4.2 and 5.1 nm in the DMPC bilayers prepared by vesicle spreading and LB-LS transfer, respectively.[107,108] In the LB-LS transferred DMPC bilayers, the average tilt of the hydrocarbon chains is 25° vs. the surface normal. However, in the DMPC bilayers obtained by vesical spreading the average tilt is 55° vs. the surface normal. Addition of cholesterol led to a decrease in the DMPC-cholesterol bilayers capacitance to 1.7 and 2.2 $\mu F\ cm^{-2}$ when the lipid bilayer is prepared by the LB-LS transfer and vesicle spreading, respectively.[53,109,110] Thus, a large decrease in the capacitance was observed when cholesterol was introduced into the lipid bilayers. The addition of cholesterol improves the order of the hydrocarbon chains for the DMPC bilayer. The average tilt decreases for the hydrocarbon chains in the adsorbed state to 30° and 22° in the DMPC-cholesterol bilayers prepared by vesicle spreading and LB-LS transfer, respectively.[53,109,110] Zawisza et al.[51] have transferred the DMPC bilayers on SiO_2|Au and Au surfaces using LB-LS

transfer. On the Au surface, the hydrocarbon chains exist in a liquid phase having *gauche* conformations.[51,111] When the DMPC bilayer is transferred onto the SiO_2|Au surface, the hydrocarbon chains exist in a ripple phase.[51,112] Thus, the supported metal surface has an effect on the structure of the DMPC bilayer formation by LB-LS transfer.[51] In addition, Garcia-Araez et al.[80] have performed studies on the bilayer formed by the LB-LS transfer building a model membrane in which the inner leaflet consisted of 1,2-dimyristoyl-d54-*sn*-glycerol-3-phoshocholine (d-DMPC) and the outer leaflet of DMPC. The use of d-DMPC molecules allowed an investigation of the orientation of the lipid moelcules in each leaflet of the bilayer.[9,109,110] PM IRRAS studies have shown that the tilt angle is smaller for the hydrocarbon chains in the inner leaflet (d-DMPC) than that of the outer leaflet (h-DMPC).[80] Madrid et al.[7] have studied the 1,2-dimyristoyl-*sn*-glycero-3-phospho-L-serine (DMPS) bilayers transferd by LB-LS deposition on the Au(111) electrode with *in situ* PM IRRAS and electrocochemical measurements. DMPS lipid molecules have a similar size and shape to DMPE lipids, but they differ in their polar head groups region. DMPS is an anionic phospholipid, while DMPE is a zwitterion. Their electrochemical properties are different. The DMPS bilayers have a minimum capacitance of 9 - 10 μF cm^{-2}. This capacitance is higher than that reported for the DMPE bilayer (2 - 3 μF cm^{-2}).[7] PM IRRA spectra showed that, in contrast to DMPE, the DMPS head groups are very well hydrated.[7]

2.2 Bacterial cell membrane

Bacterial cell membranes have a complex composition and structure.[113] Figure 2 shows schematically the structure of the cell membranes of Gram-positive and Gram-negative bacteria. The cell membrane of Gram-positive bacteria is composed of a single lipid bilayer.[114] The outer leaflet of the membrane of Gram-positive bacteria is surrounded by a 20 - 80 nm thick peptidoglycan layer (Figure 2a).[114] The cell membrane of Gram-negative bacteria is composed of two lipid bilayers: the IM and OM membranes (Figure 2b).[113,115,116] Both membranes are separated by ca. 8 nm thick hydrophilic peptidoglycan layer.[113,117] PE and PG compose both leaflets of the IM.[113,116] The IM of Gram-negative *E.coli* bacteria contains 70 - 80% PE, 20 - 25% PG and 5% cardiolipin.[55,113] Konarzewska et al.[94] have characterized the lipid bilayers composed of PE and PG as a model of IM of

E.coli. Vesicle spreading to a bilayer is a multistep process, as observed from *in situ* AFM imaging.[94] Wydro et al.[118] have investigated the influence of the PE hydrocarbon chains structure on PE miscibility with PG in Langmuir monolayers. Strong attractions were obtained resulting from the formation of hydrogen bonds in the mixed monolayers containing dipalmitoylphosphatidylglycerol (DPPG) and PE with saturated hydrocarbon chains [dopalmitoylphosphatidylethanolamine (DPPE) and distearoylphosphatidyl-ethanolamine (DSPE)].[118] These attractions slightly increased with an increase in the length of the hydrocarbon chains of PE. The presence of double bonds in the hydrocarbon chains of 1,2-diplamitoleoyl-*sn*-glycero-3-phosphoethanolamine (DOPE) prevents the DOPE molecules from a tight packing.[118] The unsaturation of the hydrocarbon chains increases the fluidity of the monolayer.[118]

The OM has an asymmetric structure.[115,119,120] The inner leaflet has a similar composition to the IM. Lipopolysaccharides (LPS) are present in the outer leaflet of the OM of Gram-negative bacteria (Figure 2b).[113,115,119] LPS have a protecting function. Lipid A is an amphiphilic part of LPS and its structure varies between bacteria.[113] The polar head group of the lipid A from *E.coli* contains β-(1,6)-linked glucosamine disaccharide backbone.[119] The phosphate, carboxylic and hydroxyl groups in LPS increase the overall negative charge of the cell membrane, which can interact with the divalent cations present in the surrounding environement.[121] Binding of the divalent cations is responsible for a rigid structure of the outer leaflet of the OM.[122,123] Specular X-ray reflectivity and simulation studies of the OM model of Gram-negative bacteria gave the first experimental evidence that divalent cations influence the orientation of LPS in the membrane and the structure of the model membrane.[122] 3-deoxy-D-manno-octulosonic acid (Kdo) is directly linked to a lipid A. This part of LPS is called the inner core. Kdo is connected with heptulose monosaccharides. The outer core of LPS contains more common hexoses including glucose (Glc), galactose (Gal), N-acetylgalactosamine (NGc) and N-acetylglucosamine (NGa). Some LPS have an O-antigen composed of repetitive subunits, which contain one to eight sugar residues.[115,119] LPS that comprise the lipid A, inner and outer core and an O-antigen are called smooth (S)-LPS, while LPS lacking the O-antigen are named rough (R)-LPS.[124] These terms refer to the smooth and rough morophologies.

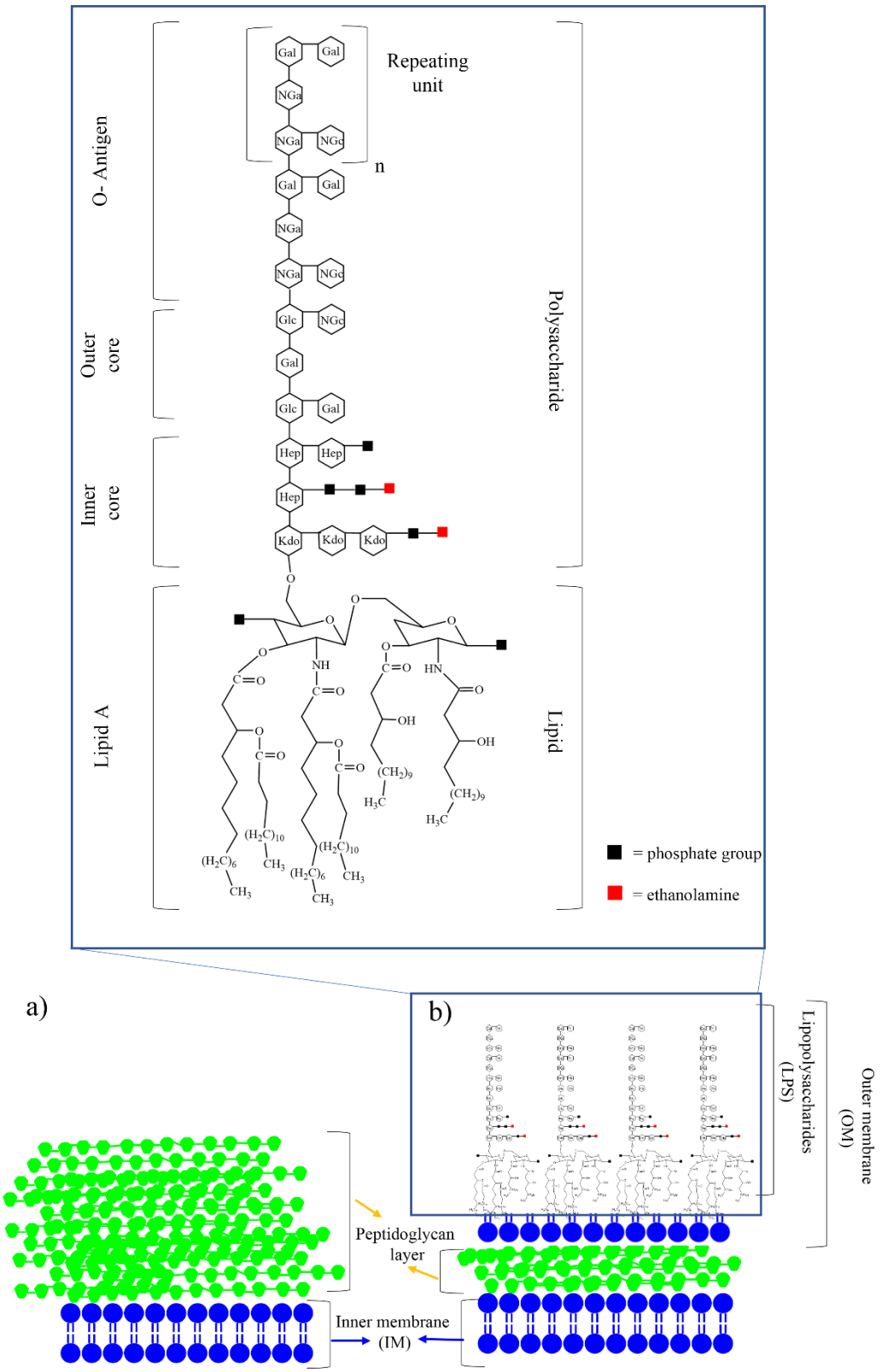

Figure 2: Schemes showing the structure and composition of the cell envelope of a) Gram-positive and b) Gram-negative bacteria. The structure of lipopolysaccharides (LPS) is shown in the upper panel. Symboles correspond to: Kdo: 3 deoxy-α-D-mannooctulosonic acid, Hep: heptulose, Glc: glucose, Gal: galactose, NGa: N-acetylgalactosamine and NGc: N-acetylglucosamine.

Wu et al.[125] have shown that an increase in the LPS molecular length has an impact on the bilayer properties. As the core and O-antigen repeating units are added, the area per lipid molecule increases and the lipid bilayer order decreases, indicating a looser packing of the LPS molecules in the lipid A region in the (S)-LPS bilayer compare to the (R)-LPS bilayer.[125] Fabrication of an asymmetric lipid bilayer compsed of LPS in the outer and phospholipids in the inner leaflet was reported in literature.[81,126–129] First structural studies were performed on lipid A and LPS monolayers at the air|electrolyte interface.[123,130,131] LPS form stable monolayers at the air|water interface. The average area per LPS molecule varies between 1.08 nm^2 and 1.27 nm^2, depending on the used LPS.[130] Structural information is avalible from computer simulation studies for the packing of hydrocarbon chains and the orientation of the polar head groups in the OM of Gram-negative bacteria.[125,126,132–134] LPS-phosphatidylcholine vesicles spread on solid surfaces to form defect-free bilayers.[135] In this model, the full asymmetry in the distribution of lipids between two leaflets, a unique feature of the OM, was not achieved. Clifton et al.[136] have used LB vertical withdrawing to deposit a phosphatidylcholine in the inner leaflet of the model membrane on the silicone oxide surface and LS transfer was used to deposit the outer LPS leaflet. Stability tests of the asymmetric distribution of the LPS revealed their gradual flip-flop into the inner leaflet in the presence and absence of divalent cations.

Divalent cations are known to be essential not only for the stability of the OM, but also for the expression of their biological activity.[137,138] Addition of 1.0 M $CaCl_2$ to the subphase reduced the collapse of the LPS monolayers by 20 % compared to pure water.[131] Jeworrek et al.[139] and Schneck et al.[123] have studied the effect of monovalent and divalent cations on the packing and molecular-scale of the LPS monolayer at the air|water interface. Addition of monovalent and divalent cations increased the order packing of LPS in the monolayer at the air|water interface.[139] Na^+ ions interact unspecifically with LPS molecules, whereas Ca^{2+} ions are likely to bind specifically to the inner core phosphate groups of the LPS by cross-linking adjacent molecules in the monolayer.[122,123,139] Le Brun et al.[130] have perfomed detailed structural analysis of *E.coli* LPS monolayers at the air|liquid interface. The structure of LPS monolayers and the chain packing were investigated using grazing incidence X-ray diffraction (GIXD) and Brewster angle microscopy (BAM). A distorted hexagonal packing of lipid A monolayers was obtained at surface pressure (Π) $\geq$ 20 mN m^{-1}. X-ray reflectometry (XR)

measurements showed that the hydrocarbon chains are slightly thicker for the lipid A and equal 18 Å and 20 Å at Π of 30 mN m^{-1} and 40 mN m^{-1}, respectively. Jeworrek et al.[139] have found that the head group thickness was 12 Å at 20 mN m^{-1} for the *Salmonella minnesota* (R)-LPS. In addition, neutron diffraction (ND) studies of the *P. aeruginosa* (S)-LPS showed that the inner core polysaccharides are 13 Å thick.[140]

2.3 Lipid-antimicrobial peptide interactions

Understanding of the lipid-peptide interactions is an important step in the development of novel therapeutics.[9,113,117,141,142] The OM of Gram-negative bacteria is the first contact surface for AMPs. AMPs consist a class of naturally occurring antibiotics.[41,143] Most of them are amphipathic peptides, which are effective at μM concentrations.[26] AMPs are usually composed of a 20 - 80 amino acids long polypeptide chain. AMPs adopt either α-helical or β-sheet structure after its interaction with a cell membrane. AMPs are classified into several groups depending on their origin, amino acid sequence, secondary structure or function.[25,27,28,41] In most cases, the interaction of AMPs with a membrane leads to a cell-lysis and death. These interactions may lead to a formation of pores and transport of peptides inside the cell, bringing them into a contact with intercellular targets.[41,143] Sterols are present in membranes of eukaryotic cells but not in prokaryotic cells. This difference may be important for the interaction of AMPs with both kinds of membranes.[25,144–146] It has been reported that the efficiency of lipid bilayer permeation by various AMPs is decreased in the presence of cholesterol in the lipid bilayer.[25,144–146] Different models of action of AMPs on the lipid membranes are described in literature (Figure 3).[27,34,38–42] The carpet, toroidal, barrel-stave and aggregate-channel models require the adsorption of AMPs on the membrane surface, changes in the peptide structure and orientation.[38–41] In the carpet model, AMPs adsorb in large quantities on the membrane surface covering it as a carpet. The aggregation of the peptide leads to a formation of patches in the membrane. Aggregates of AMPs coated by lipid molecules diffuse away from the membrane surface. This model leads to a quick collapse of the membrane (Figure 3a).[41,147] In the toroidal model, AMPs molecules adsorb on the membrane surface, aggregate, impose thinning of the membrane. This induces a bending of the bilayer so that the outer

and inner leaflets meet (Figure 3b).[148] The barrel-stave model requires the aggregation of AMPs molecules across the membrane and formation of pores (Figure 3c).[41,149,150] In the aggregate-channel model, the electrostatic interactions of AMPs with negatively charged lipids on the membrane surface lead to a phase separation of lipid molecules and formation of pores in the membrane by removal of negatively charged lipid-peptide aggregates from the membrane (Figure 3d).[41] In Gram-negative bacteria, AMPs have first to cross through the OM. Negatively charged phosphate, hydroxyl and carboxylic moieties are present at LPS. They are potential ligands for positively charged AMPs. Perivous studies of AMPs interactions with LPS in their aqueous vesicles and monolayer assemblies at the air|water interface showed clearly that the α-helical structure is enhanced for various AMPs due to the peptide binding to LPS.[151,152] The lipid-peptide interactions may lead to phase transitions in hydrocarbon chains of lipid molecules, change the thickness of the membrane, change membrane capacitance and water content in the polar head group region.[34,35] Electrochemical studies showed a significant increase in the permeability of lipid membranes to electroactive ions upon AMP binding.[36,37] In addition, the IR spectroscopy showed that the hydration of the phosphate groups increased at both, lipid A and inner core of LPS, due to the interaction with AMPs.[153] Nathoo et al.[154] have characterized the influence of the ethidium multidrug resistant protein (EmrE) on the lipid organization in the monolayer film. EmrE is a multidrug transporter, which transports ethidium into lipid membrane and binds quanternary ammonium compounds in several membranes.[154] It is an integral membrane protein spanning the IM of *E.coli*.[154] These studies showed that the chemical nature of different lipid head groups, as well as the hydrocarbon chain length and saturation determine the lipid-lipid and lipid-protein interactions.[154]

Melittin is one of the most studied AMPs.[26,28,38–40,43,45,46,155–163] It is a small linear peptide composed of 26 amino acid residues, which sequence is shown in Figure 4. It is a cationic peptide in which the N-terminus is composed of hydrophobic amino acids, whereas the C-terminus contains hydrophilic amino acids. Melittin has an amphiphilic character. Melittin has a net charge of +6 at physiological pH,[44,155,164] ensuring it a good solubility in water.[43,44,46] It is a major toxic component in the venom of the European honeybee *Apis mellifera*,[44] displays high antimicrobial[28] and antiviral[45,46] activities. In addition, it was studied as an antitumor agent.[159] Terwilliger et al.[44] have studied the crystal structure of

melittin. The axes of 1-10 and 16-26 helices intersect at 120°.[44,165] Melittin has fluorescent properties, due to the presence of a single tryptophan residue (Trptophan19), which makes it a sensitive probe to study its interaction with membranes.[130]

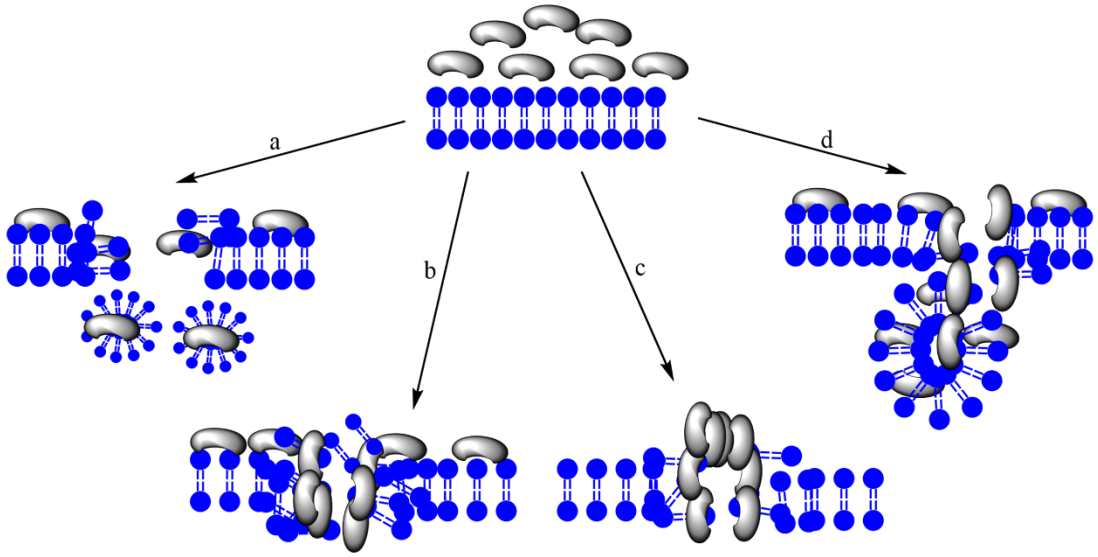

Figure 3: Different mechanisms of AMPs action on the lipid bilayers. a) Carpet mode, b) toroidal mode, c) barrel-stave mode and d) aggregate-channel mode.

In solution, mellitin undergoes a concentration-dependent change in conformation from a random-coil to α-helical tetramer.[166] At high lipid-peptide ratios (> 200 : 1) membrane-bound melittin is a monomer with its helical axis oriented parallel to the membrane surface.[144,167] As the concentration of membrane-bound melittin increases, the peptide undergoes a dynamic reorientation relative to the membrane normal, leading to its micellization.[144,167]

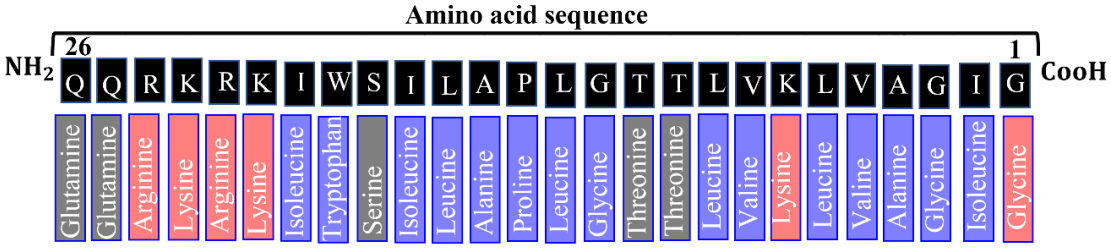

Figure 4: Amino acid sequence of melittin. Colour code: blue (hydrophobic), grey (hydrophilic) and red (charged) amino acids.

Melittin can bind to neutral membranes as well as to membranes with negative surface charge.[160,161] The adsorption of melittin on negatively charged membranes results in its

parallel orientation to the membrane surface, since this orientation facilitates electrostatic interactions between cationic melittin and anionic head groups of the lipid. The parallel orientation with respect to the membrane surface was suggested to prevent the association of the hydrophobic part of melittin with the hydrophobic core of the membrane and consequently to inhibit the reorganization required to induce membrane-lysis. Melittin adsorbed on top of the membrane, leads to a fluidization of the lipid membrane. This was accompanied by reorientation and insertion of the melittin molecules into the bilayer. It resulted in a formation of numerous defect sites and pinholes.[36,43] Juhaniewicz et al.[43] and Batenburg et al.[168] have domenstrated the affinity of melittin was greater for negativily charged membranes than for zwitterionic membranes. The presence of negative charge slows down the reorientation and insertion of melittin molecules compared to membranes composed of zwitterionic lipids.[43,168] Melittin forms toroidal pores in zwitterionic membranes and the size of the pore increases with an increase in the peptide to lipid ratio.[38–40] Ladokhin et al.[169] have shown that melittin disrupts anionic membrane in a detergent-like manner, according to the carpet mechanism (Figure 3a). The minimum capacitance increases after exposure of the anionic 1,2-dimyristoyl-*sn*-glycero-3-phosphoglycerol (DMPG) bilayers to 10 μM melittin for 12 h.[43] This showed clearly that melittin induces changes in the organization of the DMPG bilayers leading to an increase in the permeability of the DMPG bilayer.[43] AFM data showed that melittin molecules penetrate the DMPG bilayer with a formation of pores.[43] In this case melittin adopts a parallel orientation with respect to the membrane surface. A perpendicular orientation of the peptide molecules to the membrane surface was observed with increasing fraction of the peptide molecules.[30] Juhaniewicz et al.[43] have transferred DMPS bilayer on the Au(111) electrode. The structure of the DMPS bilayers seems to be less affected by melittin binding compared to the DMPG bilayer.[43] Flach et al.[170] have studied the action of melittin on the DPPC monolayer by means of IRRAS. These studies showed that melittin conformation may differ in monolayers and bilayers.[170] Melittin monolayer gave amide I mode at 1635 cm^{-1}. This value is lower than the frequency of an α-helix (amide I frequency 1656 cm^{-1} in dry or aqueous environment).[170] Verma et al.[158] have reported that melittin decreased the lipid chain mobility and caused the head group reorganization. Juhaniewicz et al.[36] have demonstrated that electrochemical methods supported by *in situ* AFM topography imaging facilitate the evaluation of mechanisms of melittin action on

the membrane. The action of 10 μM melittin leads to a quick degradation of the DMPC bilayer, which undergoes micellization and partial dissolution.[36] After exposure of the DMPC bilayer to 10 μM melittin for 30 min, an increase in the membrane capacitance was reported.[36] This may indicate that melittin molecules affect the dielectric properties of the DMPC bilayer and cause membrane thinning. These results indicate that melittin acts according to detergent-like mechanism, which corresponds to the aggregate channel mode (Figure 3d). AFM images showed that the gold electrode is covered by spherical aggregates after exposure of the DMPC bilayer to 10 μM melittin for 30 min. Melittin penetrates the lipid membrane and finally mixed micelles are formed.[36] However, the micelles are still attached to the gold surface. Further imaging showed that aggregates are removed gradually from the surface. Melittin interacts differently with DMPC bilayers when its concentration is lowered (1 μM). AFM images shown that in the DMPC bilayers the morphological changes are less rapid.[36] Juhaniewicz et al.[36] have reported different behavior of melittin for the DMPC-cholesterol bilayer. Several studies have shown that cholesterol inhibits the action of melittin.[36,145,146] Therefore, the DMPC-cholesterol bilayer is more resistant to melittin action than the bilayer composed of pure DMPC.[36] Cholesterol fills the space between DMPC hydrocarbon chains and increases the membrane stiffness, making it less susceptible for the penetration by melittin.[36,145,146] Capacitance values are lower for DMPC-cholesterol bilayers from those for the DMPC bilayers.[36]

Alamethicin is AMP, composed of 20 amino acids.[171] It has a helical structure with an α-helix at the N-terminus and 3_{10}-helix at the C-terminus.[171] A combination of *in situ* PM IRRAS with electrochemical methods was performed to investigate the structural changes in 1,2-di-O-phytanyl-*sn*-glycero-3-phosphocholine (DPhPC) bilayers during its interaction with alamethicin.[171] DPhPC phospholipids and alamethicin (9:1 mole ratio) in each leaflet were transferred onto the Au electrode by LB-LS technique.[171] The capacitance reaches a minimum (7 - 8 μF cm^{-2}) for the DPhPC-alamethicin bilayers in the potential range -0.1 V > E < 0.0 V vs. Ag|AgCl.[171] An increase in the capacitance and decrease in the resistance were obtained at E < -0.1 V vs. Ag|AgCl.[171] The maxima of absorption of the methylene stretching modes indicate that the hydrocarbon chains in the DPhPC lipid exist in a liquid state.[171] The integral intensities of the methylene stretching modes are independent of the potential applied to the Au surface. The average tilt angle

of the hydrocarbon chains in the DPhPC-alamethicin bilayers is 30° - 35° vs. the surface normal. PM IRRA spectra contain two IR absorption modes in the 1800 - 1600 cm^{-1} region: the ν(C=O) in the carbonyl ester group in DPhPC and the amide I mode in alamethicin.[171] The orientation of the alamethicin depends on the applied potential, while the orientation of the DPhPC molecules in the membrane is unaffected by the potentials applied to the electrode. These results conclude that alamethicin interacts with the membrane via barrel-stave mechanism (Figure 3c).

This research work describes details of the interaction between the model of biological membranes and melittin antimicrobial peptide. Changes in the capacitance as well as the orientation of lipid molecules in the model of the IM and OM of Gram-negative bacteria exposed to a changing potential and interacting with melittin are discussed.

3 Characterization methods

3.1 Langmuir-Blodgett and Langmuir-Schaefer technique

Modification of solid surfaces with organized and thin molecular films is an important research topic.[56,172–176] Molecular films find applications in electronics[177–180], sensing devices[177,181–184], insulators[185–188] or matrix for drug testing.[189–191] Various surface modification methods are available.[20,56,84–87,91,172,192–196] One of them is LB-LS transfer[56,85,197–201], which is described in detail below. Phospholipids are amphiphilic molecules, which contain hydrophilic (water soluble) and hydrophobic (water insoluble) parts. The hydrophilic part consists of a polar head group. The hydrophobic part is composed of hydrocarbon chains. Phospholipids are the major component of biological membranes.[197,201–203] At the air|water interface, phospholipids assembly to form an insoluble monolayer in which the polar head groups are immersed to water and their hydrophobic hydrocarbon chains oriented to air. POPE is one of the phospholipid molecules which has a phosphatidylethanolamine ($-PO_4(CH_2)_2NH_3$) head group and two hydrocarbon chains.[94,204,205] One of these chains is saturated and the other one is unsaturated. A structure of POPE molecule is shown in Figure 5. The formation of the monolayer at the air|water interface is monitored by the measurement of the Π during compression as a function of the area per molecule (A). Π is defined as:

$$\Pi = \gamma_o - \gamma \quad (1)$$

where γ_o is the surface tension of the uncovered air|water interface and γ is the surface tension of the monolayer-covered interface.

γ can be measured by the Wilhelmy plate method (Figure 6). The Wilhelmy plate is often made of a very thin, well wetted and high free surface energy material (e.g., papers, Pt). When the plate is brought in contact with a liquid, an increase in weight is obtained. The total force (F) acting on the plate is the sum of three forces: the gravity force [$\rho g l w d$], the surface tension force [$2\,\gamma(d + w)\cos\vartheta$] both are acting downwards and the buoyancy force of the plate [$\rho_l g d w h$] is acting upwards.

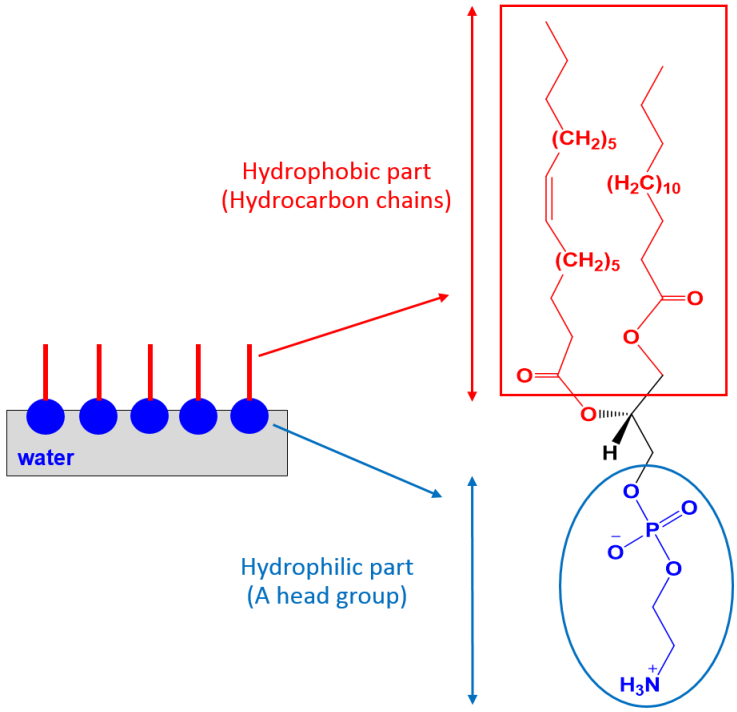

Figure 5: Structure of POPE phospholipid molecule with the hydrophilic phosphatidylethanolamine head group (blue) and the hydrophobic hydrocarbon chains (red) regions at the air|water interface.

When the plate is immersed to a depth (h) in a liquid of density (ρ_l). The F is given by equation 2:

$$F = \rho g l w d + 2\gamma(d + w)\cos\vartheta - \rho_l g d w h \quad (2)$$

where l is the length, w width, d thickness and ρ material density of the plate. γ is the liquid surface tension, ϑ the contact angle of the liquid on the plate and g the acceleration due to gravity. Π is calculated by measuring the change in F for a plate at the interface in the presence and absence of the monolayer.

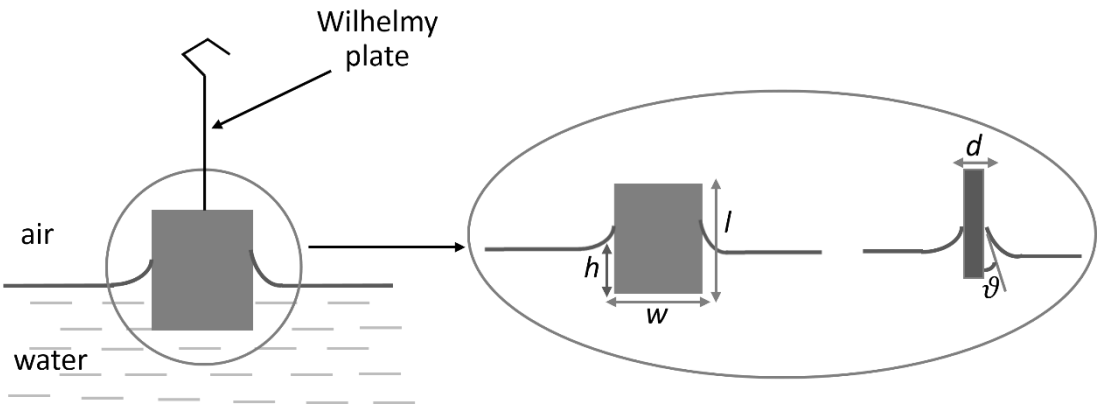

Figure 6: A scheme of a Wilhelmy plate at the air|water interface.

When the plate is completely wetted by the liquid ($\cos\vartheta = 1$), Π is then obtained from equation 3:

$$\Pi = -\Delta\gamma = -\left[{}^{\Delta F}/_{2(d+w)}\right] = -{}^{\Delta F}/_{2w} \qquad \text{if} \quad w >> d \tag{3}$$

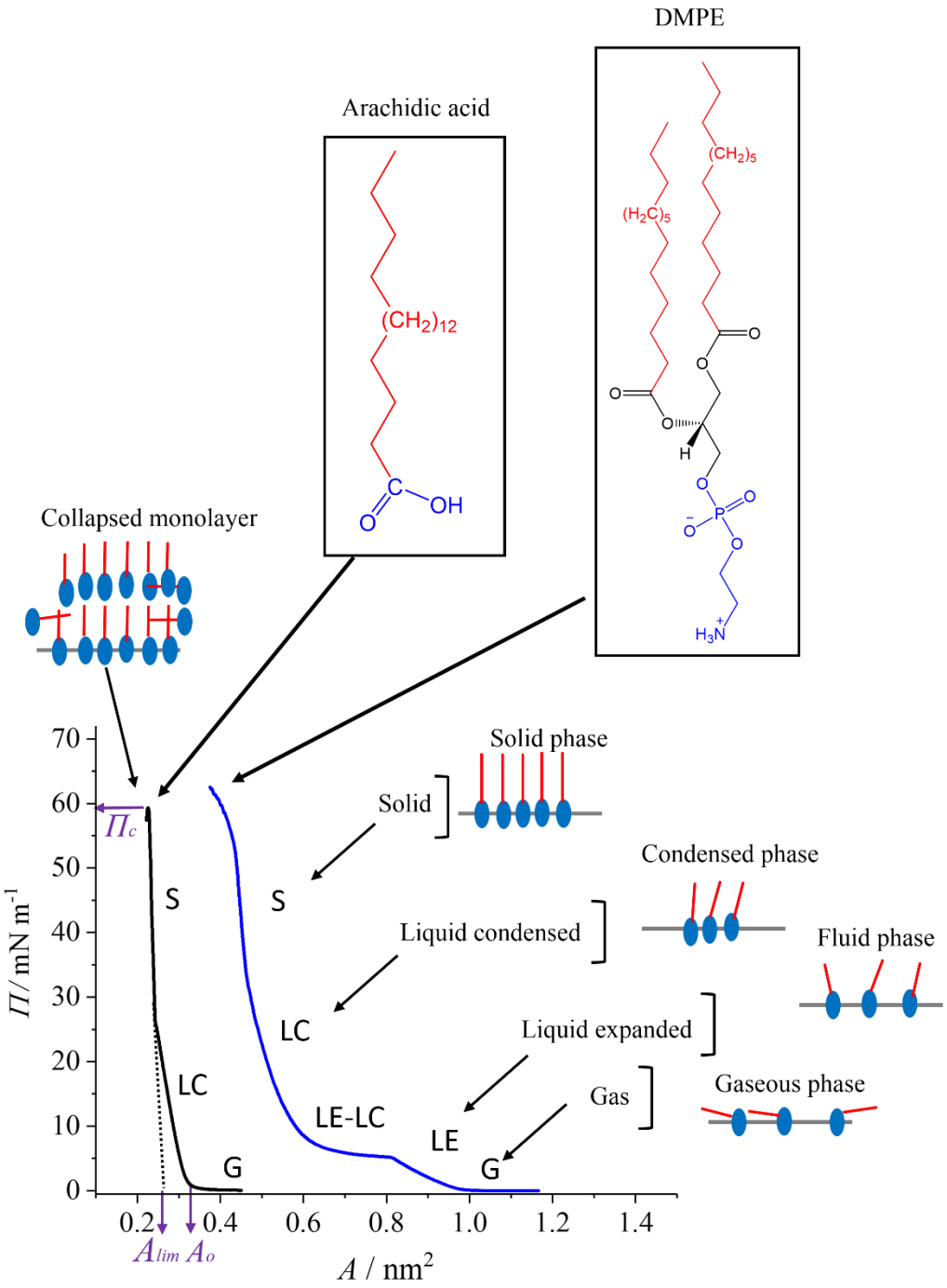

Figure 7: Plots of Π-A isotherms of arachidic acid (black) and DMPE (blue) at the air|water interface.

Π is measured as a function of *A*. Figure 7 shows isotherms of arachidic acid (black) and DMPE phospholipid (blue). During compression, barriers of the Langmuir trough move and thereby reduce the *A*. Plot of Π vs. *A* is known as a Langmuir isotherm. Π increases with the reduction in *A*.[197,201] Different phase transitions may be observed by compressing lipid monolayers. Figure 7 shows that the monolayer exists in the gaseous (G) phase at large *A*. Compression of the film leads to a phase transition to a liquid-condensed (LC) phase. The molecules are well ordered and closely packed in the LC phase. Figure 7 shows that in DMPE isotherm (blue), a plateau region is obtained between the liquid-expanded (LE) and LC phases. It corresponds to a two-phase coexistence region. A further compression leads to a sharp increase in Π, corresponding to a formation of a solid (S)-like film. The monolayer film collapses at smaller *A* and a disordered monolayer is formed at the surface pressure of the monolayer collapse (Π_c). The limiting area (A_{lim}) corresponds to the smallest *A* available per single molecule in the monolayer film. The lift-off area (A_o) corresponds to the molecular area at which an increase in Π is first detected.

The shape of the isotherm depends on the length of the hydrocarbon chains and the presence of unsaturated hydrocarbon chains.[56,197] It depends also on the experimental conditions (subphase composition, temperature, pH).[56,197] Figure 8a shows the Langmuir isotherm of DOPE at the air|water interface. The compressibility modulus (K_s) reflects the physical state of the monolayer.[58,213] K_s can be determined directly from the Langmuir isotherm according to:[56,206]

$$K_s = \left[-\left(\frac{1}{A}\right)\left(\frac{\partial A}{\partial \Pi}\right)\right]^{-1} \quad (4)$$

K_s varies from 10 to 50 mN m^{-1} in the LE phase and from 100 to 200 mN m^{-1} in the LC phase. Transition to the S phase results in an increase of K_s up to 2000 mN m^{-1}.[207] Figure 8b shows K_s vs. *A* plot. K_s reaches maximum (92 ± 5) mN m^{-1} for the monolayer of DOPE at *A* preceding the monolayer collapse, indicating that the DOPE monolayer exists in the LE phase. When a solid substrate is hydrophilic, the monolayer is deposited by a vertical withdrawing of the substrate from the subphase through the monolayer as shown in Figure 9a. The polar head group orients toward the surface and the hydrocarbon chains are

directed toward air. Figure 9b shows that when the solid substrate is hydrophobic, the monolayer is transferred by immersing the substrate into the subphase through the monolayer. The hydrocarbon chains orient toward the surface, while the polar head groups are directed toward air.

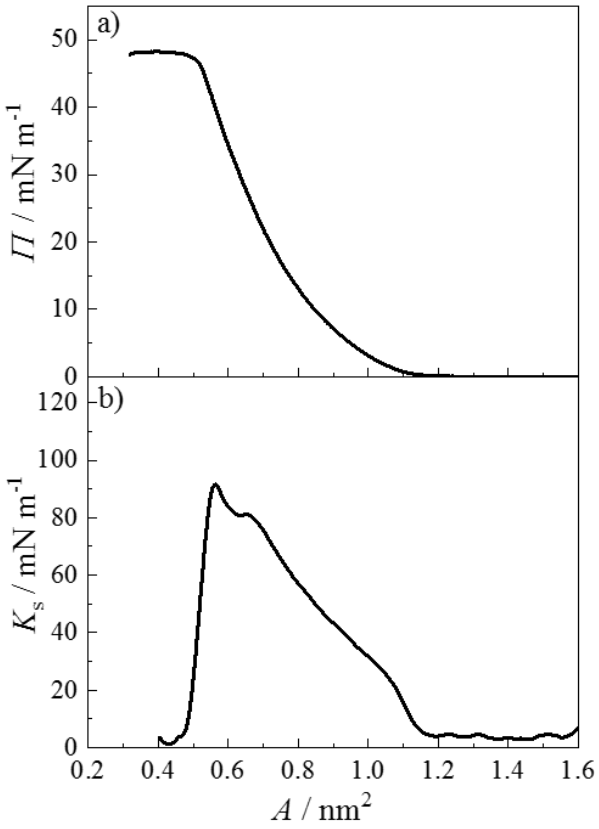

Figure 8: Plots of a) Π and b) K_s vs. A of DOPE at the air|water interface.

The quantitative transfer of the monolayer on a solid surface is measured by the transfer ratio (TR). It is defined as the ratio between the area decreases on the aqueous surface during transfer to the area of the solid surface. For quantitative transfer of a monolayer, TR is equal to 1. TR depends on the experimental conditions (subphase composition, pH, temperature), structure of the phospholipid molecules and the speed of the immersing or withdrawing of the solid substrate.

LS transfer offers another way to deposit a monolayer on a solid surface.[56,197,201,208–211] It is also called horizontal touch technique. Figure 10 illustrates that the LS transfer results in the preparation of a lipid bilayer on a solid surface.[211] As shown in Figure 10a-c, the solid substrate is horizontally oriented and lowered slowly until it is in contact with the

monolayer at the air|water interface. Afterwards it is slowly withdrawn. The produced phospholipid bilayer serves as a good model of a cell membrane as shown in Figure 10d.

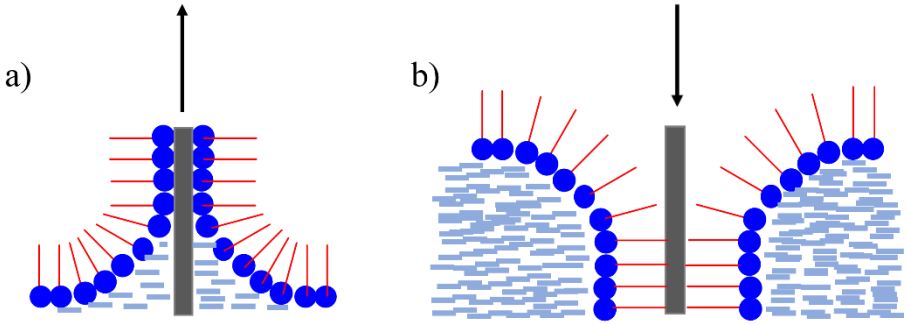

Figure 9: Arrangement and LB transfer direction of a monolayer of amphiphilic molecules onto a) hydrophilic and b) hydrophobic solid substrates.

A combination of LB-LS techniques enables the formation of symmetric and asymmetric phospholipid bilayers on the solid surface.[110,211] Different kinds of LB multilayers can be fabricated by successive deposition of monolayers onto the same substrate as illustrated in Figure 11.[56,208,209,212]

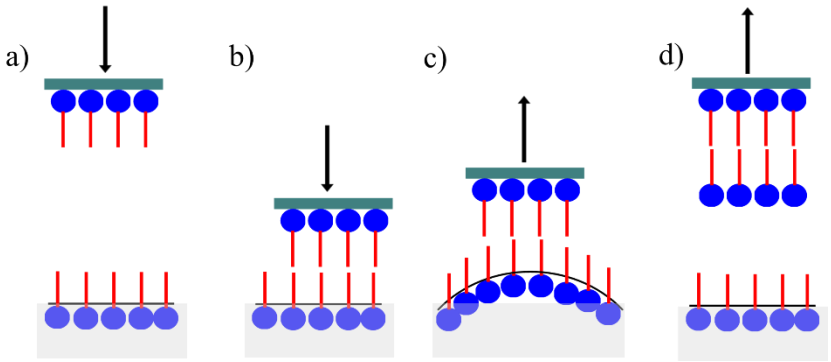

Figure 10: a-c) Steps of LS transfer of a monolayer from the air|water interface and d) resulting arrangement of lipid molecules in the bilayer. Arrows represent the immersing (a, b) and the withdrawing (c, d) directions of the solid substrate.

The Y-type multilayer is produced when the monolayer is deposited to the solid substrate in both (up and down) directions (Figure 11a). Figure 11b, c shows LB films obtained for deposition only in either down or up directions. Those multilayers are called X-type and Z-type.

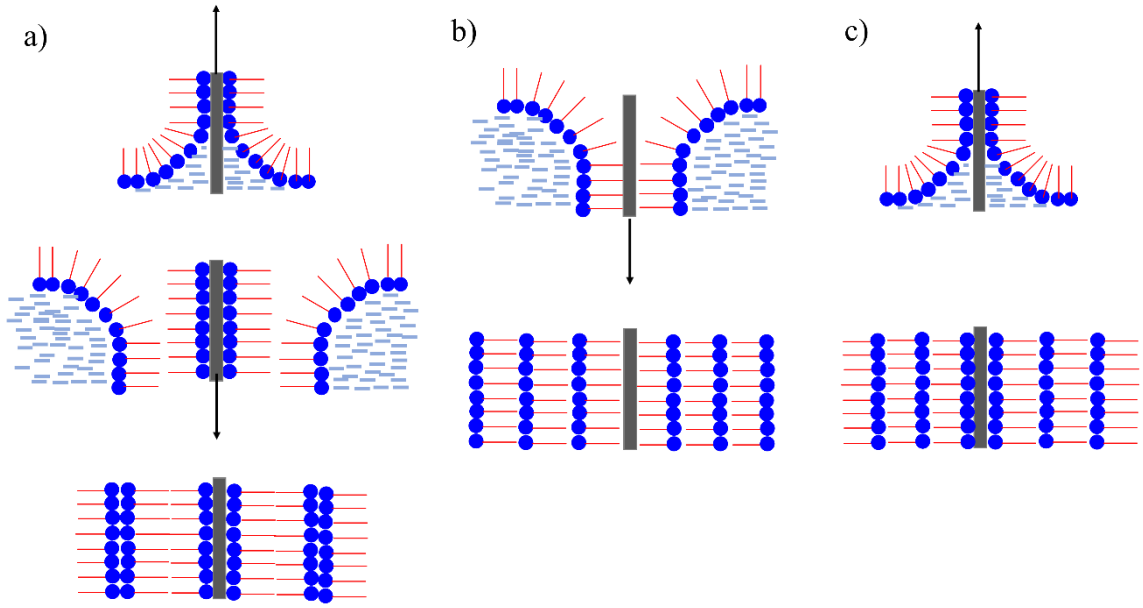

Figure 11: Deposition types of LB multilayers: a) Y-type, b) X-type and c) Z-type. Arrows represent the immersing (a, b) and the withdrawing (a, c) directions of the solid substrate through the subphase (light blue colour).

3.2 Electrochemical methods for the study of model membranes

Electrochemical studies are applicable for studies of model membranes adsorbed on electrode surfaces.[37,213–215] Phospholipids in biological membranes are exposed to electric fields in the order of $10^5 – 10^9$ V m^{-1}.[8] Deposition of a lipid bilayer on the electrode surface enables studies on the membrane capacitance as a function of electric fields.[3,4,216–218]

3.2.1 Alternating current voltammetry

In alternating current voltammetry (ACV), a sinusoidal voltage is applied to a working electrode with constant frequency and a small amplitude (5 - 25 mV) as shown in Figure 12a.[1–4,219,220] The current has a phase shift (φ) to the voltage (Figure 12b). ACV is a powerful technique for relative quantitative evaluation of the processes at the solid surface.[3,4,220,221] ACV was used to determine the capacitance of lipid bilayers.[4,110,215,219]

The in-phase (i^{in}) and out-of phase (i^{out}) alternating current are measured. The current values are used to determine the capacitance of the double layer (C).

$$C = \frac{i^{2in} + i^{2out}}{2\pi i^{out} 0.63662\ \hat{A} f a} \quad (5)$$

where $\hat{A}$ and f are the amplitude and frequency of the voltage perturbation and a is the area of the electrode. The C of biological membranes is approximately 1.0 μF cm^{-2}.[221–223] C depends on the applied potential, composition of the electrolyte solution, the metal surface and reflects the adsorption-desorption process of the model lipid bilayer transferred on the electrode.[37,214,215,224]

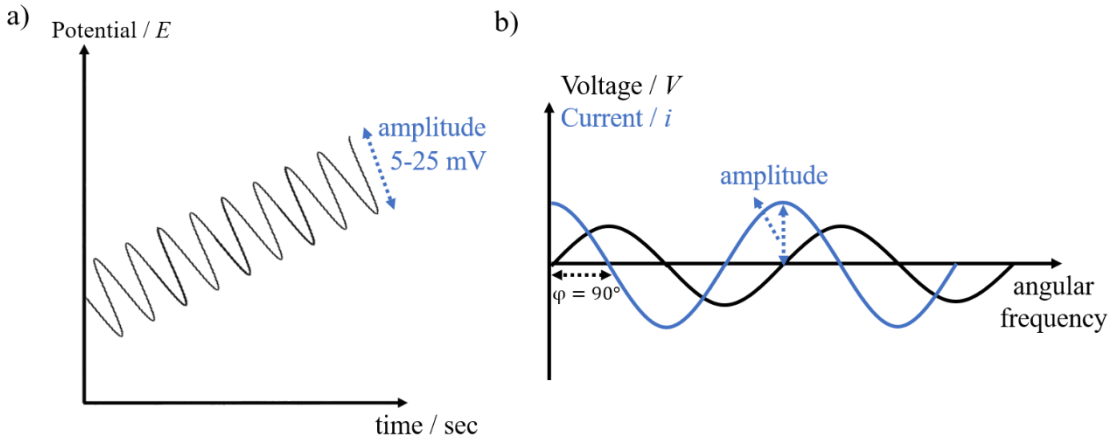

Figure 12: a) Waveform for AC voltammetry where the applied potential as a function of time is a sinusoidal alternating potential superimposed on a linearly increasing ramp and b) the relationship between alternating current and voltage signals at angular frequency.

The potential of zero charge (E_{pzc}) is used to calculate the membrane potential.[5,80,225] The difference (E- E_{pzc}) is a good approximation of the membrane potential.[5,80,225] ACV is used to determine the E_{pzc} by determination the C_{min} of unmodified Au(111) electrode surface in a lower concentration of an electrolyte solution.[225] The potential drop across a model lipid bilayer deposited on the electrode surface is described by the following equation:[5,80]

$$\Delta\emptyset_{M|S} = \frac{\sigma_M}{C} + X_M \quad (6)$$

where $\Delta\emptyset_{M|S}$ is the potential difference across the metal|solution interface and contains the sum of potential difference across the lipid membrane ($\Delta\emptyset_M = \frac{\sigma_M}{C}$) and surface potential of the membrane (X_M).[5,80] The potential difference (E - E_{pzc}) is equal to $\Delta\emptyset_{M|S}(E)$ - $\Delta\emptyset_{M|S}(E_{pzc})$.[5,80] Since $\Delta\emptyset_{M|S}(E_{pzc})$ corresponds to the X_M, the potential drop across the membrane is equal to $\Delta\emptyset_{M|S} = (E$ - $E_{pzc})$. Thus, according to equation 6 the values of $\frac{\sigma_M}{C}$ should be equal to the values of (E - E_{pzc}).[5,80]

3.3 Infrared reflection absorption spectroscopy

IRRAS has been developed by Greenler.[226] It is a powerful surface sensitive technique for the studies of the molecular structure, composition and conformation of organic molecules.[220,227–231] However, the sensitivity of these measurements is often limited, because the signals of interest from surface adsorbates are often camouflaged by atmospheric background absorption. Therefore, IRRAS is mostly applied in ultra-high vacuum.[232] When IRRAS is applied to an electrochemical experiment, the mirror of IR radiation is at the same time the working electrode. The electrode material, electrolyte composition and optical window[233] (e.g., CaF_2) have to be precisely chosen.[234] The gap thickness is determined between the prism and the electrode by comparing the experimental reflectivity spectrum of the thin layer to the reflectivity curve calculated from the optical constant of the cell.[235]

3.3.1 Polarization modulation infrared reflection absorption spectroscopy

PM IRRAS is a powerful technique for the characterization of molecules adsorbed on IR light-reflective surfaces.[3,52,54,109,236,237] The measured spectra provide information about the structure, hydration and orientation of the lipid molecules. The modulation of the IR beam is done by a photoelastic modulator (PEM). The PEM is made of a cubic IR transparent crystal such as CaF_2 or ZnSe.[79,237–239] The PEM transducer is usually set to the resonant frequency of the optical element 50 kHz. The PEM generates the alternating

linear light polarization states (*s*- and *p*-polarized components). For a linearly polarized incident IR light with the polarization axis set to 45° with respect to the optical axis of the PEM crystal, the incident electric field vector is resolved into two components which are parallel and perpendicular to the optical axis.[79,237–239] When the plane of polarization of the incoming light makes an angle of 45° to the modulator optical axis, then for radiation of a given wavelength, and at the time of maximum stress or maximum stretching of the optical element, half-wave retardation occurs.[79,237–239] Under this condition a switching between parallel and perpendicular linearly polarized light takes place. When the optical element is at rest (between compression and expansion) no retardation of the linearly polarized light occurs.[79,237–239] PEM acts as a half-wave retarder.[79,237–239] The main advantage of PM IRRAS arises from an excellent signal-to-noise ratio, which allows measurements under ambient conditions and even in liquids.[16,232,237] When electromagnetic radiation passes the border between air and the bilayer, a portion of the radiation is reflected and the other portion is transmitted into the bilayer (Figure 13).

The intensity of the reflected or transmitted light depends on the angle of incidence and the refractive indices of the different media. According to Snell`s law, the angle of the reflected light $\theta_1^{\mathrm{r}}$ is equal to the angle of incidence $\theta_1^{\mathrm{i}}$. Snell`s law describes the relation between the incident angle θ_1^{i} and the angle θ_2^{t} of the transmitted (refracted) beam:

$$n_1 \sin\theta_1^{\mathrm{i}} = n_2 \sin\theta_2^{\mathrm{t}} \tag{7}$$

where n_1 and n_2 are the refractive indices of the different media and θ^{i} and θ^{t} are the angles of incident and transmission (refraction), respectively. Fresnel equations give the intensity of the reflected *s*- and *p*-polarized light as a function of the incidence angle and describe the reflection and transmission coefficients of the *s*- and *p*-polarized incoming IR beam.[240]

Figure 14 shows the orientation of the electric field vectors of *s*- and *p*-polarized beam reflected from a mirror surface with the respect to the metal surface (z). The beam is referred to *p*-polarized when the electric field of the radiation is located in the plane of incidence. The beam is referred to be *s*-polarized when it is located perpendicular to the plane of incidence. Greenler[226,241] demonstrated that the electric field of the *p*-polarized

beam is enhanced at the metal surface as the result of the constructive interference of the incident and reflected radiation as shown in Figure 14a.

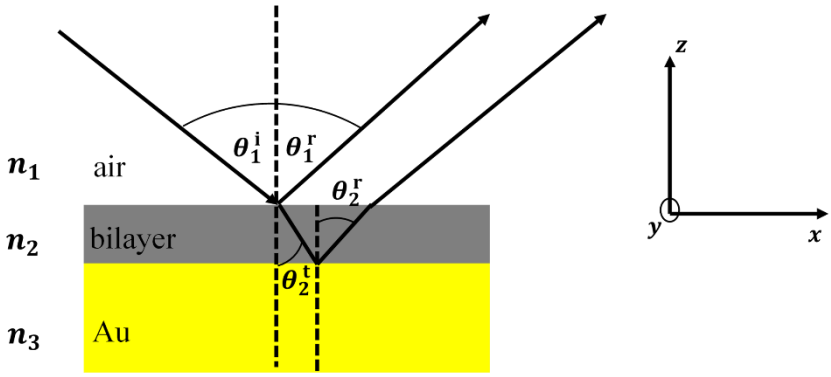

Figure 13: Reflection and transmission of light at phase boundaries. θ^i is the incidence angle, while θ_1^r and θ_2^r are the angles of reflection and $\theta^t$is the transmission (refraction) angle. The yellow part is the reflective gold electrode and the gray part is a bilayer.

Due to destructive interference, the electric field of the *s*-polarized beam is cancelled at the metal surface as represented in Figure 14b. Therefore, the *p*-polarized light contains information about the background and the sample.[242] On the other hand, *s*-polarized light contains only background information.

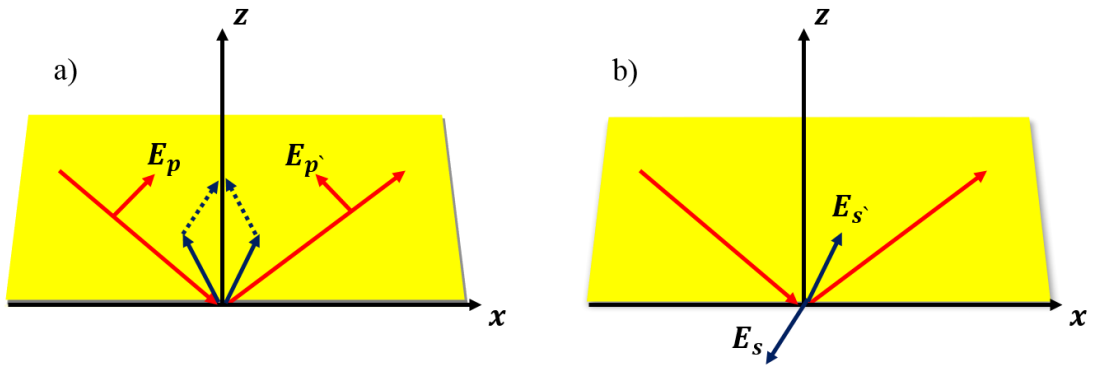

Figure 14: Reflection of a) *p*- and b) *s*-polarized light at the mirror|air interface.

The intensity of the light, which reaches to the detector during the measurement is equal:[79,243]

$$\left(\frac{\Delta I}{\langle I \rangle}\right)_{\text{exp}} = \left(\frac{(I_s - I_p)}{\left(\frac{I_s + I_p}{2}\right)}\right) J_2(\delta_0) \qquad (8)$$

where $\Delta I = (I_s - I_p)$ is the intensity of the differential and $\langle I \rangle = \frac{I_s + I_p}{2}$ is the intensity of the average signal of the *s*- and *p*-polarized IR light.[79,243,244] J_2 is the second order Bessel functions and δ_0 is the maximum phase shift of the incident light by the PEM.[79,239] The average and differential intensity spectra are plotted in Figure 15a and can be presented as:[79,243]

$$\langle I \rangle(\omega) = \left(\frac{\left(I_s(\omega) + I_p(\omega)\right)}{2} + \left| \frac{I_s(\omega) - I_p(\omega)}{2} \right| \right) J_0(\delta_0) \quad (9)$$

$$\Delta I(\omega) = \left| I_s(\omega) - I_p(\omega) \right| J_2(\delta_0) \quad (10)$$

where I_s and I_p are the intensities of *s*- and *p*-polarized light, respectively. J_0 is the zero order Bessel functions and ω is the excitation frequency of the PEM.[79,239]

If a highly reflective metal is used, ΔI is much smaller than $\langle I \rangle$. The second term in equation 9 is negligible compared to $\langle I \rangle$. Equation 9 can be simplified to:

$$\langle I \rangle(\omega) = \left(\frac{\left(I_s(\omega) + I_p(\omega)\right)}{2} + \left| \frac{I_s(\omega) - I_p(\omega)}{2} \right| \right) J_0(\delta_0) \approx \langle I \rangle \quad (11)$$

The half-wave retardation has to be set to the wavelength of interest before recording the spectrum. Figure 15b shows raw PM IRRA spectrum, calculated by using equation 8 of the h-POPE-KLA bilayer adsorbed on the Au(111) electrode surface. Weak IR absorption modes of the species adsorbed on the surface are clearly seen in the spectrum shown in Figure 15b. To substract the background from the spectrum, a basline is created as shown in Figure 15c. This background comes from the absorbance of IR radiation by the aqueous electrolyte and Bessel function.[79,237] Figure 15d shows a background-corrected spectrum of the h-POPE-KLA bilayer adsorbed on the Au(111) electrode surface in D_2O electrolyte solution.

When the polarized light is absorbed by a sample, the integral intensity (*I*) of the absorption band is proportional to the square of the absolute value of the dot product of the transition dipole moment vector and the electric field moment vector of the incident radiation $\left| \vec{\mu} \times \vec{E} \right|^2$.[245,246]

$$I = \int A_{\mathrm{bs}}\ \mathrm{d}\nu \propto\ \Gamma\ |\vec{\mu} \times \vec{E}|^2 = \Gamma\ |\vec{\mu}|^2\, \langle \vec{E} \rangle^2 \cos^2\theta \qquad (12)$$

where A_{bs} is the absorbance and $\overrightarrow{E}$ is the electric field vector of the *p*-polarized light, which is always perpendicular to the surface, Γ is the surface concentration of the molecules in this sample and θ is the angle between the direction of the $\vec{\mu}$ and $\vec{E}$ vectors.

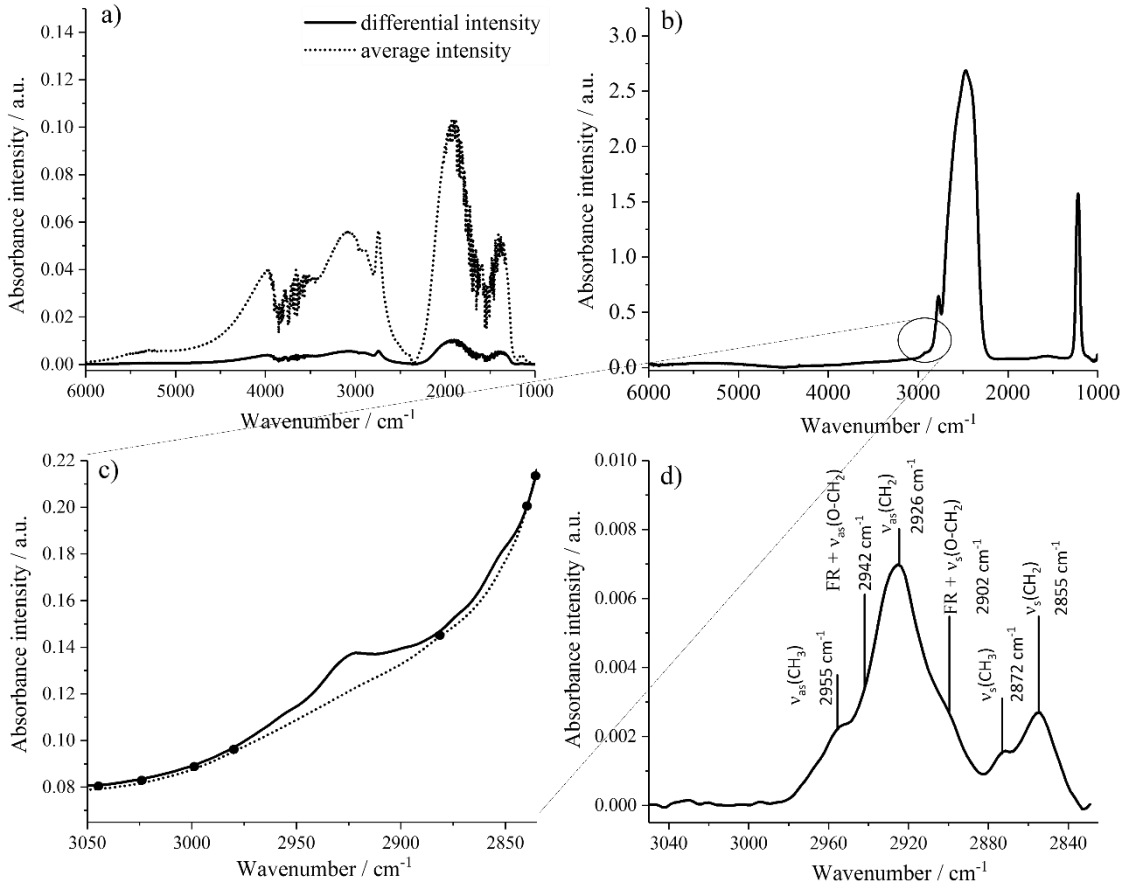

Figure 15: PM IRRA spectrum at half-wave retardation 2900 cm^{-1} a) average intensity and differential intensity spectra, b) raw PM IRRA spectrum in *in situ* measurement, c) enlargement of the raw PM IRRA spectrum in the 3050 - 2825 cm^{-1} spectral region and a spline interpolation to create basline (black circles represent template points for creating the spline) and d) basline-corrected and intensity normalized spectrum in the CH stretching region of the h-POPE-KLA bilayer adsorbed on the Au(111) electrode in D_2O electrolyte solution.

Quantitative analysis of the PM IRRA spectra allows the determination of the orientation of lipid molecules adsorbed on the gold electrode.[4,50,52,53] Figure 16 shows two different orientations of the hydrocarbon chain adsorbed on a gold surface leading to the cancellation (Figure 16a) or the enhancement (Figure 16b) of the symmetric methylene

stretching $\nu_s(CH_2)$ mode in the PM IRRA spectrum. When the angle between the $\vec{\mu}$ and $\vec{E}$ vectors is 90° (Figure 16a), according to equation 12, the integral intensity of the methylene stretching mode is equal to zero. There is no coupling of the $\vec{\mu}$ and $\vec{E}$ vectors. Zero absorbance indicates that the hydrocarbon chain is oriented perpendicular to the gold surface, because of the $\vec{\mu}$ vector of the $\nu_s(CH_2)$ mode is perpendicular to the direction of the hydrocarbon chain. Figure 16b shows a parallel orientation of the $\vec{\mu}$ and $\vec{E}$ vectors, causing a strong coupling and enhanced intensity of this IR absorption band. The direction of the $\vec{\mu}$ of $\nu_s(CH_2)$ mode is parallel to the surface normal when the hydrocarbon chain is parallel to the gold surface.

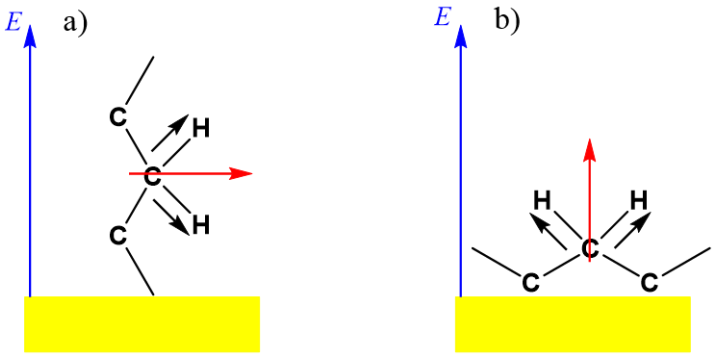

Figure 16: Different orientations of the hydrocarbon chain in an amphiphilic molecule adsorbed on the gold surface: a) perpendicular and b) parallel to the surface orientation of the hydrocarbon chain. The red arrow indicates the direction of the $\vec{\mu}$ vector of the symmetric methylene stretching mode and the blue arrow indicates the direction of the $\vec{E}$ vector of the *p*-polarized light at the phase boundary.

To determine the molecular orientation, the spectrum of randomly oriented molecules has to be calculated.[50] The isotropic optical constants of the film have to be determined from an IR transmission measurement.[239] The PM IRRA spectrum is calculated for experimental parameters (thickness of the electrolyte layer, incidence angle, optical components of the cell) identical with a previously performed *in situ* experiment. The surface concentration and thickness of the film have to be determined by an independent method. The resulting spectrum calculated from optical constants corresponds to the random distribution of investigated molecules in the studied film. The integral intensity of an IR absorption band of randomly distributed molecules gives the average θ angle equal to 53.54° (magic angle) since $\cos^2\theta = {}^1/_3$. The ratio of the integral intensity of a

given band in the experimental spectrum (I_{exp}) to the calculated one for random distribution (I_{rand}) is used to obtain θ:[245,247]

$$\cos^2\theta = \frac{\int I_{\mathrm{exp}}\,\mathrm{d}\nu}{3\int I_{\mathrm{rand}}\,\mathrm{d}\nu} \tag{13}$$

where θ is the time average angle between the $\vec{\mu}$ and $\vec{E}$ vectors and provides information about the orientation of the analyzed molecules in the film with respect to the surface normal. For a fully stretched *all-trans* conformation of hydrocarbon chains, the $\theta_{\nu\mathrm{as(CH2)}}$, $\theta_{\nu\mathrm{s(CH2)}}$ and the chain tilt angle θ_{chain} are connected by the formula: [248]

$$\cos^2\theta_{\nu\mathrm{as}}(\mathrm{CH_2}) + \cos^2\theta_{\nu\mathrm{s}}(\mathrm{CH_2}) + \cos^2\theta_{\mathrm{chain}} = 1 \tag{14}$$

where $\theta_{\nu\mathrm{as(CH2)}}$ and $\theta_{\nu\mathrm{s(CH2)}}$ are time averaged angle between the direction of $\vec{\mu}$ of the $\nu_{\mathrm{as(CH2)}}$ and $\nu_{\mathrm{s(CH2)}}$ modes and the direction of $\vec{E}$ of the *p*-polarized light. The order parameter (*S*) represents the orientational and conformational orders of the investigated molecules of a film.[249,250]

$$S = \left[\frac{1}{2}(3\cos^2\theta - 1)\right] \tag{15}$$

Equation 15 shows that *S* assumes values between 1 and -0.5, when the transition dipoles are oriented parallel or perpendicular to the surface normal, respectively. When *S* = 0, the system is disordered.

3.3.2 Infrared spectroscopy of phospholipids and peptides

Phospholipids and peptides give many IR absorption bands in the IR spectral range. Wavenumbers of the most important fundamental vibrations are listed in Table 1. The exact frequencies of the methylene modes depend on the physical state for the hydrocarbon chains. The frequencies increase from ~2849 $\mathrm{cm^{-1}}$ and ~2917 $\mathrm{cm^{-1}}$ to ~2853 $\mathrm{cm^{-1}}$ and ~2923 $\mathrm{cm^{-1}}$, respectively for $\nu_{\mathrm{s}}(\mathrm{CH_2})$ and $\nu_{\mathrm{as}}(\mathrm{CH_2})$ modes upon a transition of the lipid from the ordered gel to the disordered liquid crystalline phase.[251] The ester

carbonyl stretching band is very sensitive to hydrogen bonding.[252] The O atoms in the phosphate group of phospholipids provide hydrogen bonding acceptors. The wavenumbers are very sensitive for the $\nu_s(PO_2^-)$ and $\nu_{as}(PO_2^-)$ modes to hydrogen bonding and interactions with divalent cations.[126,253]

Table 1: IR absorption bands of hydrocarbon chain and polar region modes in phospholipids.[231,254–256]

Vibrational mode	Wavenumber / cm^{-1}
$\nu(=CH)$ stretch	~3010
$\nu_{as}(CH_3)$ asymmetric stretch	2950 - 2980
$\nu_{as}(CH_2)$ asymmetric stretch	2926 - 2915
$\nu_s(CH_3)$ symmetric stretch	2885 - 2860
$\nu_s(CH_2)$ symmetric stretch	2856 - 2849
$\nu_{as}(CD_2)$ asymmetric stretch	2200 - 2190
$\nu_s(CD_2)$ symmetric stretch	2100 - 2087
ν (CO) stretch (ester)	1745 - 1710
$\delta_{as}(^+N(CH_3)_3)$ asymmetric bend	~ 1485
$\delta_{as}(CH_3) + \delta(CH_3)$ bending	1465 - 1455
$\delta_s(^+N(CH_3)_3)$ Symmetric bend	~ 1405
CH_2 wagging band progression	1400 - 1200
$\delta_s(CH_3)$ symmetric bend	~1378
$\nu_{as}(PO_2^-)$ asymmetric stretch	1250 - 1220
$\nu_{as}(CO-O-C)$ asymmetric stretch	~1170
$\nu_s(PO_2^-)$ symmetric stretch	1090 - 1085
$\nu_s(CO-O-C)$ symmetric stretch	~1070
ν (C − O − P) stretch	~1047
$\nu_{as}(^+N(CH_3)_3)$ asymmetric stretch	~972
$\nu_{as}(P-O)$ asymmetric stretch	~820

Peptides give arise to backbone and side chain vibrations. The approximate frequencies of amide bands of peptides in D_2O solution are listed in Table 2. The primary structure describes the amino acid sequence of proteins and peptides. Proteins and peptides fold into specific conformation, which is refered to the secondary and tertiary structure. The

folding of the polypeptide chain is stabilized by hydrogen bonds, van der Waals and hydrophobic forces.[231,257] Substractures such as α-helics and β-sheets or β-strands contribute to the secondary structure of peptides and proteins. These structures appear due to the saturation of hydrogen bond donors and acceptors in the polypeptide chain.

Table 2: Amide bands of peptides in D_2O solution.[230,231,254,256,257]

Amide mode	Wavenumber / cm^{-1}	Description
Amide A	2500 - 2400	$\nu_{as}(NH)$ in resonance with overtone
Amide B	~2400	$\nu_{s}(NH)$ in resonance with overtone
Amide I	1700 - 1600	76% $\nu(CO)$, 11% $\nu(CN)$, 8% $\delta(CCN)_{in\text{-}plane}$, 5% $\delta(NH)_{in\text{-}plane}$
Amide II	1480 - 1460	45% $\delta(NH)_{in\text{-}plane}$, 30% $\nu(CN)$, 10% $\delta(CO)_{in\text{-}plane}$, 8% $\nu(CC)$, 7% $\nu(CN)$
Amide III	~960	50% $\delta(NH)_{in\text{-}plane}$, 20% $\nu(CC)$, 18% $\nu(CN)$, 12% $\delta(CO)_{in\text{-}plane}$
Amide IV	640 - 620	45% $\delta(CO)_{in\text{-}plane}$, 35% $\nu(CC)$, 20% $\nu(CNC)$
Amide V	520 - 500	62% $(CN)_{torsion}$, 38% $\delta(NH)_{out\text{-}plane}$
Amide VI	650 - 600	85% $\delta(CO)_{out\text{-}plane}$, 15% $(CN)_{torsion}$
Amide VII	165 - 150	68% $\delta(NH)_{out\text{-}plane}$, 20% $(CN)_{torsion}$, 12% $\delta(CO)_{out\text{-}plane}$

Amide I band is the most important for the analysis of the secondary structure of peptides.[257–259] The amide I band consists of a number of overlapping components as represented in Table 3.[231]

Table 3: Amide I frequencies of secondary structure of a polypeptide or a protein in D_2O solution.[230,257]

Secondary structure	Wavenumber/cm^{-1}
α-helix	1655 - 1638
α-helical coiled coil	1640 - 1630
3_{10}-helix	1665 - 1655
Parallel β-sheet	1636 - 1630
Antiparallel β-sheet	1636 - 1630 (strong) 1680 - 1670 (weak)
Intermolecular β-sheet	1625 - 1613
β-turns	1675 - 1640
γ-turns	1690 - 1650
Unordered structure	1648 - 1640

4 Experimental part

4.1 Chemicals and materials

KLA, DMPE, POPE, d-POPE, DOPE, DMPG, 1-plamitoyl-2-oleoyl-*sn*-glycerol-3-phospho-(1`rac glycerol) (sodium salt) (POPG) and DPPG were purchased from Avanti Polar Lipids (Alabaster, Alabama, USA). Structures of the studied lipids are shown in Table 4. All lipids were used as received. Synthetic melittin was used (melittin ≥ 97 %, Cat. No. M4171, Sigma-Aldrich, Steinheim, Germany), because the natural melittin isolated from bee venom contains a small amount of phospholipase A2, which could damage the membranes.[155,156,165] Chloroform ≥ 99 %, ethanol ≥ 99.8 %, methanol, potassium perchlorate ≥ 99.99%, ethylenediaminetetraacetic acid-sodium salt dihydrate (EDTA), sodium chloride, tris (hydroxyl methyl) aminomethane (TRIS) and magnesium perchlorate hexahydrate ($Mg(ClO_4)_2 \times 6H_2O$) 99% were purchased from Sigma-Aldrich (Steinheim, Germany). All aqueous solusions were prepared from deionized water with a resistivity of 18.3 MΩ cm (PureLab Classic, Elga LabWater, Celle, Germany).

Small unilamellar vesicles (SUVs) were prepared freshly to measure the transmission spectra of the randomly oriented molecules. 10 mg ml^{-1} stock solutions of lipid mixtures DMPE-DMPG (0.5:0.5 mole), POPE-POPG:DPPG (0.5:0.475:0.025 mole), DOPE-POPG:DPPG (0.5:0.475:0.025 mole) and POPE-KLA (3.2:1 mole) were dissolved in [chloroform: methanol (4:1)] volume ratio. A small volume (0.5 ml) was dried for the stock solution in a small vial under a flow of argon. In order to remove any remaining solvent residues, the vials were placed in a vacuum desiccator for at least 2 h. Then a small volume (0.5 ml) of 0.05 M $KClO_4$ with/without 0.005 M $Mg(ClO_4)_2$ in D_2O solution was added to the completely dry lipid film in the vial and the mixture was sonicated (EMAG-Technologies, Mörfelden-Walldorf, Germany) at room temperature for at least 1 h.

Microscopic glass slides (Menzel-Glaeser, Braunschweig, Germany) were cut in (2.5 cm × 2.5 cm) pieces and used as substrates for the gold coating. These glass slides were cleaned in water and isopropanol in ultrasonic bath (Bandelin Sonorex, Berlin, Germany) for 5 min and dried in a stream of argon. On the cleaned glass surface, 5 nm of an adhesive

chromium layer and 200 nm of gold were evaporated using a Tectra Mini Coater (Tectra GmbH, Frankfurt, Germany). These substrates were used to deposit LB-LS lipid bilayers. Two kinds of substrates were used to investigate asymmetric lipid bilayers adsorbed on the electrode surfaces: a single crystal gold Au(111) disc electrode [diameter of 15 mm and 3 mm] (MaTeck, Jülich, Germany) and gold film vapor-deposited on a glass slide.

Table 4: Chemical structures of the studied lipids.

Lipid	Chemical structure
Kdo_2-lipid A (KLA)	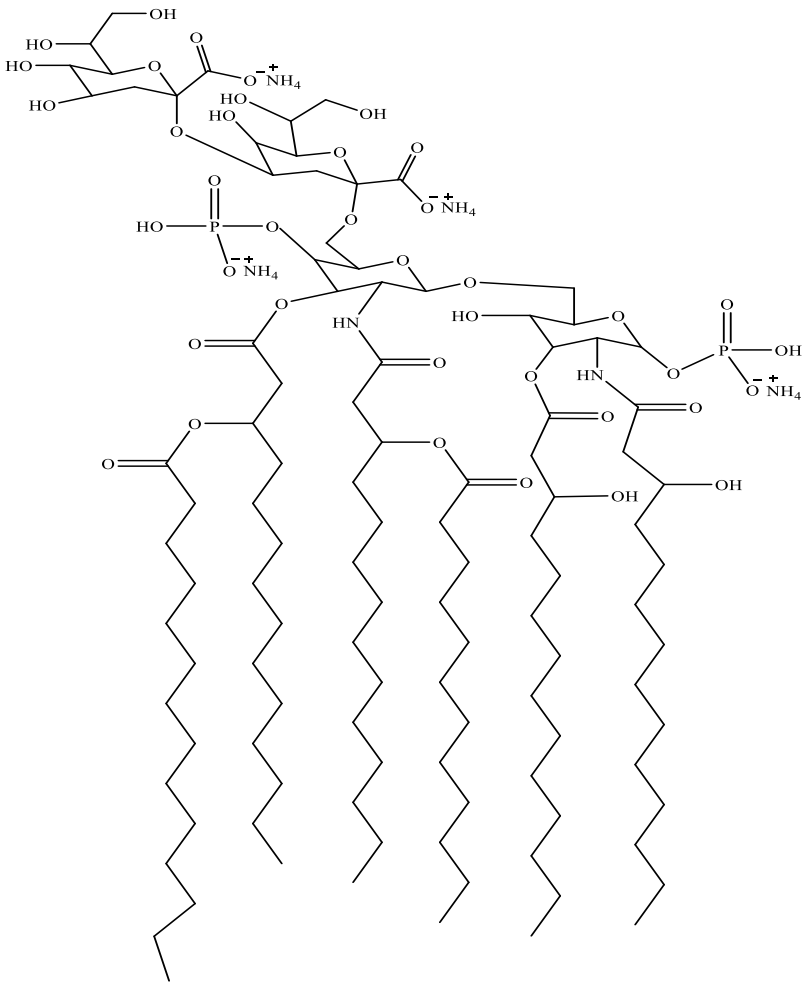

DMPE (C14:0- C14:0)	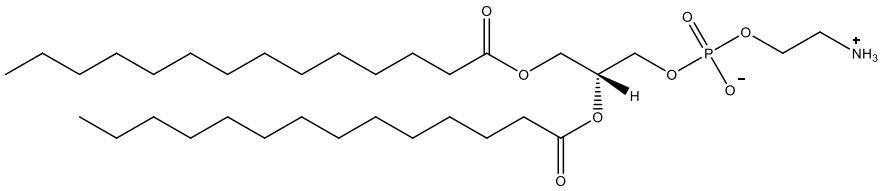
POPE (C16:0- C18:1)	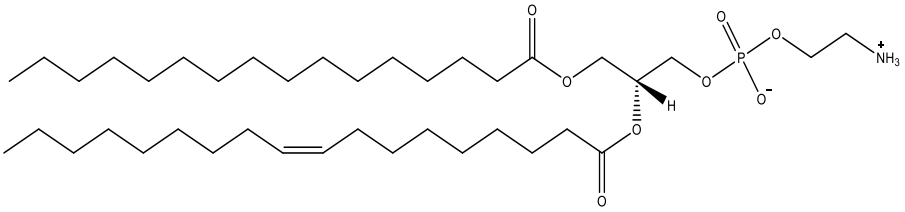
d-POPE (C16:0- d31-C18:1)	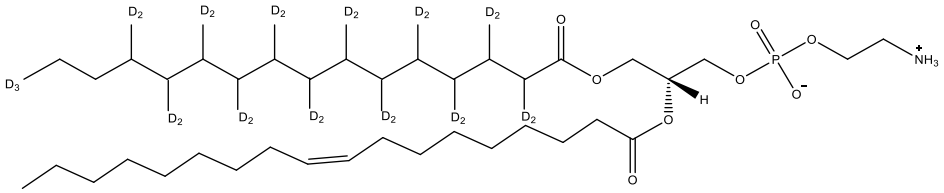
DOPE (C16:1- C16:1)	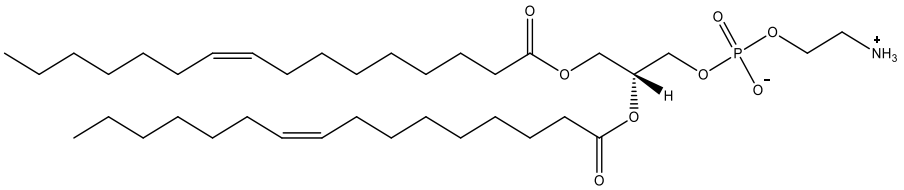
DMPG (C14:0- C14:0)	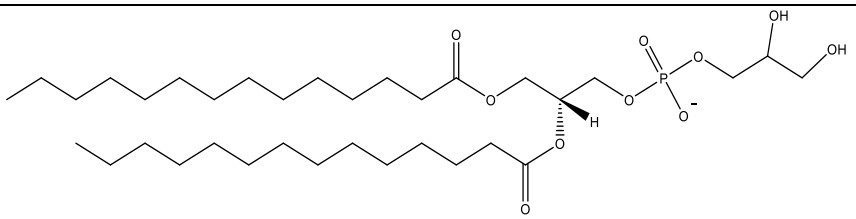
DPPG (C16:0- C16:0)	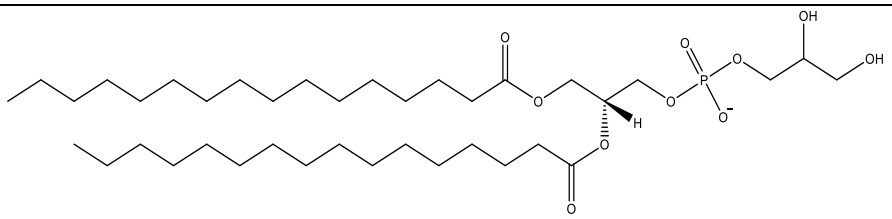
POPG (C16:0- C18:1)	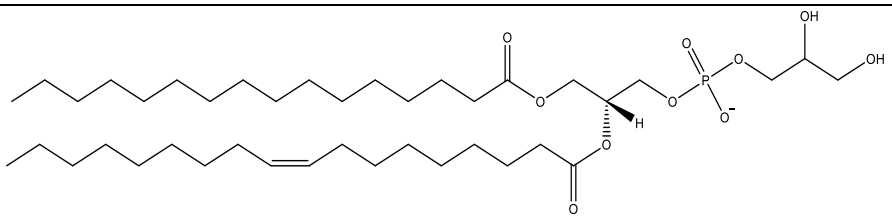

4.2 Langmuir-Blodgett and Langmuir-Schaefer technique

Fresh lipid solutions were prepared by dissolving h-POPE, d-POPE, DOPE, DMPG or POPG in chloroform. DMPE and DPPG were dissolved in a mixture of chloroform and methanol (Sigma-Aldrich, Steinheim, Germany) in (4:1) volume ratio. KLA was dissolved in a mixture of chloroform, methanol and water in (13:6:1) volume ratio. The lipid concentration of KLA, DMPE and DMPG was 1 mg ml^{-1}. The concentration of POPE, d-POPE, DOPE and POPG:DPPG (0.95:0.05) was equal to 1 μmol ml^{-1}. The experiments were conducted in a Langmuir teflon trough (KSV Ltd., Helsinki, Finland) equipped with two movable hydrophilic barriers. The trough and barriers were cleaned before each use. They were rinsed with deionized water and ethanol. Then the trough and the barriers were cleaned with a Kimtech tissue soaked in chloroform followed by rinsing with ethanol and water. Small teflon parts like substrate holders were rinsed with ethanol and left for drying. The subphase was cleaned by moving the barriers together and siphoning off the surface subphase layer. The cleanliness was checked for the air|water interface by the measurement of Π. The trough was ready to start the measurement after retraction of the barriers.

Using a microsyringe (Hamilton, Nevada, USA) several μl of the lipid solution were placed at the liquid|air interface of the Langmuir trough. The lipid solution was left for 10 min to evaporate the solvent. Barriers moved at the rate of 10 mm min^{-1}, while Π was recorded. Π was measured with a Wilhelmy paper plate. The accuracy of measurements was ± 0.02 nm^2 for A and ± 0.1 mN m^{-1} for Π.

LB-LS transfer was used to prepare asymmetric lipid bilayers containing PE in the inner (facing the Au surface) and PG in the outer (solution-oriented) leaflet on the gold electrode. The asymmetric lipid bilayers composed of h-POPE-KLA, d-POPE-KLA, DMPE-DMPG, POPE-POPG:DPPG (0.95:0.05) and DOPE-POPG:DPPG (0.95:0.05) were transfered on electrode surfaces. The experiments were performed in a laminar flow hood to avoid the dust. The first monolayer was transferred from water onto the Au(111) single crystal electrode by LB vertical withdrawing at a speed of 15 mm min^{-1}. TR was (1.10 ± 0.20). In this monolayer, the head groups of PE face the metal substrate and the hydrophobic hydrocarbon chains are directed toward air. The monolayer-covered

Au(111) single crystal substrate was allowed to dry for 1 h. The second lipid monolayer, which models the outer leaflet was transferred from water for DMPG and from [0.1 M $KClO_4$ + 0.005 M $Mg(ClO_4)_2$] for KLA and the mixture POPG:DPPG (0.95:0.05) using LS method, which used to deposit the second monolayer at Π = 30 mN m^{-1}. The hydrocarbon chains of the phospholipid are directed toward the Au(111) electrode and the polar head groups are directed toward air in the monolayer transferred using LS technique. This is a Y-type asymmetric lipid bilayers. All lipid bilayers were dried for 24 h before use in further experiments.

4.3 Interaction of melittin with the model of biological membranes

The concentration of melittin in a buffer solution [0.02 M TRIS, 0.15 M NaCl and 0.005 M EDTA, pH (7.3 ± 0.1)] was either 1 μM or 10 μM. Gold electrodes modified with h-POPE-KLA and d-POPE-KLA bilayers were incubated in the buffer solution containing melittin in a hanging meniscus configuration. For the melittin concentration of 1 μM, the incubation time was 1 h. The incubation time was 15 min in 10 μM melittin. After this time the modified electrodes were carefully rinsed with water and transferred to either the electrochemical or spectroelectrochemical cell.

4.4 Electrochemical measurement for the study of model membranes

Electrochemical measurements were performed in an all-glass three-electrode cell using the Au(111) single crystal disc (diameter 3 mm, MaTeck, Jülich, Germany) as a working electrode (WE) in a hanging meniscus configuration as illustrated in Figure 17. The hanging meniscus configuration allows the single crystal surface to be in contact with an electrolyte solution. A flame-annealed colied gold wire served as a counter electrode (CE) and Ag|AgCl|saturated KCl (VWR-Chemicals, Leuven, Belgium) Ag|AgCl served as a reference electrode (RE). It was separated from an electrolyte solution by a salt bridge. Electrolyte solution was either 0.1 M $KClO_4$ or 0.1 M $KClO_4$ + 0.005 M $Mg(ClO_4)_2$ in H_2O. A Methrom Autolab potentiostat (Methrom Autolab, Utrecht, Holland) was used to

perform the electrochemical measurements. Prior to the experiment, the bare electrode was rinsed with water, flame-annealed, cooled in air and dried with argon to avoid contact of the hot electrode with an electrolyte solution. The electrochemical cell and its parts were cleaned with piranha solution [3:1 mixture of (H_2SO_4) and 30% (H_2O_2)], ethanol and rinsed with water. The cell parts were soaked in water for several hours and rinsed again with water before use. The cell was purged with argon for 1 h before the measurement to remove oxygen from an electrolyte solution. An argon blanket was maintained over the solution throughout the experiment to prevent the influx of oxygen. The cleanness of the electrochemical cell was tested by recording the cyclic voltammograms in an electrolyte solution.

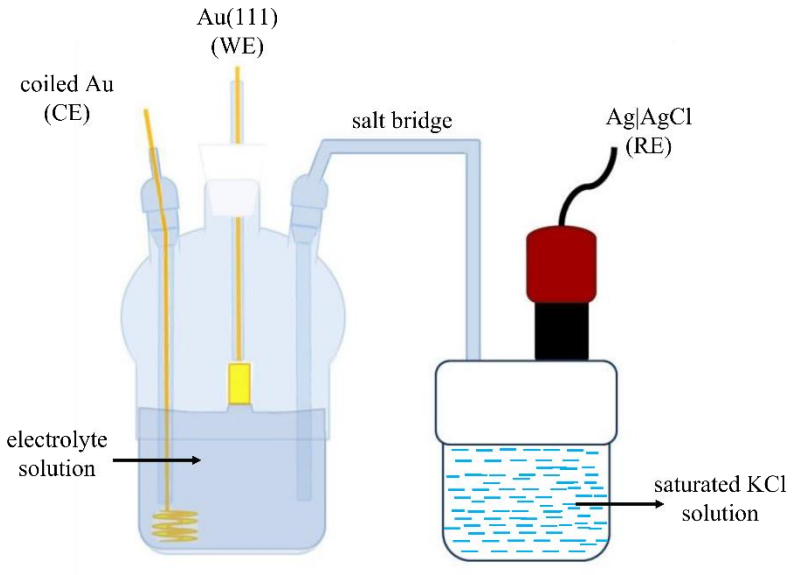

Figure 17: Schematic representation of the electrochemical cell used in the ACV measurements.

4.4.1 Alternating current voltammetry

ACV was used to determine the capacitance of unmodified and lipid bilayer modified Au(111) electrode. The area of the Au(111) electrode was 0.071 cm^2. The AC voltammograms were recorded in the negative and the positive going potential scans at a rate 5 mV s^{-1} with a perturbation of 20 Hz frequency and 10 mV amplitude. The differential capacitance vs. potential plots were calculated from the in-phase and out-of phase components of the AC signal assuming the cell was equivalent to a resistor in series

with a capacitor using equation 5. A Methrom Autolab potentiostat (Methrom Autolab, Utrecht, Holland) was used to perform the electrochemical measurements.

4.5 Polarization modulation infrared reflection absorption spectroscopy measurements

PM IRRA spectra were recorded using a Vertex 70 spectrometer with a photoelastic modulation (PMA 50, Bruker, Ettlingen, Germany) and a demodulator (Hinds Instruments, Hillsboro, USA).

4.5.1 Polarization modulation infrared reflection absorption spectroscopy at air|gold interface

The setup of *ex situ* PM IRRAS experiment is shown in Figure 18. The angle of incidence of the IR light was set to 80°. The half-wave retardation was set to 2900 cm^{-1} for the CH stretching bands, at 2100 cm^{-1} for the CD stretching bands and at 1600 cm^{-1} for the C=O stretching and amide I bands analysis. All spectra were processed using the OPUS v5.5 software (Bruker, Ettlingen, Germany). 500 spectra were measured with a resolution of 4 cm^{-1}. All IR spectra were collected in dry air atmosphere.

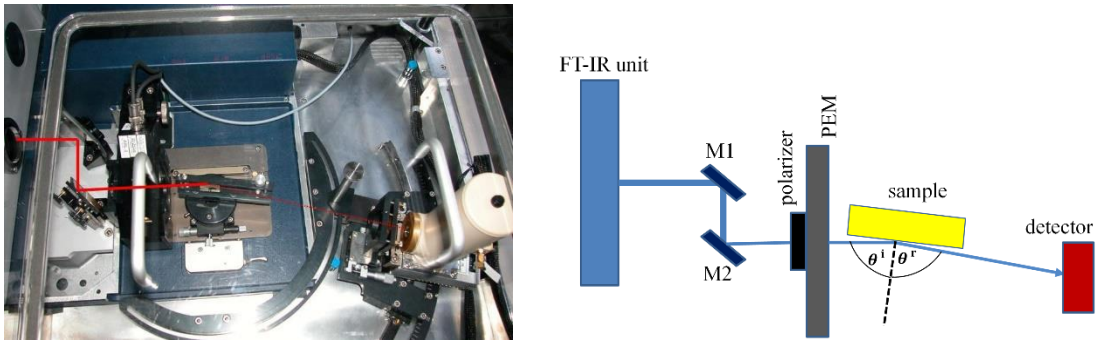

Figure 18: The setup for the *ex situ* PM IRRAS experiments. M1 and M2 refer to the mirrors.

4.5.2 *In situ* polarization modulation infrared reflection absorption spectroscopy measurements

A scheme of the spectroelectrochemical glass cell is shown in Figure 19. It was washed in water, ethanol and soaked in water for 4 h and finally rinsed with water. The components of the spectroelectrochemical cell were dried in an oven at 60°C before use. The CaF_2 prism was rinsed with water, ethanol and placed in UV-ozone chamber (Bioforce Nanosciences, Inc. Ames, IA, USA) for 10 min. The spectroelectrochemical cell has a build-in platinum CE. The reference electrode (RE) was Ag|AgCl in 3M KCl in D_2O. A disc Au(111) single crystal (diameter. 15 mm, MaTeck, Jülich, Germany) was used as the WE and mirror for the IR radiation. The setup of *in situ* PM IRRAS experiment is shown in Figure 20. A lipid bilayer was transferred on the WE surface using the LB-LS transfer, as described in section 4.2.

The 0.05 M $KClO_4$ in D_2O solution was used to study the DMPE-DMPG bilayer. While the 0.05 M $KClO_4$ + 0.005 M $Mg(ClO_4)_2$ in D_2O solution was used to study the POPE-POPG:DPPG, DOPE-POPG:DPPG, POPE-KLA bilayers and POPE-KLA bilayer with bound melittin. The angle of incidence was set to 55°. The half-wave retardation was set to either 2900 cm^{-1} or 1600 cm^{-1}. All solutions were prepared in D_2O and purged for 1 h with argon to remove oxygen. To study the CD stretching bands in d-POPE-KLA bilayer, an electrolyte solution was 0.05 M $KClO_4$ + 0.005 M $Mg(ClO_4)_2$ in H_2O and the angle of inceidence was set to 52° at half-wave retardation 2100 cm^{-1}.

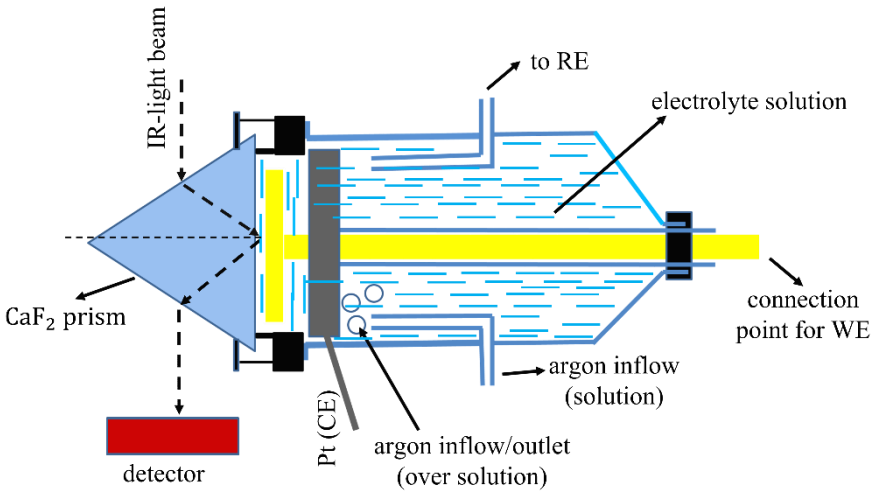

Figure 19: A scheme of the spectroelectrochemical cell for the *in situ* PM IRRAS experiments.

At each potential applied to the Au electrode, 400 spectra were measured with a resolution of 4 cm^{-1}. In each experiment, five negative and positive going potential scans were recorded. Each potential scan was analyzed separately. In the negative going potential scan, the following potentials were applied to the Au(111) electrode: 0.40, 0.25, 0.10, 0.00, -0.10, -0.20, -0.30, -0.40, -0.55, -0.65, -0.80 V, while in the positive going potential scan -0.80, -0.60, -0.40, -0.30, -0.20, -0.10, 0.00, 0.10, 0.25, 0.40 V. The thickness of an electrolyte layer varied between 4 and 5 μm between the Au(111) electrode and the CaF_2 prism in different experiments.

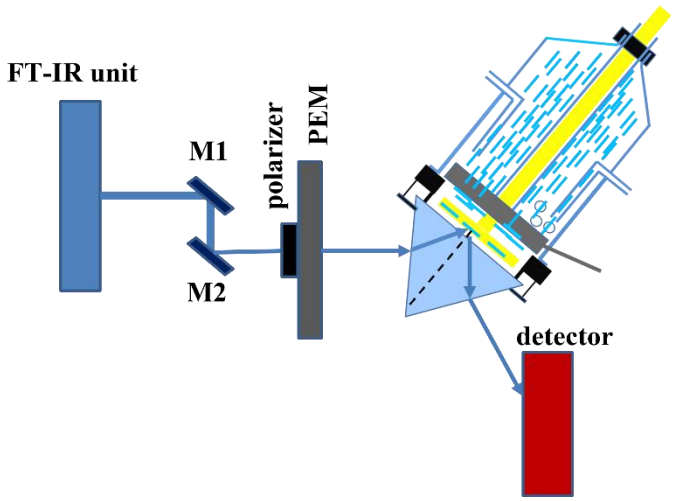

Figure 20: The setup of the *in situ* PM IRRAS experiments. M1 and M2 refer to the mirrors.

4.6 FTIR transmittance measurements

The IR transmission spectra were recorded for 0.05 M $KClO_4$ with/without 0.005 M $Mg(ClO_4)_2$ in D_2O solution and vesicles of lipids in D_2O solution in a flow cell between two ZnSe windows (Sigma-Aldrich, Steinheim, Germany) and a 50 μm Teflon spacer. By using a Vertex 70 spectrometer (Bruker, Ettlingen, Germany), 64 spectra were recorded with a resolution of 4 cm^{-1}. In each measurement, the exact thickness was determined for the spacer.

The transmission IR spectra were used to obtain the refractive index (*n*) and the attenuation coefficient (*k*) of the lipid mixture using a computer program written by Prof. Dr. Zamlynny (Acadia University, Canada).[237] Lambert-Beer law is used to calculate the

approximate value of the attenuation coefficient of the analyte (k^{Analyte}) from the IR transmission spectrum:[237,260]

$$\frac{I}{I_{\circ}} = exp\left(\frac{-4\pi f^{Analyte} k^{Analyte}\, d}{\lambda}\right) \tag{16}$$

where I and I_o are the intensities of the IR radiation transmitted by the analyte and solvent, respectively. λ is the wavelength of the incoming IR radiation, d is the cell thickness and f^{Analyte} is the volume fraction of the analyte dissolved in the electrolyte solution.[237,260] The f^{Analyte} is equal to:

$$f^{Analyte} = c^{Analyte}\left(\frac{M^{Analyte}}{\rho^{Analyte}}\right) \tag{17}$$

where c^{Analyte} is the molar concentration, M^{Analyte} molar mass and ρ^{Analyte} the density of the analyte in the solution. The approximate k was first used to determine the refractive index of the pure analyte (n^{Analyte}) using the Kramer-Kroenig transformation.[237,260]

$$n^{Analyte}\widetilde{\nu_o} = n_{\infty}^{Analyte} + \frac{2}{\pi}\, P \int_{\widetilde{\nu_1}}^{\widetilde{\nu_2}} \left(\frac{\tilde{\nu} k^{Analyte}\,(\tilde{\nu})}{(\tilde{\nu}^2 - \tilde{\nu}_o^2)}\right) d\tilde{\nu} \tag{18}$$

where $n_{\infty}^{Analyte}$ is the average refraction index of the analyte in the spectral regions where no absorption of the IR light by the analyte takes place and P is the Cauchy principal value of the integral.

The n^{Analyte} is calculated in the spectra region between $\widetilde{\nu_1}$and $\widetilde{\nu_2}$ for $k^{\text{Analyte}} \neq$ zero. $\widetilde{\nu_1}$and $\widetilde{\nu_2}$ is the difference in wavenumbers between the maximum (or minimum) of the last and first fringe in the spectral region. The refractive index is calculated as a function of wavenumber ($\tilde{\nu}$) $\tilde{\nu}$ >> ($\tilde{\nu}$ - $\widetilde{\nu_o}$) where $\widetilde{\nu_o}$ is the frequency at which the refractive index is evaluated. The calculated refractive index contains the contribution of all absorbing species in the analyte and the solvent.

The *n* and the *k* of the solution containg the analyte are calculated using equations 19 and 20.[237,260]

$$\sum x^{Analyte} \frac{M^{Analyte}}{\rho} \frac{n^2 - 1}{n^2 + 2} = \sum x^{Analyte} \frac{M^{Analyte}}{\rho^{Analyte}} \frac{n^{2\,Analyte} - 1}{n^{2\,Analyte} + 2} \quad (19)$$

$$\sum x^{Analyte} \frac{M^{Analyte}}{\rho} k = \sum x^{Analyte} \frac{M^{Analyte}}{\rho^{Analyte}} k^{Analyte} \quad (20)$$

Where ρ and $\rho^{Analyte}$ are the densities of the solution with the analyte and the pure analyte, respectively. The terms *n*, *k* and $n^{Analyte}$, $k^{Analyte}$ represent the refractive index and attenuation coefficient of the solution and pure analyte, respectively. The $x^{Analyte}$ and $M^{Analyte}$ represent the mole fraction and molar mass of the analyte, respectively. The calculated *n* and *k*, obtained from equations 19 and 20, were introduced to the Frensel matrix to calculate the transmittion spectrum of the pure substance. The refractive index and attenuation coefficient of the analyte were obtained. These optical constants are used to calculate the PM IRRA spectrum of a randomly oriented film using the Fresnel matrix method.[237]

Optical constants of pure lipids were used to calculate the PM IRRA spectra in the following regions: ν(CH) (3050 - 2700 cm^{-1}), ν(C=O) stretching modes and amide I (1800 - 1500 cm^{-1}).

4.7 Atomic force microscopy measurements

In situ electrochemical AFM measurements were carried out with 5500 AFM instrument (Keysight Technology, Santa Rosa, California, USA). Images were acquired in MAC Mode using type VII MAC cantilevers with nominal spring constant of 0.14 N m^{-1} and a resonance frequency of 18 kHz. The POPE-POPG:DPPG bilayer was deposited on single crystal Au(111) substrate at Π = 30 mN m^{-1}. The image of POPE-POPG:DPPG was recorded in 0.05 M $KClO_4$ + 0.005 M $Mg(ClO_4)_2$ under electrochemical control. Single

crystal Au(111) substrate (MaTeck, Jülich, Germany) served as a working electrode, while a quasi-reference and counter electrode were made of Pt wires. Teflon parts of the electrochemical cell were cleaned in piranha solution for at least 2 h and rinsed with water. The single crystal Au(111) electrode was flame annealed before lipid film deposition.

5 Results

5.1 Studying model systems of the inner membrane of Gram-negative bacteria

Asymmetric phospholipid bilayers composed of PE in the inner leaflet and PG in the outer leaflet were deposited using LB-LS transfer onto a gold electrode. These bilayers represent simple models of the IM of Gram-negative bacteria. Phospholipid molecules were used to fabricate the IM of Gram-negative bacteria containing two saturated (DMPE and DMPG), one monounsaturated (POPE and POPG) and two monounsaturated hydrocarbon chains (DOPE). DMPE and DMPG had shorter hydrocarbon chains than POPE and DOPE.

5.1.1 Surface pressure-area isotherms

Figure 21a, c shows the recorded *Π-A* isotherms of the studied PE and PG. K_s was calculated using equation 4 and the corresponding plots are shown in Figure 21b, d. Isotherms were compared for phospholipids with the same length of the hydrocarbon chains (DMPE and DMPG). Both isotherms have a similar shape. The A_o and A_{lim} were smaller in the DMPE monolayer than in the DMPG monolayer (Table 5). Both isotherms showed a plateau region, indicating the coexistence of the LE and LC phases. At *A* below 0.6 nm^2, *Π* increased rapidly until the monolayer collapsed. Moreover, the isotherm was shifted for the DMPE monolayer to smaller areas compared to the DMPG isotherm. It is a consequence of a less bulky polar head group of the PE compared to the PG. Table 5 summerizes the A_o, A_{lim}, maximum K_s at the Π_c and Π_c extracted from the DMPE, POPE, DOPE, DMPG and POPG:DPPG (0.95:0.05) mixture monolayers. These values are in agreement with literature.[6,94,118,154,261,262] DMPE, POPE and DOPE molecules differ in the length of the hydrocarbon chains. The isotherm for the DMPE was shifted to smaller areas as compared to POPE and DOPE isotherms (Figure 21a). This indicated that, the DMPE monolayer molecules were packed denser than the monolayers of the POPE and DOPE. Isotherms recorded for POPE and DOPE were different than those of phospholipids having saturated hydrocarbon chains. It can be concluded that the presence of a double

bond in the hydrocarbon chains prevented the POPE and DOPE molecules from a tight packing. POPE isotherm showed a plateau region at Π = 38 – 40 mN m^{-1}, indicating the coexistence of the LE and LC phases. In addition, the isotherm for the DOPE monolayer was situated at larger areas than the isotherms obtained for the POPE and DMPE monolayers.

Table 5: The A_o, A_{lim}, Π_c and maximum K_s at the Π_c of the DMPE, POPE, DOPE, DMPG and POPG:DPPG (0.95:0.05) mixture monolayers.

Monolayer	A_o / nm^2	A_{lim} / nm^2	Π_c / mN m^{-1}	K_s / mN m^{-1}
DMPE	0.96 ± 0.02	0.41 ± 0.02	59 ± 2	353 ± 5
POPE	1.00 ± 0.02	0.40 ± 0.01	57 ± 2	102 ± 3
DOPE	1.12 ± 0.02	0.52 ± 0.02	47 ± 2	92 ± 3
DMPG	1.32 ± 0.03	0.45 ± 0.03	68 ± 2	429 ± 3
POPG:DPPG (0.95:0.05)	1.80 ± 0.01	0.75 ± 0.02	46 ± 2	87 ± 2

Furthermore, the maximal value of the K_s at the Π_c was much lower for the DOPE monolayer [K_s = (92 ± 3) mN m^{-1}] than that for the DMPE monolayer [K_s = (353 ± 5) mN m^{-1}]. This proved that unsaturation of the hydrocarbon chains increased the fluidity of the monolayer.[263] The isotherm of DMPG was shifted to smaller areas compared to the isotherm of the POPG:DPPG (0.95:0.05) mixture (Figure 21c). This indicated that molecules were packed denser in the DMPG monolayer than in the POPG:DPPG (0.95:0.05) monolayer. The monolayer of DMPG collapsed at A_{lim} = (0.45 ± 0.03) nm^2 and Π_c = (68 ± 2) mN m^{-1}. The A_{lim} was (0.75 ± 0.02) nm^2 and Π_c was (46 ± 2) mN m^{-1} in the two component POPG:DPPG (0.95:0.05) monolayer (Figure 21c and Table 5). Furthermore, the maximum value of K_s at the Π_c was lower for the POPG:DPPG (0.95:0.05) monolayer [K_s = (87 ± 2) mN m^{-1}] than the K_s value of the DMPG monolayer [K_s = (429 ± 3) mN m^{-1}].

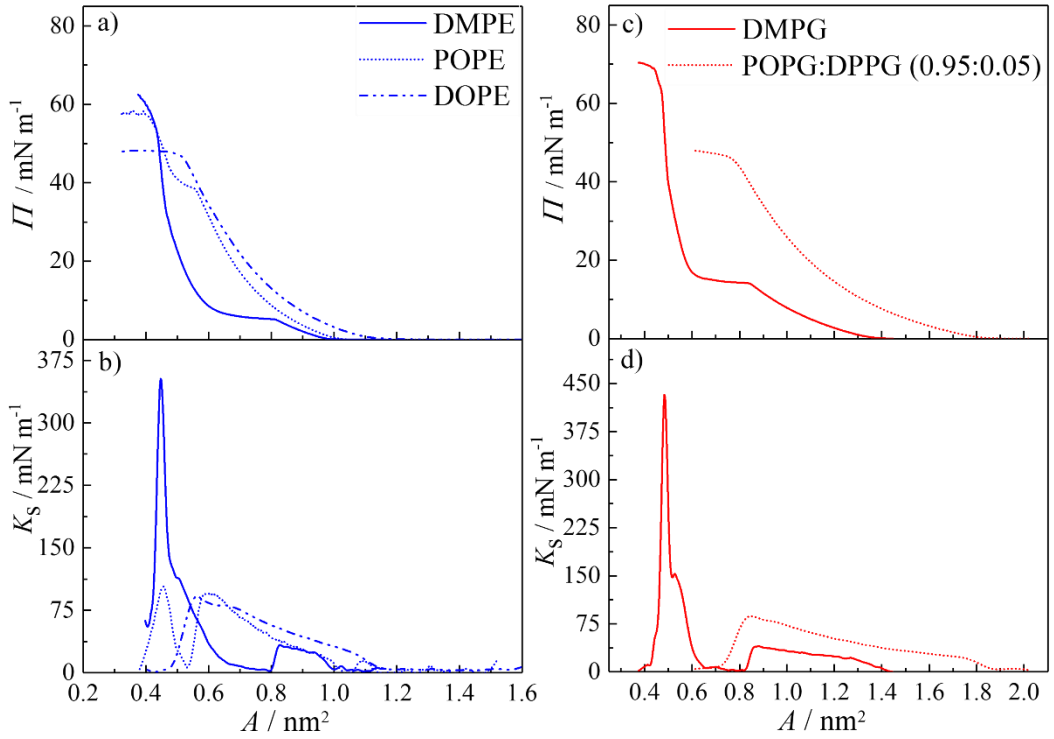

Figure 21: Plots of a), c) Π and b), d) K_s vs. A of the studied phospholipids: a), b) PE (blue): DMPE (solid blue line), POPE (short dot blue line) and DOPE (dash dot blue line) on water subphase and c), d) DMPG (solid red line) on water subphase and POPG:DPPG (0.95:0.05) (short dot red line) on 0.1 M $KClO_4$ + 0.005 M $Mg(ClO_4)_2$ subphase.

5.1.2 Electrochemical characterization of the studied lipid bilayers

Figure 22 shows cyclic voltammograms for a bare Au(111) electrode in 0.1 M $KClO_4$ + 0.005 M $Mg(ClO_4)_2$ solution [pH (5.9 ± 0.2)]. A small peak at E = 0.49 V vs. Ag|AgCl corresponded to the oxidation of gold on an electrode surface in the anodic scan, while the reduction peak appeared at E = 0.39 V vs. Ag|AgCl.

Capacitance-potential curves of the three studied phospholipid bilayers: DMPE-DMPG, POPE-POPG:DPPG and DOPE-POPG:DPPG on the Au(111) electrode showed different electrochemical characteristics (Figure 23). The potential of zero charge (E_{pzc}) of the Au(111) electrode in 0.1 M $KClO_4$ + 0.005 M $Mg(ClO_4)_2$ solution equals 0.305 V vs. Ag|AgCl. It was determined from the minimum in the double layer capacitance at lower electrolyte concentration [5×10^{-3} M $KClO_4$ + 1×10^{-5} M $Mg(ClO_4)_2$]. Figure 23 and Table 6 show that the minimum capacitance (C_{min}) equals to (5.5 ± 0.6) µF cm^{-2} for the studied phospholipid bilayers. This value was larger than the capacitance expected for a defect-

free phospholipid bilayer (~0.8 - 1.0 μF cm^{-2})[1], indicating the presence of some defects in the model membranes.[264–266] The C_{min} (5.7 ± 0.5) μF cm^{-2} remains constant in a wide range of the membrane potentials (-0.60 V < E - E_{pzc} < 0.10 V) in the DMPE-DMPG bilayer. In this potential region, the phospholipid bilayer was adsorbed directly on the Au(111) electrode.

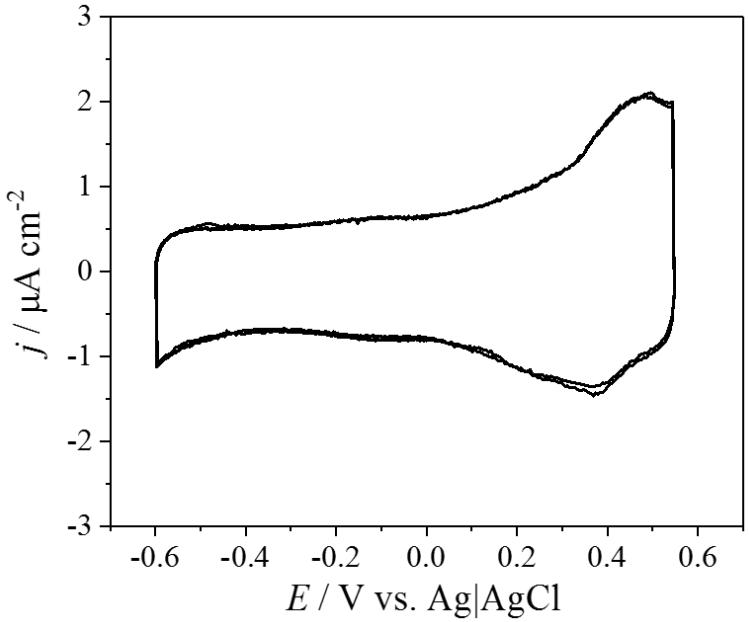

Figure 22: Cyclic voltammograms of a bare Au(111) electrode in 0.1 M $KClO_4$ + 0.005 M $Mg(ClO_4)_2$ solution. The scan rate is 0.025 V s^{-1}.

The capacitance-membrane potential plot shows a desorption peak (E_{des}) in the negative going potential scan at E - E_{pzc} = -0.92 V (Figure 23a). Below this potential, the capacitance was the same for the DMPE-DMPG bilayer modified Au(111) as the capacitance of unmodified Au(111) electrode, indicating desorption of the phospholipid film from the electrode surface. The presence of a peak ($E_{re\text{-}ads}$) indicated some rearrangements in the desorbed bilayer at E - E_{pzc} = -0.89 V in the positive going potential scan, which lead to a fast decrease in the capacitance and re-adsorption of the bilayer on the Au(111) electrode (Figure 23a). The electrochemical characteristics were different for the POPE-POPG:DPPG and DOPE-POPG:DPPG bilayers from that of the DMPE-DMPG bilayer (Figure 23).

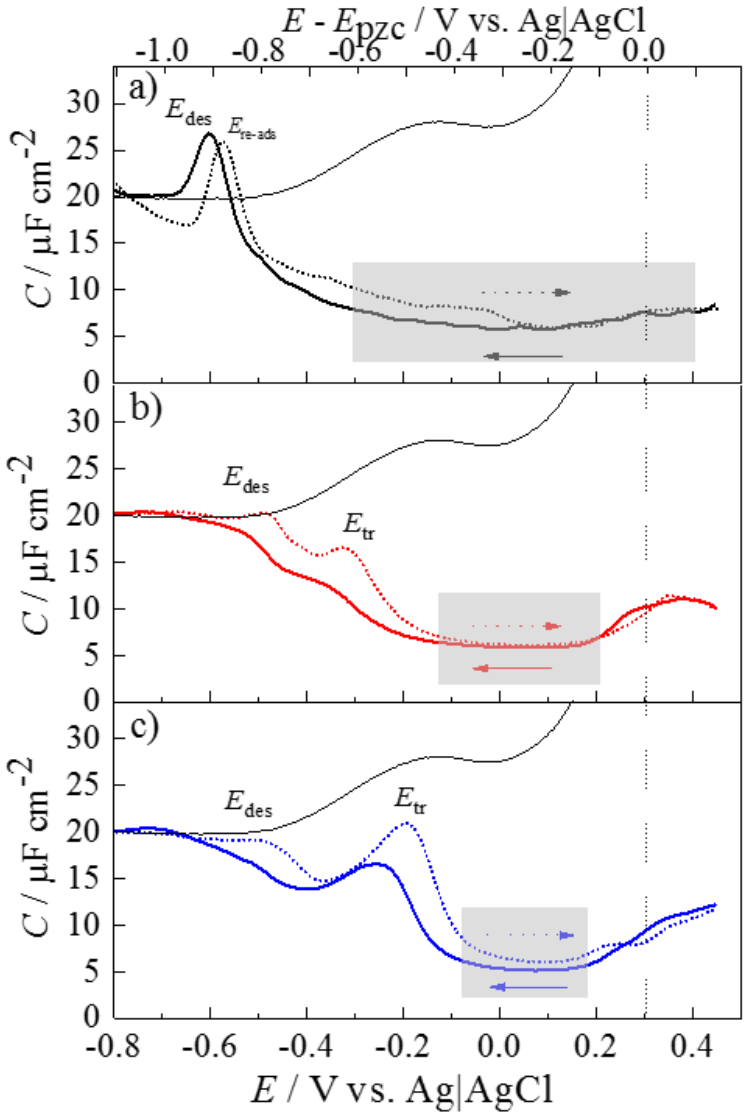

Figure 23: Plot of C vs. E and E - E_{pzc} potentials for a) the DMPE-DMPG bilayer in 0.1 M $KClO_4$, b) the POPE-POPG:DPPG bilayer in 0.1 M $KClO_4$ + 0.005 M $Mg(ClO_4)_2$ solution and c) the DOPE-POPG:DPPG bilayer in 0.1 M $KClO_4$ + 0.005 M $Mg(ClO_4)_2$ solution. All the model membranes were prepared on the Au(111) electrode; solid lines - negative, short dotted lines - positive going potential scans. Grey marked fields show the potential range of C_{min}. Thin solid black curve represents the capacitance of the unmodified Au(111) electrode in 0.1 M $KClO_4$ + 0.005 M $Mg(ClO_4)_2$ solution.

The adsorption-desorption process displayed two steps. In the POPE-POPG:DPPG and DOPE-POPG:DPPG bilayers, the potential window of the C_{min} (5.7 ± 0.5) µF cm^{-2} was reduced compared to the DMPE-DMPG bilayer. The phospholipid bilayers were adsorbed directly on Au(111) surfaces at negative membrane potentials. The phase transition peaks were obtained in the negative going potential scan at E - E_{pzc} = -0.68 V and E - E_{pzc} = -0.56 V in the POPE-POPG:DPPG and DOPE-POPG:DPPG bilayers, respectively (Figure 23b, c).

Table 6: Membrane potential of the phospholipid bilayer desorption $(E - E_{pzc})_{des}$, C_{min} and the membrane potential window of the C_{min}, phase transitions $(E - E_{pzc})_{tr-}$ in the negative going potential scans and $(E - E_{pzc})_{tr+}$ in the positive going potential scans of the DMPE-DMPG, POPE-POPG:DPPG and DOPE-POPG:DPPG bilayers on the Au(111) electrode surface.

Phospholipid bilayer	$(E - E_{pzc})_{des}$ / V	C_{min} / μF cm^{-2}	$(E - E_{pzc})$ range of C_{min} / V	$(E - E_{pzc})_{tr-}$ / V	$(E - E_{pzc})_{tr+}$ / V
DMPE-DMPG	-0.92	5.7 ± 0.5	-0.60 < $E - E_{pzc}$ < 0.10	n.o.	n.o.
POPE-POPG:DPPG	-0.85	5.8 ± 0.7	-0.46 < $E - E_{pzc}$ < -0.11	-0.68	-0.63
DOPE-POPG:DPPG	-0.83	5.1 ± 0.5	-0.38 < $E - E_{pzc}$ < -0.16	-0.56	-0.50

n.o. –not observed

This transition caused an appearance of a new state in the adsorbed membrane, which was characterized by the capacitance of 12 – 15 μF cm^{-2}. A further negative potential shift caused a continuous increase in the capacitance. No clearly defined desorption peak was observed in the POPE-POPG:DPPG and DOPE-POPG:DPPG bilayers (Figure 23b, c). The capacitance of the Au(111) electrode modified by lipid bilayers merged with the capacitance of unmodified Au(111) electrode at $E - E_{pzc}$ < -0.94 V (Figure 23b, c). In the positive going potential scan at membrane potentials $E - E_{pzc}$ < -0.78 V, a small decrease in the capacitance was followed by the appearance of (E_{tr}) peaks at $E - E_{pzc}$ = -0.63 V and $E - E_{pzc}$ = -0.50 V in the POPE-POPG:DPPG and DOPE-POPG:DPPG bilayers, respectively (Figure 23b, c and Table 6). This transition caused a decrease in the capacitance and spreading of the phospholipid bilayer on the Au(111) electrode. A small hysteresis was observed between the negative and positive going potential scans. The presence of the hysteresis pointed on a slow kinetics of the adsorption-desorption process.[267] The capacitance started to increase at membrane potentials -0.1 V < $E - E_{pzc}$ < 0.1 V, suggesting some rearrangements in bilayers. Figure 24 shows that the capacitance-membrane potential plots of the DOPE-POPG:DPPG bilayer on the Au(111) electrode in 0.1 M $KClO_4$ (Figure 24a) and 0.1 M $KClO_4$ + 0.005 M $Mg(ClO_4)_2$ (Figure 24b). In 0.1 M $KClO_4$ + 0.005 M $Mg(ClO_4)_2$ solution, the C_{min} of the DOPE-POPG:DPPG bilayer was (5.1 ± 0.5) μF cm^{-2}, which was lower than in 0.1 M $KClO_4$ electrolyte (5.8 ± 0.3) μF cm^{-2}.

The potential window of C_{min} was nearly the same in both cases (Figure 24 and Table 7). In the negative going scan at E - E_{pzc} = -0.44 V, a small increase in the capacitance was followed by the appearance of a phase transition peak (E_{tr}) at E - E_{pzc} = -0.54 V (Figure 24a). A desorption peak (E_{des}) was obtained at E - E_{pzc} = -0.94 V (Figure 24a). The presence of a re-adsorption peak ($E_{re\text{-}ads}$) indicated some rearrangements in the desorbed DOPE-POPG:DPPG bilayer in the positive going potential scan at E - E_{pzc} = -1.0 V, which was followed by a phase transition peak (E_{tr}) at E - E_{pzc} = -0.57 V (Figure 24a).

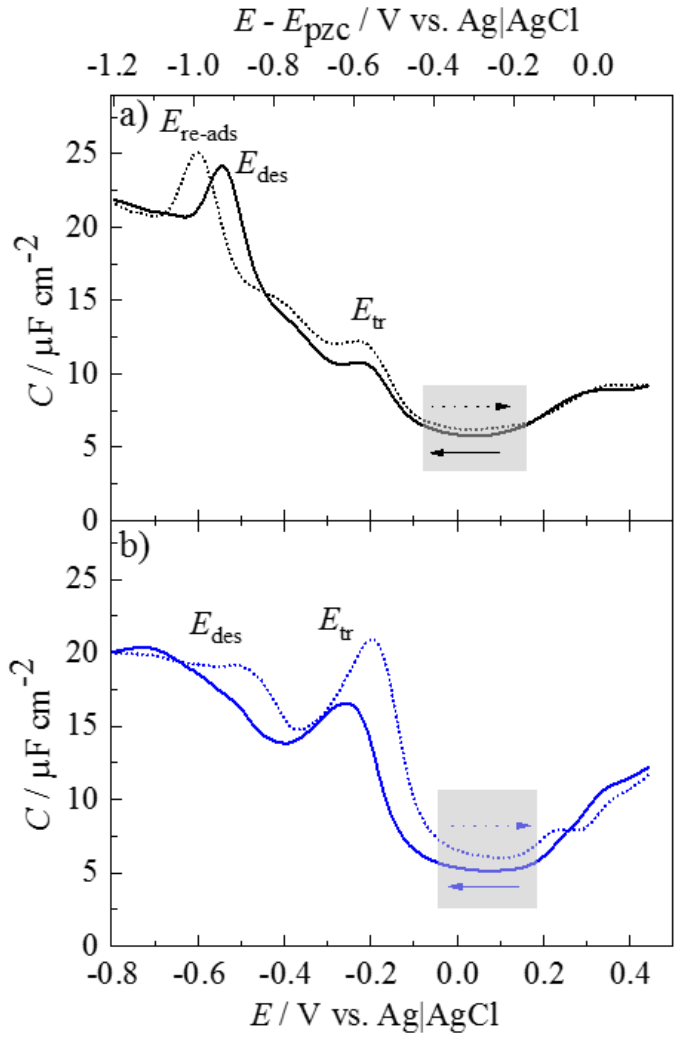

Figure 24: Plots of C vs. E and E - E_{pzc} potentials of the DOPE-POPG:DPPG bilayer on the Au(111) electrode in a) 0.1 M $KClO_4$ and b) 0.1 M $KClO_4$ + 0.005 M $Mg(ClO_4)_2$. Solid lines - negative, short dotted lines - positive going potential scans. Grey marked fields show the potential range of the C_{min}.

Table 7: Membrane potential of the phospholipid bilayer desorption (E - $E_{pzc})_{des}$, C_{min} and the membrane potential window of the C_{min}, phase transitions (E - $E_{pzc})_{tr-}$ in the negative going potential scans and (E - $E_{pzc})_{tr+}$ in the positive going potential scans of the DOPE-POPG:DPPG bilayer on the Au(111) electrode in 0.1 M $KClO_4$ and 0.1 M $KClO_4$ + 0.005 M $Mg(ClO_4)_2$ solution.

Electrolyte solution	$(E - E_{pzc})_{des}$ / V	C_{min} / μF cm^{-2}	$(E - E_{pzc})$ range of C_{min} / V	$(E - E_{pzc})_{tr-}$ / V	$(E - E_{pzc})_{tr+}$ / V
0.1 M $KClO_4$	-0.94	5.8 ± 0.3	-0.43 < E - E_{pzc} < -0.18	-0.54	-0.57
0.1 M $KClO_4$ + 0.005 M $Mg(ClO_4)_2$	-0.83	5.1 ± 0.5	-0.38 < E - E_{pzc} < -0.16	-0.56	-0.50

In situ electrochemical AFM measurements were performed for the POPE-POPG:DPPG bilayer under supervision of Prof. Sek (Faculty of Chemistry, Biological and Chemical Research Centre, University of Warsaw, Warsaw, Poland). Figure 25 shows the presence of aggregated islands and some defects in the POPE-POPG:DPPG bilayer at E = 0.0 V vs. Pt wire quasi-reference electrode at (21 ± 1) °C. This explained the increased differential capacitance of the studied bilayer compared to defect-free phospholipid membranes (Figure 23b).

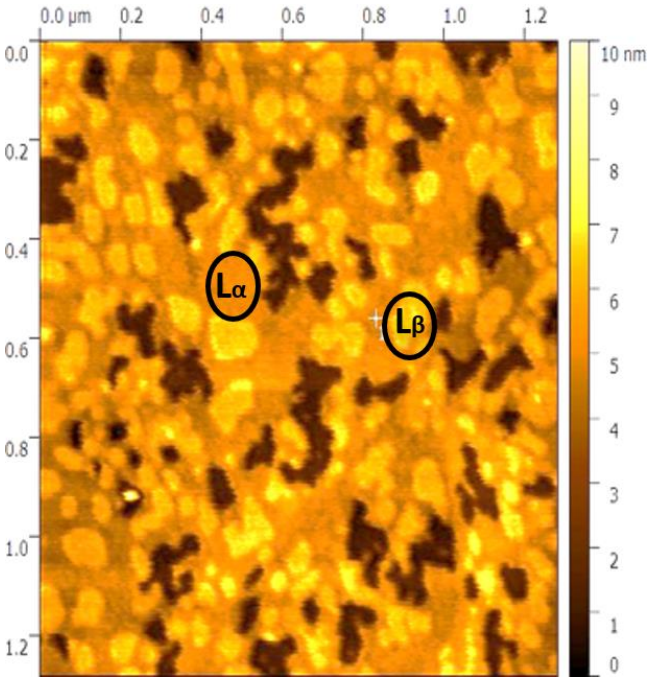

Figure 25: *In situ* AFM image recorded for the POPE-POPG:DPPG bilayer deposited by LB-LS technique on the Au(111) surface at Π = 30 mN m^{-1}. The image was collected in 0.05 M $KClO_4$ + 0.005 M $Mg(ClO_4)_2$ solution at E = 0.0V vs. Pt wire quasi-reference electrode. Yellow bright spots represent a gel phase (L_β), while orange areas refer to a liquid phase (L_α).

The topography image of the POPE-POPG:DPPG bilayer was non-uniform and contained some defects. Island of phospholipids existed in gel and liquid phases. Yellow bright spots represented a gel phase (L_β), while orange area can be assigned to a liquid phase (L_α). Dark brown areas corresponded most likely to the bare Au(111) substrate, indicating the presence of some defects in the POPE-POPG:DPPG bilayer. The coexistence of two phases may result from the difference in the main phase transition temperature (T_m) for the studied phospholipid components.

The temperature, at which the image was recorded was slightly below the main phase transition temperature of POPE phospholipid (T_m of POPE = 25.2 °C)[268,269] and higher than the T_m of POPG (T_m of POPG = -5 °C)[270]. In that case, the POPE molecules were arranged in L_β and POPG molecules were in L_α. Moreover, POPE phospholipids were known to increase the chain order in phospholipid mixtures.[94] The coexistence of two phases for supported phospholipid bilayers composed of a POPE-POPG mixture was reported by Suárez-Germà et al.[271], Konarzewska et al.[94] and Picas et al.[205] , who showed two phases in the topography images for a POPE-POPG mixture on the mica surface at (23 ± 1) °C.

5.1.3 PM IRRAS measurements of the studied lipid bilayers in the CH stretching region

Figure 26 shows background-corrected PM IRRA spectra of the DMPE-DMPG, POPE-POPG:DPPG and DOPE-POPG:DPPG bilayers. IR absorption modes originating from $\nu_{as}(CH_3)$, $\nu_{as}(CH_2)$, $\nu_s(CH_3)$ and $\nu_s(CH_2)$ in the hydrocarbon chains in the phospholipid molecules are well resolved in the PM IRRA spectra. The intensities of the methylene stretching modes depended on both the potential applied to the electrode and the structure of the phospholipid composing the model membrane. A decrease in the intensity of the methylene stretching modes was observed at potentials preceding the desorption of the phospholipid bilayers containing saturated myristoyl chains from the Au(111) electrode (Figure 26a). The same spectral behavior was reported for DMPC bilayers.[5] The wavenumbers of the absorption maxima of the methylene stretching modes depend on the structure and conformation of the hydrocarbon chains.[272,273] In the DMPE-DMPG bilayer, the absorption maximum of the $\nu_s(CH_2)$ mode was centered at (2851 ± 1) cm^{-1} (Figure

27a). The $\nu_{as}(CH_2)$ mode was centered at (2924 ± 1) cm^{-1} in the adsorbed state of the DMPE-DMPG bilayer (E - E_{pzc} > -0.91 V), while it is shifted to (2919 ± 1) cm^{-1} in the desorbed state (E - E_{pzc} < -0.96 V) (Figure 27d).

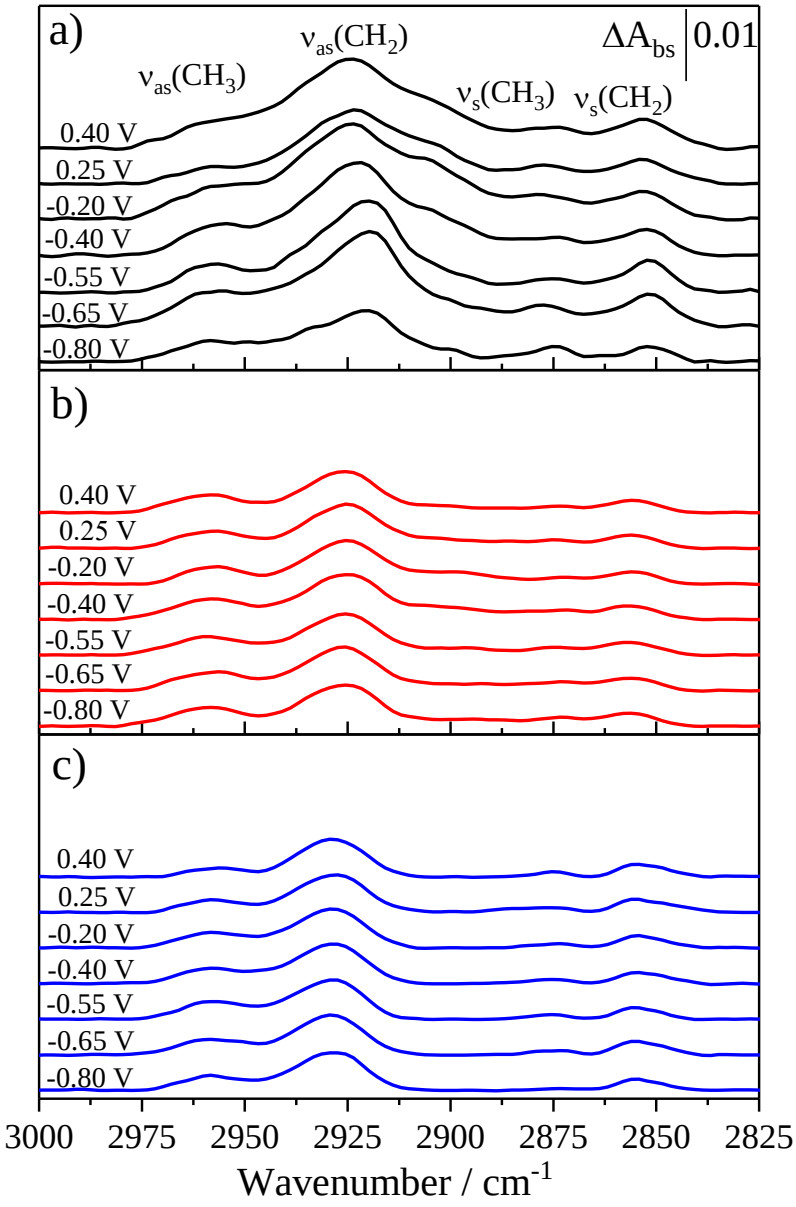

Figure 26: PM IRRA spectra in the 3000 - 2825 cm^{-1} spectral region of a) the DMPE-DMPG bilayer in 0.05 M $KClO_4$ in D_2O, b) the POPE-POPG:DPPG bilayer in 0.05 M $KClO_4$ + 0.005 M $Mg(ClO_4)_2$ in D_2O and c) the DOPE-POPG:DPPG bilayer in 0.05 M $KClO_4$ + 0.005 M $Mg(ClO_4)_2$ in D_2O. All model membranes were prepared on the Au(111) electrode. The spectra shown in the figure were recorded in a negative going potential scan at potentials marked in the figure.

A transition from a liquid crystalline phase of myristoyl chains in the adsorbed state to a gel phase in the desorbed state of the DMPE-DMPG bilayer was observed (Figure 27a). The absorption maximum of $\nu_s(CH_2)$ and $\nu_{as}(CH_2)$ modes was independent of the electrode potential in the POPE-POPG:DPPG bilayer (Figure 27b, e). The absorption maximum of the $\nu_s(CH_2)$ mode appeared at 2855 - 2856 cm^{-1} (Figure 27b). The corresponding $\nu_s(CH_2)$ mode appeared at 2854 - 2855 cm^{-1} in the DOPE-POPG:DPPG bilayer (Figure 27c). The absorption maximum of the $\nu_{as}(CH_2)$ mode was centered at (2925 ± 1) cm^{-1} for the POPE-POPG:DPPG bilayer (Figure 27e), while it was located at (2928 ± 1) cm^{-1} in the DOPE-POPG:DPPG bilayer (Figure 27f). The wavenumbers of the $\nu_s(CH_2)$ and $\nu_{as}(CH_2)$ modes were characteristic for the liquid state of a hydrocarbon chain in the phospholipid bilayers containing monounsaturated chain(-s).[272]

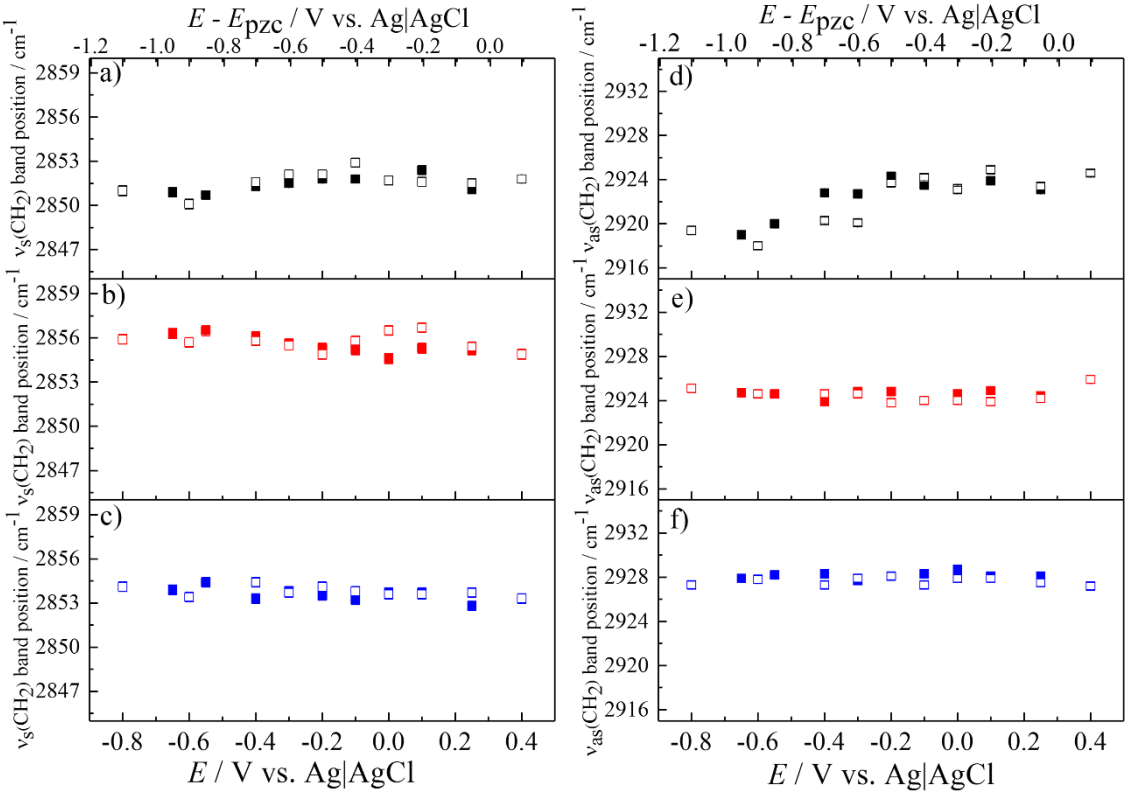

Figure 27: Position of the absorption maximum of $\nu_s(CH_2)$ and $\nu_{as}(CH_2)$ modes vs. E and E - E_{pzc} potential plots in a), d) the DMPE-DMPG bilayer in 0.05 M $KClO_4$ in D_2O, b), e) the POPE-POPG:DPPG bilayer in 0.05 M $KClO_4$ + 0.005 M $Mg(ClO_4)_2$ in D_2O and c), f) the DOPE-POPG:DPPG bilayer in 0.05 M $KClO_4$ + 0.005 M $Mg(ClO_4)_2$ in D_2O. All model membranes were prepared on the Au(111) electrode. Filled and opened points represent the negative and the positive going potential scans, respectively.

In the POPE-POPG:DPPG and DOPE-POPG:DPPG bilayers, the integral intensities of $\nu_s(CH_2)$ and $\nu_{as}(CH_2)$ modes were comparable to those in the desorbed DMPE-DMPG bilayer and DMPC bilayer[5]. In the DMPE-DMPG bilayer, intensities of the methylene stretching modes decreased at desorption potentials (Figure 26a). However, the re-adsorption caused a reversible increase in intensities of the methylene stretching modes of the DMPE-DMPG bilayer on the Au(111) electrode. The surface concentration was constant for the phospholipid molecules in the bilayer and therefore had no influence on the variation of intensities of the methylene stretching modes during the potential scan. These changes were connected with the potential-dependent reorientation of the hydrocarbon chains in the bilayer. Intensities of the $\nu_s(CH_2)$ modes did not change during the potential scan in bilayers containing unsaturated chain(-s). Figure 28 shows the calculated opical constants of the studied phospholipid mixtures from their transmission spectra.

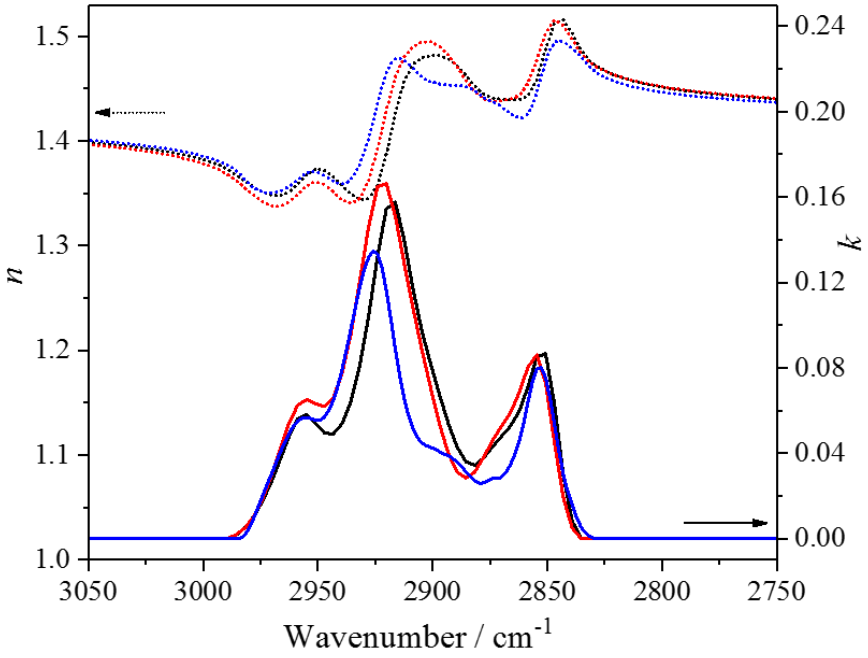

Figure 28: Optical constants: refractive index *n* (short dot lines) and attenuation coefficient *k* (solid lines) in the 3050 - 2750 cm^{-1} spectral region of the DMPE-DMPG (black), POPE-POPG:DPPG (0.95:0.05 mole) (red) and DOPE-POPG:DPPG (0.95:0.05 mole) (blue) phospholipid mixtures.

The optical constants were used to calculate the PM IRRA spectra of randomly oriented phospholipids in the studied films using the angle of the incidence of the incoming IR radiation of 55° and the optical constants of gold, CaF_2 (optical window) and D_2O

(electrolyte) from literature.[274] Air is not absorbing in the mid IR spectral region, thus in the calculation k_{Air} = 0 and n_{Air} = 1. The surface coverage (Φ) was calculated for the phospholipids on the metal surface from the area per molecule of each phospholipid monolayer at the transfer pressure (A_t) and the limiting area (A_{lim}). They gave the interfacial concentration Γ_t and Γ_{lim}, from which the surface coverage ($\Phi_{ML} = \Gamma_t / \Gamma_{lim}$) was obtained. The surface coverage of the phospholipid bilayer (Φ_{BL}) is the average of the surface coverage of the phospholipid molecules in the bilayer [$\Phi_{BL} = (\Phi_{ML1} + \Phi_{ML2}) / 2$] (Table 8).

Table 8: Area per molecule at the surface pressure (A_t) of the monolayer transfer (Π = 30 mN m^{-1}), limiting area (A_{lim}), surface concentration (Γ_t) of the phospholipid in the LB monolayers at the transfer pressure, the maximal surface concentration (Γ_{lim}), the surface coverage (Φ) of monolayers and bilayers and the thickness (d) of the phospholipid bilayer on the gold surface.

Phospholipid	A_t / nm^2	A_{lim} / nm^2	Γ_t / 10^{-10} mol cm^{-2}	Γ_{lim} / 10^{-10} mol cm^{-2}	Φ	d / nm Ref.
DMPE	0.47 ± 0.02	0.41 ± 0.02	3.53 ± 0.18	4.05 ± 0.12	0.87 ± 0.02	4.30[106]
DMPG	0.53 ± 0.01	0.45 ± 0.03	3.13 ± 0.15	3.69 ± 0.11	0.85 ± 0.02	4.60[275]
DMPE-DMPG	0.50 ± 0.02	0.43 ± 0.02	3.33 ± 0.15	3.87 ± 0.10	0.86 ± 0.02	4.50
POPE	0.61 ± 0.02	0.72 ± 0.01	3.02 ± 0.10	3.86 ± 0.13	0.78 ± 0.01	4.18[204,276]
POPG:DPPG	0.94 ± 0.02	0.75 ± 0.02	1.76 ± 0.13	2.16 ± 0.05	0.82 ± 0.01	4.36[204]
POPE-POPG:DPPG	0.91 ± 0.02	0.59 ± 0.01	2.39 ± 0.11	3.01 ± 0.07	0.80 ± 0.01	4.27
DOPE	0.63 ± 0.02	0.87 ± 0.01	2.64 ± 0.10	3.26 ± 0.11	0.81 ± 0.01	4.02[277]
DOPE-POPG:DPPG	0.78 ± 0.02	0.63 ± 0.02	2.20 ± 0.11	2.71 ± 0.06	0.81 ± 0.01	4.20

Figure 29 shows that intensities of all experimental spectra were lower than intensities of the calculated spectra of randomly oriented phospholipid molecules in the studied films. The thickness (d) of the phospholipid bilayers, which was reported in Table 8, was taken from the single crystal structure data of these films in lietrature.

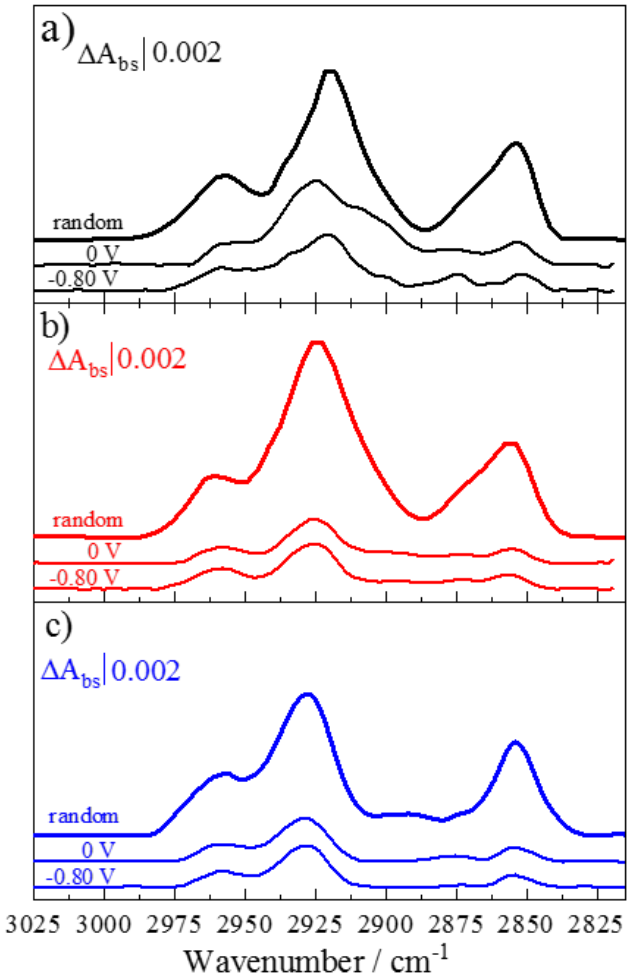

Figure 29: Experimental PM IRRA spectra in the 3025 - 2820 cm^{-1} spectral region of the studied bilayers at *E* = -0.8 V and *E* = 0.0 V vs. Ag|AgCl and the calculated PM IRRA spectra of randomly oriented phospholipid molecules in the studied films of a) the DMPE-DMPG bilayer in 0.05 M $KClO_4$ in D_2O, b) the POPE-POPG:DPPG bilayer in 0.05 M $KClO_4$ + 0.005 M $Mg(ClO_4)_2$ in D_2O and c) the DOPE-POPG:DPPG bilayer in 0.05 M $KClO_4$ + 0.005 M $Mg(ClO_4)_2$ in D_2O. All model membranes were prepared on the Au(111) electrode.

The PM IRRA spectra were deconvoluted to determine the integral intensities of the methylene stretching modes as a function of the electrode potential. Figure 30 shows the deconvoluted PM IRRA spectra of the studied phospholipid bilayers, which were done by me and corrected by Dr. Brand. IR absorption modes originating from the $\nu_{as}(CH_3)$, $\nu_{as}(CH_2)$, $\nu_s(CH_3)$ and $\nu_s(CH_2)$ were well seen in the spectra for the hydrocarbon chains in the phospholipid molecules. Two shoulders on $\nu_{as}(CH_2)$ band located at ~2940 cm^{-1} and ~2900 cm^{-1} originated from the Fermi resonance (FR). The high frequency shoulder at ~2940 cm^{-1} corresponded to FR between the $\nu_s(CH_3)$ and the overtone of the

asymmetric methyl bending mode $\delta_{as}(CH_3)$.[6,273,278] The second shoulder at ~2900 cm^{-1} originated from FR between the $\nu_s(CH_2)$ and the overtone of the methylene bending mode $\delta(CH_2)$.[6,273,278]

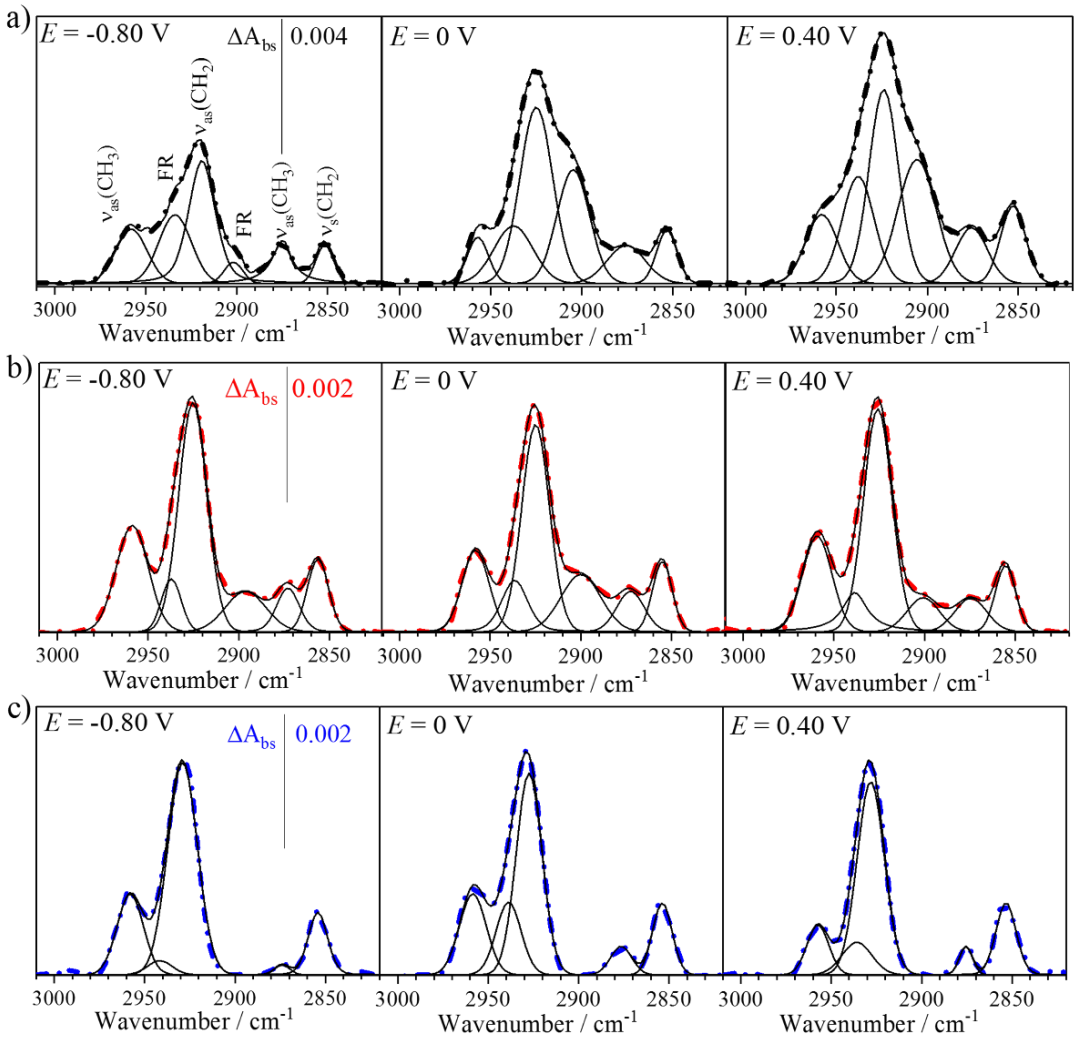

Figure 30: Deconvoluted PM IRRA spectra in the ν(CH) stretching modes region of a) the DMPE-DMPG bilayer in 0.05 M $KClO_4$ in D_2O, b) the POPE-POPG:DPPG bilayer in 0.05 M $KClO_4$ + 0.005 M $Mg(ClO_4)_2$ in D_2O and c) the DOPE-POPG:DPPG bilayer in 0.05 M $KClO_4$ + 0.005 M $Mg(ClO_4)_2$ in D_2O. All model membranes were prepared on the Au(111) electrode at potentials marked in the figures. Colored dashed lines: measured spectrum, black thin lines: envelope and deconvoluted modes.

The second shoulder at ~2900 cm^{-1} originated from FR between the $\nu_s(CH_2)$ and the overtone of the methylene bending mode $\delta(CH_2)$.[6,273,278] The FR involves a coupling between the symmetric stretching and the second harmonic of CH_2 bending vibrations, which have the same direction of their transition dipoles.[112] As a result of coupling, a

broad band appears in the region where the $\nu_s(CH_2)$ vibration is obtained. This broad band is seen in Figure 30 as a shoulder at the right of the $\nu_{as}(CH_2)$ band and is obscured by the $\nu_{as}(CH_3)$ band to the left. FR forms by spilitting of two vibrational bands that have nearly the same energy. The two bands are usually a fundamental vibration and either an overtone or combination band.[112] Overtone bands in an IR spectrum are multiples of the fundamental absorption frequency. The energy required for the first overtone is twice the fundamental, assuming evenly spaced energy levels. Scince the energy is proportional to the frequency absorbed and this is proportional to the wavenumber, the first overtone will appear in the spectrum at twice the wavenumber of the fundamental.

Angles $\theta_{\nu(CH2)}$ for symmetric and asymmetric methylene stretching modes were calculated using equation 12 (Figure 31).

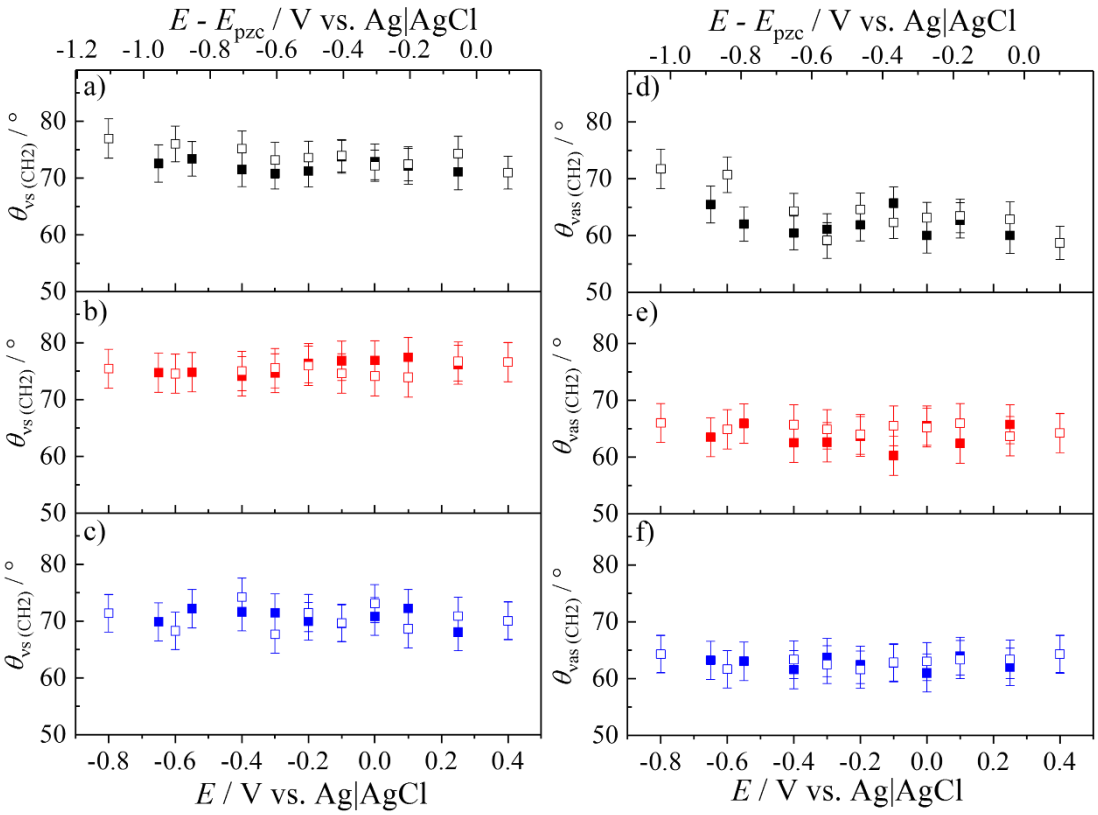

Figure 31: Angles $\theta\nu_{s(CH2)}$ and $\theta\nu_{as(CH2)}$ vs. E and E - E_{pzc} potential plots in a), d) the DMPE-DMPG bilayer in 0.05 M $KClO_4$ in D_2O, b), e) the POPE-POPG:DPPG bilayer in 0.05 M $KClO_4$ + 0.005 M $Mg(ClO_4)_2$ in D_2O and c), f) the DOPE-POPG:DPPG bilayer in 0.05 M $KClO_4$ + 0.005 M $Mg(ClO_4)_2$ in D_2O. All model membranes were prepared on the Au(111) electrode. Filled and opened points represent negative and positive going potential scans, respectively.

In the adsorbed state of the DMPE-DMPG bilayer (E - E_{pzc} > -0.91 V), the average angles $\theta_{vs(CH2)}$ and $\theta_{vas(CH2)}$ were (73 ± 5)° and (62 ± 5)°, respectively. In the desorbed state (E - E_{pzc} < -0.96 V), the average angles $\theta_{vs(CH2)}$ and $\theta_{vas(CH2)}$ were (76 ± 5)° and (70 ± 5)°, respectively (Figure 31a, b). In the POPE-POPG:DPPG bilayer, the average angles $\theta_{vs(CH2)}$ and $\theta_{vas(CH2)}$ were independent of the electrode potential. The average angles $\theta_{vs(CH2)}$ and $\theta_{vas(CH2)}$ were (75 ± 4)° and (64 ± 5)°, respectively (Figure 31b, e). In the DOPE-POPG: DPPG bilayer, the average angles $\theta_{vs(CH2)}$ and $\theta_{vas(CH2)}$ were (72 ± 5)° and (63 ± 5)°, respectively (Figure 31c, f).

The order parameter (S) expresses the conformational order of the investigated fragments of a bilayer. $S_{v(CH2)}$ of the methylene stretching modes were calculated from equation 15 (Figure 32).

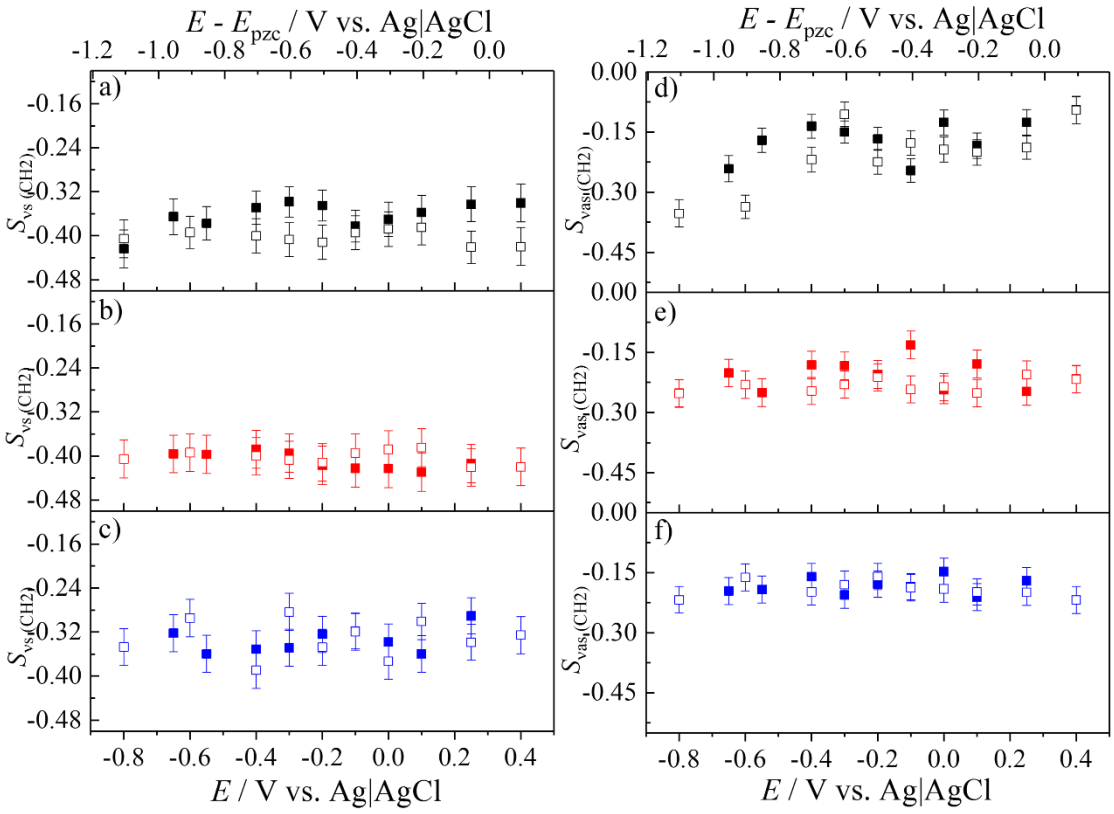

Figure 32: Plots of $S_{vs(CH2)}$ and $S_{vas(CH2)}$ vs. E and E - E_{pzc} potentials in a), d) the DMPE-DMPG bilayer in 0.05 M $KClO_4$ in D_2O, b), e) the POPE-POPG:DPPG bilayer in 0.05 M $KClO_4$ + 0.005 M $Mg(ClO_4)_2$ in D_2O and c), f) the DOPE-POPG:DPPG bilayer in 0.05 M $KClO_4$ + 0.005 M $Mg(ClO_4)_2$ in D_2O. All model membranes were prepared on the Au(111) electrode. Filled and opened points represent negative and positive going potential scans, respectively.

$S_{vs(CH2)}$ of the DMPE-DMPG bilayer was negative and displayed a poor dependence on the electrode potential (Figure 32a). In the DMPE-DMPG bilayer, a small effect of the electrode potential on $S_{vas(CH2)}$ was observed (Figure 32d). $S_{vas(CH2)}$ changed from (-0.29 ± 0.08) at desorption to (-0.16 ± 0.07) at adsorption potentials (Figure 32d). In the POPE-POPG:DPPG bilayer, $S_{vs(CH2)}$ and $S_{vas(CH2)}$ were (-0.42 ± 0.05) and (-0.22 ± 0.07), respectively. They were independent of the electrode and membrane potentials (Figure 32b, e). In the DOPE-POPG:DPPG bilayer, $S_{vs(CH2)}$ and $S_{vas(CH2)}$ were potential-independent and $S_{vs(CH2)}$ was (-0.35 ± 0.07), while $S_{vas(CH2)}$ was (-0.19 ± 0.05) (Figure 32c, f). The calculated chain order parameter S_{chain} in the studied phospholipid bilayers is shown in Figure 33. S_{chain} assumed high positive values of 0.8 to 0.45, indicating that the long axis of the hydrocarbon chains has an upwards orientation.

In the DMPE-DMPG bilayer, S_{chain} depended on the electrode and membrane potentials (Figure 33a). S_{chain} was (0.54 ± 0.06) in the membrane potential range 0.1 V < E - E_{pzc} < -0.6 V, indicating that the average tilt of the extended fragment of the hydrocarbon chains was close to 33° vs. the surface normal. The desorption of the DMPE-DMPG bilayer caused an increase in S_{chain} to 0.8 which corresponded to the average tilt of ~20°. The dependence of S_{chain} on the electrode and membrane potentials was in agreement with previous studies of myristoylated glyceropospholipid bilayers such as DMPC[5,53,80] and DMPS[7]. In the POPE-POPG:DPPG and DOPE-POPG:DPPG bilayers, S_{chain} were (0.62 ± 0.04) and (0.53 ± 0.04), respectively (Figure 33b, c). S_{chain} indicated a larger average inclination of the hydrocarbon chains in the phospholipid bilayer containing unsaturated chains than in the DMPE-DMPG bilayer. Such a behavior was already reported for the DMPE bilayer[6] and a three-component lipid bilayers containing PC, cholesterol and gangliosides[110]. The electric potentials have a large impact on the molecular scale order in the phospholipid membrane. The shape of the phospholipid molecule affected the potential-driven rearrangements in the bilayer and introduction of unsaturated chain(-s) into phospholipid molecules forming a phospholipid bilayer caused a decrease in S_{chain}.[279,280]

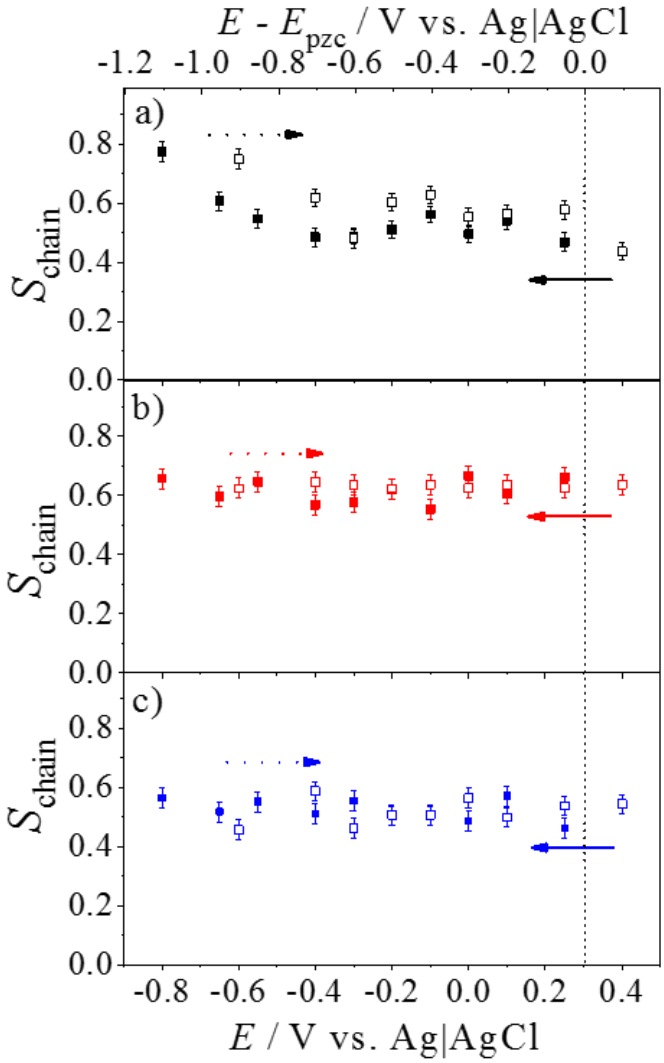

Figure 33: Plots of S_{chain} vs. E and E - E_{pzc} potentials in: a) the DMPE-DMPG bilayer, b) the POPE-POPG:DPPG bilayer and c) the DOPE-POPG:DPPG bilayer adsorbed on the Au(111) electrode. Filled and opened points represent negative and positive going potential scans, respectively.

5.1.4 PM IRRAS measurements of the studied lipid bilayers in the head group region

In phospholipids, the ester carbonyl group was located in the region joining the hydrophobic hydrocarbon chains with the polar head group. The ester carbonyl groups absorbed the IR light in the 1750 - 1720 cm^{-1} spectral region. Figure 34 shows the background-corrected spectra of the DMPE-DMPG, POPE-POPG:DPPG and DOPE-POPG:DPPG bilayers.

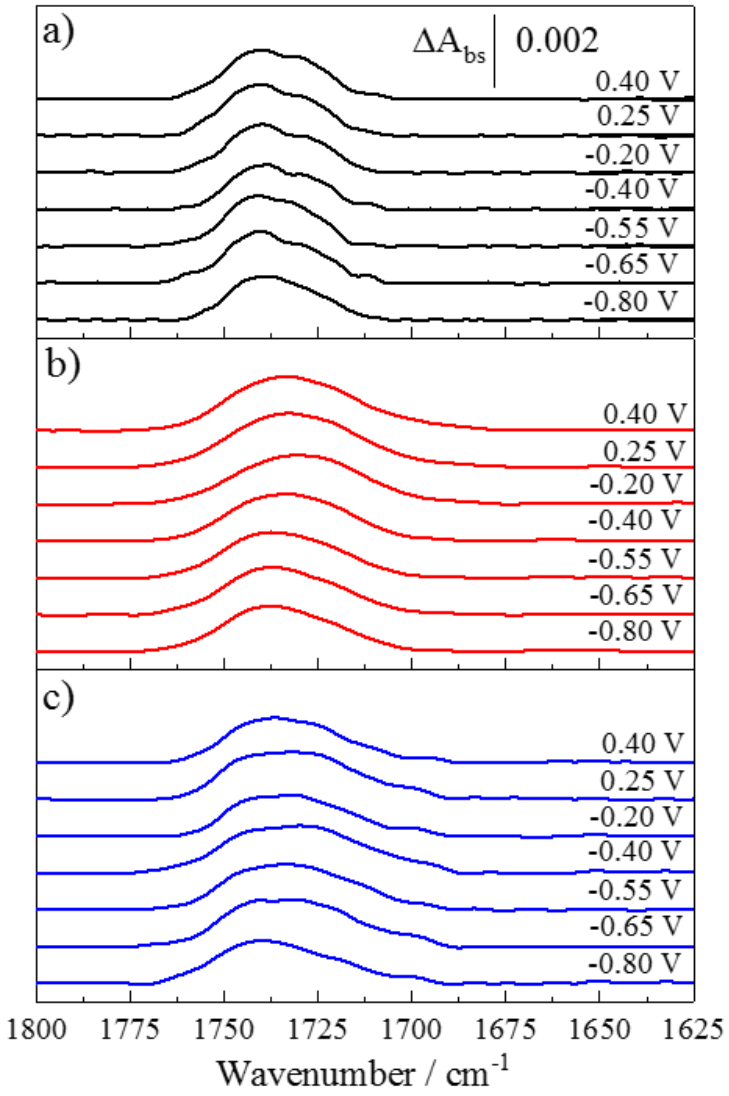

Figure 34: PM IRRA spectra in the ν(C=O) mode region of a) the DMPE-DMPG bilayer in 0.05 M $KClO_4$ in D_2O, b) the POPE-POPG:DPPG bilayer in 0.05 M $KClO_4$ + 0.005 M $Mg(ClO_4)_2$ in D_2O and c) the DOPE-POPG:DPPG bilayer in 0.05 M $KClO_4$ + 0.005 M $Mg(ClO_4)_2$ in D_2O. All model membranes were prepared on the Au(111) electrode. The spectra shown in the figure were recorded in a negative going potential scan at potentials marked in the figure.

Similar spectral changes were obtained in the studied bilayers. The broad ν(C=O) mode was composed of two overlapped modes, reflecting differences in the degree of hydration of the polar head groups in the phospholipid bilayers.[5,54,252] Figure 35 shows the position of the deconvoluted C=O stretching modes in the studied phospholipid bilayers adsorbed on the Au(111) surface. In the DMPE-DMPG bilayer, the ν(C=O) mode has two components at (1727 ± 2) cm^{-1} (Figure 35a) and at (1742 ± 2) cm^{-1} (Figure 35d). In the POPE-POPG:DPPG bilayer, the corresponding ν(C=O) modes appeared at (1722 ± 1)

cm^{-1} (Figure 35b) and at (1742 ± 3) cm^{-1} (Figure 35e), while in the DOPE-POPG:DPPG bilayer at (1725 ± 2) cm^{-1} (Figure 35c) and at (1742 ± 3) cm^{-1} (Figure 35f).

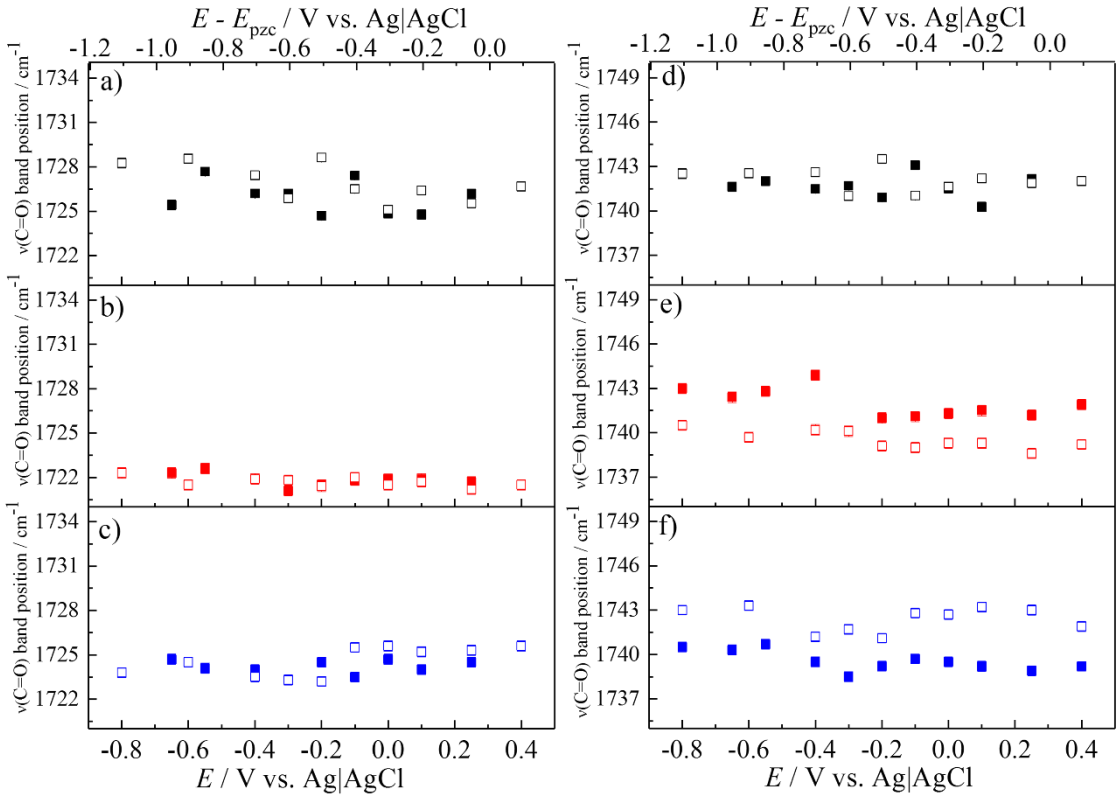

Figure 35: Position of the deconvoluted ν(C=O) band vs. E and E - E_{pzc} potentials in a), d) the DMPE-DMPG bilayer in 0.05 M $KClO_4$ in D_2O. b), e) the POPE-POPG:DPPG bilayer in 0.05 M $KClO_4$ + 0.005 M $Mg(ClO_4)_2$ in D_2O and c), f) the DOPE-POPG:DPPG bilayer in 0.05 M $KClO_4$ + 0.005 M $Mg(ClO_4)_2$ in D_2O. All model membranes were prepared on the Au(111) electrode. Filled and opened points represent negative and positive going potential scans, respectively.

The transmission spectra of the studied phospholipid bilayers were measured and used to calculate the optical constants of these bilayers. Figure 36 shows results of these calculations. The experimently measured intensities of the ν(C=O) mode were lower than intensities of the calculated spectra of randomly oriented phospholipids in a bilayer of thick films (Figure 37). The calculated and experimental PM IRRA spectra were deconvoluted by me and corrected by Dr. Brand. The deconvoluted PM IRRA spectra in the ν(C=O) mode region of the studied phospholipid bilayers at different potentials applied to the Au(111) electrode are shown in Figure 38. In the POPE-POPG:DPPG bilayer, the intensity of the ν(C=O) mode centered at 1725 cm^{-1} decreased at E - E_{pzc} < -0.9 V (Figure 38b). These spectral changes indicate a dehydration of the ester carbonyl

groups in the POPE-POPG:DPPG bilayer desorbed from the Au(111) electrode (Figure 38b).

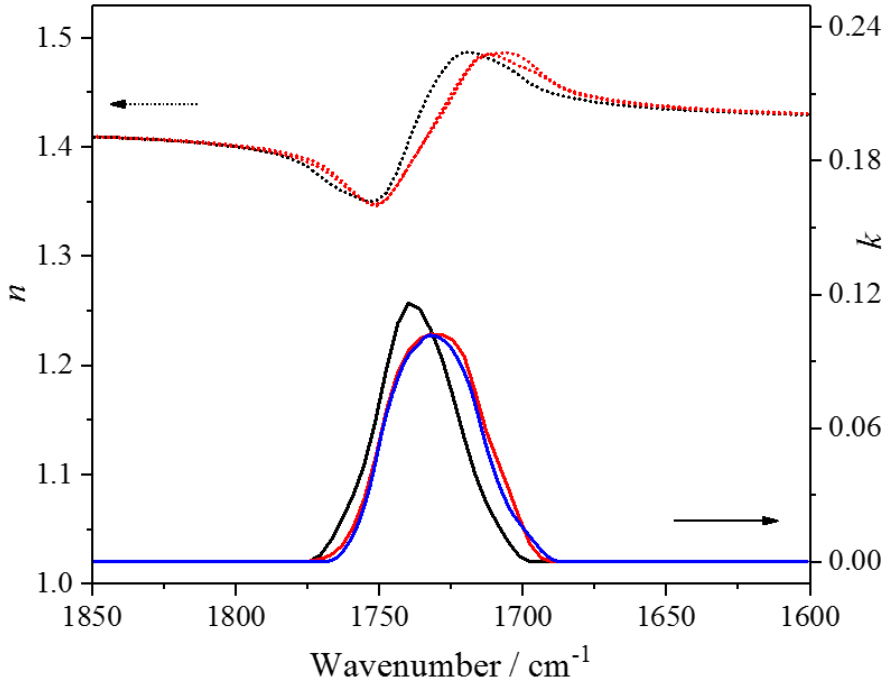

Figure 36: Refractive index *n* (short dot lines) and attenuation coefficient *k* (solid lines) in the 1850 - 1600 cm^{-1} spectral region of the DMPE-DMPG (black), POPE-POPG:DPPG (0.95:0.05 mole) (red) and DOPE-POPG:DPPG (0.95:0.05 mole) (blue) phospholipid mixtures.

Figure 39 shows the angle $\theta_{\nu(C=O)}$ between the transition dipole vector of the ester carbonyl group ν(C=O) and the electric field vector. In the DMPE-DMPG bilayer, the average angle $\theta_{\nu(C=O)}$ was potential-independent and it was (69 ± 4)° (Figure 39a). In the POPE-POPG:DPPG bilayer, the average angle $\theta_{\nu(C=O)}$ was (64 ± 5)° (Figure 39b), while in the DOPE-POPG:DPPG bilayer the average angle $\theta_{\nu(C=O)}$ was (64 ± 5)° (Figure 39c). Figure 40 shows the $S_{\nu(C=O)}$ of the phospholipid bilayers as a function of the electrode and membrane potentials. $S_{\nu(C=O)}$ were negative and displayed a poor dependence on the electrode and membrane potentials. $S_{\nu(C=O)}$ was (-0.31 ± 0.03), independently of the electrode and membrane potentials in the DMPE-DMPG bilayer (Figure 40a). A small effect of the potential on the $S_{\nu(C=O)}$ was obtained in bilayers containing phospholipids with unsaturated chains.

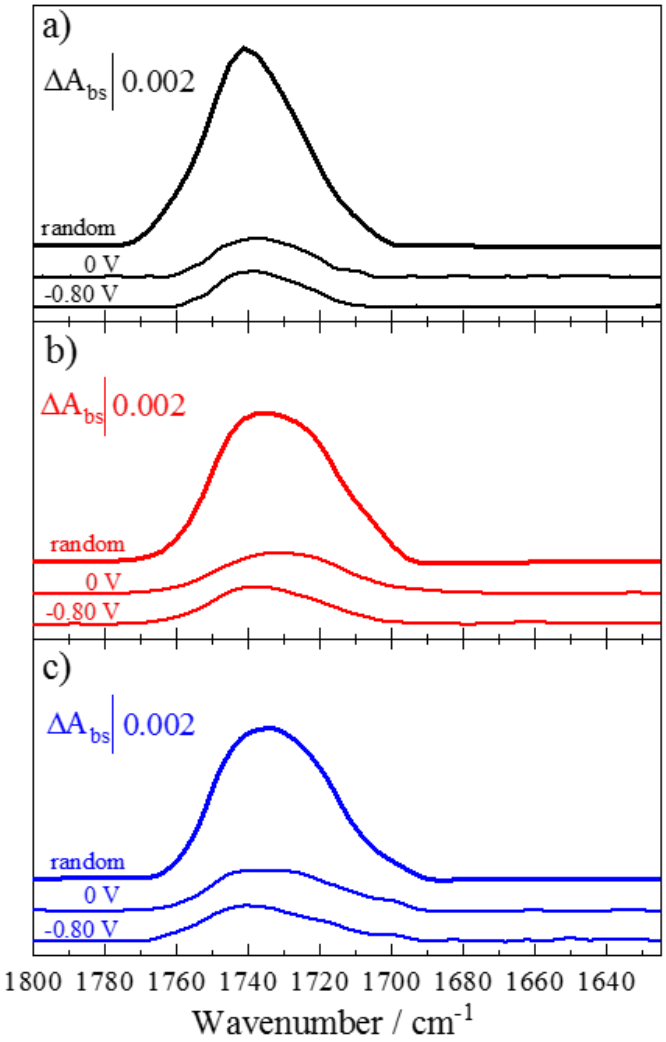

Figure 37: Experimental PM IRRA spectra in the 1800 -1625 cm^{-1} spectral region of the studied bilayers at E = -0.8 V and E = 0.0 V vs. Ag|AgCl and the calculated PM IRRA spectra of randomly oriented phospholipid molecules in the studied films of a) the DMPE-DMPG bilayer in 0.05 M $KClO_4$ in D_2O, b) the POPE-POPG:DPPG bilayer in 0.05 M $KClO_4$ + 0.005 M $Mg(ClO_4)_2$ in D_2O and c) the DOPE-POPG:DPPG bilayer in 0.05 M $KClO_4$ + 0.005 M $Mg(ClO_4)_2$ in D_2O. All model membranes were prepared on the Au(111) electrode.

In the POPE-POPG:DPPG bilayer, $S_{\nu(C=O)}$ changed from (-0.24 ± 0.03) at desorption to (-0.16 ± 0.04) at adsorption potentials (Figure 40b). In the DOPE-POPG:DPPG bilayer, $S_{\nu(C=O)}$ varied between -0.16 and -0.24 (Figure 40c). $S_{\nu(C=O)}$ indicated that the carbonyl groups have a very restricted mobility in the bilayer assembly. They adopted a preferential orientation parallel to the metal surface, which did not change during the potential driven adsorption-desorption process of the model membranes.

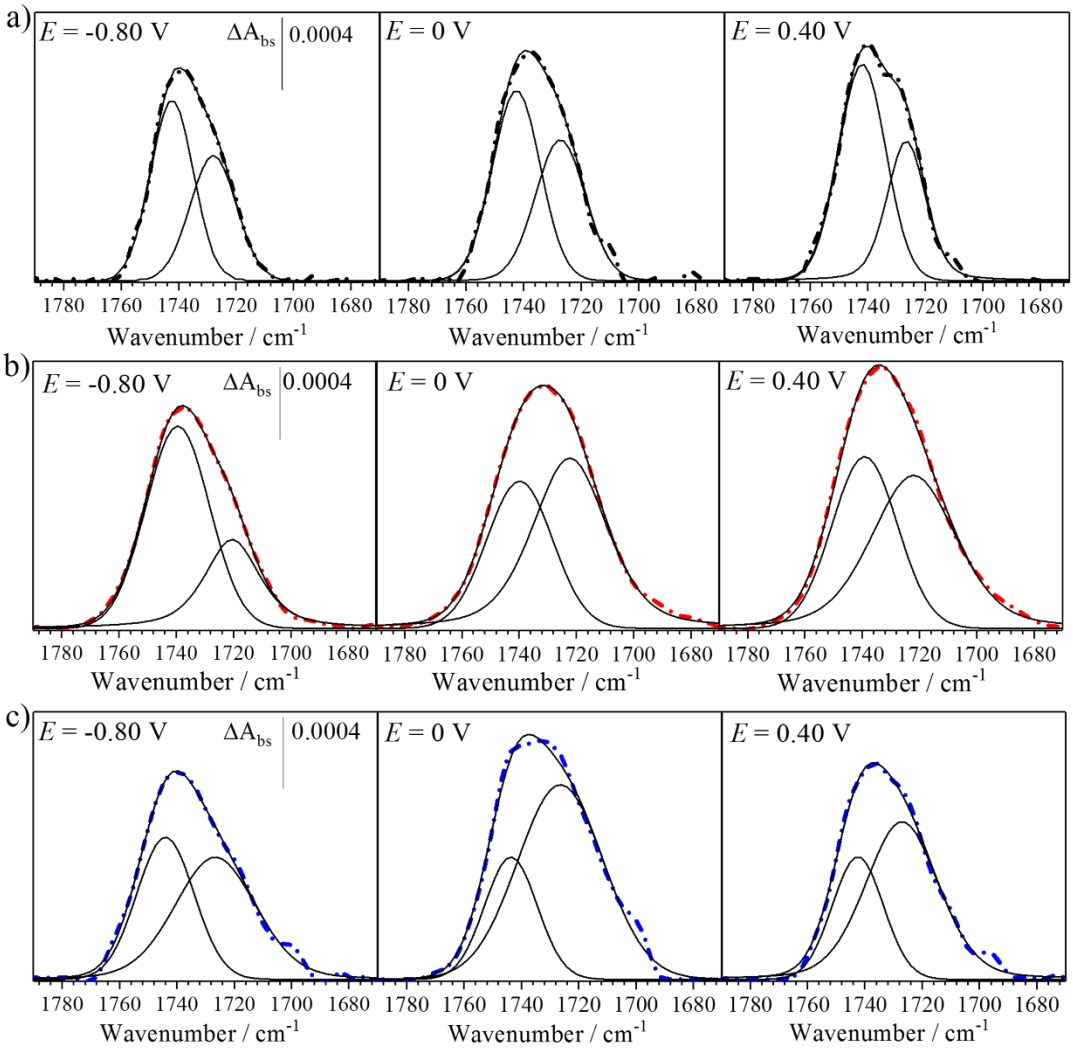

Figure 38: Deconvoluted PM IRRA spectra in the region of the ν(C=O) mode of a) the DMPE-DMPG bilayer in 0.05 M $KClO_4$ in D_2O, b) the POPE-POPG:DPPG bilayer in 0.05 M $KClO_4$ + 0.005 M $Mg(ClO_4)_2$ in D_2O and c) the DOPE-POPG:DPPG bilayer in 0.05 M $KClO_4$ + 0.005 M $Mg(ClO_4)_2$ in D_2O. All model membranes were prepared on the Au(111) electrode at potentials marked in the figures. Colored dashed lines: measured spectrum, black thin lines: envelope and deconvoluted modes.

To learn more about the hydration in the potential-dependent characteristics of the phospholipid bilayers, electrochemical QCM-D experiments were performed in cooperation with Dr. Juhaniewicz-Debinska and Prof. Sek (Faculty of Chemistry, Biological and Chemical Research Centre, University of Warsaw, Warsaw, Poland). QCM-D is a powerful technique to study phase transitions within the substrate modified phospholipid bilayers. Figure 41 shows the changes of Δf and ΔD of asymmetric phospholipid bilayers in the negative going potential scan.

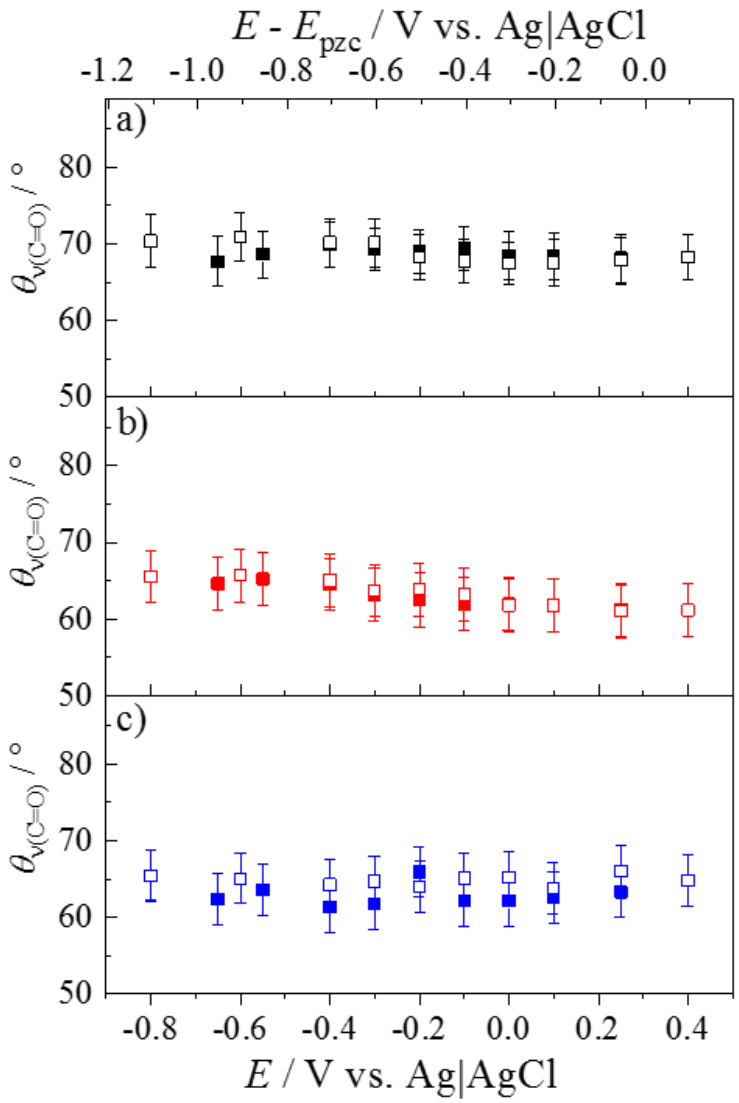

Figure 39: Angles $\theta_{\nu(C=O)}$ vs. E and E - E_{pzc} potentials in a) the DMPE-DMPG bilayer in 0.05 M $KClO_4$ in D_2O, b) the POPE-POPG:DPPG bilayer in 0.05 M $KClO_4$ + 0.005 M $Mg(ClO_4)_2$ in D_2O and c) the DOPE-POPG:DPPG bilayer in 0.05 M $KClO_4$ + 0.005 M $Mg(ClO_4)_2$ in D_2O. All model membranes were prepared on the Au(111) electrode. Filled and opened points represent negative and positive going potential scans, respectively.

Differences in Δf and ΔD were noticed as a function of potentials in the DMPE-DMPG bilayer compared to the bilayer-containing monounsaturated chain(-s). No changes occurred in Δf and ΔD at potentials corresponding to the capacitance minimum of the phospholipid bilayers. Little changes were noticed in Δf and ΔD in the membrane potential range 0.095 V < E - E_{pzc} < -0.705 V in the DMPE-DMPG bilayer (Figure 41a). In this potential range, the DMPE-DMPG bilayer was adsorbed directly on the Au(111) electrode.

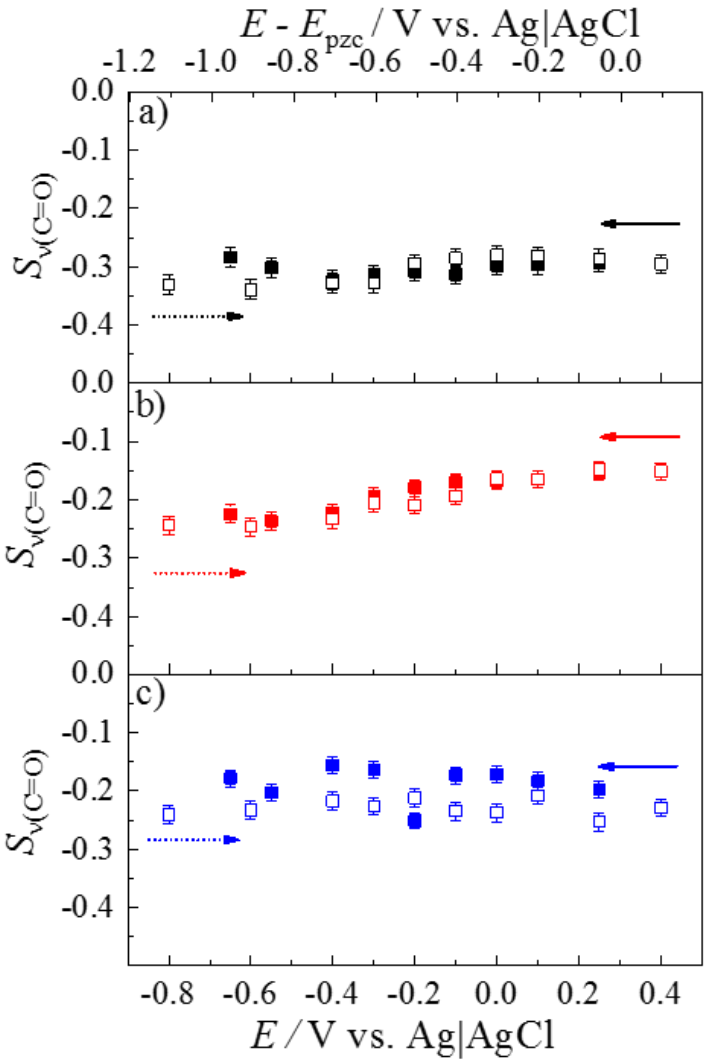

Figure 40: Plots of $S_{v(C=O)}$ vs. E and E - E_{pzc} potentials in: a) the DMPE-DMPG bilayer in 0.05 M $KClO_4$ in D_2O, b) the POPE-POPG:DPPG bilayer in 0.05 M $KClO_4$ + 0.005 M $Mg(ClO_4)_2$ in D_2O and c) the DOPE-POPG:DPPG bilayer in 0.05 M $KClO_4$ + 0.005 M $Mg(ClO_4)_2$ in D_2O. All model membranes were prepared on the Au(111) electrode. Filled and opened points represent negative and positive going potential scans, respectively.

A significant decrease in frequency (Δf ~ -35 Hz) occurred at E - $E_{pzc} \leq$ -0.705 V. Water molecules and ions flowed through the bilayer and accumulated between the metal surface and the DMPE-DMPG bilayer. The same behavior was observed in *in situ* neutron reflectivity studies of potential-driven changes in DMPC bilayers.[19] The formation of a water cushion decreased the interaction between the bilayer and the sensor surface affecting the viscoelastic properties of the interfacial region. Changes were more complex for Δf and ΔD as a function of the electrode and membrane potentials in bilayers composed of lipids with monounsaturated chain(-s).

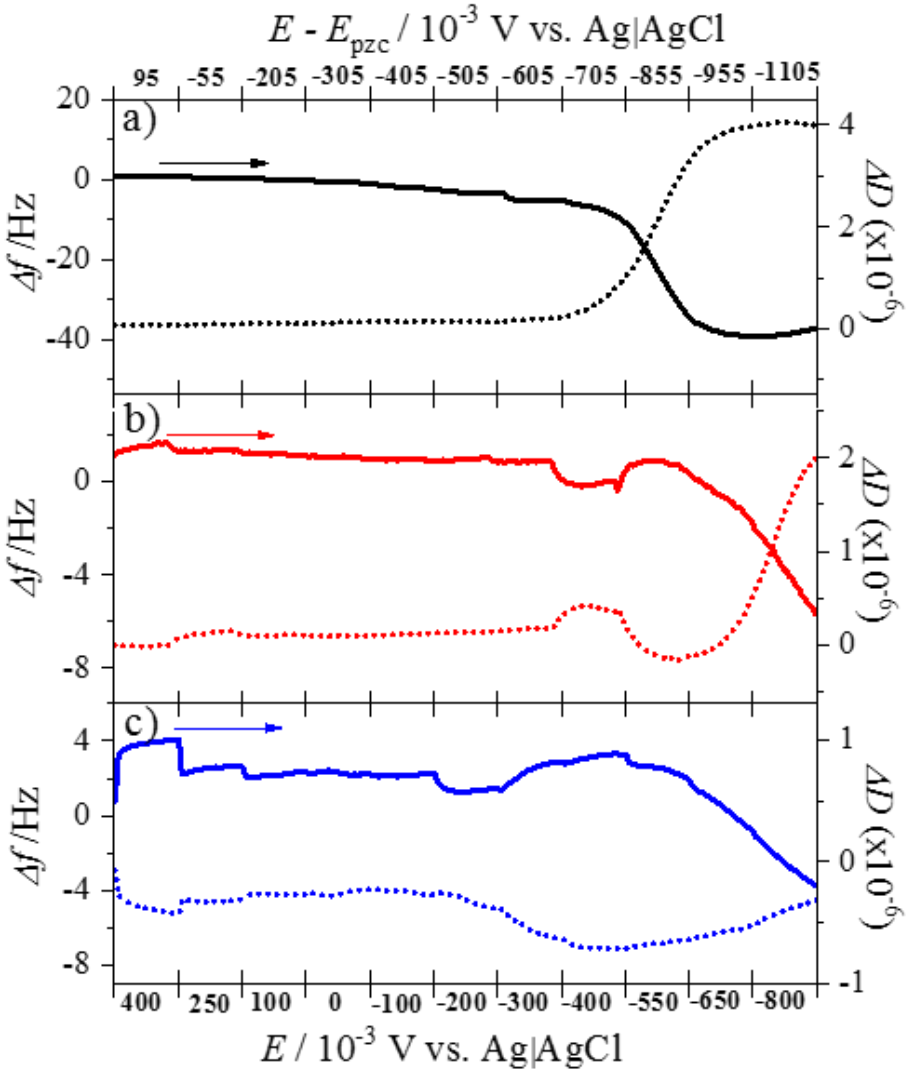

Figure 41: Plots of Δf (solid lines) and ΔD (short dot lines) vs. E and E - E_{pzc} potentials recorded for a) the DMPE-DMPG bilayer, b) the POPE-POPG:DPPG bilayer and c) the DOPE-POPG:DPPG bilayer on the Au(111) surface in the negative going potential steps: 400, 250, 100, 0, -100, -200, -300, -400, -550, -650 and -800 / 10^{-3} V vs. Ag|AgCl in 0.1 M $KClO_4$ + 0.005 M $Mg(ClO_4)_2$ solution. This figure is taken from own publication and modified.[18]

In the POPE-POPG:DPPG bilayer, no changes obtained in frequency and energy dissipation in the membrane potential range -0.055 V < E - E_{pzc} < -0.605 V (Figure 41b). A small decrease was reported at membrane potentials -0.605 V < E - E_{pzc} < -0.705 V, that was followed by a slight increase in the frequency of the QCM-D. This fluctuation corresponded to a loss of water and an increase in the mass in the supramolecular assembly. This result indicated that water flows from and then into the phospholipid bilayer. A further negative potential shift resulted in a steep decrease in Δf, which is

explained by a lifting of the bilayer from the gold surface and simultaneous water accumulation at the interface. A similar behavior was obtained in the DOPE-POPG:DPPG bilayer that was, however shifted towards less negative potentials (Figure 41c). An increase was obtained in Δf and a decrease in ΔD at most positive potentials (0.095 V < E - E_{pzc} < -0.055 V). It was followed by a region of stable Δf and ΔD at membrane potentials corresponding to the capacitance minimum. Next, a slight lowering was observed for Δf at E - E_{pzc} = -0.505 V. These changes were more pronounced compared to the POPE-POPG:DPPG bilayer, indicating that more water can be accumulated in the DOPE leaflet than in the POPE leaflet. A steep decrease was obtained in frequency at E - E_{pzc} ≤ -0.855 V (Figure 41c). Δf was ~ 35 Hz and ΔD was ~ 4×10^{-6} for the DMPE-DMPG bilayer. Δf was ~ 6 Hz and ΔD was ~ 2×10^{-6} for the POPE-POPG:DPPG bilayer; while Δf was ~ 5 Hz and ΔD was ~ 0.5×10^{-6} for the DOPE-POPG:DPPG bilayer. An abrupt decrease took place in Δf at membrane potentials lower than -0.705 V in the studied bilayers. A decrease in energy dissipation indicated that the order level and the disturbance in the membrane homogeneity decreased with increasing unsaturation of hydrocarbon chains in phospholipid molecules.

The PM IRRAS and electrochemical QCM-D results, that are described above, showed two different kinds of electric potential-dependent structural rearrangements in the phospholipid bilayers. They were correlated with the geometry of the lipid molecules expressed by the packing parameter (PP). PP correlates the cross-sectional area of the hydrophobic and hydrophilic parts of amphiphilic molecules. PP expresses the ratio of the volume of the hydrophobic part of the molecule V_{chain} to the maximal length of the hydrophobic chain l_{chain} multiplied by the cross-sectional area at the hydrophilic-hydrophobic $A_{h\text{-}g}$ interface of a lipid molecule.[281]

$$\mathrm{PP} = \frac{V_{\mathrm{chain}}}{l_{\mathrm{chain}}\, A_{\mathrm{h\text{-}g}}} = \frac{A_{\mathrm{chain}}}{A_{\mathrm{h\text{-}g}}} \tag{21}$$

The hydrocarbon chains were tilted with respect to the bilayer plane and the polar head groups were well hydrated in bilayers composed of lipids with PP < 1. In the bilayers composed of lipids PP ≥ 1, electric potentials have a negligible effect on the membrane structure. The flow of the electrolyte solution into the lipid bilayer was connected directly

with the response of membranes to electric potentials. The flow of water into the membrane was accompanied by a dehydration of the polar head group region of lipid bilayers (Figure 34). A continuous flow of water leaded to desorption of the lipid bilayer from the gold electrode at E - E_{pzc} < -0.855 V (Figure 41). These rearrangements in the membrane resulted in two kinds of the molecular scale responses of the lipid bilayers to electric potentials. The area varied for the hydrophobic part of the outer leaflet lipid molecules in the model lipid bilayers, while the area remained constant for the polar head group region of the inner leaflet. The existence of two pathways of the model membrane behavior under electric potentials is well documented in literature.[5–7,19,53,80,110,219] The tilt of the hydrocarbon chains changed as a function of the electrode potentials in some membranes. Data collected in Table 9 indicated that this behavior was obtained only in membranes of lipid molecules with PP < 1.[18]

$A_{h\text{-}g}$ was larger than A_{chain} in lipid molecules with PP < 1 (Table 9). In the DMPE-DMPG bilayer, the two saturated myristoyl chains occupied the cross-sectional area of 0.38 nm^2.[282] The PE head group has a comparable area to the cross-sectional area of two hydrocarbon chains[106], while the area was larger (0.44 nm^2) for the PG group. In the DMPE-DMPG bilayer, the additivity resulted for the packing parameter of lipids in the average PP of 0.93 - 0.96.[283] The bulky PC group occupies the area of 0.46 nm^2 in a symmetric DMPC bilayer existing in a gel state (transferred on the Au surface at Π > 40 mN m^{-1}),[106]giving PP = 0.80. This value was in agreement with literature.[283] Actually, S_{chain} have highest values in the DMPE-DMPG and DMPC bilayers adsorbed directly on the Au electrode.[5,53,80] They corresponded to the average tilt of the hydrocarbon chains of 33° and 25° vs. the surface normal in the DMPE-DMPG and DMPC bilayers, respectively. Figure 42a shows a scheme of the molecular scale packing in the DMPE-DMPG bilayer. In the bilayer with tilted chains, the available area per polar head group increased and therefore some water molecules may accumulate in the polar head group region. The PM IRRA spectra confirmed a good hydration of the ester groups in the DMPE-DMPG (Figure 34a) and DMPC[5,53,80] bilayers. PM IRRAS experiments showed that the hydrocarbon chains underwent a transition from liquid crystalline in the adsorbed state to a gel phase in the desorbed state for the DMPE and DMPG phospholipids in the bilayer assembly.

Table 9: The area of the polar head group $A_{h\text{-}g}$, critical area of the hydrocarbon chains A_{chain}, the packing parameter PP, the dependence of the chain tilt in the model bilayer as a function of the electrode potential [S_{chain} f(E)] and the corresponding value of the chain order parameter S_{chain} for different lipid bilayers deposited on the Au electrode. Symboles corresponded to: chol (cholesterol), GM1 (ganglipside) and GD1a (disialoganglioside)

Lipid bilayer	$A_{h\text{-}g}$/ nm^2	A_{chain}/ nm^2	PP	S_{chain} f(E)	S_{chain} (E range) / E_{ads} - E_{des}	Ref.
DMPE-DMPG				+	0.81 - 0.88	this thesis
Leaflet 1: DMPE	0.38	0.38	1.00			
Leaflet 2: DMPG	0.44	0.38 - 0.40	0.86 - 0.91			
DMPC	0.46	0.38	0.80	+	0.73 - 0.85	5
DMPS	0.42	0.38 - 0.40	0.90 - 0.95	+	0.82 - 0.62	7
DMPC:chol (0.7:0.3)	0.392	0.395	1.01	+	-0.03 - 0.48	55
POPE-POPG: DPPG				-	0.82	this thesis
Leaflet 1: POPE	0.38	0.42 - 0.46	1.10 - 1.21			
Leaflet 2: POPG:DPPG	0.44	0.42 - 0.40	0.95 - 1.05			
DOPE-POPG:DPPG				-	0.78	this thesis
Leaflet 1: DOPE	0.38	0.48 - 0.60	1.26 - 1.57			
Leaflet 2: POPG:DPPG	0.44	0.42 - 0.46	0.95 - 1.05			
DMPE	0.38	0.38 - 0.40	1.00 - 1.05	-	0.89	6
DMPC:chol: GM1				-	0.89	111
Leaflet 1: DMPC:chol	0.382	0.395	1.039			

Leaflet 2: DMPC:chol: GM1	0.388	0.396	1.020			
DMPC:chol: GM1				-	0.86	17
Leaflet 1: DMPC:chol	0.382	0.395	1.039			
Leaflet 2: DMPC:chol: GD1a	0.394	0.397	1.008			

With potential change, the DMPE-DMPG bilayer desorbed from the electrode surface, which in QCM-D experiments resulted in changes in frequency and energy dissipation values. At negative potentials, the flow of water through the bilayer leaded to a dehydration of the polar head group region. The rearrangement in the hydrophobic fragment provided space for the pore (defects) formation in the membrane and flow of water between the bilayer and the electrode (Figure 42a).

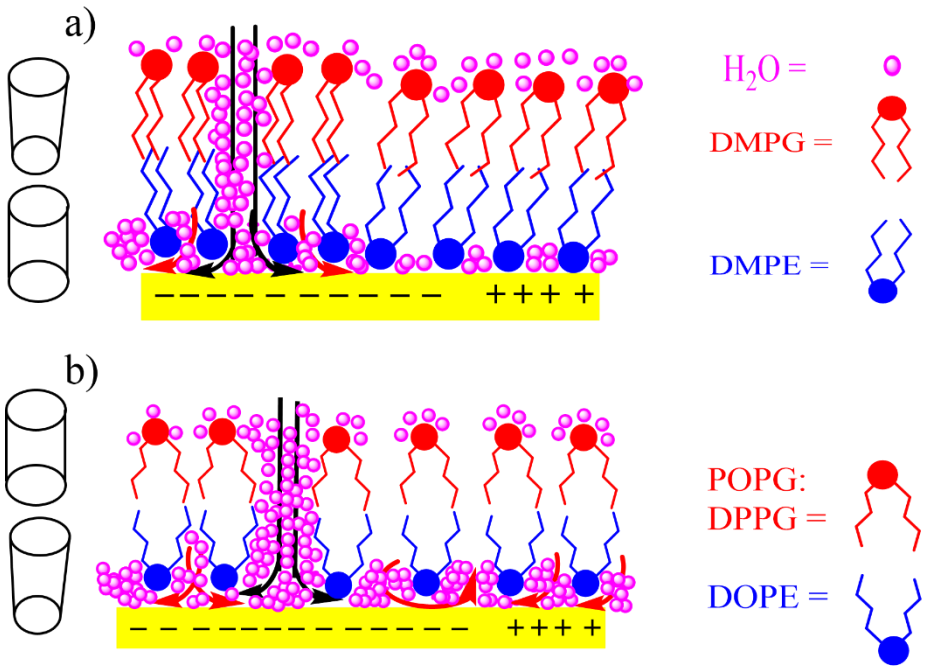

Figure 42: Schematic packing of the phospholipid molecules with packing parameter a) PP < 1 on the schematic example of the DMPE-DMPG bilayer and b) PP > 1 on the schematic example of the DOPE-POPG:DPPG bilayer as a function of the potential applied to the gold electrode. Black arrows show the direction of the flow of water through the membrane, while red arrows show the direction of flow of water in the polar head group region.

To compensate the loss of water from the polar head group region, the hydrocarbon chains reoriented themselves and adopted an orientation close to the surface normal. A change of the direction of the potential scan leaded to the uptake of water by the polar head groups and a fast bilayer re-adsorption on the metal surface. The second kind of the membrane behavior showed no potential-dependent changes in the orientation of the hydrophobic hydrocarbon chains in the phospholipid molecules. It was observed in the POPE-POPG:DPPG and DOPE-POPG:DPPG bilayers. The presence of phospholipids with monounsaturated hydrocarbon chain(-s) in model membranes results in larger values of A_{chain} compareded to the area of their head groups.[263,284] In the DMPE bilayer composed of a phospholipid with two saturated myristoyl chains, no change was reported for the chain tilt on potential applied to the Au electrode.[6] The cross-sectional area of the PE group was similar to the cross-sectional area of the two myristoyl chains.[6,106] In these lipid molecules, PP equalled 1 (Table 9). The polar head group region had a smaller area than the hydrophobic chains in phospholipid molecules with PP $\geq$ 1 (Figure 42b). In the model bilayer adsorbed directly on the Au surface, the hydrocarbon chains had a different orientation compared to the model of the DMPE-DMPG bilayer (Figure 42b). To compensate the larger cross-sectional area of the hydrocarbon chains, water accumulated in the polar head group region. At membrane potentials deviating from the capacitance minimum, water circulated in the hydrophilic fragment of the membrane. In this hydrated supramolecular assembly, less water and less negative membrane potentials were required to lift the membrane from the gold surface and to form the water cushion. This conclusion was supported by smaller changes in QCM-D frequency response with increasing unsaturation of phospholipids. The flow of water into the interfacial region between the electrode and a phospholipid bilayer leaded to a dehydration of the polar head group, reducing the average area of $A_{h\text{-}g}$, thus providing space for the formation of water channels without any rearrangement of the hydrocarbon chains (Figure 42b). In addition, the electrochemical results indicated that the structure of the hydrophobic inner leaflet of the membrane had a large impact on the response of the supramolecular assembly of the phospholipid membrane to electric potentials.

5.2 Model of the outer membrane of Gram-negative bacteria

LB-LS transfer was used to deposit a model of the outer membrane of Gram-negative bacteria containing POPE in the inner and KLA in the outer leaflet on the Au(111) electrode. In this section, the molecular scale changes in the model membrane exposed to changing electric fields are discussed.

5.2.1 Surface pressure-area isotherms

Figure 43a, c shows *Π-A* isotherms of d-POPE, h-POPE phospholipids and KLA. These isotherms were used to calculate K_s of the lipid molecules using equation 4. Plots of K_s vs. *A* were shown in Figure 43b, d. *Π-A* isotherm and the corresponding K_s were compared between d-POPE and h-POPE (Figure 43a, b and Table 10). The deuteration of the hydrocarbon chains in lipids causes usually small changes in the Langmuir isotherms of lipids. In the case of h-POPE and d-POPE monolayers differences were observed (Figure 43a). Table 10 summerized A_o, A_{lim}, Π_c and maximum K_s values at Π_c of d-POPE, h-POPE and KLA monolayers.

Table 10: The A_o, A_{lim}, Π_c and maximum K_s at the Π_c of the d-POPE, h-POPE and KLA monolayers.

Lipid monolayer	A_o / nm^2	A_{lim} / nm^2	Π_c / mN m^{-1}	K_s / mN m^{-1}
d-POPE	1.08 ± 0.02	0.51 ± 0.02	46 ± 2	95 ± 2
h-POPE	1.00 ± 0.02	0.41 ± 0.01	57 ± 2	102 ± 3
KLA	3.19 ± 0.02	1.53 ± 0.02	56 ± 2	195 ± 4

The A_o of h-POPE is lower than of the d-POPE, being characteristic for an increase in volume of the per-deuterated hydrocarbon chain. Both isotherms have a similar shape at surface pressures proceeding a phase transition in the h-POPE monolayer, which ocuured at Π = 38 - 40 mN m^{-1}. After the phase transition the surface pressure of the POPE monolayer increased to (57 ± 2) mN m^{-1} at A_{lim} = (0.41 ± 0.01) nm^2. The isotherm data agree with literature.[262,285,286] In contrast, in the d-POPE monolayer no phase ransition

was observed. The monolayer collapse was observed at Π = (46 ± 2) mN m^{-1} and A_{lim} = (0.51 ± 0.02) nm^2. In the h-POPE monolayer after the phase transion to the LC phase K_s increased to (102 ± 3) mN m^{-1}. Thus, the perdeuterated POPE has a greater fluidity than h-POPE. Analogous isotherm behavior was reported for h-DMPC and d-DMPC.[287] Main phase transition temperature of h-POPE equals 25.2 °C.[268,269] Deuteration of the hydrocarbon chain in lipids, due to a reduction in van der Waals interactions, leads to a 4 - 6 °C reduction of the main phase transition temperature of lipids.[288] In described here experiments, the temperature of the aqueous subphase in experiments was (22 ± 1) °C. Under these experimental conditions at Π = (37 ± 1) mN m^{-1} a phase transition to a LC phase in the h-POPE monolayer was observed whereas the d-POPE monlayer remains in the liquid expanded state.

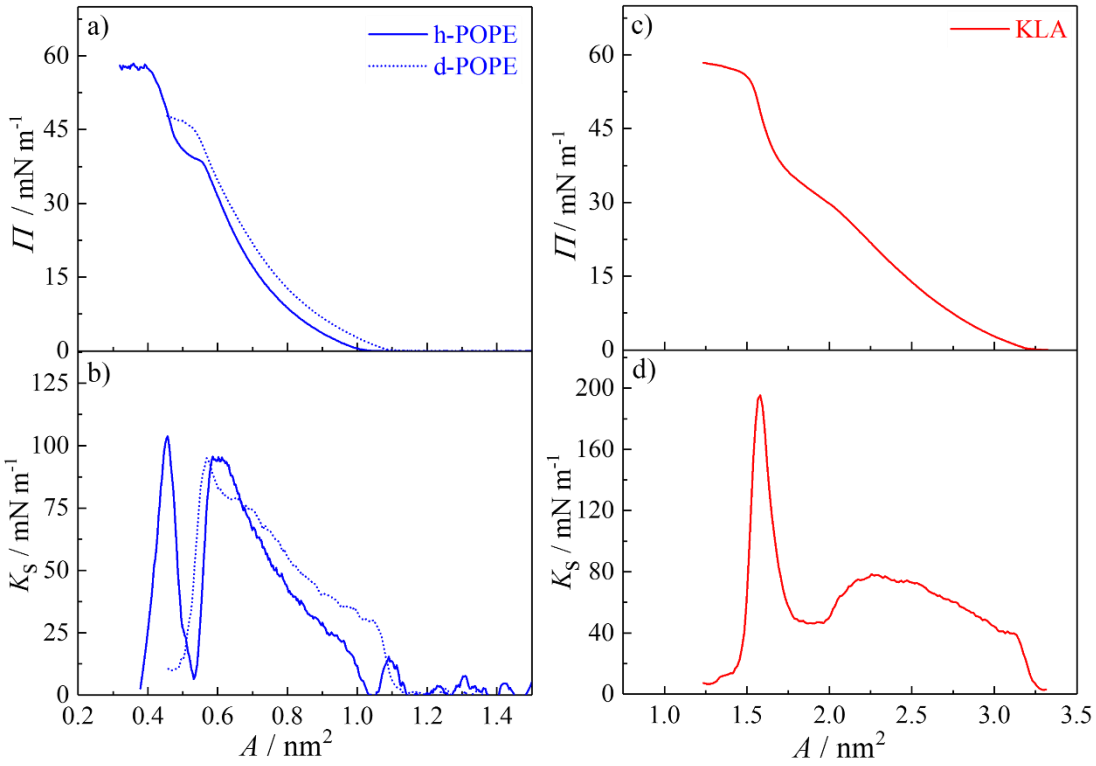

Figure 43: Plots of a), c) Π and b), d) K_s vs. A of the studied lipids: a), b) PE (blue): h-POPE (solid blue line) and d-POPE (short dot blue line) on water subphase and c), d) KLA (red solid line) on 0.1 M $KClO_4$ + 0.005 M $Mg(ClO_4)_2$ subphase.

Isotherms of the h-POPE and d-POPE monolayers were located at smaller areas compared to the isotherm of the KLA monolayer, due to a smaller size of the polar head groups of

PE compared to KLA head groups and an increase in volume of the hydrocarbon chains in KLA. The effect of the ionic strength was tested on KLA monolayer formation. Isotherms of the KLA monolayer on pure water and on 0.1 M $KClO_4$ + 0.005 M $Mg(ClO_4)_2$ solution are shown in Figure 44a. Both isotherms have a similar shape. A_o and A_{lim} were smaller for KLA monolayer on pure water than in KLA monolayer on the electrolyte solution (Figure 44a). Π started to increase at A_o = (2.84 ± 0.03) nm^2 in KLA monolayer on pure water subphase and Π increased until the monolayer collapsed at Π_c = (52 ± 3) mN m^{-1} at A_{lim}= (1.37 ± 0.02) nm^2 (Figure 44a). Both isotherms show a plateau region, indicating the coexistence of the LE and the LC phases (Figure 44a). A_o equalled (3.19 ± 0.02) nm^2 for KLA monolayer on the electrolyte solution (Figure 44a and Table 10). KLA monolayer collapsed at Π_c = (56 ± 2) mN m^{-1} and A_{lim}= (1.53 ± 0.02) nm^2 (Figure 44a and Table 10).

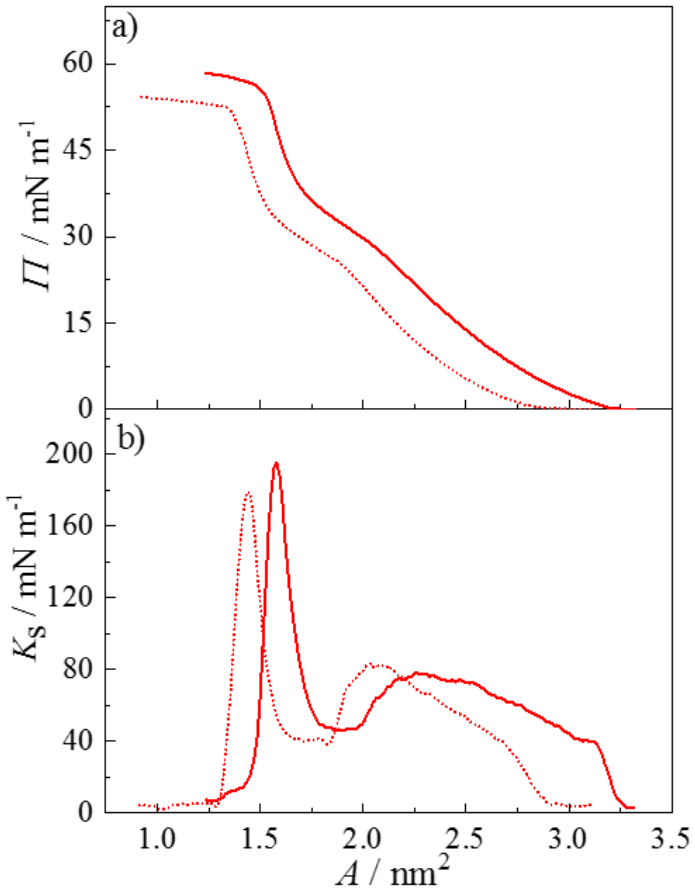

Figure 44: Plots of a) Π and b) K_s vs. A of KLA monolayer on 0.1 M $KClO_4$ + 0.005 M $Mg(ClO_4)_2$ (solid red line) and on pure water subphase (short dot red line).

The electrostatic interaction between Mg^{2+} ions and the anionic polar head groups of KLA molecules stabilized the monolayer. The maximum K_s was (179 ± 3) mN m^{-1} at Π_c of KLA monolayers on pure water, while it was (195 ± 4) mN m^{-1} on 0.1 M $KClO_4$ + 0.005 M $Mg(ClO_4)_2$ (Figure 44b). KLA monolayers exist in a liquid state.

5.2.2 Electrochemical characterization of the model outer membrane

Figure 45 shows C vs. E and E - E_{pzc} potential plots of the h-POPE-KLA bilayer on the Au(111) surface in 0.1 M $KClO_4$ + 0.005 M $Mg(ClO_4)_2$ electrolyte solution. The h-POPE monolayer was transferred from water subphase at Π = 30 mN m^{-1} and KLA monolayer was transferred from the 0.1 M $KClO_4$ + 0.005 M $Mg(ClO_4)_2$ subphase at Π = 30 mN m^{-1}.

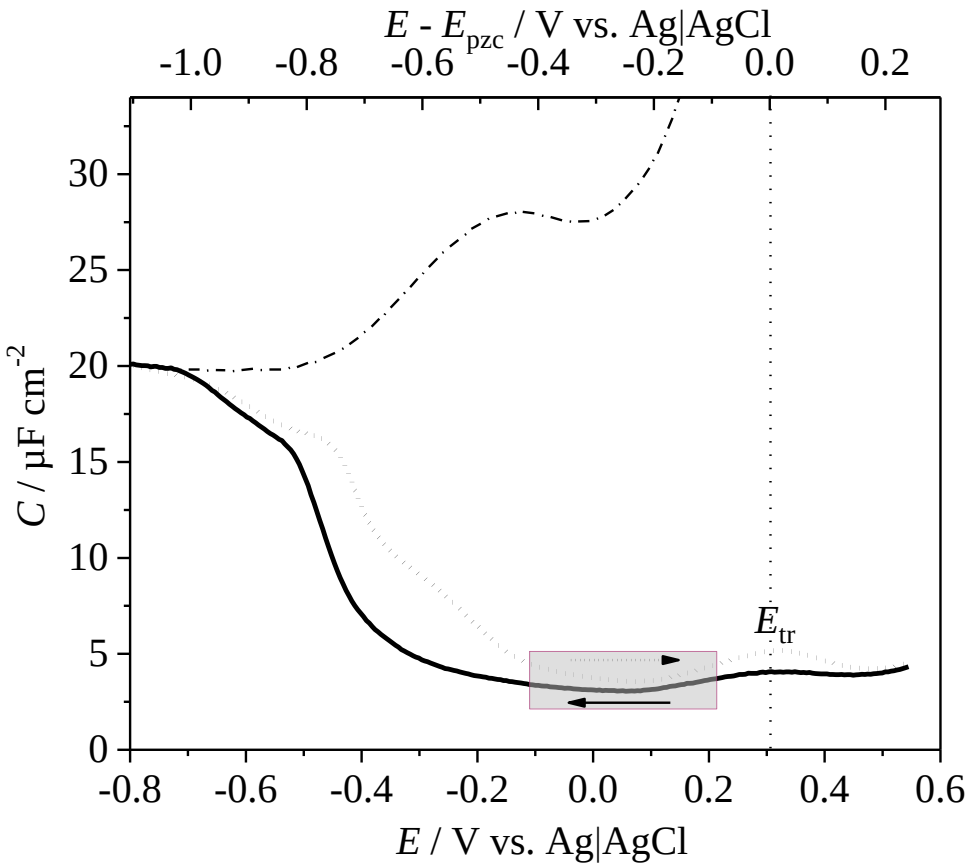

Figure 45: Plots of C vs. E and E - E_{pzc} potentials of the h-POPE-KLA bilayer on the Au(111) surface in 0.1 M $KClO_4$ + 0.005 M $Mg(ClO_4)_2$ solution. Solid lines: negative, short dotted line: positive going potential scan. Dash dot black line: C of the unmodified Au(111) electrode in 0.1 M $KClO_4$ + 0.005 M $Mg(ClO_4)_2$ solution. Grey marked field shows the potential range of the C_{min}.

In the negative going potential scan, the capacitance was (3.1 ± 0.1) μF cm^{-2} for the h-POPE-KLA bilayer at -0.42 V < E - E_{pzc} < -0.11 V. A further negative potential shift caused a fast increase in the capacitance (Figure 45). At membrane potential (E - E_{pzc}) < -1.0 V, the h-POPE-KLA bilayer was detached from the Au(111) electrode and the capacitance increased to (20 ± 1) μF cm^{-2}, merging with the curve corresponding to the unmodified Au(111) electrode in 0.1 M $KClO_4$ + 0.005 M $Mg(ClO_4)_2$. In the positive going potential scan, a gradual decrease in the capacitance corresponded to the re-adsorption of the h-POPE-KLA bilayer on the Au(111) electrode surface was observed. In this potential scan, a poorly-defined peak appeared at $(E - E_{pzc})_{tr}$ = 0.02 V (Figure 45). This weak capacitance peak indicated some potential-driven reorientations in the OM. It was associated with the flow of the electrolyte solution in the polar head group region of the lipid membrane. In the studied OM, h-POPE molecules were present in the inner leaflet. Thus, some rearrangements in the inner leaflet of the membrane at membrane potential (E - E_{pzc}) close to 0 V could be responsible for the appearance of this peak. A small hysteresis was obtained between the negative and positive going potential scans (Figure 45). The presence of the hysteresis indicated a slow kinetics of the adsorption-desorption process.[267]

Piggot et al.[133] have reported molecular dynamic simulations of the OM of Gram-negative *E.coli* bacteria. The electroporation process of the OM of Gram-negative *E.coli* affected the orientation of the lipid molecules in the inner leaflet.[133] The electrochemical measurements provided information about the capacitance change in the entire OM and not in each leaflet.

5.2.3 PM IRRAS measurements of the model of the outer membrane of Gram-negative bacteria in the CH/CD stretching region

The asymmetric bilayers composed of h-POPE-KLA and d-POPE-KLA were transferred on Au(111) electrode surfaces. These bilayers serve as model of the OM of Gram-negative bacteria. Figure 46 shows background-corrected PM IRRA spectra of the h-POPE-KLA and d-POPE-KLA bilayers. POPE and KLA have different structure of the head groups and hydrocarbon chains, thus their packing and orientation may be different in both leaflets. In the h-POPE-KLA bilayer, there is a decrease in the intensities of the

methylene stretching modes at potentials preceding the membrane desorption from the Au(111) electrode (Figure 46a). This indicated potential-induced changes in the orientation of the hydrocarbon chains in lipid molecules in the model membrane. Re-adsorption caused a reversible increase in the intensities of the methylene stretching modes for the h-POPE-KLA bilayer on the Au(111) surface. The surface concentration was constant for lipid molecules in the bilayer and therefore had no influence on the variation of the intensities of the methylene stretching modes during the potential scan. These changes were connected with the potential-dependent reorientation of the hydrocarbon chains in the model membrane. In the h-POPE-KLA bilayer, $\nu_{as}(CH_2)$ mode was very broad with two shoulders corresponding to the $\nu_{as}(O\text{-}CH_2)$, $\nu_{s}(O\text{-}CH_2)$ modes and FR (Figure 46a).[6,273,278] KLA has methylene groups, which are coordinated to O atoms ($O\text{-}CH_2$). The presence of the O atom adjacent to the methylene group caused a shift of the methylene stretching modes.[289,290] $\nu_{as}(O\text{-}CH_2)$ was overlapped with FR at around (2938 ± 2) cm^{-1}, while $\nu_{s}(O\text{-}CH_2)$ mode appeared at around (2900 ± 2) cm^{-1} (Figure 46a). The position of the absorption maximum of $\nu(CH_2)$ modes indicated that the hydrocarbon chains existed in the liquid state in the h-POPE-KLA bilayer (Figure 46a). The integral intensities had higher intensities for these modes than those in the POPE-POPG:DPPG (0.95:0.05) and DMPC[80] bilayers.

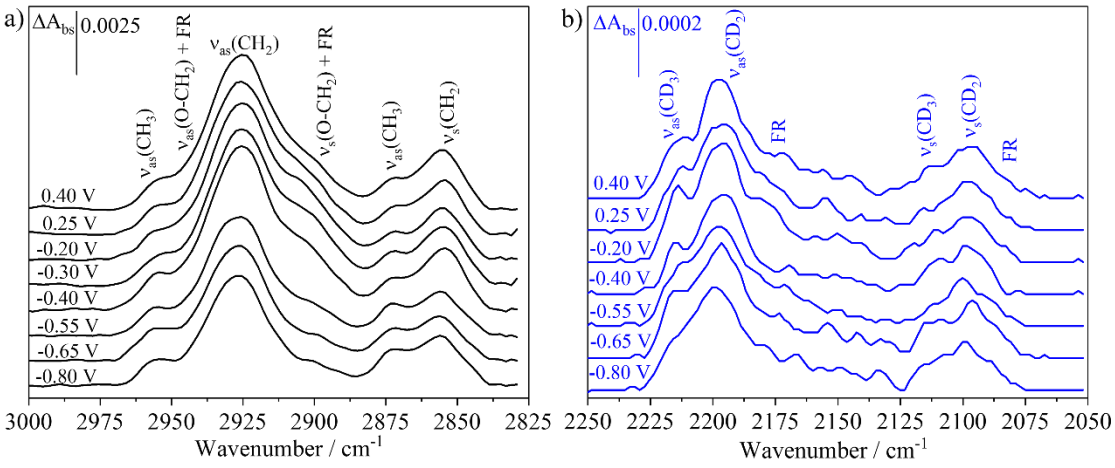

Figure 46: PM IRRA spectra a) in the 3000 - 2825 cm^{-1} spectral region of the h-POPE-KLA bilayer in 0.05 M $KClO_4$ + 0.005 M $Mg(ClO_4)_2$ in D_2O and b) in the 2250 - 2050 cm^{-1} spectral region of the d-POPE-KLA bilayer in 0.05 M $KClO_4$ + 0.005 M $Mg(ClO_4)_2$ in H_2O. All model membranes were prepared on the Au(111) electrode. The spectra shown in the figure were recorded in a negative going potential scan at potentials marked in the figure.

To distinguish the hydrocarbon chains in POPE molecules, d-POPE was used in which the saturated chain was perdeuterated. The CD stretching bands were shifted to lower wavenumbers in the d-POPE-KLA bilayer and were located between 2250 and 2050 cm^{-1} (Figure 46b). Methyl and methylene groups give four IR absorption modes as listed in Table 11. The position of the absorption maximum of $\nu(CD_2)$ modes indicated that the hydrocarbon chains existed in the liquid state in the d-POPE molecules (Table 11).[291,292]

Table 11: Wavenumber of IR absorption bands of methyl and methylene groups in the d-POPE-KLA bilayer on the Au(111) electrode surface.

Vibrational mode	Wavenumber / cm^{-1}
$\nu_{as}(CD_3)$	2216 ± 1
$\nu_{as}(CD_2)$	2197 ± 1
$\nu_{s}(CD_3)$	2114 ± 1
$\nu_{s}(CD_2)$	2096 ± 1

There were two shoulders at (2175 ± 2) cm^{-1} and (2079 ± 2) cm^{-1}, which corresponded to FR (Figure 46b).[110,291,292] Intensities of the CD stretching modes were independent of the electrode and membrane potentials in the d-POPE-KLA bilayer (Figure 46b). To perform quantitative analysis, the transmission spectra were measured for the studied models of the OM and used to calculate the optical constants. Figure 47 shows the calculated optical constants in the 3050 - 2750 cm^{-1} and 2250 - 2050 cm^{-1} spectral regions.

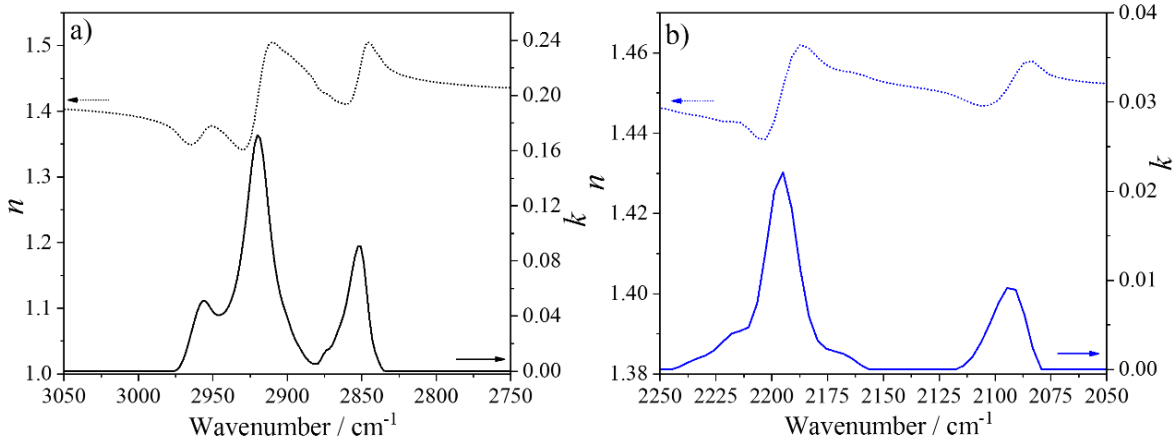

Figure 47: Refractive index *n* (short dot lines) and attenuation coefficient *k* (solid lines) in a) the 3050 - 2750 cm^{-1} spectral region of the h-POPE-KLA bilayer and b) the 2250 - 2050 cm^{-1} spectral region of the d-POPE-KLA bilayer.

The optical constants of the POPE and KLA mixture (3.2:1 mole) were used to calculate PM IRRA spectra of randomly oriented lipid molecules. In the spectrum of randomly oriented molecules of the h-POPE-KLA film, $\nu_{as}(CH_2)$ was centered at 2921 cm^{-1} and $\nu_s(CH_2)$ was located at 2853 cm^{-1}. In the calculation, the angle of incidence of the incoming IR radiation was set to 55° in the h-POPE-KLA bilayer and to 52° in the d-POPE-KLA bilayer. The optical constants were taken from literature for gold, CaF_2 (optical window), D_2O (electrolyte in case of the h-POPE-KLA bilayer) and H_2O (electrolyte in case of the d-POPE-KLA bilayer).[274] Γ_t and Γ_{lim} were calculated for the lipid molecules from the Langmuir isotherms measurements (Table 12). The average Γ_t were $(1.93 \pm 0.05)\times10^{-10}$ mol cm^{-2} and $(1.80 \pm 0.06)\times10^{-10}$ mol cm^{-2} for the lipids in the h-POPE-KLA and d-POPE-KLA bilayers, respectively. Γ_{lim} were $(2.49 \pm 0.07)\times10^{-10}$ mol cm^{-2} and $(2.29 \pm 0.04)\times10^{-10}$ mol cm^{-2} for the h-POPE-KLA and d-POPE-KLA bilayers, respectively. The thickness were 5.50 nm and 5.55 nm for the h-POPE-KLA and d-POPE-KLA bilayers, respectively. Φ were calculated from the LB-LS transfer condition (Table 12). Figure 48 shows that the intensities of all experimental PM IRRA spectra of these model bilayers adsorbed on the Au(111) electrode were lower than the spectra of randomly oriented lipids in the studied films. PM IRRA spectra were deconvoluted to determine the integral intensities of the methylene stretching modes. Deconvolution was performed for the bands using a mixed Gaussian-Lorentzian function. Figure 49 shows the deconvoluted PM IRRA spectra for the studied lipid bilayers.

Table 12: The A_t of the monolayer transfer (Π = 30 mN m^{-1}), limiting area (A_{lim}) the Γ_t of the lipid in the LB monolayers at the transfer pressure, Γ_{lim}, Φ of monolayers and d of the lipid bilayers on the gold surface.

Lipid	A_t / nm^2	A_{lim} / nm^2	Γ_t /10^{-10} mol cm^{-2}	Γ_{lim} / 10^{-10} mol cm^{-2}	Φ	d / nm Ref.
h-POPE	0.61 ± 0.01	0.72 ± 0.01	3.02 ± 0.10	3.86 ± 0.13	0.78 ± 0.01	4.18[204,276]
d-POPE	0.64 ± 0.01	0.85 ± 0.02	2.77 ± 0.08	3.45 ± 0.05	0.80 ± 0.02	4.30
KLA	1.98 ± 0.03	1.48 ± 0.03	0.84 ± 0.05	1.12 ± 0.04	0.75 ± 0.02	6.80[130]

Using the integral intensities of $\nu(CH_2)$ and $\nu(CD_2)$ modes, angles $\theta_{\nu(CH2)}$ and $\theta_{\nu(CD2)}$ were calculated between the electric field vector and the transition dipole moments of $\nu_{as}(CH_2)$ and $\nu_s(CH_2)$ in the h-POPE-KLA bilayer (Figure 50a, b) and $\nu_{as}(CD_2)$ and $\nu_s(CD_2)$ stretching modes in the d-POPE-KLA bilayer (Figure 50c, d). The average angle $\theta_{\nu s(CH2)}$ was (74 ± 4)° for the h-POPE-KLA bilayer (Figure 50a). The integral intensity of the asymmetric methylene stretching mode depended on the membrane potential in the h-POPE-KLA bilayer. The average angle $\theta_{\nu as(CH2)}$ was (60 ± 3)° in the adsorbed state (E - E_{pzc} ≥ -0.80 V), while the average angle $\theta_{\nu as(CH2)}$ was (69 ± 3)° in the desorbed state (E - E_{pzc} < -0.80 V) (Figure 50b). The average angles $\theta_{\nu s(CD2)}$ and $\theta_{\nu as(CD2)}$ were independent of the membrane potential in the d-POPE-KLA bilayer. The average angles $\theta_{\nu s(CD2)}$ and $\theta_{\nu as(CD2)}$ were (70 ± 5)° and (71 ± 4)°, respectively (Figure 50c, d). The average angles $\theta_{\nu(CH2)}$ and $\theta_{\nu(CD2)}$ were comparable (Figure 50).

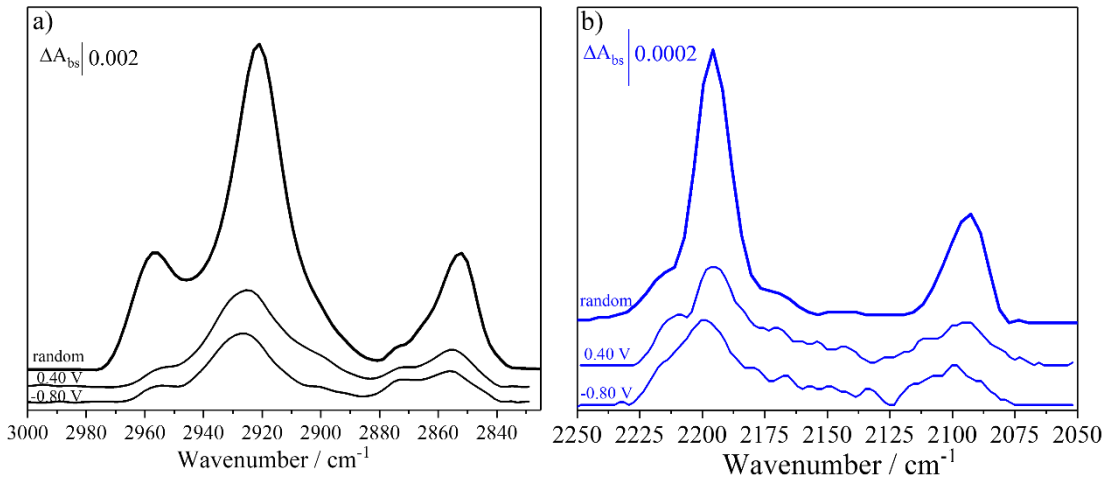

Figure 48: Experimental PM IRRA spectra of the studied bilayers at E = -0.8 V and E = 0.4 V vs. Ag|AgCl and the calculated PM IRRA spectra of randomly oriented lipid molecules in the studied film in a) ν(CH) stretching modes of the h-POPE-KLA bilayer in 0.05 M $KClO_4$ + 0.005 M $Mg(ClO_4)_2$ in D_2O and in b) ν(CD) stretching modes of the d-POPE-KLA bilayer in 0.05 M $KClO_4$ + 0.005 M $Mg(ClO_4)_2$ in H_2O on the Au(111) electrode.

The order parameters were calculated for the symmetric and asymmetric methylene stretching modes $S_{\nu(CH2)}$ of the OM of Gram-negative bacteria as a function of the electrode and membrane potentials (Figure 51a, b). The average $S_{\nu s(CH2)}$ was negative for the h-POPE-KLA bilayer. It was not dependent on the applied potentials (Figure 51a). The average $S_{\nu s(CH2)}$ was (-0.38 ± 0.05) for the h-POPE-KLA bilayer (Figure 51a).

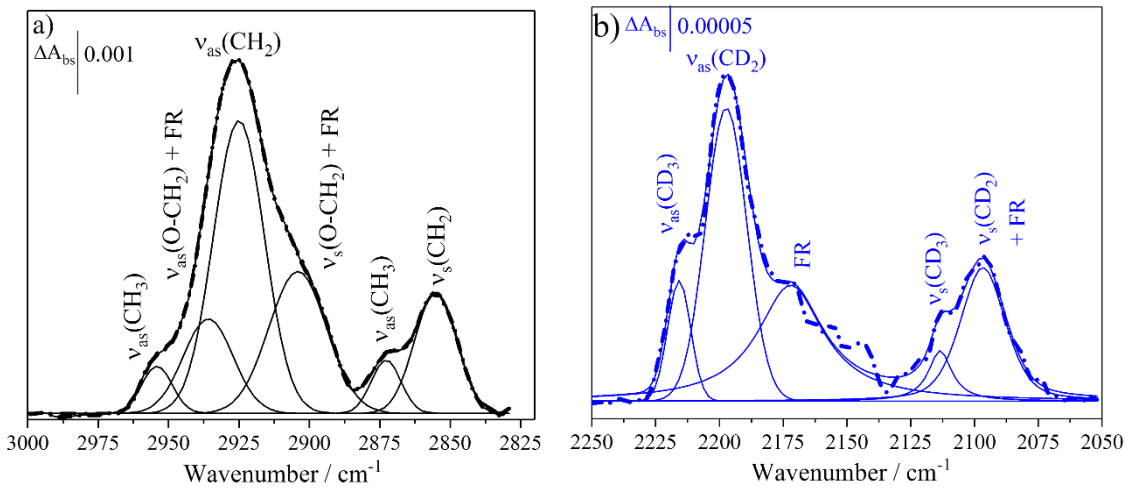

Figure 49: Deconvoluted PM IRRA spectra in a) ν(CH) stretching modes region of the h-POPE-KLA bilayer in 0.05 M $KClO_4$ + 0.005 M $Mg(ClO_4)_2$ in D_2O at E = 0.40 V vs. Ag|AgCl and in b) ν(CD) stretching modes region of the d-POPE-KLA bilayer in 0.05 M $KClO_4$ + 0.005 M $Mg(ClO_4)_2$ in H_2O at E = 0.40 V vs. Ag|AgCl. All model membranes were prepared on the Au(111) electrode; colored dashed lines: measured spectrum, black and blue thin lines: envelope and deconvoluted modes.

The average $S_{vas(CH2)}$ of the h-POPE-KLA bilayer depended on the membrane potential. It changed from (-0.30 ± 0.04) at desorption to (-0.15 ± 0.04) at adsorption potentials (Figure 51b).

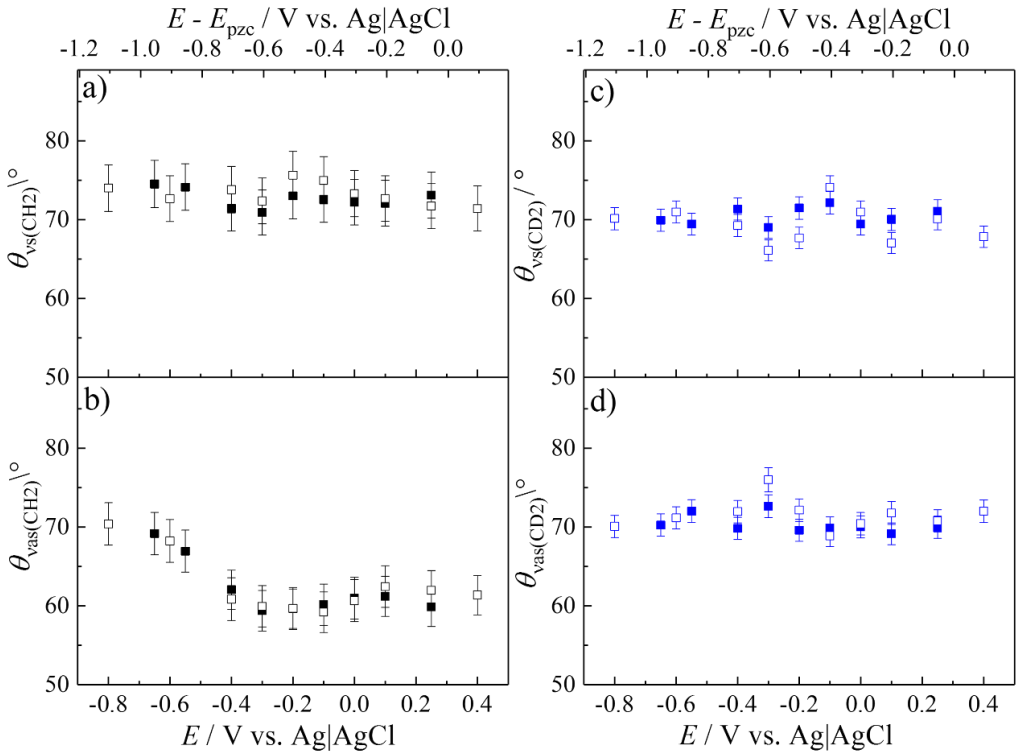

Figure 50: Angles a) $\theta\nu_{s(CH2)}$, b) $\theta\nu_{as(CH2)}$, c) $\theta\nu_{s(CD2)}$ and d) $\theta\nu_{as(CD2)}$ vs. E and E - E_{pzc} in a), b) the h-POPE-KLA bilayer in 0.05 M $KClO_4$ + 0.005 M $Mg(ClO_4)_2$ in D_2O and in c), d) the d-POPE-KLA bilayer in 0.05 M $KClO_4$ + 0.005 M $Mg(ClO_4)_2$ in H_2O. All model membranes were prepared on the Au(111) electrode. Filled and opened points represent negative and positive going potential scans, respectively.

In the d-POPE-KLA bilayer, the average $S_{vs(CD2)}$ and $S_{vas(CD2)}$ were (-0.33 ± 0.08) and (-0.35 ± 0.05), respectively (Figure 51c, d). In the h-POPE-KLA bilayer, the average S_{chain} depended on the membrane potential (Figure 52b). S_{chain} was (0.50 ± 0.05) in the bilayer adsorbed directly on the Au(111) electrode and indicated an average tilt of the hydrocarbon chains of (~35 ± 3)° vs. the surface normal (Figure 52a, b). S_{chain} increased to (0.69 ± 0.05) in the desorbed state at E - E_{pzc} < -0.80 V, which corresponded to the tilt of (28 ± 3)° (Figure 52a, b).

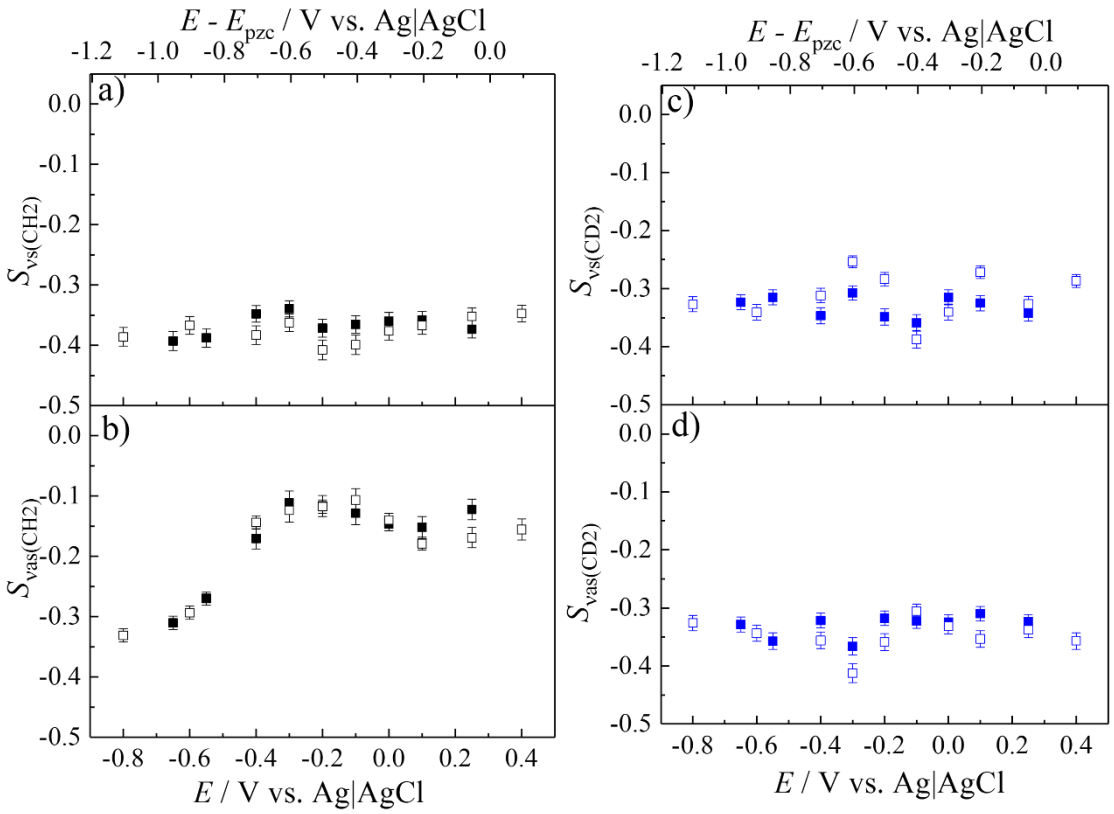

Figure 51: Plots of a) $S_{vs(CH2)}$, b) $S_{vas(CH2)}$, c) $S_{vs(CD2)}$ and d) $S_{vas(CD2)}$ vs. E and E - E_{pzc} in a), b) the h-POPE-KLA bilayer in 0.05 M $KClO_4$ + 0.005 M $Mg(ClO_4)_2$ in D_2O and in c), d) the d-POPE-KLA bilayer in 0.05 M $KClO_4$ + 0.005 M $Mg(ClO_4)_2$ in H_2O. All model membranes were prepared on the Au(111) electrode. Filled and opened points represent negative and positive going potential scans, respectively.

In the h-POPE-KLA bilayer, minor changes in the average orientation of the hydrocarbon chains were reported. In addition, the average S_{chain} was larger for the h-POPE-KLA bilayer than that reported for a bilayer of LPS.[125,293] Wu et al.[125] and Jefferies et al.[293] have calculated the average S_{chain} of the LPS bilayer. Their studies showed that the average S_{chain} was below (0.30 ± 0.03) for LPS bilayer. In the d-POPE-KLA bilayer, S_{chain} was (0.65 ± 0.05), which corresponded to the tilt of (29 ± 3)° (Figure 52c, d).

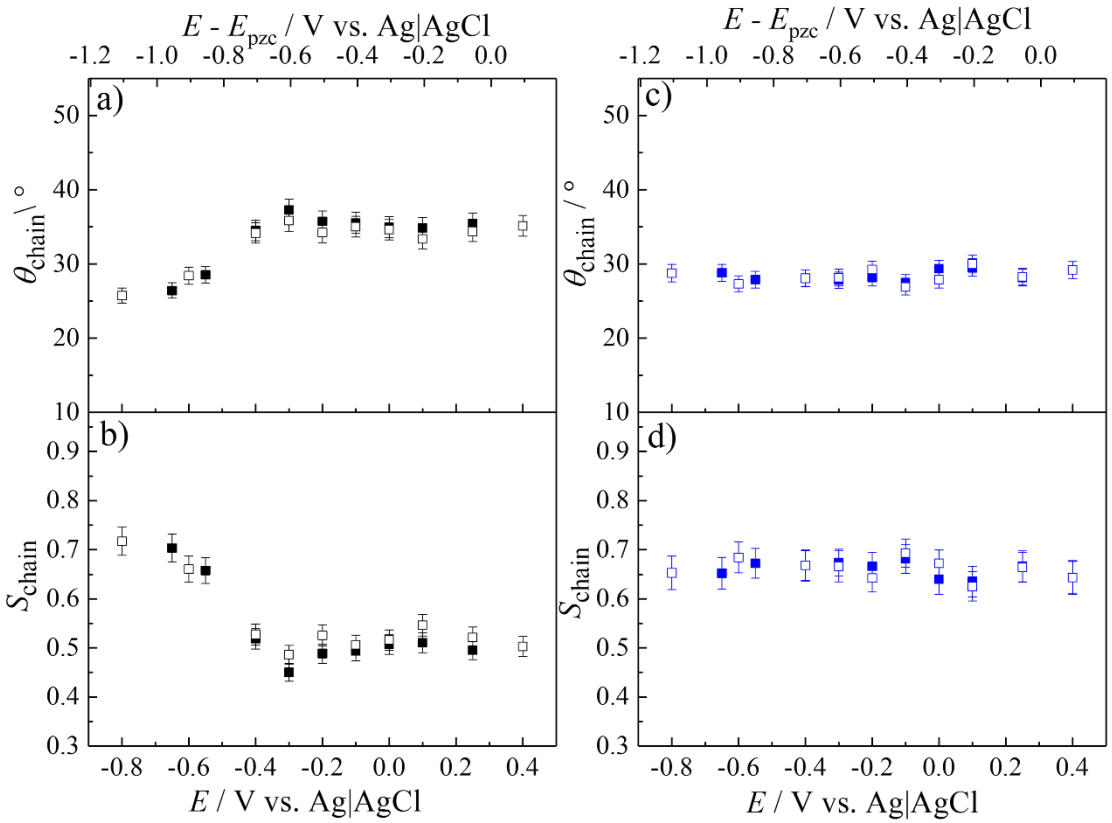

Figure 52: Plots of a), c) θ_{chain}, b), d) S_{chain} vs. E and E - E_{pzc} in a), b) the h-POPE-KLA bilayer in 0.05 M $KClO_4$ + 0.005 M $Mg(ClO_4)_2$ in D_2O and in c), d) the d-POPE-KLA bilayer in 0.05 M $KClO_4$ + 0.005 M $Mg(ClO_4)_2$ in H_2O. All model membranes were prepared on the Au(111) electrode. Filled and opened points represent negative and positive going potential scans, respectively.

5.2.4 PM IRRAS measurements of the model of the outer membrane of Gram-negative bacteria in the polar head group region

Figure 53 shows background-corrected PM IRRA spectra in the 1850 - 1550 cm^{-1} spectral region of the h-POPE-KLA bilayer adsorbed on the Au(111) surface. These bands contained valuable information concerning the hydration and orientation for the head group of the OM of Gram-negative bacteria. The h-POPE and KLA lipid molecules gave three IR absorption modes in this spectral region (Figure 53). The IR absorption mode around 1615 - 1600 cm^{-1} was assigned to $\nu_{as}(COO^-)$ mode in the 2-keto-3-deoxy-octulosonate fragment for the polar head group of KLA molecules (Figure 53).[294,295] A very weak mode around (1632 ± 2) cm^{-1} arised from the amide groups in KLA molecules

(Figure 53). The intensive mode centered around 1733 cm^{-1} was assigned to ν(C=O) in ester groups in the h-POPE and KLA lipid molecules (Figure 53).

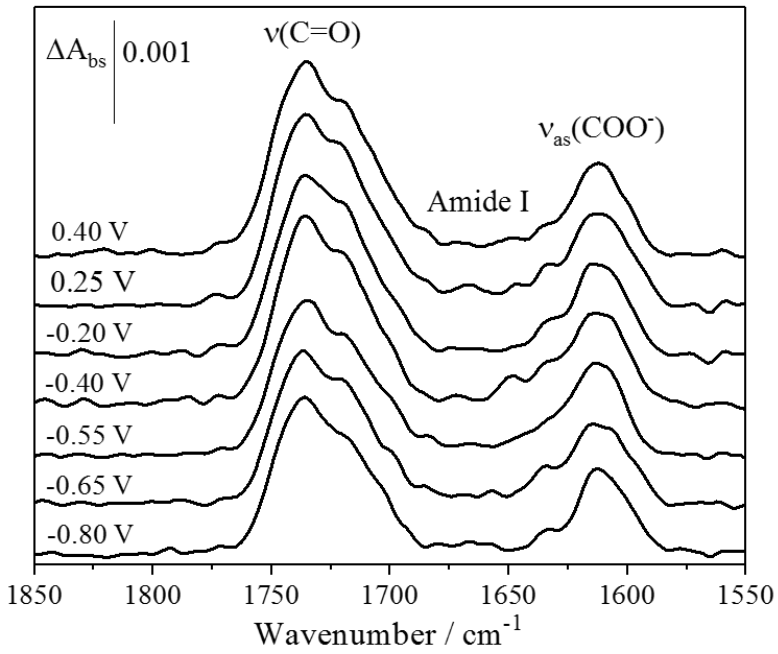

Figure 53: PM IRRA spectra in the 1850 - 1550 cm^{-1} spectral region of the h-POPE-KLA bilayer in 0.05 M $KClO_4$ + 0.005 M $Mg(ClO_4)_2$ in D_2O on the Au(111) electrode. The spectra shown in the figure were recorded in a negative going potential scan at potentials marked in the figure.

In KLA, the carboxylic acid groups were dissociated[295] and coordinated to Mg^{2+} ions present in the electrolyte solution [pH (5.9 ± 0.1)].[125,126,133] The IR spectra seen in Figure 53 showed that the $\nu_{as}(COO^-)$ mode was asymmetric and composed of two components. The position of the high wavenumber mode did not depend on the membrane potential and was centered at (1613 ± 4) cm^{-1} (Figure 54). The high wavenumber mode was assigned to the carboxylate groups with monodentate coordinated Mg^{2+} ions.[296] The second $\nu_{as}(COO^-)$ mode was located around at 1600 - 1604 cm^{-1}. A fraction of carboxylate groups in KLA made hydrogen bonds to water. The position of the low wavenumber of the $\nu_{as}(COO^-)$ mode depended on the membrane potential. It underwent to a shift from 1603 cm^{-1} at $E - E_{pzc} < -0.70$ V to 1600 cm^{-1} at $-0.62 \text{ V} < E - E_{pzc} < 0.13$ V (Figure 54), reflecting changes in the hydration of the carboxylate group in the KLA molecules present in the outer leaflet. The transmission spectrum of the h-POPE-KLA bilayer was measured and used to calculate the optical constants. Figure 55 shows the result of these calculations.

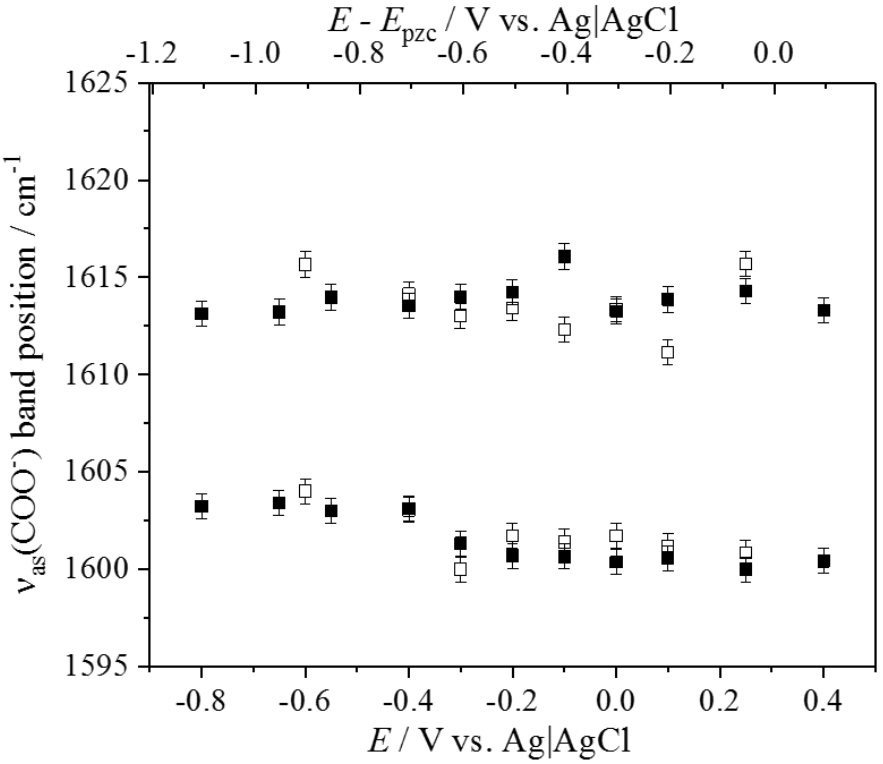

Figure 54: Position of $\nu_{as}(COO^-)$ stretching band vs. E and E - E_{pzc} in the h-POPE-KLA bilayer in 0.05 M $KClO_4$ + 0.005 M $Mg(ClO_4)_2$ in D_2O on the Au(111) electrode. Filled and opened points represent negative and positive going potential scans, respectively.

Figure 56 shows that intensities of ν(C=O) mode in all experimental spectra were lower than the spectra of randomly oriented lipid bilayer in the thick film.

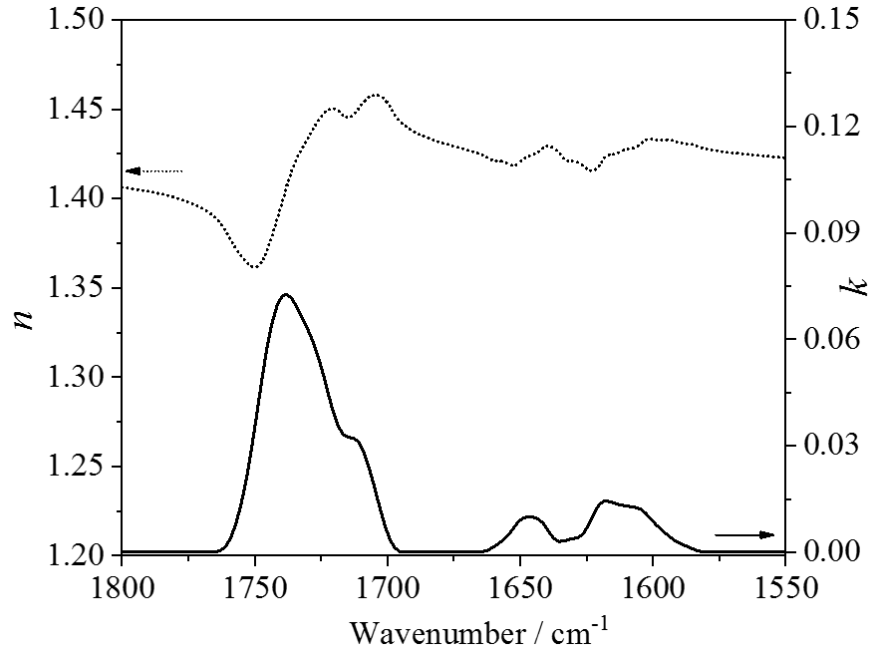

Figure 55: Refractive index n (short dot lines) and attenuation coefficient k (solid line) in the 1800 - 1550 cm^{-1} spectral region of the h-POPE-KLA bilayer.

The calculated and experimental PM IRRA spectra were deconvoluted to determine the integral intensities of ν(C=O) and $\nu_{as}(COO^-)$ modes as a function of the membrane potential. Figure 57 shows the deconvolution for the PM IRRA spectrum in the ν(C=O) and $\nu_{as}(COO^-)$ modes of the h-POPE-KLA bilayer. It was performed using a mixed Gaussian-Lorentzian function. The ν(C=O) peak was composed of three overlapping bands. The low frequency band appeared at (1708 ± 2) cm^{-1} and was assigned to ester carbonyl groups in KLA. It indicated that some ester groups were involved in a formation of strong hydrogen bonds.[294]

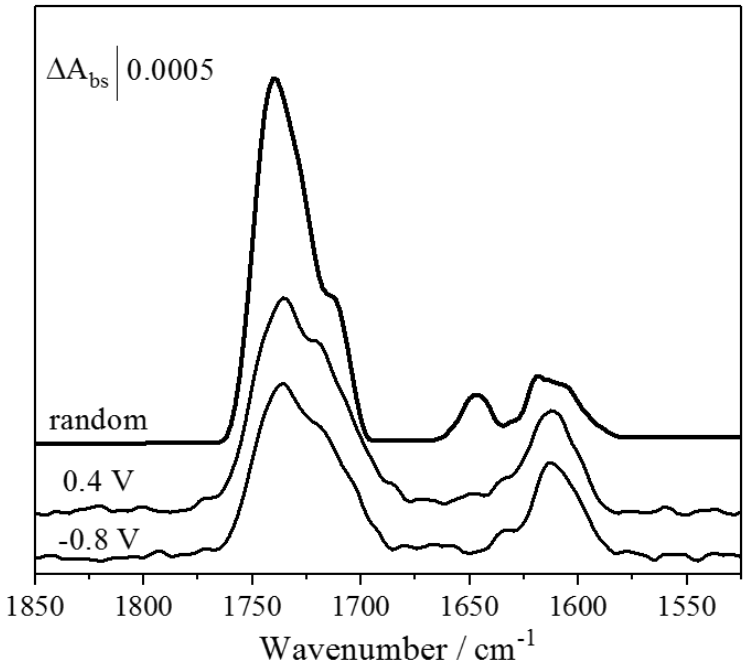

Figure 56: Experimental PM IRRA spectra in the 1850 - 1525 cm^{-1} spectral region of the h-POPE-KLA bilayer at *E* = -0.8 V and *E* = 0.4 V vs. Ag|AgCl and the calculated PM IRRA spectrum of randomly oriented lipid molecules in the studied film in 0.05 M $KClO_4$ + 0.005 M $Mg(ClO_4)_2$ in D_2O on the Au(111) electrode.

The two high wavenumbers bands were centered for ν(C=O) modes at (1718 ± 4) cm^{-1} and (1738 ± 2) cm^{-1}, corresponding to the hydrogen bonded and non-hydrogen bonded ester carbonyl groups, respectively. These two bands were assigned to both h-POPE and KLA lipids and reflected the asymmetry in the hydration of the lipid molecules of the inner and outer leaflets.[294,297] Wu et al.[125] have showed that water molecules penetrate the inner core region and the hydration was critical to keep the integrity of the bilayer structure. Angles of the stretching modes of the ester carbonyl group $\theta_{\nu(C=O)}$ and carboxylate group $\theta_{\nu as(COO^-)}$ were calculated between the transition dipole moment and the electric field vector (Figure 58a, c). The average angles $\theta_{\nu(C=O)}$ and $\theta_{\nu as\ (COO^-)}$ were

dependent on the membrane potentials. In the adsorbed state of the h-POPE-KLA bilayer (-0.50 V < E - E_{pzc} < -0.05 V), the average angle $\theta\nu_{as\,(COO^-)}$ changed between 25° and 37° vs. the surface normal (Figure 58a). It corresponded to a change in the average of $S\nu_{as\,(COO^-)}$ between (0.40 ± 0.03) and (0.70 ± 0.02) (Figure 58b). The average angle $\theta\nu_{as\,(COO^-)}$ was (30 ± 2)° in the desorbed state (-1.1 V < E - E_{pzc} < -0.9 V) (Figure 58a).

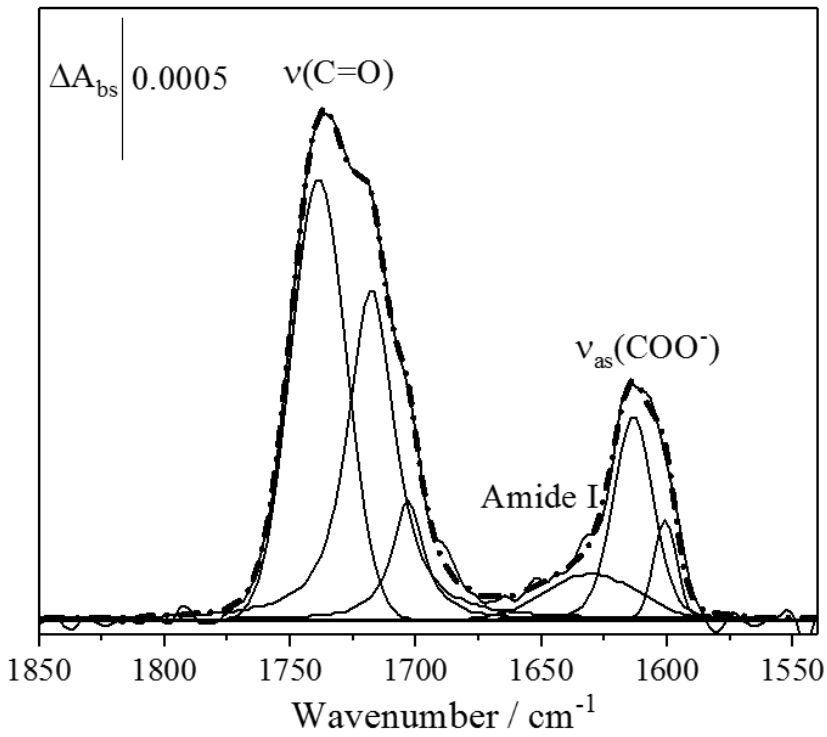

Figure 57: Deconvoluted PM IRRA spectrum in the 1850 - 1525 cm^{-1} spectral region of the h-POPE-KLA bilayer in 0.05 M $KClO_4$ + 0.005 M $Mg(ClO_4)_2$ in D_2O on the Au(111) electrode at E = 0 V vs. Ag|AgCl. Black thick line: measured spectrum, black thin lines: envelope and deconvoluted modes.

In the adsorbed state of the h-POPE-KLA bilayer, the average angle $\theta_{\nu(C=O)}$ was (59 ± 5)° (Figure 58c), which corresponded to $S_{\nu(C=O)}$ = (-0.11 ± 0.05) (Figure 58d). In the desorbed state (E - E_{pzc} < -0.80 V), the average $\theta_{\nu(C=O)}$ was (63 ± 3)° (Figure 58c), giving $S_{\nu(C=O)}$ ~ (-0.18 ± 0.02) (Figure 58d). The direction of the transition dipole moment of the ester carbonyl bond is approximately normal (90°) to the hydrocarbon chains.[52,298–301] Therefore, the large angles obtained for the C=O stretching modes (59° - 63°) were consistent with a small tilt angle of the hydrocarbon chains (29° - 35°) in the h-POPE-KLA bilayer. In the h-POPE-KLA bilayer, $S_{\nu(C=O)}$ was negative. It depended on the

membrane potential (Figure 58d) and indicated that the ester carbonyl groups adopt a preferentially parallel orientation to the bilayer plane.[5]

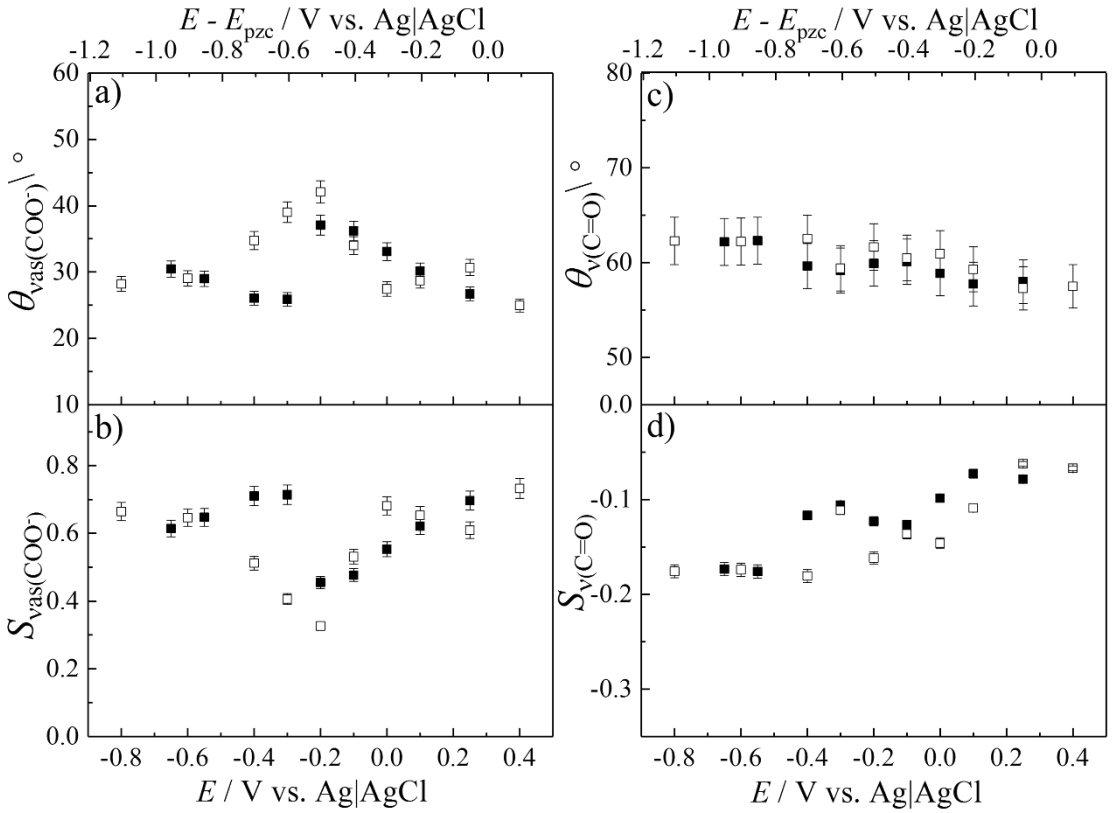

Figure 58: Plots of a) $\theta_{vas(COO^-)}$, b) $S_{vas(COO^-)}$, c) $\theta_{\nu(C=O)}$ and d) $S_{\nu(C=O)}$ vs. E and E - E_{pzc} in the h-POPE-KLA bilayer in 0.05 M $KClO_4$ + 0.005 M $Mg(ClO_4)_2$ in D_2O on the Au(111) electrode. Filled and opened points represent negative and positive going potential scans, respectively.

The results in section 5.2 show that LB-LS transfer allowed the deposition of an asymmetric POPE-KLA bilayer on the Au(111) electrode. An asymmetric POPE-KLA bilayer acted as a model of the OM of Gram-negative bacteria. The bottom leaflet (h-POPE or d-POPE) was in contact with the Au(111) surface, while the top leaflet (KLA) was exposed to an electrolyte solution. PM IRRAS measurements gave average orientation and packing of the hydrocarbon chains in the hydrophobic part of the h-POPE-KLA and d-POPE-KLA bilayers. The average orientation of the hydrocarbon chains in the h-POPE-KLA and d-POPE-KLA bilayers is shown in Figure 59. The average orientation of the hydrocarbon chains was potential-dependent for the h-POPE-KLA bilayer and was potential-independent for the d-POPE molecules in the d-POPE-KLA bilayer.

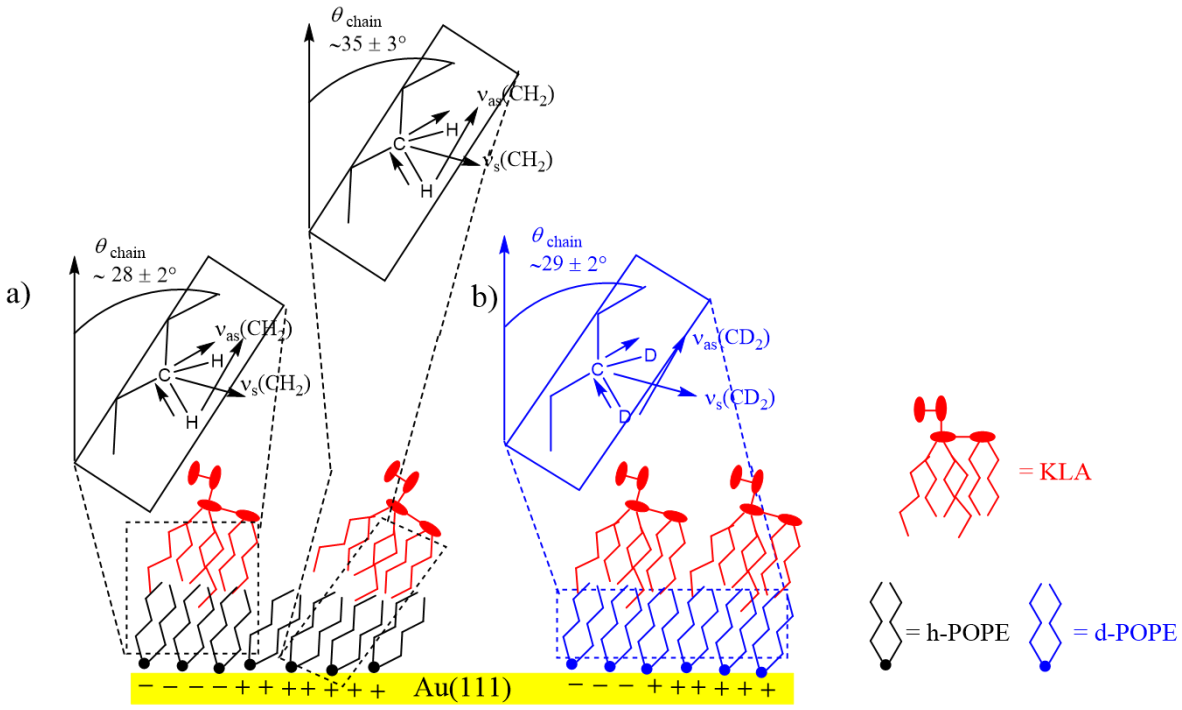

Figure 59: Average orientation of the hydrocarbon chains in a) the h-POPE-KLA bilayer and b) the d-POPE-KLA bilayer with respect to the surface normal in the two leaflets of the bilayer supported on the Au(111) electrode.

For the h-POPE-KLA bilayer, the average tilt angle was (35 ± 3)° for the hydrocarbon chains in the adsorbed state and slightly decreased to (28 ± 2)° in the desorbed state (Figure 59a). The tilt angle was (29 ± 2)° for the hydrocarbon chains in d-POPE molecules which was the same as in the desorbed state of the h-POPE-KLA bilayer (Figure 59).

5.3 Effect of melittin on the model of the outer membrane of Gram-negative bacteria

LB-LS transfer was used to deposit a model for the OM of Gram-negative bacteria on the Au(111) containing POPE in the inner and KLA in the outer leaflet. Structural changes occurring in the OM interacting with melittin as a function of the membrane potential are discussed below.

5.3.1 Electrochemical characterization of the model membrane interacting with melittin

Figure 60 shows C vs. E and E - E_{pzc} potential plots for the h-POPE-KLA bilayer on the Au(111) electrode in 0.1 M $KClO_4$ + 0.005 M $Mg(ClO_4)_2$ electrolyte solution after interaction with 10 µM and 1 µM melittin for 15 min. Interaction of melittin with the OM caused an increase in C_{min} (Figure 60 and Table 13).

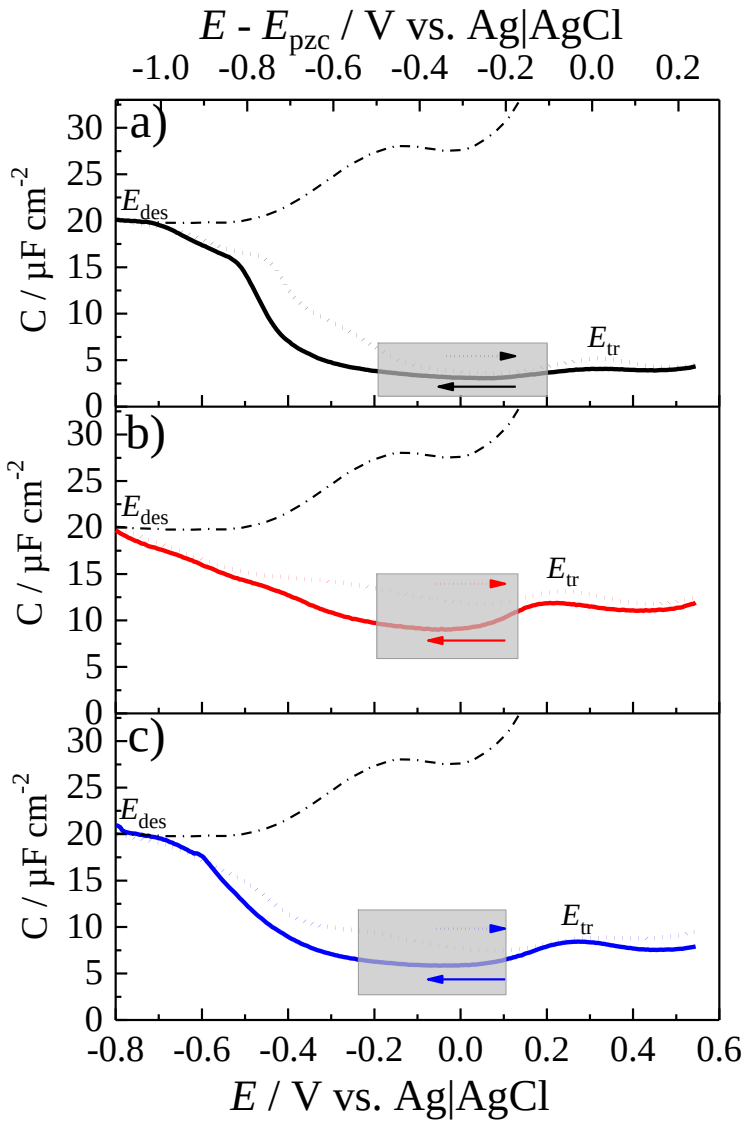

Figure 60: Plots of C vs. E and E - E_{pzc} potentials of a) the pure POPE-KLA bilayer, b) the POPE-KLA bilayer after interaction with 10 µM melittin for 15 min and c) the POPE-KLA bilayer after interaction with 1 µM melittin for 15 min. All model membranes were prepared on the Au(111) electrode and characterized in 0.1 M $KClO_4$ + 0.005 M $Mg(ClO_4)_2$ solution. Solid lines: negative, short dotted lines: positive going potential scans; dash dot black line: C of the unmodified Au(111) electrode. Gray marked fields show the potential range of C_{min}.

In addition, the membrane potential window of C_{min} decreased slightly after interaction with melittin. An increase in the C_{min} of the h-POPE-KLA bilayer upon interatction with melittin was already observed in literature.[36] In Table 13 the C_{min}, the membrane potential range of C_{min}, desorption potential and phase transitions of an OM interacting with melittin are listed. In the negative going potential scans, C_{min} was (5.8 ± 0.3) μF cm^{-2} for the h-POPE-KLA bilayer after its interaction with 1 μM melittin for 15 min, while it increased to (9.2 ± 0.2) μF cm^{-2} after interaction with 10 μM melittin for 15 min (Figure 60 and Table 13). A fast increase in the capacitance was observed at E - E_{pzc} < -0.50 V leading to the bilayer desorption at E - E_{pzc} < -1.1 V (Figure 60). In the h-POPE-KLA bilayer interacting with melittin, the potential of the phase transition (E_{tr}) underwent a negative shift, indicating a destabilization of the adsorbed state of the OM at E_{tr} < 0.305 V (Figure 60b, c). Becucci et al.[302] have pointed out that at negative membrane potential melittin forms a channel in the lipid bilayer. The desorption potentials of the OM did not change by interaction with melittin (Figure 60 and Table 13). Thus, the stability of the OM with bound melittin was not affected at negative membrane potentials, but it decreased at positive membrane potentials. Burgess et al.[19] have showed that the lipid molecules become permeable to an electrolyte solution at negative membrane potentials, causing the desorption of the bilayer from the metal surface.[19]

Table 13: Membrane potential of the bilayer desorption (E - $E_{pzc})_{des}$, C_{min} and the membrane potential window of the C_{min} , phase transitions (E - $E_{pzc})_{tr-}$ in the negative going potential scans and (E - $E_{pzc})_{tr+}$ in the positive going potential scans in the pure POPE-KLA bilayer and after its interaction with 10 μM and 1 μM melittin for 15 min.

Conc. of melittin / μM	(E - $E_{pzc})_{des}$ / V	C_{min} / μF cm^{-2}	(E - $E_{pzc})_{range}$ of C_{min} / V	(E - $E_{pzc})_{tr-}$ / V	(E - $E_{pzc})_{tr+}$ / V
0	-1.1	3.2 ± 0.2	-0.10 < E - E_{pzc} < -0.5	0.00	0.02
1	-1.1	5.8 ± 0.3	-0.26 < E - E_{pzc} < -0.5	-0.04	-0.01
10	-1.1	9.2 ± 0.2	-0.13 < E - E_{pzc} < -0.5	-0.10	-0.06

5.3.2 Effect of melittin on the orientation of the hydrocarbon chains in the model of the outer membrane of Gram-negative bacteria

Figure 61 shows background-corrected PM IRRA spectra of the pure h-POPE-KLA bilayer (Figure 61a) and the h-POPE-KLA bilayer after incubation in 10 μM melittin for 15 min (Figure 61b) and in 1 μM melittin for 1 h (Figure 61c). Methyl and methylene groups give four IR absorption modes for the OM of Gram-negative bacteria incubated in melittin. These modes are listed in Table 14.

Table 14: Wavenumber of the IR absorption bands of methyl and methylene groups in the h-POPE-KLA bilayer incubated in melittin on the Au(111) electrode surface.

Vibrational mode	Wavenumber / cm^{-1}
$\nu_{as}(CH_3)$	2954 ± 2
$\nu_{as}(CH_2)$	2924 ± 2
$\nu_{s}(CH_3)$	2871 ± 2
$\nu_{s}(CH_2)$	2853 ± 2

Interaction of melittin with the OM caused approximately 1 cm^{-1} bathochromic shift of methylene stretching modes (Figure 61). No significant change in the intensity of the methylene stretching modes was observed in the OM bound with melittin at potentials preceding the membrane desorption from the Au(111) electrode (Figure 61). Table 14 shows the position of the absorption maximum of $\nu_s(CH_2)$ and $\nu_{as}(CH_2)$ modes after interaction the h-POPE-KLA bilayer with melittin. It indicated that the hydrocarbon chains existed in the liquid state in the OM incubated in melittin (Table 14). After interaction of the OM with melittin, the integral intensities of methylene stretching modes were independent of the membrane potential. On the other hand, they were potential-dependent in the pure OM. Therefore, melittin interacted with the hydrocarbon chains region of the OM. The angle $\theta_{\nu(CH2)}$ was calculated between the electric field vector and the transition dipole moment of $\nu_s(CH_2)$ and $\nu_{as}(CH_2)$ in the OM incubated in melittin (Figure 62). In the OM incubated in 10 μM melittin for 15 min, the average $S_{\nu s(CH2)}$ was (-0.36 ± 0.03) (Figure 62b), which corresponding to tilt of (73 ± 3)° (Figure 62a). In the

OM incubated in 1 µM melittin for 1 h, $S_{vs(CH2)}$ was (-0.42 ± 0.02) (Figure 62d), which corresponding to tilt of (78 ± 3)° (Figure 62c).

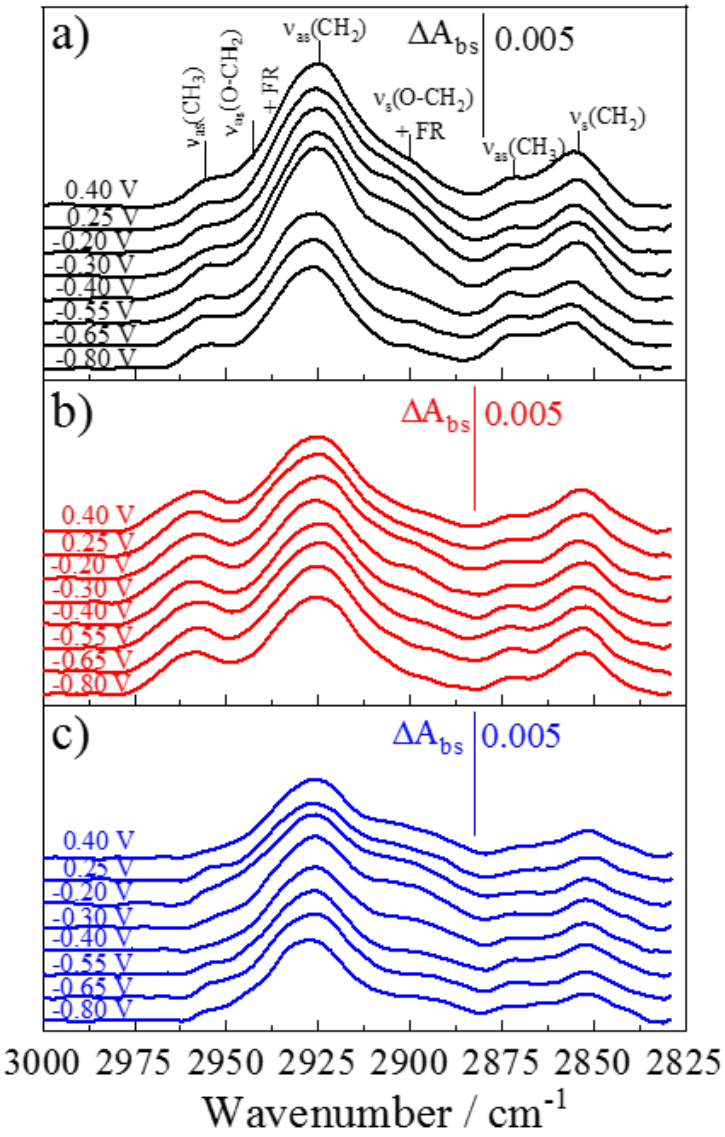

Figure 61: PM IRRA spectra in the 3000 - 2825 cm^{-1} spectral region of a) the pure h-POPE-KLA bilayer, b) after interaction the h-POPE-KLA bilayer with 10 µM melittin for 15 min and c) after interaction the h-POPE-KLA bilayer with 1 µM melittin for 1 h. The model membranes were prepared on the Au(111) electrode and characterized in 0.05 M $KClO_4$ + 0.005 M $Mg(ClO_4)_2$ in D_2O. The spectra shown in the figure were recorded in a negative going potential scan at potentials marked in the figure.

In the OM incubated in 10 µM melittin for 15 min, the average $S_{vas(CH2)}$ was (-0.21 ± 0.07) (Figure 63b), which corresponding to tilt of (62 ± 4)° (Figure 63a). In the OM incubated in 1 µM melittin for 1 h, $S_{vas(CH2)}$ was (-0.25 ± 0.04) (Figure 63d), which corresponding to tilt of (67 ± 4)° (Figure 63c).

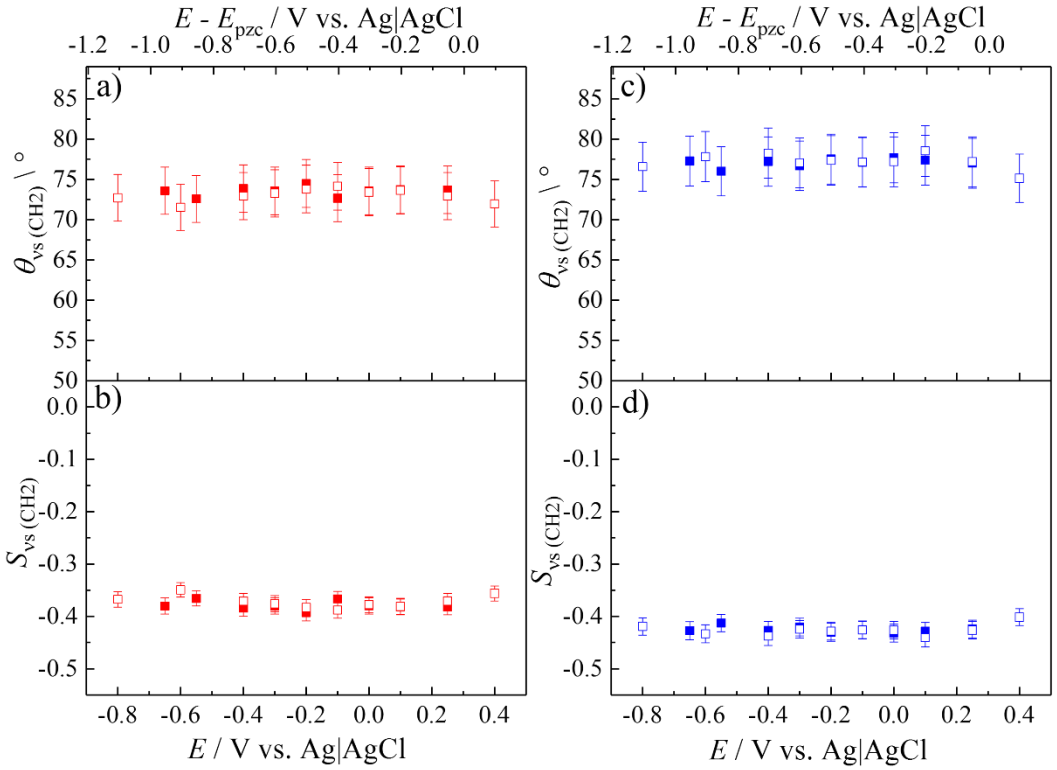

Figure 62: Plots of a), c) angle $\theta_{vs(CH2)}$ and b), d) the $S_{vs(CH2)}$ vs. E and E - E_{pzc} a), b) after interaction of the h-POPE-KLA bilayer with 10 µM melittin for 15 min and c), d) after interaction of the h-POPE-KLA bilayer with 1 µM melittin for 1 h. The model membranes were prepared on the Au(111) electrode and characterized in 0.05 M $KClO_4$ + 0.005 M $Mg(ClO_4)_2$ in D_2O. Filled and opened points represent negative and positive going potential scans, respectively.

Figure 64 shows the calculated S_{chain} in the studied OM incubated in melittin as a function of the electrode and membrane potentials. The angle θ_{chain} and S_{chain} of the OM incubated in melittin were independent of the membrane potential. S_{chain} was comparable for the OM incubated in melittin to S_{chain} of the pure OM. The average S_{chain} of the OM incubated in 10 µM melittin for 15 min in the membrane potential range -0.7 V < E - E_{pzc} < 0.1 V was (0.59 ± 0.02), indicating an average tilt of the hydrocarbon chains of (34 ± 2)° vs. the surface normal (Figure 64a, b). The average S_{chain} of the OM incubated in 1 µM melittin for 1 h was (0.69 ± 0.03), which corresponded to an average tilt of the hydrocarbon chains of (28 ± 2)° vs. the surface normal (Figure 64c, d). The packing order increased slightly for the hydrocarbon chains in the OM after incubation with melittin. Results of the h-POPE-KLA bilayer incubated with melittin are analogous to findings of Fery et al.[303] for POPC-POPC:POPG bilayers who found an increase in the packing order of the hydrocarbon chains after interaction of the POPC-POPC:POPG bilayers with melittin.

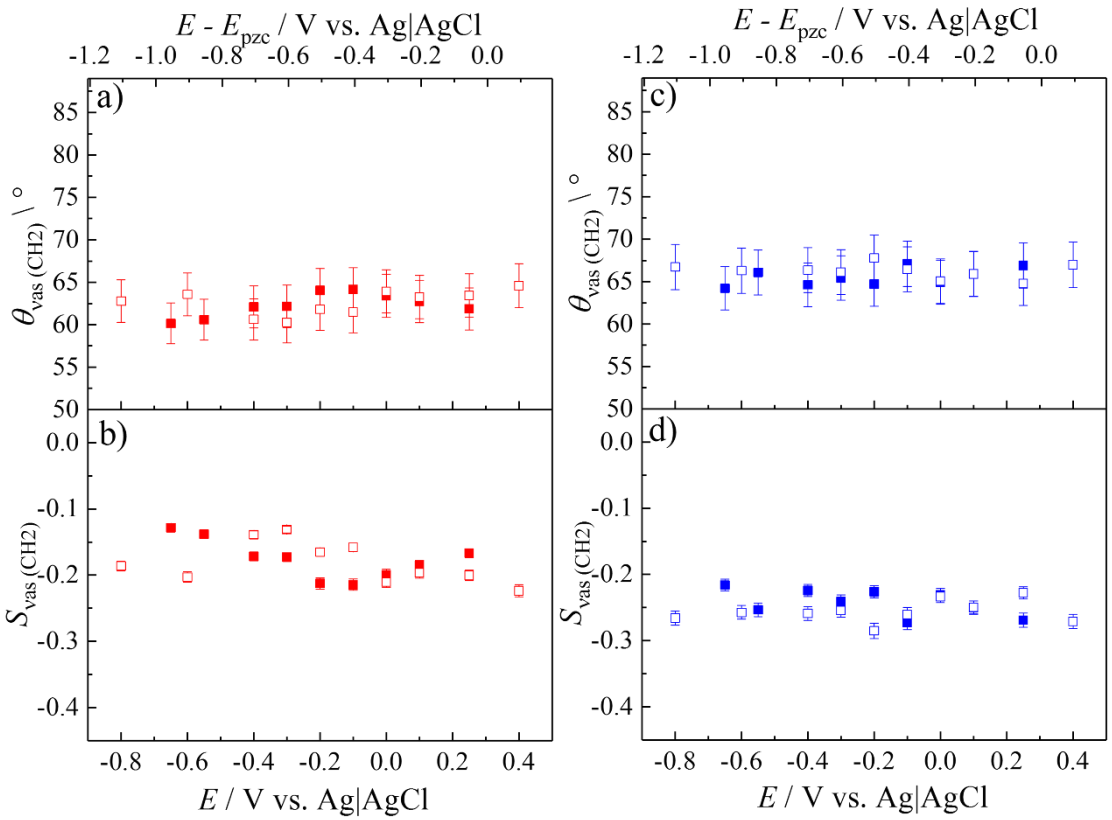

Figure 63: Plots of a), c) angle $\theta_{vas(CH2)}$ and b), d) $S_{vas(CH2)}$ vs. E and E - E_{pzc} a), b) after interaction of the h-POPE-KLA bilayer with 10 µM melittin for 15 min and c), d) after interaction of the h-POPE-KLA bilayer with 1 µM melittin for 1 h. The model membranes were prepared on the Au(111) electrode and characterized in 0.05 M $KClO_4$ + 0.005 M $Mg(ClO_4)_2$ in D_2O. Filled and opened points represent negative and positive going potential scans, respectively.

In order to learn more about the effect of melittin on the inner leaflet of the OM of Gram-negative bacteria, d-POPE was used with one per-deuterated hydrocarbon chain. Figure 65 shows PM IRRA spectra of the d-POPE-KLA bilayer after interaction of the bilayer with 10 µM melittin for 15 min and 1 µM melittin for 1 h. Methyl and methylene groups of the d-POPE-KLA bilayer incubated in melittin gave four IR absorption modes. These modes are listed in Table 15. It indicated that the hydrocarbon chains existed in a liquid state in the d-POPE-KLA bilayer incubated in melittin. No change in the intensity of the CD stretching modes in the d-POPE-KLA bilayer incubated in melittin was observed over the applied potential (Figure 65).

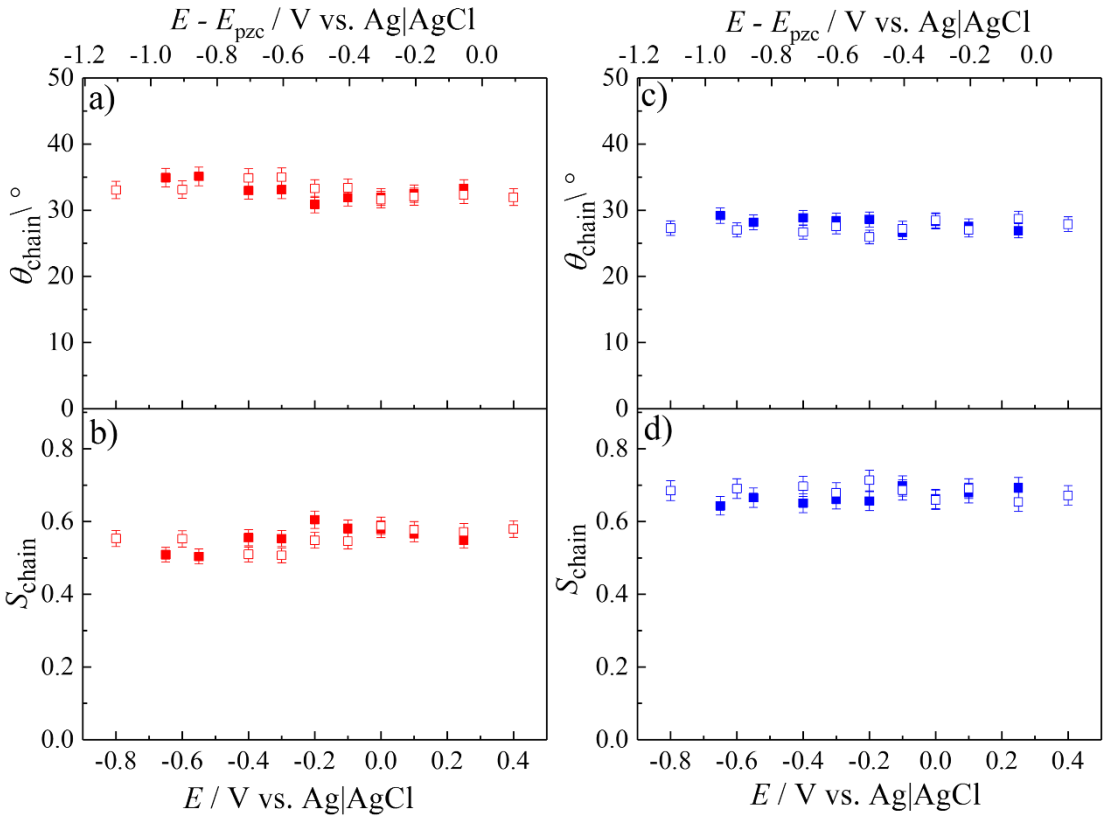

Figure 64: Plots of a), c) angle θ_{chain} and b), d) S_{chain} vs. E and E - E_{pzc} a), b) after interaction of the h-POPE-KLA bilayer with 10 µM melittin for 15 min and c), d) after interaction of the h-POPE-KLA bilayer with 1 µM melittin for 1 h. The model membranes were prepared on the Au(111) electrode and characterized in 0.05 M $KClO_4$ + 0.005 M $Mg(ClO_4)_2$ in D_2O. Filled and opened points represent negative and positive going potential scans, respectively.

Using the integral intensities of the ν(CD_2) modes, the angle $\theta_{\nu(CD2)}$ was calculated between the electric field vector and the transition dipole moments of $\nu_{as}(CD_2)$ and $\nu_s(CD_2)$ stretching modes in the d-POPE-KLA bilayer incubated with melittin (Figure 66). In the d-POPE-KLA bilayer incubated in 10 µM melittin for 15 min, the average angles $\theta_{\nu s(CD2)}$ and $\theta_{\nu as(CD2)}$ were (68 ± 4)° and (67 ± 3)°, respectively (Figure 66a, b), while in the d-POPE-KLA bilayer incubated in 1 µM melittin for 1 h, the average angles $\theta_{\nu s(CD2)}$ and $\theta_{\nu as(CD2)}$ were (69 ± 5)° and (68 ± 5)°, respectively (Figure 66c, d). The average angles $\theta_{\nu(CH2)}$ and $\theta_{\nu(CD2)}$ were the same in the d-POPE-KLA bilayer incubated in 10 µM melittin and 1 µM melittin. In addition, no change was obtained for the average angles $\theta_{\nu s(CD2)}$ and $\theta_{\nu as(CD2)}$ in the pure d-POPE-KLA bilayer and the d-POPE-KLA bilayer incubated in melittin.

Table 15: Wavenumber of the IR absorption bands of methyl and methylene groups in the d-POPE-KLA bilayer incubated in melittin on the Au(111) electrode surface.

Vibrational mode	Wavenumber / cm^{-1}
$\nu_{as}(CD_3)$	2213 ± 1
$\nu_{as}(CD_2)$	2197 ± 1
$\nu_s(CD_3)$	2117 ± 1
$\nu_s(CD_2)$	2096 ± 2

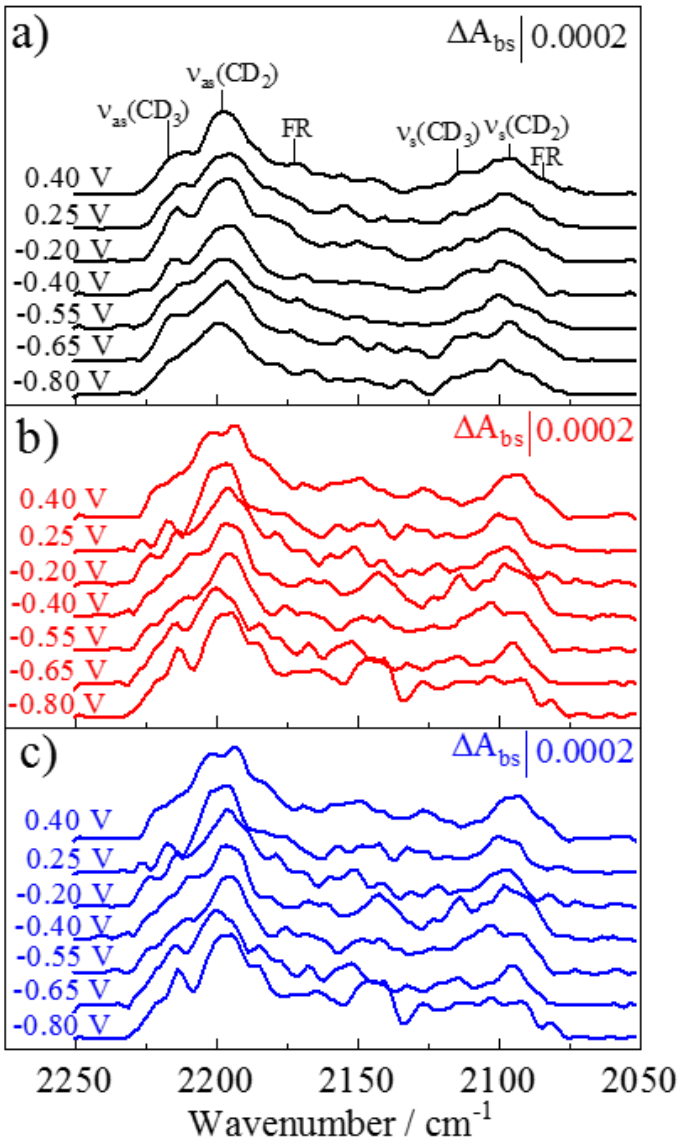

Figure 65: PM IRRA spectra in the 2280 - 2050 cm^{-1} spectral region of a) the pure d-POPE-KLA bilayer, b) after interaction of the d-POPE-KLA bilayer with 10 µM melittin for 15 min and c) after interaction of the d-POPE-KLA bilayer with 1 µM melittin for 1 h. The model membranes were prepared on the Au(111) electrode and characterized in 0.05 M $KClO_4$ + 0.005 M $Mg(ClO_4)_2$ in H_2O. The spectra shown in the figure were recorded in a negative going potential scan at potentials marked in the figure.

Figure 67 shows the calculated $S_{\nu(CD2)}$ for the d-POPE-KLA bilayer incubated in melittin as a function of the electrode and membrane potentials. In the d-POPE-KLA bilayer incubated in melittin, the average $S_{\nu(CD2)}$ were negative. In the d-POPE-KLA bilayer incubated in 10 µM melittin for 15 min, the average $S_{\nu s(CD2)}$ and $S_{\nu as(CD2)}$ were (-0.30 ± 0.05) and (-0.25 ± 0.05), respectively (Figure 67a, b).

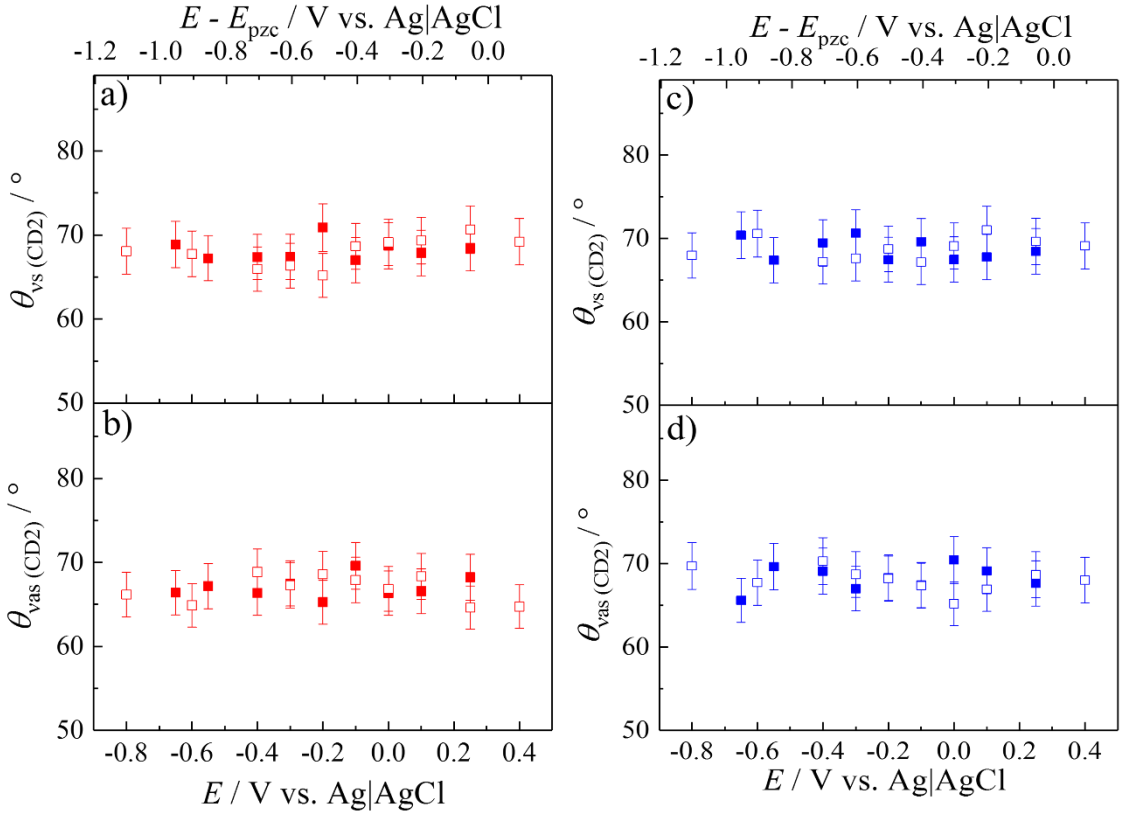

Figure 66: Plots of angles a), c) $\theta_{\nu s(CD2)}$ and b), d) $\theta_{\nu as(CD2)}$ vs. E and E - E_{pzc} a), b) after interaction of the d-POPE-KLA bilayer with 10 µM melittin for 15 min and c), d) after interaction of the d-POPE-KLA bilayer with 1 µM melittin for 1 h. The model membranes were prepared on the Au(111) electrode and characterized in 0.05 M $KClO_4$ + 0.005 M $Mg(ClO_4)_2$ in H_2O. Filled and opened points represent negative and positive going potential scans, respectively.

In the d-POPE-KLA bilayer incubated in 1 µM melittin for 1 h, the average $S_{\nu s(CD2)}$ and $S_{\nu as(CD2)}$ were (-0.30 ± 0.04) and (-0.29 ± 0.06), respectively (Figure 67c, d). Figure 68 shows the calculated angle θ_{chain} and S_{chain} of the d-POPE-KLA bilayer incubated in 10 µM melittin and 1 µM melittin as a function of the electrode and membrane potentials. In the d-POPE-KLA bilayer incubated in 10 µM melittin for 15 min, S_{chain} was (0.55 ± 0.05), which corresponded to the tilt of (34 ± 3)° (Figure 68a, b).

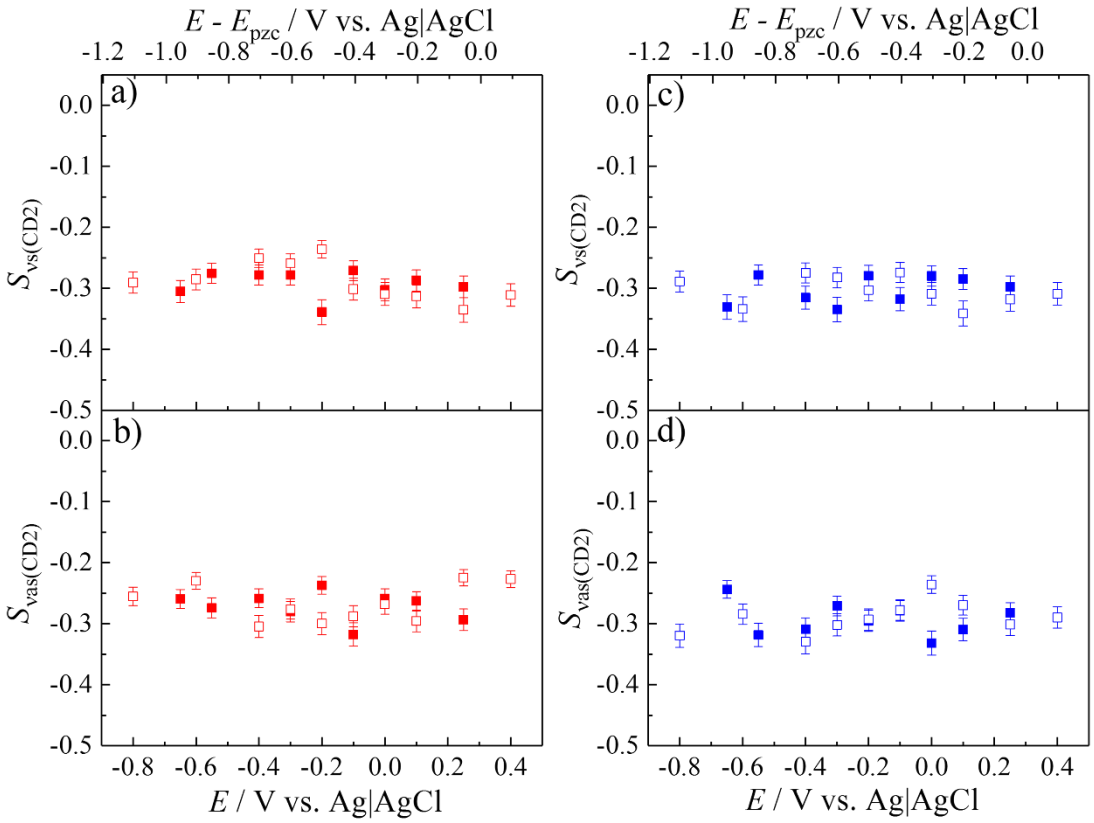

Figure 67: Plots of a), c) $S_{vs(CD2)}$ and b), d) $S_{vas(CD2)}$ vs. E and E - E_{pzc} a), b) after interaction of the d-POPE-KLA bilayer with 10 µM melittin for 15 min and c), d) after interaction of the d-POPE-KLA bilayer with 1 µM melittin for 1 h. The model membranes were prepared on the Au(111) electrode and characterized in 0.05 M $KClO_4$ + 0.005 M $Mg(ClO_4)_2$ in H_2O. Filled and opened points represent negative and positive going potential scans, respectively.

In the d-POPE-KLA bilayer after its interaction with 1 µM melittin for 1 h, S_{chain} was (0.60 ± 0.05) and indicated an average tilt of the hydrocarbon chains of (32 ± 4)° vs. the surface normal (Figure 68c, d). The orientation of the hydrocarbon chains was insensitive to the membrane potentials. This kind of behavior was already reported in literature for the POPC-cholesterol bilayer incubated in 1 µM cecropin B.[304] Cecropin B did not show any pronounced effect on the POPC-cholesterol bilayer.[304] S_{chain} of the d-POPE-KLA bilayer incubated in melittin were slightly lower than S_{chain} of the pure d-POPE-KLA bilayer adsorbed directly on the Au(111) surface (0.65 ± 0.03). This result indicated a small decrease in the packing orders of the hydrocarbon chains in the bilayer incubated in melittin.

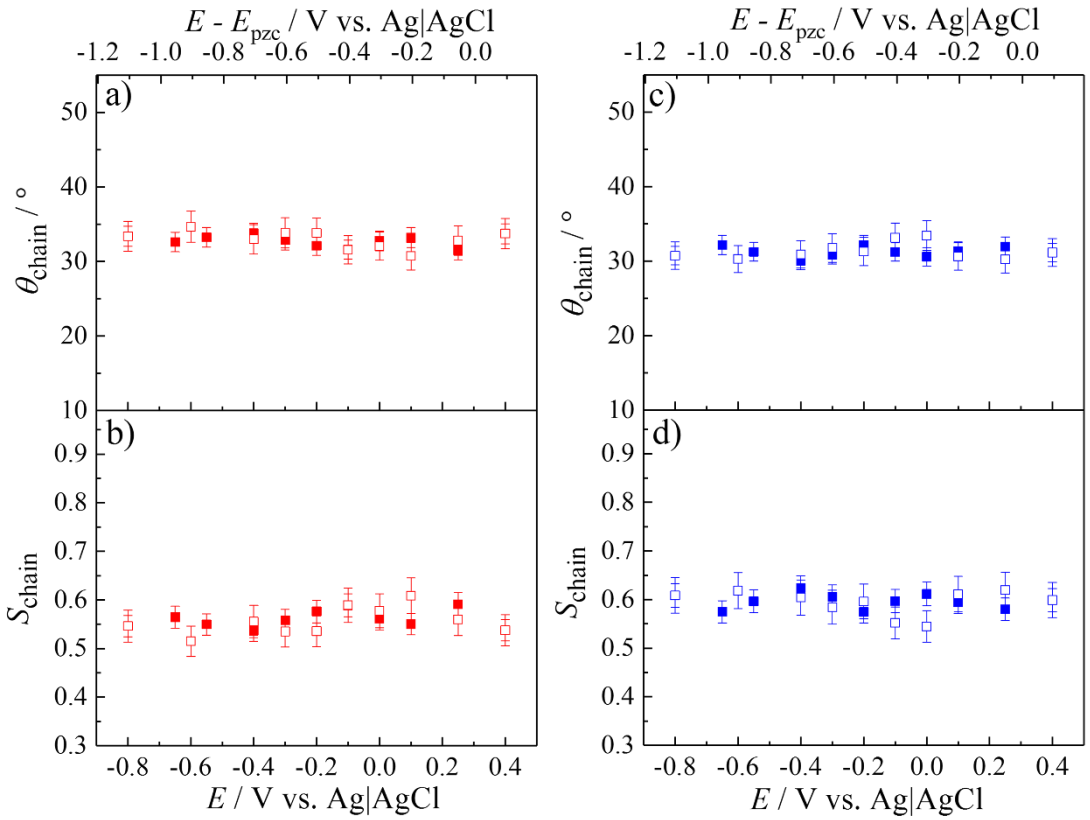

Figure 68: Plots of a), c) θ_{chain} and b), d) S_{chain} vs. E and E - E_{pzc} a), b) after interaction of the d-POPE-KLA bilayer with 10 µM melittin for 15 min and c), d) after interaction of the d-POPE-KLA bilayer with 1 µM melittin for 1 h. The model membranes were prepared on the Au(111) electrode and characterized in 0.05 M $KClO_4$ + 0.005 M $Mg(ClO_4)_2$ in H_2O. Filled and opened points represent negative and positive going potential scans, respectively.

5.3.3 Effect of melittin on the orientation and hydration of the polar head groups in the model of the outer membrane of Gram-negative bacteria

Figure 69 shows the background-corrected PM IRRA spectra in the 1830 - 1500 cm^{-1} spectral region of the pure h-POPE-KLA bilayer and after its interaction with melittin on the Au(111) electrode. Three IR absorption modes were obtained in this spectral region. The ester carbonyl mode ν(C=O) in POPE and KLA was located at 1733 cm^{-1}. In the pure h-POPE-KLA bilayer, the deconvolution of the ester carbonyl mode gave three components at (1738 ± 2) cm^{-1}, (1718 ± 4) cm^{-1} and (1708 ± 2) cm^{-1} (Figure 70a).

In the OM incubated in 10 µM melittin, the deconvolution of this band gave two components at (1736 ± 3) cm^{-1} and (1715 ± 4) cm^{-1} (Figure 70b). However, incubation of

the OM in 1 μM melittin gave three different ν(C=O) modes at (1739 ± 1) cm^{-1}, (1721 ± 3) cm^{-1} and (1711 ± 2) cm^{-1} (Figure 70c, d).

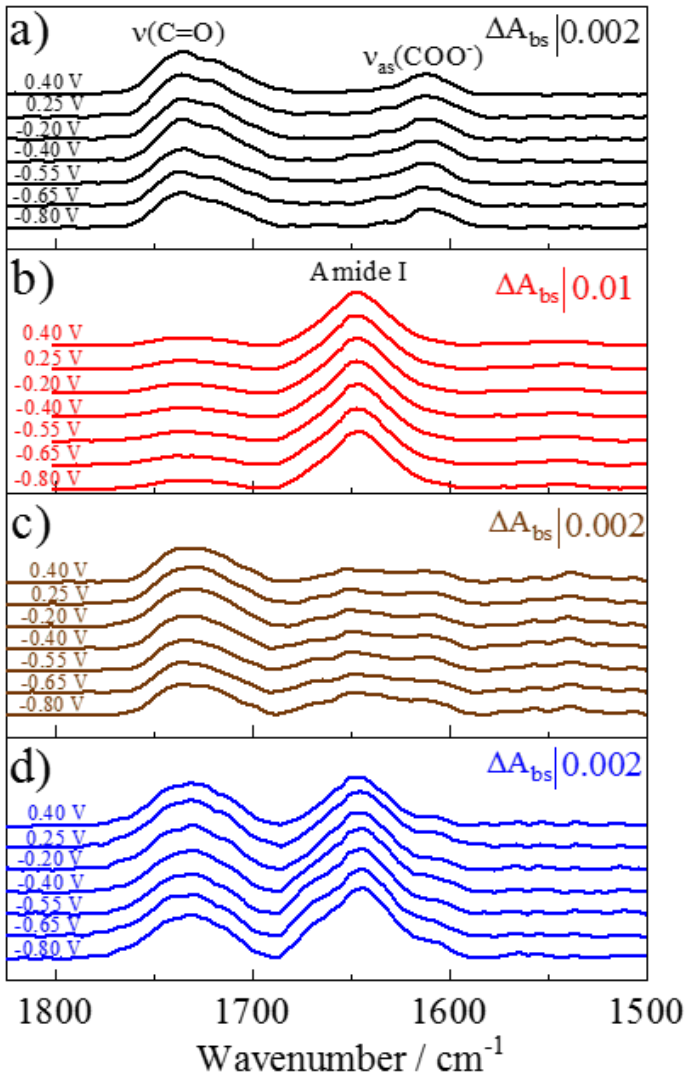

Figure 69: PM IRRA spectra in the 1830 - 1500 cm^{-1} spectral region of a) the pure h-POPE-KLA bilayer, b) the h-POPE-KLA bilayer after its interaction with 10 μM melittin for 15 min, c) the h-POPE-KLA bilayer after its interaction with 1 μM melittin for 15 min and d) the h-POPE-KLA bilayer after its interaction with 1 μM melittin for 1 h. The model membranes were prepared on the Au(111) electrode and characterized in 0.05 M $KClO_4$ + 0.005 M $Mg(ClO_4)_2$ in D_2O. The spectra shown in the figure were recorded in a negative going potential scan at potentials marked in the figure.

A change in the hydration of the ester carbonyl groups was observed in the lipids in the OM after its interaction with melittin. The amide I band of melittin was centered at (1646 ± 2) cm^{-1}, confirming that melittin was bound to the h-POPE-KLA bilayer. The intensity and shape of amide I band depended on the concentration and incubation time of the OM in melittin-containing solution (Figure 69 b-d).

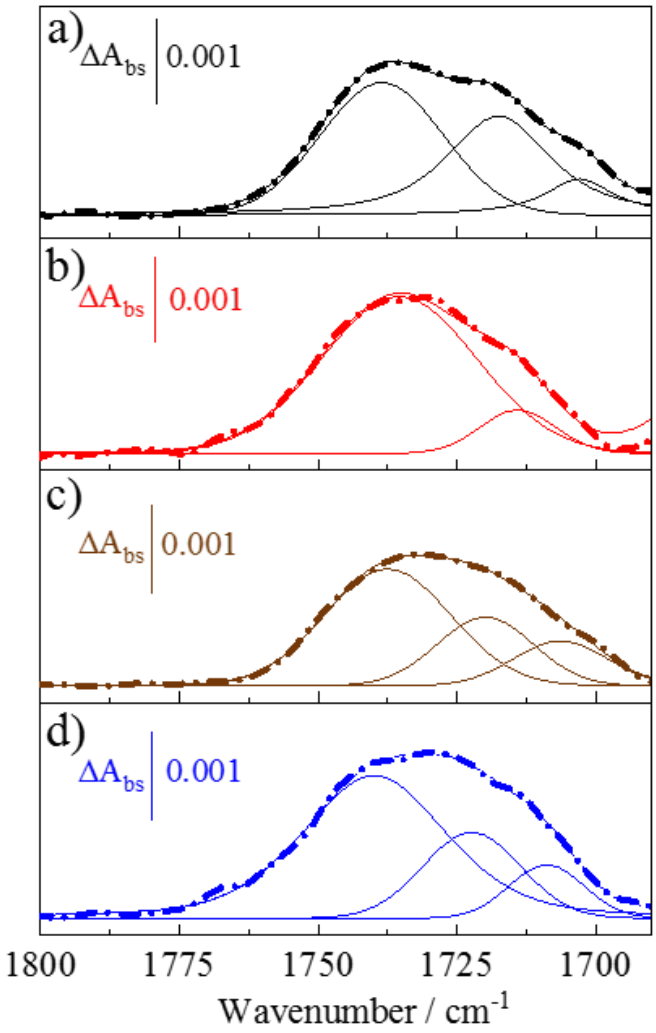

Figure 70: Deconvoluted PM IRRA spectra in ν(C=O) mode region of a) the pure h-POPE-KLA bilayer, b) the h-POPE-KLA bilayer after its interaction with 10 µM melittin for 15 min, c) the h-POPE-KLA bilayer after its interaction with 1 µM melittin for 15 min and d) the h-POPE-KLA bilayer after its interaction with 1 µM melittin for 1 h. The model membranes were prepared on the Au(111) electrode and characterized in 0.05 M $KClO_4$ + 0.005 M $Mg(ClO_4)_2$ in D_2O at E = 0 V vs. Ag|AgCl. Colored dashed lines: envelope spectrum, black thin lines: measured and deconvoluted modes.

Interaction of the pure h-POPE-KLA bilayer with melittin caused changes in this spectral region. The $\nu_{as}(COO^-)$ mode was shifted to (1609 ± 3) cm^{-1} after interaction of the OM with 10 µM melittin for 15 min (Figure 71a). After the incubation of the OM in 1 µM melittin for 15 min and for 1 h, the $\nu_{as}(COO^-)$ mode shifted to (1611 ± 3) cm^{-1} (Figure 71b) and to (1606 ± 2) cm^{-1} (Figure 71c), respectively. Indeed, the coordination and the hydration of the carbonyl groups changed significantly after interaction of the OM with melittin. The position of $\nu_{as}(COO^-)$ mode differed in the OM after its interaction with

melittin compared to the pure OM, suggesting that the carboxylate groups formed hydrogen bonds to the amine groups of melittin.

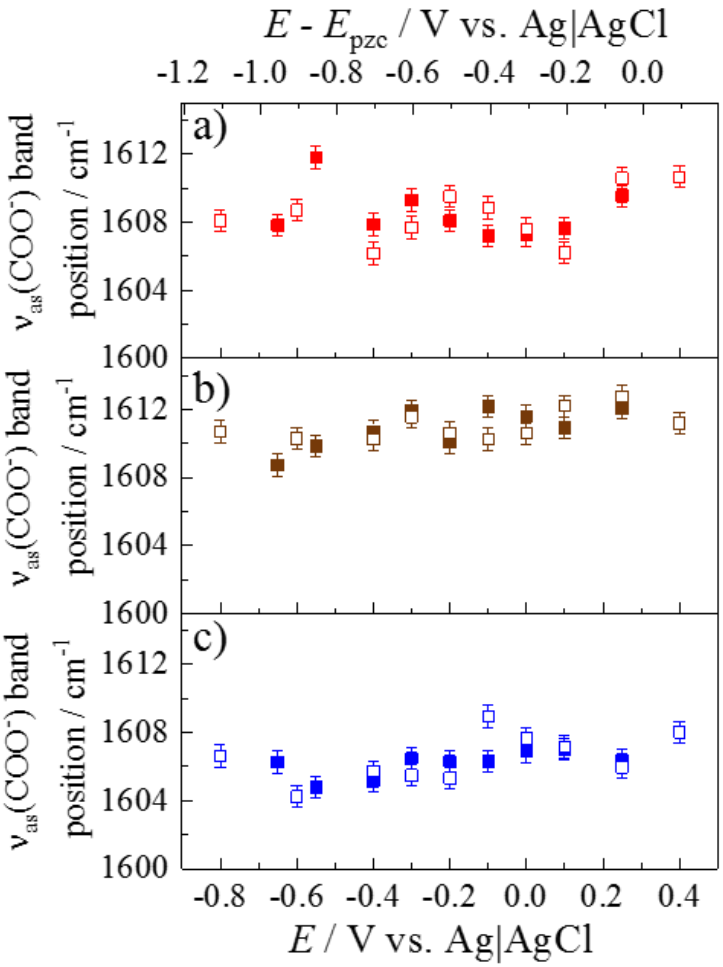

Figure 71: Position of the absorption maximum of $\nu_{as}(COO^-)$ mode vs. E and E - E_{pzc} in a) the h-POPE-KLA bilayer after its interaction with 10 µM melittin for 15 min, b) the h-POPE-KLA bilayer after its interaction with 1 µM melittin for 15 min and c) the h-POPE-KLA bilayer after its interaction with 1 µM melittin for 1 h. The model membranes were prepared on the Au(111) electrode and characterized in 0.05 M $KClO_4$ + 0.005 M $Mg(ClO_4)_2$ in D_2O. Filled and opened points represent negative and positive going potential scans, respectively.

Figure 72 shows $\theta_{vas(COO^-)}$ and $S_{vas(COO^-)}$ for the asymmetric stretching modes of the carboxylic groups between the electric field vector and the transition dipole moments of these modes in the OM after its interaction with melittin. In the adsorbed state of the h-POPE-KLA bilayer after its interaction with 10 µM melittin for 15 min (-0.7 V < E - E_{pzc} < 0.1 V), the average $S_{vas\ (COO^-)}$ was (-0.15 ± 0.06), which corresponding to the tilt of

(65 ± 4) °. In the desorbed state (-1.1 V < E - E_{pzc} < -0.8 V), the average $S_{vas\ (COO^-)}$ was (0.20 ± 0.05), which corresponding to the tilt of (48 ± 5)° (Figure 72a, d).

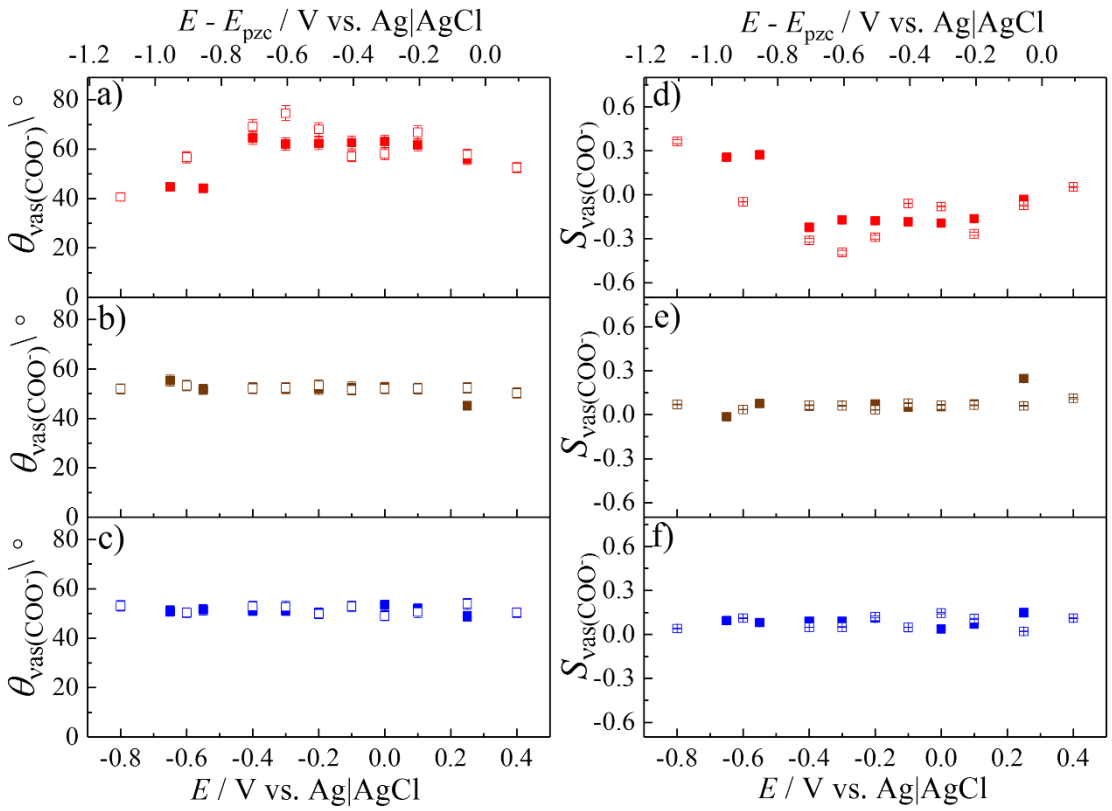

Figure 72: Plots of a), b), c) $\theta_{vas(COO^-)}$ and d), e), f) $S_{vas(COO^-)}$ vs. E and E - E_{pzc} in a), d) the h-POPE-KLA bilayer after its interaction with 10 μM melittin for 15 min, b), e) the h-POPE-KLA bilayer after its interaction with 1 μM melittin for 15 min and c), f) the h-POPE-KLA bilayer after its interaction with 1 μM melittin for 1 h. The model membranes were prepared on the Au(111) electrode and characterized in 0.05 M $KClO_4$ + 0.005 M $Mg(ClO_4)_2$ in D_2O. Filled and opened points represent negative and positive going potential scans, respectively.

In the case of the OM interacting with 1 μM melittin for 15 min and 1 h, the average $S_{vas(COO^-)}$ did not depend on the electrode and membrane potentials (Figure 72e, f). The average $S_{vas\ (COO^-)}$ were (0.10 ± 0.05) (Figure 72e) and (0.14 ± 0.03) (Figure 72f), which corresponding to the tilt of (50 ± 2)° (Figure 72b) and (51 ± 2)° (Figure 72c), respectively. The interaction of the OM with melittin caused a significant decrease in $S_{vas(COO^-)}$ compared to the pure OM. In the OM after its interaction with 1 μM and 10 μM melittin, the average $S_{v(C=O)}$ were negative and did not depend on the electrode and membrane potentials (Figure 73d-f).

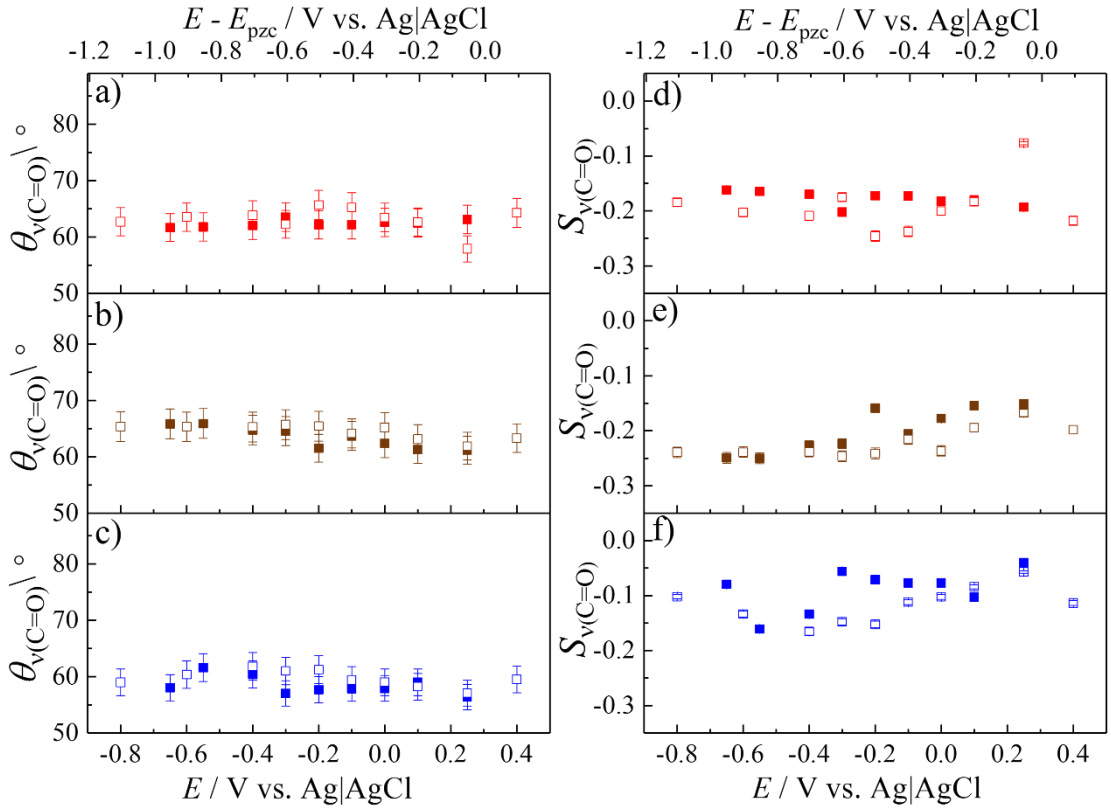

Figure 73: Plots of a), b), c) $\theta_{\nu(C=O)}$ and d), e), f) $S_{\nu(C=O)}$ vs. E and E - E_{pzc} in a), d) the h-POPE-KLA bilayer after its interaction with 10 μM melittin for 15 min, b), e) the h-POPE-KLA bilayer after its interaction with 1 μM melittin for 15 min and c), f) the h-POPE-KLA bilayer after its interaction with 1 μM melittin for 1 h. The model membranes were prepared on the Au(111) electrode and characterized in 0.05 M $KClO_4$ + 0.005 M $Mg(ClO_4)_2$ in D_2O. Filled and opened points represent negative and positive going potential scans, respectively.

Exposure of the OM to melittin caused orientation changes in the ester carbonyl ν(C=O) groups. In the OM after its interaction with 10 μM melittin, the average $S_{\nu(C=O)}$ was (-0.19 ± 0.04), giving an average angle $\theta_{\nu(C=O)}$ of (64 ± 4)° between the direction of the C=O bonds and the surafce normal (Figure 73a, d). After longer incubation time (1 h) of the OM in 1 μM melittin, a decrease in the $S_{\nu(C=O)}$ to (-0.11 ± 0.05) was observed (Figure 73f), giving an average angle $\theta_{\nu(C=O)}$ of (59 ± 5°) (Figure 73c). A negatively charged h-POPE-KLA bilayer underwent significant structural changes after exposure to melittin. The results showed that lipids were involved in the interaction with melittin in both leaflets (h-POPE and KLA) of the OM. Melittin interacted electrostatically with carboxylate groups in the inner core of KLA and this interaction caused changes in the hydration and orientation of the carboxylate groups of the OM. Balusek et al.[305] demonstrated that the sugar, carboxylate and phosphate groups in the inner core of KLA

are able to form hydrogen bonds to arginin, lysine and tryptophan amino acids of membrane TonB-dependent transporter proteins leading to high affinity binding with the asymmetric OM of Gram-negative bacetria. Lysine, arginine and glutamine amino acids in melittin are involved in the formation of the hydrogen bonds with carboxylate groups in the inner core of KLA.[44] These results indicated that melittin was able to make hydrogen bonds to the carboxylate groups in the inner core of KLA. An increase in the tilt of the carboxylate group was reported at desorption membrane potentials in the h-POPE-KLA bilayer. Thus, the carboxylate groups in the outer leaflet have well-defined orientation in the POPE-KLA bilayer. The interaction of the bilayer with melittin introduced large reorientations of the carboxylate groups in the inner core of the KLA. Melittin interacted directly with the inner core of the KLA and this direct interaction anchored melittin to the h-POPE-KLA bilayer. Melittin interacted not only with the polar head group in KLA but also with the hydrophobic region of the h-POPE-KLA bilayer. *In situ* PM IRRAS results showed that the order parameter of the hydrocarbon chains changed in the h-POPE-KLA bilayer after its interaction with melittin. On the other hand, no changes were reported in the packing and orientation of $\nu(CD_2)$ stretching modes in the d-POPE-KLA bilayer after its interaction with melittin. The hydration of the ester carbonyl groups changed in the h-POPE-KLA bilayer after its interaction with melittin. However, the orientation and hydrogen bond network changed drastically for the carboxylate groups in KLA in the h-POPE-KLA bilayer after its interaction with melittin. Electrochemical results indicated an increase in the membrane capacitance after interaction of the h-POPE-KLA bilayer with melittin. The electrostatic interactions were stabilized between melittin and negatively charged h-POPE-KLA bilayer at negative membrane potentials and weakened at positive membrane potentials. It could be connected with the insertion of melittin into the hydrophobic membrane fragment. Sek et al.[43] showed that significant changes were reported in AFM topography images after exposure of the DMPG and DMPS bilayers to 10 μM melittin.[43] The DMPG bilayer film appeared to be more affected by the interaction with melittin compared to the DMPS bilayer.[43] Exposure of the DMPS bilayer to 10 μM melittin for 12 h did not lead to rupture of the DMPS bilayer, but caused a formation of some defects.[43] The structure became less compact for the DMPG bilayer after its interaction with 10 μM melittin for 12 h and some defects were reported in the bilayer.[43] Such behavior reflected initial adsorption of

melittin on the bilayer and further insertion which caused a formation of pores or partial micellization of the lipid bilayer. Thus, melittin showed some selectivity with respect to the composition of the lipid bilayer. Figure 74 shows a schematic representation of the h-POPE-KLA (Figure 74a) and d-POPE-KLA (Figure 74b) bilayers after its interaction with melittin. Results indicated that the use of realistic models of the OM of Gram-negative bacteria was essential to understand the molecular-level behavior of the reaction of microorganisms to melittin.

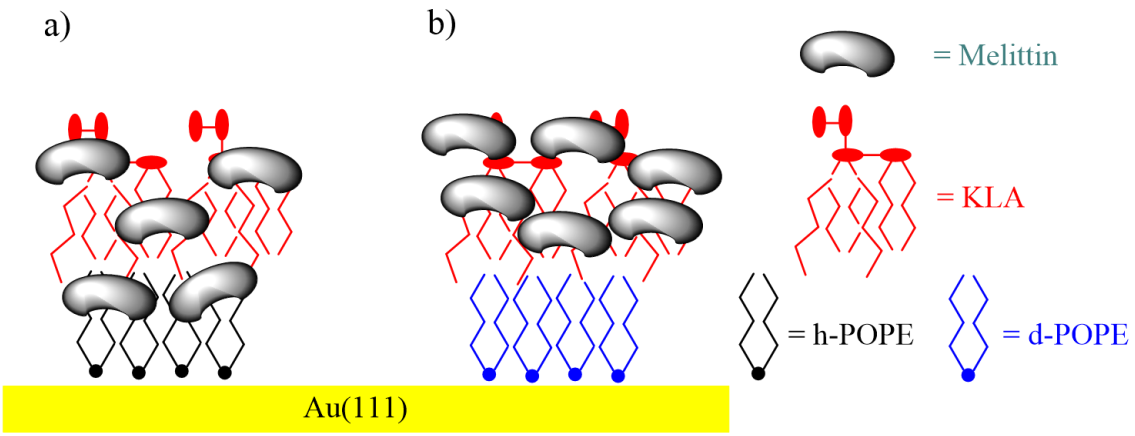

Figure 74: Schematic representation of a) the h-POPE-KLA bilayer and b) the d-POPE-KLA bilayer exposed to melittin on the Au(111) electrode.

6 Conclusions and Outlook

LB-LS transfer allowed the deposition of bilayers with transverse asymmetry on a solid surface. The structure of the lipid molecules has a large impact on the molecular-scale order in the model membranes of Gram-negative bacteria. The capacitance depended on the potential drop across the membrane. Water flow through the membrane and water circulation depended on both the electrode potential and the structure of the lipid molecules in the polar head group region of the bilayer. The calculation of the packing parameter of the lipid molecules facilated understanding of the molecular-scale behavior of lipid bilayers at electrified interfaces. Results showed two different types of structural rearrangements caused by the electric potentials. An abrupt flow of water into the DMPE-DMPG bilayer was accompanied by a dehydration of the polar head group region and reorientation of the hydrocarbon chains. The presence of POPE or DOPE lipids caused an increase in the hydration of the polar region of the membrane in the inner leaflet of the lipid bilayer. Water circulated in the hydrophilic fragment of the membrane at membrane potentials deviating from the capacitance minimum. Less water and less negative membrane potentials (at E - E_{pzc} = -0.50 V) were required to lift the membrane from the gold surface and to form a water cushion between the bilayer and the electrode. Smaller changes were reported in the QCM-D frequency response with increasing unsaturation of lipids. Water flow into the interfacial region between the electrode and the lipid bilayer led to a dehydration of the polar head groups.

The average orientation of the hydrocarbon chains was potential-dependent for the h-POPE-KLA bilayer and was potential-independent for the d-POPE molecules in the d-POPE-KLA bilayer. Thus, the observed variations in the intensities of the CH stretching modes arose from reorientations of the hydrocarbon chains in KLA.

The OM of Gram-negative bacteria interacting with AMPs represented a complex supramolecular assembly. The electrochemical and PM IRRAS results indicated that the use of realistic microbial cell membrane models was essential to understand the molecular-level response of the cell membrane to AMPs. The orientation of the lipid molecules in the pure h-POPE-KLA bilayer was dependent on the membrane potentials. The electric potentials caused changes in the packing and orientation of the hydrocarbon chains in the pure h-POPE-KLA bilayer. An increase in the membrane capacitance was

observed due to the insertion of melittin into the h-POPE-KLA bilayer. Differences between the 10 μM and 1 μM melittin on the h-POPE-KLA bilayer were found. Melittin interacted electrostatically with carboxylate groups in KLA, involving changes in the hydration and orientation of the carboxylate groups. The packing of the hydrocarbon chains was affected by the interaction of the h-POPE-KLA bilayer with melittin. S_{chain} decreased after interaction of the h-POPE-KLA bilayer with melittin. The hydration of the ester carbonyl groups changed in the h-POPE-KLA bilayer after its interaction with melittin.

To elucidate the mechanism of action of melittin on the OM of Gram-negative bacteria, studies of the orientation of bound melittin when the OM is exposed to changing electric fields are necessory. The amdie I mode indicated that the OM associated melittin underwent conformation and orientation changes. In the future work the secondary structure of melittin as a function of the membrane potential could be characterized. Selection of other AMPs (e.g., cecropin B, alamethicin) has to be studied in the future work to distinguish the action mechanism of these AMPs with the OM of Gram-negative bacteria.

7 Appendix

7.1 Abbreviations

AC	Alternating current
ACV	Alternating current voltammetry
AFM	Atomic force microscopy
AMPs	Antimicrobial peptides
BAM	Brewster angle microscopy
CE	Counter electrode
DMPC	1,2-dimyristoyl-*sn*-glycerol-3-phoshocholine
DMPE	1,2-dimyristoyl-*sn*-glycerol-3-phoshoethanolamine
DMPG	1,2-dimyristoyl-*sn*-glycerol-3-phoshoglycerol
DMPS	1,2-ditetradecanoyl-*sn*-glycero-3-phospho-L-serine (sodium salt)
DOPC	1,2-dioleoyl-*sn*-glycero-3-phosphocholine
DOPE	1,2-diplamitoleoyl-*sn*-glycero-3-phosphoethanolamine
DPhPC	1,2-di-O-phytanyl-*sn*-glycero-3-phosphocholine
DPPC	1,2-dipalmitoyl-*sn*-glycero-3-phosphocholine
DPPE	1,2-dipalmitoyl-*sn*-glycero-3-phosphorylethanolamine
DPPG	1,2-diplamitoyl-*sn*-glycero-3-phospho-(1`rac glycerol) (sodium salt)
DSPE	1,2-distearoyl-*sn*-glycero-3-phosphorylethanolamine
d-DMPC	1,2-dimyristoyl-d54-*sn*-glycerol-3-phoshocholine
d-POPE	1-palmitoyl-d31-2-oleoyl-*sn*-glycero-3-phosphoethanolamine
EDTA	Ethylenediaminetetraacetic acid-sodium salt dihydrate
EmrE	Ethidium multidrug resistant protein
FR	Fermi resonance
FTIR	Fourier-transform infrared spectroscopy
G-phase	Gaseous phase
GIXD	Grazing incidence X-ray diffraction
IM	Inner membrane
IR	Infrared
IRRAS	Infrared reflection absorption spectroscopy
IRS	Infrared spectroscopy
Kdo	3-deoxy-D-manno-octonate
KLA	Di [3-deoxy-D-manno-octulosonyl]- lipid A (ammonium salt) Kdo_2-Lipid A
LB-LS	Langmuir Blodgett and Langmuir Schaefer
L_α	Liquid phase
L_β	Gel phase
LC	Liquid condensed
LE	Liquid expanded

LPS	Lipopolysaccharides
ND	Neutron diffraction
NR	Neutron reflectometry
OM	Outer membrane
PC	Phosphocholine
PE	Phosphoethanolamine
PEM	Photoelastic modulator
PG	Phosphoglycerol
PM IRRAS	Polarization modulation infrared reflection absorption spectroscopy
POPE	1-palmitoyl-2-oleoyl-s*n*-glycero-3-phosphoethanolamine
POPG	1-plamitoyl-2-oleoyl-s*n*-glycerol-3-phospho-(1`rac glycerol) (sodium salt)
PP	Packing parameter
PS	Phosphoserine
QCM-D	Quartz crystal microbalance with energy dissipation
RE	Reference electrode
S-phase	Solid phase
SUVs	Small unilamellar vesicles
TR	Transfer ratio
TRIS	Tris (hydroxyl methyl) aminomethane
WE	Working electrode
XR	X-ray reflectivity

7.2 Symbols

A	Area per molecule
$\hat{A}$	Amplitude
A_{bs}	Absorbance
A_{chain}	Critical area of the hydrocarbon chain
$A_{h\text{-}g}$	Cross-sectional area at the hydrophilic-hydrophobic interface
A_{lim}	Limiting area
A_o	Lift-off area
A_t	Area per molecule at the surface pressure of the monolayer transfer
a	Area of electrode surface
C	Capacitance
C_{min}	Capacitance minimum
c^{Analyte}	Molar concentration of the analyte in the solution
D	Energy dissipation
d	Thickness
E	Potential
$\vec{E}$	Electric field vector

$E - E_{pzc}$	Membrane potential
E_{pzc}	Potential of zero charge
F	Force
f	Frequency
f^{Analyte}	Volume fraction of the analyte in the solution
g	Acceleration due to gravity
h	Depth
I	Intensity of IR radiation transmitted by the analyte
I_{exp}	Integral band intensity in the experimental spectrum
I_o	Intensity of IR radiation transmitted by the solvent
I_p	Intensity of *p*-polarized light
I_{rand}	Integral band intensity in the calculated random spectrum
I_s	Intensity of *s*-polarized light
i	Current
i^{in}	In-phase current
i^{out}	Out-of phase current
J_o	Zero order Bessel function
J_2	Second order Bessel function
j	Current density
l	Length
l_{chain}	Maximal length of the hydrocarbon chain
M^{Analyte}	Molar mass of the pure analyte in the solution
n	Refractive index
n^{Analyte}	Refractive index of the pure analyte
$n_\infty^{\text{Analyte}}$	Refractive index of the analyte in IR in the spectral regions where no absorption of the IR light by the analyte takes place
P	Cauchy principal value
S	Order parameter
T_m	Main phase transition temperature
V	Voltage
V_{chain}	Volume of the hydrocarbon chain
w	Width
X_M	Surface potential of the membrane
x^{Analyte}	Molar fraction of the pure analyte in the solution
Γ	Surface concentration
Γ_{lim}	Maximal surface concentration
Γ_t	Surafce concentration at the transfer pressure
γ	Surface tension of monolayer covered interface
γ_o	Surface tension of uncovered interface
δ_o	Maximum phase shift of the incident light by the PEM
θ	Angle between the direction of $\vec{E}$ and $\vec{\mu}$ vectors
θ_{chain}	Angle of chain tilt

θ^{i}	Angle of incidence
θ^{r}	Angle of reflection
θ^{t}	Angle of transmission
ϑ	Contact angle
K_s	Compressibility modulus
k	Attenuation coefficient
$k^{Analyte}$	Attenuation coefficient of the pure analyte
λ	Wavelength
$\vec{\mu}$	Transition dipole vector
$\tilde{\nu}$	Wavenumber
$\tilde{\nu_o}$	Frequency at which the refractive index is evaluated
ν_{as}	Frequency of asymmetric stretching band
ν_s	Frequency of symmetric stretching band
Π	Surface pressure
Π_c	Surface pressure of the monolayer collapse
ρ	Density
$\rho^{Analyte}$	Density of the analyte in the solution
ρ_l	Denisty of liquid
σ_M	Charge density of the membrane
Φ	Surface coverage
φ	Phase shift
$\phi_{M\|S}$	Potential across the metal|solution interface
ω	Excitation frequency of the PEM

8 References

1. R. Guidelli, G. Aloisi, L. Becucci, A. Dolfi, M. R. Moncelli and F. T. Buoninsegni, *J. Electroanal. Chem.*, 2001, **504**, 1.
2. J. Lipkowski, *Phys. Chem. Chem. Phys.*, 2010, **12**, 13874.
3. S. L. Horswell, V. Zamlynny, H.-Q. Li, A. R. Merrill and J. Lipkowski, *Faraday Discuss.*, 2002, **121**, 405.
4. I. Zawisza, A. Lachenwitzer, V. Zamlynny, S. L. Horswell, J. D. Goddard and J. Lipkowski, *Biophys. J.*, 2003, **85**, 4055.
5. I. Zawisza, X. Bin and J. Lipkowski, *Langmuir*, 2007, **23**, 5180.
6. E. Madrid and S. L. Horswell, *Langmuir*, 2013, **29**, 1695.
7. E. Madrid and S. L. Horswell, *Electrochim. Acta*, 2014, **146**, 850.
8. T. Y. Tsong and R. D. Astumian, *Annu. Rev. Physiol.*, 1988, **50**, 273.
9. M. Nullmeier, H. Koliwer-Brandl, S. Kelm, P. Zägel, K.-W. Koch and I. Brand, *ChemPhysChem.*, 2011, **12**, 1066.
10. S. Ye, H. Li, F. Wei, J. Jasensky, A. P. Boughton, P. Yang and Z. Chen, *J. Am. Chem. Soc.*, 2012, **134**, 6237.
11. J. J. Leitch, C. L. Brosseau, S. G. Roscoe, K. Bessonov, J. R. Dutcher and J. Lipkowski, *Langmuir*, 2013, **29**, 965.
12. T. Laredo, J. R. Dutcher and J. Lipkowski, *Langmuir*, 2011, **27**, 10072.
13. Z. Su, M. Shodiev, J. Jay Leitch, F. Abbasi and J. Lipkowski, *J. Electroanal. Chem.*, 2018, **819**, 251.
14. M. Osawa, K. Ataka, K. Yoshii and T. Yotsuyanagi, *J. Electron Spectrosc.*, 1993, **64/65**, 371.
15. K. Ataka, T. Yotsuyanagi and M. Osawa, *J. Chem. Phys.*, 1996, **100**, 10664.
16. J.W. Russell, J. Overend, K. Scanion, M. Severson and A. Bewick, *J. Phys. Chem.*, 1982, **86**, 3066.
17. T. Davidson, B. S. Pons, A. Bewick and P. P. Schmidt, *J. Electroanal. Chem.*, 1981, **125**, 237.
18. B. Khairalla, J. Juhaniewicz-Debinska, S. Sek and I. Brand, *Bioelectrochemistry*, 2020, **132**, 107443.
19. I. Burgess, M. Li, S. L. Horswell, G. Szymanski, J. Lipkowski, J. Majewski and S. Satija, *Biophys. J.*, 2004, **86**, 1763.

20. C. W. Meuse, S. Krueger, C. F. Majkrzak, J. A. Dura, J. Fu, J. T. Connor and A. L. Plant, *Biophys. J.*, 1998, **74**, 1388.
21. F. Neville, Y. Ishitsuka, C. S. Hodges, O. Konovalov, A. J. Waring, R. Lehrer, K. Y. C. Lee and D. Gidalevitz, *Soft Matter*., 2008, **4**, 1665.
22. S. E. Blondelle and K. Lohner, *Curr. Pharm. Des.*, 2010, **16**, 3204.
23. L. Rivas, J. R. Luque-Ortega, M. Fernández-Reyes and D. Andreu, *J. Appl. Biomed.*, 2010, **8**, 159.
24. Y. Shai, *Biochim. Biophys. Acta*, 1999, **1462**, 55.
25. A. A. Strömstedt, L. Ringstad, A. Schmidtchen and M. Malmsten, *Curr. Opin. Colloid Interface Sci.*, 2010, **15**, 467.
26. G. Saberwal and R. Nagaraj, *Biochim. Biophys. Acta*, 1994, **1197**, 109.
27. H. Sato and J. B. Feix, *Biochim. Biophys. Acta*, 2006, **1758**, 1245.
28. S. Dosler and A. A. Gerceker, *J. Chemother.*, 2012, **24**, 137.
29. S. Galdiero, A. Falanga, M. Cantisani, M. Vitiello, G. Morelli and M. Galdiero, *Int. J. Mol. Sci.*, 2013, **14**, 18758.
30. H. W. Huang, *Biochemistry*, 2000, **39**, 8347.
31. A.G. Lee, *Biochim. Biophys. Acta*, 2003, **1612**, 1.
32. C. Hunte and S. Richers, *Curr. Opin. Struct. Biol.*, 2008, **18**, 406.
33. M. Esmann and D. Marsh, *Chem. Phys. Lipids*, 2006, **141**, 94.
34. O. G. Mouritsen and M. Bloom, *Annu. Rev. Biophys. Biomol. Struct.*, 1993, **22**, 145.
35. U. Harzer and B. Bechinger, *Biochemistry*, 2000, **39**, 13106.
36. J. Juhaniewicz and S. Sek, *Electrochim. Acta*, 2015, **162**, 53.
37. L. Ringstad, E. Protopapa, B. Lindholm-Sethson, A. Schmidtchen, A. Nelson and M. Malmsten, *Langmuir*, 2008, **24**, 208.
38. S. Rex, *Biophys. Chem.*, 1996, **58**, 75.
39. L. Yang, T. A. Harroun, T. M. Weiss, L. Ding and H. W. Huang, *Biophys. J.*, 2001, **81**, 1475.
40. K. Matsuzaki, S. Yoneyama and K. Miyajima, *Biophys. J.*, 1997, **73**, 831.
41. Y. Li, Q. Xiang, Q. Zhang, Y. Huang and Z. Su, *Peptides*, 2012, **37**, 207.
42. H. Khandelia, J. H. Ipsen and O. G. Mouritsen, *Biochim. Biophys. Acta*, 2008, **1778**, 1528.

43. J. Juhaniewicz and S. Sek, *Electrochim. Acta*, 2016, **197**, 336.
44. T. C. Terwilliger and D. Eisenberg, *J. Biol. Chem.*, 1982, **257**, 6016.
45. W. F. Degrado, G. F. Musso, M. Lieber, E. T. Kaiser and F. J. Kézdy, *Biophys. J.*, 1982, **37**, 329.
46. M. Wachinger, A. Kleinschmidt, D. Winder, N. Von Pechmann, A. Ludvigsen, M. Neumann, R. Holle, B. Salmons, V. Erfle and R. Brack-Werner, *J. Gen. Virol.*, 1998, **79**, 731.
47. E. Sackmann, *Science*, 1996, **271**, 43.
48. L. M. Goldenberg, *J. Electroanal. Chem.*, 1994, **379**, 3.
49. J. D. Swalen, D. L. Allara, J. D. Andrade, E. A. Chandross, S. Garoff, J. Israelachvili, T. J. McCarthy, R. Murray, R. F. Pease, J. F. Rabolt, K. J. Wynne and H. Yu, *Langmuir*, 1987, **3**, 932.
50. I. Zawisza and J. Lipkowski, *Langmuir*, 2004, **20**, 4579.
51. I. Zawisza, G. Wittstock, R. Boukherroub and S. Szunerits, *Langmuir*, 2008, **24**, 3922.
52. X. Bin, I. Zawisza, J. D. Goddard and J. Lipkowski, *Langmuir*, 2005, **21**, 330.
53. X. Bin, S. L. Horswell and J. Lipkowski, *Biophys. J.*, 2005, **89**, 592.
54. X. Bin and J. Lipkowski, *J. Phys. Chem. B*, 2006, **110**, 26430.
55. W. Dowhan, *Annu. Rev. Biochem.*, 1997, **66**, 199.
56. G. Roberts, ed., *Langmuir-Blodgett films*, Plenum Press, New York, 1990.
57. P. L. Yeagle, ed., *The structure of biological membranes*, CRC Press, Boca Raton, London, New York, Washington, D.C, 2005.
58. A. Wardak and H. Ti Tien, *Bioelectrochem. Bioenerg.*, 1990, **24**, 1.
59. G. van Meer, D. R. Voelker and G. W. Feigenson, *Nat. Rev. Mol. Cell Biol.*, 2008, **9**, 112.
60. E. Gorter and F. Grendel, *J. Exp. Med.*, 1925, **41**, 439.
61. V. Vogel and M. Sheetz, *Nat. Rev. Mol. Cell Biol.*, 2006, **7**, 265.
62. R. Phillips, T. Ursell, P. Wiggins and P. Sens, *Nature*, 2009, **459**, 379.
63. O. G. Mouritsen and M. Bloom, *Biophys. J.*, 1984, **46**, 141.
64. A. Kleinzeller, *News Physiol. Sci.*, 1997, **12**, 49.
65. I. Langmuir, *J. Am. Chem. Soc.*, 1917, **39**, 1848.
66. J. F. Danielli, *J. Cell. Comp. Physiol.*, 1936, **7**, 393.

67. J. D. Roberston, *J. Cell Biol.*, 1981, **91**, 189s.
68. S. J. Singer and G. L. Nicolson, *Science*, 1972, **175**, 720.
69. J. N. Israelachvili, S. Marčelja and R. G. Horn, *Q. Rev. Biophys.*, 1980, **13**, 121.
70. K. Simons and W. L.C. Vaz, *Annu. Rev. Biophys. Biomol. Struct.*, 2004, **33**, 269.
71. D. Lingwood and K. Simons, *Science*, 2010, **327**, 46.
72. L. Rajendran and K. Simons, *J. Cell Sci.*, 2005, **118**, 1099.
73. W. Fan and R. M. Evans, *Cell*, 2015, **161**, 962.
74. S. Garcia-Manyes and F. Sanz, *Biochim. Biophys. Acta*, 2010, **1798**, 741.
75. R. A. Cooper, *J. Supramol. Struct.*, 1978, **8**, 413.
76. R. M. A. Sullan, J. K. Li, C. Hao, G. C. Walker and S. Zou, *Biophys. J.*, 2010, **99**, 507.
77. M. R. Vist and J. H. Davis, *Biochemistry*, 1990, **29**, 451.
78. A. G. Clamp, S. Ladha, D. C. Clark, R. F. Grimble and E. K. Lund, *Lipids*, 1997, **32**, 179.
79. V. Zamlynny, I. Zawisza and J. Lipkowski, *Langmuir*, 2003, **19**, 132.
80. N. Garcia-Araez, C. L. Brosseau, P. Rodriguez and J. Lipkowski, *Langmuir*, 2006, **22**, 10365.
81. P. Sondhi, D. Lingden and K. J. Stine, *Coatings*, 2020, **10**, 981.
82. M. H. Wood, D. C. Milan, R. J. Nichols, M. T. L. Casford and S. L. Horswell, *RSC Adv.*, 2021, **11**, 19768.
83. M. Zaborowska, M. Broniatowski, P. Wydro, D. Matyszewska and R. Bilewicz, *J. Mol. Liq.*, 2020, **313**, 113570.
84. A. A. Brian and H. M. McConnell, *Proc. Natl. Acad. Sci. USA*, 1984, **81**, 6159.
85. L. K. Tamm and H. M. McConnell, *Biophys. J.*, 1985, **47**, 105.
86. M. Tanaka and E. Sackmann, *Nature*, 2005, **437**, 656.
87. A. L. Plant, *Langmuir*, 1993, **9**, 2764.
88. H. T. Cheng, Megha and E. London, *J. Biol. Chem.*, 2009, **284**, 6079.
89. Z. Xiao, N. Huang, M. Xu, Z. Lu and Y. Wei, *Chem. Lett.*, 1998, **27**, 225.
90. G. Elender, M. Kuehner and E. Sackmann, *Biosens. Bioelectron.*, 1996, **11**, 565.
91. W. Knolla, C.W. Frank, C. Heibel, R. Naumann, A. Offenhausser,J. Rühe, E.K. Schmidt, W.W. Shen and A. Sinner, *Rev. Mol. Biotechnol.*, 2000, **74**, 137.
92. J. Yuan, C. Hao, M. Chen, P. Berini and S. Zou, *Langmuir*, 2013, **29**, 221.

93. I. Reviakine, A. Simon and A. Brisson, *Langmuir*, 2000, **16**, 1473.
94. D. Konarzewska, J. Juhaniewicz, A. Guzeloglu and S. Sek, *Biochim. Biophys. Acta*, 2017, **1859**, 475.
95. M. Winterhalter, *Colloids Surf., A*, 1999, **149**, 161.
96. E. Bamberg and R. Benz, *Biochim. Biophys. Acta*, 1976, **426**, 570.
97. E.-L. Florin and H. E. Gaub, *Biophys. J.*, 1993, **64**, 375.
98. D. F. Sargent, *J. Membr. Biol.*, 1975, **23**, 227.
99. L. J. Breckenridge and W. Almers, *Nature*, 1987, **328**, 814.
100. K. Debus, J. Hartmann, G. Kilic and M. Lindau, *Biophys. J.*, 1995, **69**, 2808.
101. I. Burgess, M. Li, S. L. Horswell, G. Szymanski, J. Lipkowski, S. Satija and J. Majewski, *Colloids Surf., B*, 2005, **40**, 117.
102. P. A. Janmey and P. K. J. Kinnunen, *Trends Cell Biol.*, 2006, **16**, 538.
103. K. Simons and E. Ikonen, *Nature*, 1997, **387**, 569.
104. D. A. Brown and E. London, *J. Biol. Chem.*, 2000, **275**, 17221.
105. K. Simons and E. lkonen, *Science*, 2000, **290**, 1721.
106. H. Hauser, I. Pascher, R.M. Pearson and S. Sundell, *Biochim. Biophys. Acta*, 1981, **650**, 21.
107. M. Chen, M. Li, C. L. Brosseau and J. Lipkowski, *Langmuir*, 2009, **25**, 1028.
108. J. Pencer, M.-P. Nieh, T. A. Harroun, S. Krueger, C. Adams and J. Katsaras, *Biochim. Biophys. Acta*, 2005, **1720**, 84.
109. C. L. Brosseau, X. Bin, S. G. Roscoe and J. Lipkowski, *J. Electroanal. Chem.*, 2008, **621**, 222.
110. C. L. Brosseau, J. Leitch, X. Bin, M. Chen, S. G. Roscoe and J. Lipkowski, *Langmuir*, 2008, **24**, 13058.
111. M. L. Mitchell and R. A. Dluhy, *J. Am. Chem. Soc.*, 1988, **110**, 712.
112. R. G. Snyder, S. L. Hsut and S. Krimm, *Spectrochim. Acta*, 1978, **34A**, 395.
113. C. R. H. Raetz, *Annu. Rev. Biochem.*, 1990, **59**, 129.
114. A. Som and G. N. Tew, *J. Phys. Chem. B*, 2008, **112**, 3495.
115. C. R. H. Raetz and C. Whitfield, *Annu. Rev. Biochem.*, 2002, **71**, 635.
116. D. L. Diedrich and E. H. Cota-Robles, *J. Bacteriol.*, 1974, **119**, 1006.
117. R. Heinzmann, S. L. Grage, C. Schalck, J. Bürck, Z. Bánóczi, O. Toke and A. S. Ulrich, *Eur. Biophys. J.*, 2011, **40**, 463.

118. P. Wydro and K. Witkowska, *Colloids Surf., B*, 2009, **72**, 32.
119. M. Caroff and D. Karibian, *Carbohydr. Res.*, 2003, **338**, 2431.
120. R. M. Shroll and T. P. Straatsma, *Biopolymers*, 2002, **65**, 395.
121. C. Alexander and E. T. Rietschel, *J. Endotoxin Res.*, 2001, **7**, 167.
122. E. Schneck, E. Papp-Szabo, B. E. Quinn, O. V. Konovalov, T. J. Beveridge, D. A. Pink and M. Tanaka, *J. R. Soc., Interface*, 2009, **6**, S671.
123. E. Schneck, T. Schubert, O. V. Konovalov, B. E. Quinn, T. Gutsmann, K. Brandenburg, R. G. Oliveira, D. A. Pink and M. Tanaka, *Proc. Natl. Acad. Sci. U. S. A.*, 2010, **107**, 9147.
124. A. Steimle, I. B. Autenrieth and J.-S. Frick, *Int. J. Med. Microbiol.*, 2016, **306**, 290.
125. E. L. Wu, O. Engström, S. Jo, D. Stuhlsatz, M. S. Yeom, J. B. Klauda, G. Widmalm and W. Im, *Biophys. J.*, 2013, **105**, 1444.
126. W. Im and S. Khalid, *Annu. Rev. Phys. Chem*, 2020, **71**, 8.1.
127. N. Paracini, L. A. Clifton, M. W. A. Skoda and J. H. Lakey, *Proc. Natl. Acad. Sci. U. S. A.*, 2018, **115**, E7587-E7594.
128. A. Ebbensgaard, H. Mordhorst, F. M. Aarestrup and E. B. Hansen, *Front. Microbiol.*, 2018, **9**, 2153.
129. K. Kochan, D. Perez-Guaita, J. Pissang, J.-H. Jiang, A. Y. Peleg, D. McNaughton, P. Heraud and B. R. Wood, *J. R. Soc. Interface*, 2018, **15**, 20180115.
130. A. P. Le Brun, L. A. Clifton, C. E. Halbert, B. Lin, M. Meron, P. J. Holden, J. H. Lakey and S. A. Holt, *Biomacromolecules*, 2013, **14**, 2014.
131. T. Abraham, S. R. Schooling, T. J. Beveridge and J. Katsaras, *Biomacromolecules*, 2008, **9**, 2799.
132. P. Hsu, F. Samsudin, J. Shearer and S. Khalid, *J. Phys. Chem. Lett.*, 2017, **8**, 5513.
133. T. J. Piggot, D. A. Holdbrook and S. Khalid, *J. Phys. Chem. B*, 2011, **115**, 13381.
134. M. Lima, M. Nader, D. Santos and T. Soares, *J. Braz. Chem. Soc.*, 2019, **30**, 2219.
135. S. Kaufmann, K. Ilg, A. Mashaghi, M. Textor, B. Priem, M. Aebi and E. Reimhult, *Langmuir*, 2012, **28**, 12199.
136. L. A. Clifton, M. W. A. Skoda, E. L. Daulton, A. V. Hughes, A. P. Le Brun, J. H. Lakey and S. A. Holt, *J. R. Soc. Interface*, 2013, **10**, 20130810.
137. K. Brandenburg, S. Kusumoto and U. Seydel, *Biochim. Biophys. Acta*, 1997, **1329**, 183.

138. G. Emmerling, U. Henning, and T. Gulik-Krzywicki, *Eur. J. Biochem.*, 1977, **78**, 503.
139. C. Jeworrek, F. Evers, J. Howe, K. Brandenburg, M. Tolan and R. Winter, *Biophys. J.*, 2011, **100**, 2169.
140. T. Abraham, S. R. Schooling, M. Nieh, N. Kučerka, T. J. Beveridge and J. Katsaras, *J. Phys. Chem. B*, 2007, **111**, 2477.
141. S. Sek, T. Laredo, J. R. Dutcher and J. Lipkowski, *J. Am. Chem. Soc.*, 2009, **131**, 6439.
142. J. Lin, J. Motylinski, A. J. Krauson, W. C. Wimley, P. C. Searson and K. Hristova, *Langmuir*, 2012, **28**, 6088.
143. R. E. W. Hancock, T. Falla and M. Brown, *Adv. Microb. Physiol.*, 1995, **37**, 135.
144. B. Bechinger, *Biochim. Biophys. Acta*, 1999, **1462**, 157.
145. T. Benachir, M. Monette, J. Grenier and M. Lafleur, *Eur. Biophys. J.*, 1997, **25**, 201.
146. P. Wessman, A. A. Strömstedt, M. Malmsten and K. Edwards, *Biophys. J.*, 2008, **95**, 4324.
147. E. Gazit, I. R. Miller, P. C. Biggin, M. S. P. Sansom and Y. Shai, *J. Mol. Biol.*, 1996, **258**, 860.
148. Z. O. Shenkarev, S. V. Balandin, K. I. Trunov, A. S. Paramonov, S. V. Sukhanov, L. I. Barsukov, A. S. Arseniev and T. V. Ovchinnikova, *Biochemistry*, 2011, **50**, 6255.
149. M. Smetanin, S. Sek, F. Maran and J. Lipkowski, *Biochim. Biophys. Acta*, 2014, **1838**, 3130.
150. F. Jean-François, J. Elezgaray, P. Berson, P. Vacher and E. J. Dufourc, *Biophys. J.*, 2008, **95**, 5748.
151. T. Gutsmann, M. Fix, J. W. Larrick and A. Wiese, *J. Membr. Biol.*, 2000, **176**, 223.
152. L. Wang, J. W. Brauner, G. Mao, E. Crouch, B. Seaton, J. Head, K. Smith, C. R. Flach and R. Mendelsohn, *Biochemistry*, 2008, **47**, 8103.
153. Y. Rosenfeld and Y. Shai, *Biochim. Biophys. Acta*, 2006, **1758**, 1513.
154. S. Nathoo, J. K. Litzenberger, D. C. Bay, R. J. Turner and E. J. Prenner, *Chem. Phys. Lipids*, 2013, **167-168**, 33.
155. I. Rady, I. A. Siddiqui, M. Rady and H. Mukhtar, *Cancer Lett.*, 2017, **402**, 16.

156. A. Glättli, I. Chandrasekhar and W. F. van Gunsteren, *Eur. Biophys. J.*, 2006, **35**, 255.
157. D. Allende, *Chem. Phys. Lipids*, 2003, **122**, 65.
158. S. P. Verma, D. F. H. Wallach and I. C. P. Smith, *Biochim. Biophys. Acta*, 1974, **345**, 129.
159. S. Liu, M. Yu, Y. He, L. Xiao, F. Wang, C. Song, S. Sun, C. Ling and Z. Xu, *Hepatology*, 2008, **47**, 1964.
160. R. Smith, F. Separovic, T. J. Milne, A. Whittaker, F. M. Bennett, B. A. Cornell and A. Makriyannis, *J. Mol. Biol.*, 1994, **241**, 456.
161. G. van den Bogaart, J. V. Guzmán, J. T. Mika and B. Poolman, *J. Biol. Chem.*, 2008, **283**, 33854.
162. A. A. Strömstedt, P. Wessman, L. Ringstad, K. Edwards and M. Malmsten, *J. Colloid Interface Sci.*, 2007, **311**, 59.
163. F. R. Svensson, P. Lincoln, B. Nordén and E. K. Esbjörner, *Biochim. Biophys. Acta*, 2011, **1808**, 219.
164. T.C. Terwilliger, L. Weissman and D. Eisenberg, *Biophys. J.*, 1982, **37**, 353.
165. Y.-H. Lam, S. R. Wassall, C. J. Morton, R. Smith and F. Separovic, *Biophys. J.*, 2001, **81**, 2752.
166. C. Altenbach and W.L. Hubbell, *Proteins: Struct., Funct., Genet.*, 1988, **3**, 230.
167. B. Bechinger, *J. Membr. Biol.*, 1997, **156**, 197.
168. A. M. Batenburg, J. H. Van Esch, J. Leunissen-Bijvelt, A. J. Verkleij and B. De Kruijff, *FEBS Lett.*, 1987, **223**, 148.
169. A. S. Ladokhin and S. H. White, *Biochim. Biophys. Acta*, 2001, **1514**, 253.
170. C. R. Flach, F. G. Prendergast and R. Mendelsohn, *Biophys. J.*, 1996, **70**, 539.
171. Z. Su, J. Jay Leitch, F. Abbasi, R. J. Faragher, A. L. Schwan and J. Lipkowski, *J. Electroanal. Chem.*, 2018, **812**, 213.
172. M. C. Petty, *Encycl. Nanosci. Nanotechnol.*, 2004, **8**, 295.
173. J. C. Love, L. A. Estroff, J. K. Kriebel, R. G. Nuzzo and G. M. Whitesides, *Chem. Rev.*, 2005, **105**, 1103.
174. A. J. Bard, H. D. Abruiia, C. E. Chidsey, L. R. Faulkner, S. W. Feldberg, K. Itaya, M. Majda, O. Melroy, R. W. Murray, M. D. Porter, M. P. Soriaga and H. S. White, *J. Phys. Chem.*, 1993, **97**, 7147.

175. T. Govindarajan and R. Shandas, *Polymers*, 2014, **6**, 2309.
176. S. H. Lee, S. M. Kim and S.-T. Wu, *J. Soc. Inf. Disp.*, 2009, **17**, 551.
177. H. E. Katz and J. Huang, *Annu. Rev. Mater. Res.*, 2009, **39**, 71.
178. P. J. Liew, C. Y. Yap, J. Wang, T. Zhou and J. Yan, *Int. J. Extrem. Manuf.*, 2020, **2**, 12004.
179. A. Vilan and D. Cahen, *Chem. Rev.*, 2017, **117**, 4624.
180. E. P. Tomlinson, M. E. Hay and B. W. Boudouris, *Macromolecules*, 2014, **47**, 6145.
181. G. Ozaydin-Ince, A. M. Coclite and K. K. Gleason, *Rep. Prog. Phys.*, 2012, **75**, 16501.
182. A. Luzio, E. V. Canesi, C. Bertarelli and M. Caironi, *Materials*, 2014, **7**, 906.
183. D. M. Adams, L. Brus, C. E. D. Chidsey, S. Creager, C. Creutz, C. R. Kagan, P. V. Kamat, M. Lieberman, S. Lindsay, R. A. Marcus, R. M. Metzger, M. E. Michel-Beyerle, J. R. Miller, M. D. Newton, D. R. Rolison, O. Sankey, K. S. Schanze, J. Yardley and X. Zhu, *J. Phys. Chem. B*, 2003, **107**, 6668.
184. M. Trojanowicz, *Fresenius J. Anal. Chem.*, 2001, **371**, 246.
185. D. M. Burn, L. B. Duffy, R. Fujita, S. L. Zhang, A. I. Figueroa, J. Herrero-Martin, G. van der Laan and T. Hesjedal, *Sci. Rep.*, 2019, **9**, 10793.
186. A. Richardella, A. Kandala, J. S. Lee and N. Samarth, *APL Mater.*, 2015, **3**, 83303.
187. W. Tian, W. Yu, J. Shi and Y. Wang, *Materials*, 2017, **10**, 814.
188. B.-H. Chou, Z.-Q. Huang, C.-H. Hsu, F.-C. Chuang, Y.-T. Liu, H. Lin and A. Bansil, *New J. Phys.*, 2014, **16**, 115008.
189. A. Heller, *AIChE J.*, 2005, **51**, 1054.
190. S. Karki, H. Kim, S.-J. Na, D. Shin, K. Jo and J. Lee, *Asian J. Pharm. Sci.*, 2016, **11**, 559.
191. B. B. Hsu, M.-H. Park, S. R. Hagerman and P. T. Hammond, *Proc. Natl. Acad. Sci. U. S. A.*, 2014, **111**, 12175.
192. W. Chen and T. J. McCarthy, *Macromolecules*, 1997, **30**, 78.
193. M. G. Moloney, *J. Phys. D: Appl. Phys.*, 2008, **41**, 174006.
194. F. Zaera, *J. Phys. Chem. C*, 2008, **112**, 16196.
195. L. T. de Jonge, S. C. G. Leeuwenburgh, J. G. C. Wolke and J. A. Jansen, *Pharm. Res.*, 2008, **25**, 2357.

196. A. Vioux, J. Bideau, P. H. Mutin and D. Leclercq, *Top. Curr. Chem.*, 2004, **232**, 145.
197. D. K. Martin, *Nanobiotechnology of biomimetic membranes*, Springer, New York, 2007.
198. S. Acharya, J. P. Hill and K. Ariga, *Adv. Mater.*, 2009, **21**, 2959.
199. A. Modlinska and D. Bauman, *Int. J. Mol. Sci.*, 2011, **12**, 4923.
200. S. Malik and C. C. Tripathi, *J. Surf. Eng. Mater. Adv. Technol.*, 2013, **3**, 235.
201. A. Blume, *ChemTexts*, 2018, **4**, 1.
202. E. Fahy, S. Subramaniam, H. A. Brown, C. K. Glass, A. H. Merrill, R. C. Murphy, C. R. H. Raetz, D. W. Russell, Y. Seyama, W. Shaw, T. Shimizu, F. Spener, G. van Meer, M. S. VanNieuwenhze, S. H. White, J. L. Witztum and E. A. Dennis, *Eur. J. Lipid Sci. Technol.*, 2005, **107**, 337.
203. R. R. Watson and F. de Meester, eds., *Handbook of lipids in human function: fatty acids*, Elsevier, Amsterdam, 2016.
204. K. Murzyn, T. Róg, and M. P-Gierula, *Biophys. J.*, 2005, **88**, 1091.
205. L. Picas, C. S-Germa`, M. T. Montero, and J. H.-Borrell, *J. Phys. Chem. B*, 2010, **114**, 3543.
206. J. M. Smaby, M. Momsen, V. S. Kulkarni, and R. E. Brown, *Biochemistry*, 1996, **35**, 5696.
207. R. Almog and C.A. Mannella, *Biophys. J.*, 1996, **71**, 3311.
208. S. A. Hussain, S. Deb and D. Bhattacharjee, *J. Sc. Dev. Env. Res.*, 2005, **4**, 1.
209. T. Bjørnholm,T. Hassenkam and N. Reitzel, *J. Mater. Chem.*, 1999, **9**, 1975.
210. O. N. Oliveira Jr., *Braz. J. Phys.*, 1992, **22**, 60.
211. M. Nullmeier, H. Koliwer-Brandl, S. Kelm and I. Brand, *J. Electroanal. Chem.*, 2010, **649**, 177.
212. S. A. Hussain, B. Dey, D. Bhattacharjee and N. Mehta, *Heliyon*, 2018, **4**, e01038.
213. R. B. Dabke, A. Dhanabalan, S. Major, S. S. Talwar, R. Lal and A. Q. Contractor, *Thin Solid Films*, 1998, **335**, 203.
214. A. Nelson, *J. Chem. Soc., Faraday Trans.*, 1993, **89**, 2977.
215. J. Lipkowski, *Can. J. Chem.*, 1999, **77**, 1163.
216. H. T. Tien, *Bilayer lipid membranes (BLM): theory and practice*, Marcel Dekker, New York, 1974.

217. R. Coronado, *Annu. Rev. Biophys. Biophys. Chem.*, 1986, **15**, 259.
218. J. Richer and J. Lipkowski, *J. Electrochem.Soc*, 1986, **133**, 121.
219. A. R. Hillman, K. S. Ryder, E. Madrid, A. W. Burley, R. J. Wiltshire, J. Merotra, M. Grau, S. L. Horswell, A. Glidle, R. M. Dalgliesh, A. Hughes, R. Cubitte and A. Wildese, *Faraday Discuss.*, 2010, **145**, 357.
220. A. J. Bard and L. R. Faulkner, eds., *Electrochemical methods: fundamentals and applications*, John Wiley & Sons, Inc, New York, 2001.
221. S. Lingler, I. Rubinstein, W. Knoll and A. Offenhäusser, *Langmuir*, 1997, **13**, 7085.
222. V. I. Passechnik, T. Hianik, S. A. Ivanov and B. Sivak, *Electroanalysis*, 1998, **10**, 295.
223. J. M. Crowley, *Biophys. J.*, 1973, **13**, 711.
224. A. Nelson and A. Benton, *J. Electroanal. Chem.*, 1986, **202**, 253.
225. Z. Su, J. Leitch and J. Lipkowski, *Z. Phys. Chem.*, 2012, **226**, 995.
226. R. G. Greenler, *J. Chem. Phys.*, 1969, **50**, 1963.
227. H. H. Mantsch and D. Chapman, *Infrared spectroscopy of biomolecules*, Wiley, New York, 1996.
228. D. Naumann, *Appl. Spectrosc. Rev.*, 2001, **36**, 239.
229. W. Petrich, *Appl. Spectrosc. Rev.*, 2001, **36**, 181.
230. A. Barth, *Biochim. Biophys. Acta*, 2007, **1767**, 1073.
231. S. A. Tatulian, ed., *Structural characterization of membrane proteins and peptides by FTIR and ATR-FTIR spectroscopy*, Springer, New York, 2013.
232. W.G. Golden, K. Kunimatsu and H. Seki, *J. Phys. Chem.*, 1984, **88**, 1275.
233. R. Jackson and V. Zamlynny, *Electrochim. Acta*, 2008, **53**, 6768.
234. I. Brand, *Z. Phys. Chem.*, 2016, **230**, 133.
235. N. Li, V. Zamlynny, J. Lipkowski, F. Henglein and B. Pettinger, *J. Electroanal. Chem.*, 2002, **524-525**, 43.
236. D. Blaudez, S. Castano and B. Desbat, *Biointerface characterization by advanced IR spectroscopy.: PM-IRRAS at liquid interfaces*, Elsevier, 2011.
237. V. Zamlynny and J. Lipkowski, ed., *Quantitative SNIFTIRS and PM IRRAS of organic molecules at electrode surfaces*, Wiley-VCH, Germany, 2006.
238. W.-P. Ulrich and H. Vogel, *Biophys. J.*, 1999, **76**, 1639.

239. K. W. Hipps and G. A. Crosby, *J. Phys. Chem.*, 1979, **83**, 555.
240. W. N. Hansen, *J. Opt. Soc. Am.*, 1968, **58**, 380.
241. R. G. Greenler, *J. Chem. Phys.*, 1966, **44**, 310.
242. M. Moskovits, *J. Chem. Phys.*, 1982, **77**, 4408.
243. T. Buffeteau, B. Desbat and J. M. Turlet, *J. Appl. Spectrosc.*, 1991, **45**, 380.
244. T. Buffeteau, B. Desbat and J-M. Turlet, *Microchim. Acta*, 1988, **95**, 23.
245. D.L. Allara and J. D. Swalen, *J. Phys. Chem.*, 1982, **86**, 2700.
246. D. L. Allara and R. G. Nuzzo, *Langmuir*, 1985, **1**, 52.
247. D. L. Allara, A. Baca and C. A. Pryde, *Macromolecules*, 1978, **11**, 1215.
248. J. Umemura, T. Kamata, T. Kawai and T. Takenaka, *J. Phys. Chem.*, 1990, **94**, 62.
249. A. Seelig and J. Seelig, *Biochemistry*, 1974, **13**, 4839.
250. H. Binder and H. Schmiedel, *Vib. Spectrosc.*, 1999, **21**, 51.
251. H. H. Mantsch and R. N. McElhaney, *Chem. Phys. Lipids*, 1991, **57**, 213.
252. R. N. Lewis, R. N. McElhaney, W. Pohle and H. H. Mantsch, *Biophys. J.*, 1994, **67**, 2367.
253. I. Ueda, J-S. Chiou, P. R. Krishna and H. Kamaya, *Biochim. Biophys. Acta*, 1994, **1190**, 412.
254. R. Mendelsohn, G. Mao and C. R. Flach, *Biochim. Biophys. Acta*, 2010, **1798**, 788.
255. R. Mendelsohn and D. J. Moore, *Chem. Phys. Lipids*, 1998, **96**, 141.
256. B. H. Stuart, *Infrared spectroscopy: fundamentals and applications*, John Wiley & Sons, Ltd, Chichester, 2004.
257. J. L. R. Arrondo, A. Muga, J. Castresana and F. M. Goni, *Prog. Biophys. Mol. Biol.*, 1993, **59**, 23.
258. W. K. Surewicz and H. H. Mantsch, *Biochim. Biophys. Acta*, 1988, **952**, 115.
259. W. K. Surewicz, H. H. Mantsch and D. Chapman, *Biochemistry*, 1993, **32**, 389.
260. I. Brand, ed., *Application of polarization modulation infrared reflection absorption spectroscopy in electrochemistry*, Springer, Zwitzerland, 2020.
261. Y. F. Dufrêne, T. Boland, J. W. Schneider, W. R. Bargera and G. U. Lee, *Faraday Discuss.*, 1998, **111**, 79.
262. J. H. Borrell and Ò. Domènech, *J. Phys. Chem. B*, 2017, **121**, 6882.
263. W. Kulig, H. Korolainen, M. Zatorska, U. Kwolek, P. Wydro, M. Kepczynski and T. Róg, *Langmuir*, 2019, **35**, 5944.

264. J. M. Wenda, J. Juhaniewicz, D. Tymecka, D. Konarzewska and S. Sek, *Langmuir*, 2017, **33**, 4619.
265. B. Seantier and B. Kasemo, *Langmuir*, 2009, **25**, 5767.
266. J. Marra and J.N. Israelachvili., *Biochemistry*, 1985, **24**, 4608.
267. J. Lipkowski, L. Stolberg, D.F. Yang, B. Pettinger, S. Mirwald, F. Henglein and D.M. Kolb, *Electrochim. Acta*, 1994, **39**, 1045.
268. A. Vieler, H. A. Scheidt, P. Schmidt, C. Montag, J. F. Nowoisky, M. Lohr, C. Wilhelm, D. Huster and R. Goss, *Biochim. Biophys. Acta*, 2008, **1778**, 1027.
269. H. M. Seeger, G. Marino, A. Alessandrini and P. Facci, *Biophys. J.*, 2009, **97**, 1067.
270. A. Alessandrini and P. Facci, *Soft Matter.*, 2014, **10**, 7145.
271. C. Suárez-Germà, M. T. Montero, J. Ignés-Mullol, J. Hernández-Borrell and O. Domènech, *J. Phys. Chem. B*, 2011, **115**, 12778.
272. R. G. Snyder, H. L. Strauss and C. A. Elliger, *J. Phys. Chem.*, 1982, **86**, 5145.
273. R. A. MacPhail, H. L. Strauss, R. G. Snyder and C. A. Elliger, *J. Phys. Chem.*, 1984, **88**, 334.
274. E. Palik, *Handbook of optical constants of solids II*, Academic Press, San Diego, 1998.
275. I. Pascher, S. Sundell, K. Harlos and H. Eibl, *Biochim. Biophys. Acta*, 1987, **896**, 77.
276. H. W. Ng, C. A. Laughton and S. W. Doughty, *J. Chem. Inf. Model.*, 2014, **54**, 573.
277. W. Ding, M. Palaiokostas, W. Wang and M. Orsi, *J. Phys. Chem. B*, 2015, **119**, 15263.
278. R.G. Snyder, G.L. Liang, H.L. Strauss and R. Mendelsohn, *Biophys. J.*, 1996, **71**, 3186.
279. W. Ding, M. Palaiokostas, G. Shahane, W. Wang and M. Orsi, *J. Phys. Chem. B*, 2017, **121**, 9597.
280. J. B. Klauda, V. Monje, T. Kim and W. Im, *J. Phys. Chem. B*, 2012, **116**, 9424.
281. J. N. Israelachvili, D. J. Mitchell and B. W. Ninham, *J. Chem. Soc., Faraday Trans. 2*, 1976, **72**, 1525.
282. D. M. Small, *J. Lipid Res.*, 1984, **25**, 1490.
283. V. V. Kumar, *Proc. Natl. Acad. Sci. USA*, 1991, **88**, 444.

284. J. Tuchtenhagen, W. Ziegler and A. Blume, *Eur. Biophys. J.*, 1994, **23**, 323.
285. O. Domènech, J. Ignés-Mullol, M. T. Montero and J. Hernandez-Borrell, *J. Phys. Chem. B*, 2007, **111**, 10946.
286. A. S. Luviano, J. Campos-Terán, D. Langevin, R. Castillo and G. Espinosa, *Langmuir*, 2019, **35**, 16734.
287. E. Madrid and S. L. Horswell, *Langmuir*, 2015, **31**, 12544.
288. G. Bryant, M. B. Taylor, T. A. Darwish, A. M. Krause-Heuer, B. Kent and C. J. Garvey, *Colloids Surf., B*, 2019, **177**, 196.
289. I. Brand, M. Nullmeier, T. Klüner, R. Jogireddy, J. Christoffers and G. Wittstock, *Langmuir*, 2010, **26**, 362.
290. T. Miyazawa, K. Fukushima and Y. Ideguchi, *J. Chem. Phys.*, 1962, **37**, 2764.
291. C. Y. Liang and M.R.J. Lytton, *J. Polymer Sci.*, 1962, **61**, S45.
292. D. C. Lee, A. A. Durrani and D. Chapman, *Biochim. Biophys. Acta*, 1984, **769**, 49.
293. D. Jefferies, J. Shearer and S. Khalid, *J. Phys. Chem. B*, 2019, **123**, 3567.
294. K. Brandenburg, *Biophys. J.*, 1993, **64**, 1215.
295. A. Barkleit, H. Foerstendorf, B. Li, A. Rossberg, H. Moll and G. Bernhard, *Dalton Trans.*, 2011, **40**, 9868.
296. T. Dudev and C. Lim, *J. Phys. Chem. B*, 2004, **108**, 4546.
297. A. Blume, W. Hubner and G. Messnert, *Biochemistry*, 1988, **27**, 8239.
298. M. Bollati, R. Villa, L. J. Gourlay, M. Benedet, G. Dehò, A. Polissi, A. Barbiroli, A. M. Martorana, P. Sperandeo, M. Bolognesi and M. Nardini, *FEBS J.*, 2015, **282**, 1980.
299. S. Qiao, Q. Luo, Y. Zhao, X. C. Zhang and Y. Huang, *Nature*, 2014, **511**, 108.
300. N. Kato, T. Sugiyama, S. Naito, Y Arakawa, H. Ito, N. Kido, M. Ohta and K. Sasaki, *Mol. Microbiol.*, 2000, **36**, 796.
301. A. Gorelik, K. Illes and B. Nagar, *Proc. Natl. Acad. Sci. USA*, 2018, **115**, E896.
302. L. Becucci and R. Guidelli, *Langmuir*, 2007, **23**, 5601.
303. S. Frey and L.K. Tamm, *Biophys. J.*, 1991, **60**, 922.
304. J. Juhaniewicz, L. Szyk-Warszyńska, P. Warszyński and S. Sęk, *Electrochim. Acta*, 2016, **204**, 206.
305. C. Balusek and J. C. Gumbart, *Biophys. J.*, 2016, **111**, 1409.

9 Own publications and conference contributions

9.1 Publications

- **B. Khairalla,** J. Juhaniewicz-Debinskab, S. Sek and I. Brand, The shape of lipid molecules affects potential-driven molecular-scale rearrangements in model cell membranes on electrodes, *Bioelectrochemistry*, 2020, **132**, 107443.

- I. Brand and **B. Khairalla,** Structural changes in the model of the outer cell membrane of Gram-negative bacteria interacting with melittin: An in situ spectrochemical study, *Faraday Discuss.*, 2021, **232**, 68.

- **B. Khairalla** and I. Brand**,** Membrane potentials trigger molecular-scale rearrangements in the outer membrane of Gram-negative bacteria, *Langmuir* 2022, **38**, 446.

9.2 Posters in national and international conferences

- **B. Khairalla** and I. Brand, Spectroelectrochemistry of asymmetric lipid bilayers, **International conference on adhesion in aqueous media: from biology to synthetic materials, AAM2019 conference**, September 2019, Dresden, Germany.
- **B. Khairalla** and I. Brand, Electric field induced changes in the structure of models of the outer membrane of Gram-negative bacteria adsorbed on the gold electrode surface. **Electrochemistry 2018 conference**, September 2018, Ulm, Germany.

- **B. Khairalla**, S. Sek and I. Brand, Impact of the acyl chain fluidity on the structure of models of the outer membrane of Gram-negative bacteria adsorbed on the gold electrode surface, **11. Treffen der Norddeutschen Biophysiker 2018**, Junary 2018, Borstel, Germany.
- **B. Khairalla**, S. Sek and I. Brand, How to prepare a biomimetic model of the outer membrane of cell membrane of Gram-negative bacteria, **SMCBS 2017**, November 2017, Żelechów, Polen.

10 Curriculum vitae

Personal information

Full Name:	Bishoy Hakim Latif Abosetta Khairalla
Date of birth:	22nd March 1989
Place of birth:	Alexandria (Egypt)
Nationality:	Egyptian

Education

Since 01/2017	Doctoral candidate at the University of Oldenburg, Oldenburg, Germany
10/2012 – 07/2015	M.Sc in Science (Chemistry) at University of Siegen, Siegen, Germany
09/2006 − 05/2010	B.Sc in Science (Chemistry & Biochemistry) at University of Alexandria, Alexandria, Egypt

Professional experience

01/2017 – 12/2019	Scientific coworker at the University of Oldenburg in the research group of Prof. Dr. Wittstock, Oldenburg, Germany
12/2017 – 02/2019	Instructor for "Kinetics of the enzymatic hydrolyse of urea" (basic electrochemical lab course for B.Sc. students), University of Oldenburg, Oldenburg, Germany
10/2019 – 12/2019	Instructor for "Photometric determination of copper (ions) in water" (basic electrochemical lab course for B.Sc. students), University of Oldenburg, Oldenburg, Germany

Grants and Awards

09/2018 – 09/2018	GDCh-travel grant to Electrochemistry 2018 conference in Ulm, Germany
04/2015 – 06/2015	DAAD Award (STIBET) from University of Siegen, Siegen, Germany
10/2013 – 10/2014	Scholarship award from University of Siegen, Siegen, Germany

Additional Qualifications

Techniques	Electrochemical techniques: cyclic voltammetry and chronocoulometry Polarization modulation infrared reflection absorption spectroscopy (PM IRRAS) Fourier-transform infrared spectroscopy (FTIR) Ellipsometry Atomic force microscopy (AFM) Surface plasmon resonance (SPR) Ultraviolet visible spectroscopy (UV-Vis Spectroscopy) Contact angle
Computer Skills	General softwares: Microsoft Office, Microsoft Windows and Citavi Chemistry packages: Origin lab, Chemdraw, Autolab Potentiostat, CH-Potentiostat, OPUS and NanpScope Analysis
Languages	Arabic (Mother tongue) English (Fluent) German (B1 level)

Ich versichere hiermit, dass ich diese Arbeit selbstständig verfasst und nur die angegebenen Quellen und Hilfsmittel benutzt habe. Während der Dissertation sind die unter “Publications” aufgelisteten Veröffentlichungen entstanden. Die Dissertation hat weder zu Teilen noch in Gänze einer anderen wissenschaftlichen Hochschule zur Begutachtung in einem Promotionsverfahren vorgelegen.

Oldenburg, den

Bishoy Khairalla